

**INSTITUT FÜR MECHANIK  
RUHR-UNIVERSITÄT BOCHUM**

**Jörn Mosler**

**On the numerical modeling of  
localized material failure at finite strains  
by means of variational mesh adaption and  
cohesive elements**

MITTEILUNGEN AUS DEM INSTITUT FÜR MECHANIK NR. 140

Februar 2007

Herausgeber:

Institut für Mechanik

— Schriftenreihe —

Ruhr-Universität Bochum

D-44780 Bochum

---

ISBN 978-3-935892-15-5

---

Dieses Werk ist urheberrechtlich geschützt. Die dadurch begründeten Rechte, insbesondere die der Übersetzung, des Nachdrucks, des Vortrags, der Entnahme von Abbildungen und Tabellen, der Funksendung, der Mikroverfilmung oder der Vervielfältigung auf anderen Wegen und der Speicherung in Datenverarbeitungsanlagen, bleiben, auch bei nur auszugsweiser Verwertung, vorbehalten. Eine Vervielfältigung dieses Werkes oder von Teilen dieses Werkes ist zulässig. Sie ist grundsätzlich vergütungspflichtig. Zuwiderhandlungen unterliegen den Strafbestimmungen des Urheberrechtsgesetzes.

©2007 Institut für Mechanik der Ruhr-Universität Bochum

Printed in Germany

## Zusammenfassung

Das Ziel der vorliegenden Arbeit liegt in der Entwicklung eines dreidimensionalen Finite-Elemente-Modells zur numerischen Simulation von Versagensformen unter Berücksichtigung endlicher Formänderung. Um auch komplexe Versagensvorgänge effizient beschreiben zu können, wird ein kohäsives Materialmodell verwendet. Hierzu wird eine konstitutive Gleichung betrachtet, welche den Spannungsvektor an einer Fläche mit einer Verschiebungsdiskontinuität, wie z.B. der Rissöffnung, koppelt. Die numerische Implementierung dieser erweiterten Materialbeschreibung stellt einen wesentlichen Themenkomplex der vorliegenden Arbeit dar. Im Gegensatz zu bisherigen Modellen erlaubt die vorgeschlagene Methode, dass beliebige konstitutive Gleichungen integriert werden können. Auch die Wahl der Approximationsgüte des stetigen Anteils der Deformationsabbildung unterliegt keinen Restriktionen. Um die Qualität des numerischen Modells abschätzen und gegebenenfalls verbessern zu können, wird im zweiten Teil der Arbeit ein neues adaptives Verfahren entwickelt. Unter der Annahme, das zu analysierende mechanische Problem sei durch einen variationellen Rahmen charakterisiert, wie z.B. die Minimierung eines Energiepotenzials, werden so genannte *variationelle adaptive Finite-Elemente-Methoden* ausgearbeitet. Diese Verfahren verwenden das zugrundeliegende variationelle Konzept sowohl zur Berechnung der Zustandsvariablen und der Deformationsabbildung als auch zur Verbesserung der Finite-Elemente-Diskretisierung. Die Leistungsfähigkeit dieser Methoden wird anhand zweier Prototypen ( $r$ -Adaptivität und  $h$ -Adaptivität) aufgezeigt und die Kopplung mit den zuvor beschriebenen kohäsiven Modellen skizziert.

## Abstract

This thesis is concerned with the development of three-dimensional finite element formulations suitable for the analysis of material failure at finite strains. Focus is on the simulation of complex failure patterns. For that purpose, a cohesive-type constitutive model is adopted and further elaborated. More precisely, a traction-separation law connecting the stress vector acting at a certain surface to a displacement jump such as a crack opening displacement is considered. A numerically efficient implementation of this non-standard model is one of the ultimate goals of the present thesis. The advocated finite element formulation allows for a broad range of different constitutive models. Furthermore, no restrictions regarding the space of the continuous displacement approximations are required, i.e., higher-order polynomials can be applied as well. For estimating the quality of the numerical solution a novel class of adaptive methods is presented in the second part of the thesis. Assuming the considered mechanical problem is driven by a variational principle such as energy minimization, so-called *variational adaptive finite element formulations* are developed. Within those methods, the state variables and the deformation mapping as well as an improved discretization are computed from the same overriding principle. The performance of those variational mesh adaptations is illustrated by means of two prototypes: variational  $r$ -adaptivity and variational  $h$ -adaptivity. Finally, the coupling of cohesive finite element formulations and variational mesh adaptation is briefly discussed.



# Contents

|          |  |           |
|----------|--|-----------|
| <b>1</b> | <b>Introduction</b>  | <b>1</b>  |
| 1.1      | Motivation . . . . .   | 1         |
| 1.2      | State of the art review . . . . .                                    | 4         |
| 1.3      | Structure of the present work . . . . .                              | 14        |
| <b>2</b> | <b>Constitutive modeling at finite strains</b>                       | <b>17</b> |
| 2.1      | Kinematics . . . . .   | 18        |
| 2.2      | Balance equations . . . . .  | 19        |
| 2.2.1    | Conservation of linear momentum . . . . .                            | 19        |
| 2.2.2    | Conservation of energy . . . . .                                     | 20        |
| 2.2.3    | The second law of thermodynamics / Balance of entropy . . . . .      | 21        |
| 2.3      | Hyperelasticity . . . . .  | 22        |
| 2.3.1    | Examples . . . . .   | 24        |
| 2.3.2    | Principle of minimum potential energy . . . . .                      | 24        |
| 2.4      | Plasticity theory . . . . .  | 25        |
| 2.4.1    | Fundamentals . . . . .   | 27        |
| 2.4.2    | Example: Single-crystal plasticity / single slip system . . . . .    | 30        |
| 2.4.3    | Numerical implementation . . . . .                                   | 31        |
| 2.5      | Standard dissipative media . . . . .                                 | 33        |
| 2.5.1    | Fundamentals . . . . .   | 34        |
| 2.5.2    | Numerical implementation . . . . .                                   | 36        |
| 2.5.3    | Example: VON MISES plasticity model . . . . .                        | 38        |
| 2.6      | Variational, thermomechanically coupled formulation . . . . .        | 41        |
| 2.7      | Range of application of classical local continuum theories . . . . . | 43        |

|          |  |           |
|----------|--|-----------|
| <b>3</b> | <b>Modeling of localized material failure by strong discontinuities</b>                            | <b>45</b> |
| 3.1      | Kinematics induced by strong discontinuities . . . . .   | 46        |
| 3.1.1    | Fundamentals . . . . .   | 46        |
| 3.1.2    | The strong discontinuity approach . . . . .  | 47        |
| 3.1.3    | Numerical implementation . . . . .   | 49        |
| 3.1.4    | Comparison to other SDA-based finite element formulations . . . . .                                | 53        |
| 3.2      | Constitutive equations . . . . .   | 55        |
| 3.2.1    | Constitutive Equations for $\mathbf{X} \in \Omega^\pm$ : Stress-strain laws . . . . .              | 55        |
| 3.2.2    | Constitutive Equations for $\mathbf{X} \in \partial_s \Omega$ : Traction-separation laws . . . . . | 55        |
| 3.3      | Numerical implementation . . . . .   | 61        |
| 3.3.1    | Fundamentals . . . . .   | 62        |
| 3.3.2    | Elastic unloading . . . . .  | 65        |
| 3.3.3    | Inelastic loading . . . . .  | 68        |
| 3.3.4    | Linearization . . . . .  | 70        |
| 3.3.5    | Extension to higher order elements . . . . .   | 73        |
| 3.4      | Computation of the normal vector . . . . .   | 76        |
| 3.4.1    | Formation of discontinuities in rate independent media . . . . .                                   | 77        |
| 3.4.2    | Uniqueness of the solution . . . . .   | 80        |
| 3.5      | Computation of the topology of the singular surface $\partial_s \Omega$ . . . . .                  | 83        |
| 3.6      | Numerical examples . . . . .   | 85        |
| 3.6.1    | Two-dimensional problem: Extension of a strip with a circular hole . . . . .                       | 85        |
| 3.6.2    | Three-dimensional problems using geometrically exact kinematics . . . . .                          | 88        |
| 3.7      | Open problems concerning strong discontinuity approaches . . . . .                                 | 96        |
| <b>4</b> | <b>A variational r-adaptive finite element formulation</b>   | <b>97</b> |
| 4.1      | Introduction to Arbitrary Lagrangian-Eulerian (VALE) formulations . . . . .                        | 97        |
| 4.2      | Introduction to Variational Arbitrary Lagrangian-Eulerian (VALE) formulations . . . . .            | 99        |
| 4.3      | ALE approximation of the deformed and the undeformed configuration . . . . .                       | 100       |
| 4.4      | Fundamentals of VALE formulations . . . . .  | 102       |
| 4.5      | Optimization of the positions of the nodal coordinates . . . . .                                   | 103       |
| 4.5.1    | Fundamentals . . . . .   | 104       |

|          |  |            |
|----------|--|------------|
| 4.5.2    | Numerical ill-posedness of the optimization problem . . . . .                                  | 106        |
| 4.5.3    | Viscous regularization of the configurational forces . . . . .                                 | 109        |
| 4.6      | Numerical examples . . . . .   | 111        |
| 4.6.1    | Stretching of a slab . . . . .   | 111        |
| 4.6.2    | Uniaxial tensile test of a notched specimen . . . . .  | 114        |
| 4.7      | Node migration in and out of the boundary . . . . .  | 118        |
| 4.7.1    | Fundamentals . . . . .   | 118        |
| 4.7.2    | Example: Bending of a cantilever beam . . . . .  | 120        |
| 4.8      | Extension of the VALE formulation to standard dissipative media . . . . .                      | 121        |
| 4.9      | Further improvements of the VALE formulation . . . . .   | 123        |
| <b>5</b> | <b>A variational-based remeshing strategy</b>  | <b>125</b> |
| 5.1      | Introduction . . . . .   | 125        |
| 5.2      | Fundamentals . . . . .   | 126        |
| 5.3      | Coupling of the energy-based remeshing strategy with variational VALE formulations . . . . .   | 128        |
| 5.4      | Numerical examples . . . . .   | 129        |
| 5.4.1    | Cantilever slab . . . . .  | 129        |
| 5.4.2    | Bending of a notched beam . . . . .  | 131        |
| 5.5      | Further improvements of the VALE formulation and the energy-based remeshing strategy . . . . . | 132        |
| <b>6</b> | <b>A variational h-adaptive finite element formulation</b>                                     | <b>133</b> |
| 6.1      | Introduction . . . . .   | 133        |
| 6.2      | A local refinement strategy . . . . .  | 134        |
| 6.2.1    | A local refinement strategy based on marked edges . . . . .                                    | 135        |
| 6.2.2    | A local refinement strategy based on marked elements . . . . .                                 | 135        |
| 6.3      | Variational refinement criteria . . . . .  | 137        |
| 6.4      | Bisection criteria derived from local energy bounds . . . . .                                  | 140        |
| 6.5      | Comparison of the proposed refinement criteria to classical error estimates                    | 141        |
| 6.6      | h-adaption combined with VALE formulations . . . . .   | 142        |
| 6.7      | Energy-based mesh coarsening . . . . .   | 143        |
| 6.8      | Transfer of history variables . . . . .  | 145        |

---

|          |   |            |
|----------|---|------------|
| 6.9      | Numerical examples . . . . .                                  | 146        |
| 6.9.1    | Uniaxial tensile test of a notched specimen . . . . .         | 147        |
| 6.9.2    | Indentation of a block: fixed force . . . . .                 | 150        |
| 6.9.3    | Indentation of a block: moving force . . . . .                | 155        |
| <b>7</b> | <b>Conclusion and outlook</b>                                 | <b>157</b> |
| 7.1      | Conclusion . . . . .  | 157        |
| 7.2      | Outlook and future work . . . . .                             | 160        |
| <b>A</b> | <b>A tetrahedral shape measure</b>                            | <b>185</b> |
| <b>B</b> | <b>Derivatives of a neo-HOOKEAN energy functional</b>         | <b>189</b> |
| <b>C</b> | <b>Data structure for coarsening of a finite element mesh</b> | <b>190</b> |

# Chapter 1

## Introduction

### 1.1 Motivation

The finite element method represents one of the most powerful and versatile tools available for the numerical analysis of complex engineering structures. In many cases, it provides the only avenue for ascertaining the physical behavior of a system under investigation. This approach was originally developed in the field of computational solid mechanics and continues to be widely used in this context. A typical application is the computation of the ultimate load of a structure which is a significance design parameter for practical engineering problems. However, commonly adopted procedures for computing this maximal load are based on rather crude approximations which naturally lead to certain drawbacks. On the one hand, the design of a structure developed by applying these estimates may be too conservative resulting in relatively low cost effectiveness. On the other hand, and even more importantly, the resistance of a structure may be overestimated. It is obvious that this can lead to disastrous consequences. The aforementioned problems demonstrate clearly the need of reliable and efficient numerical methods for the analysis of engineering structures.

The maximal loading of a mechanical system depends either on local material instabilities such as strain-softening or on global stability problems like buckling. While global effects can be accounted for by using an exact geometric description of the deformation, the phenomena associated with material instabilities are far less understood. In recent decades, much effort in the field of computational mechanics has been spent on the efficient and physically sound modeling of dissipative material behavior. In particular, realistic simulations of the failure of structures resulting from strain-softening represent one of the most active research areas nowadays. Strain-softening can be interpreted as a local material instability, characterized by decreasing stresses with increasing strains, which ultimately leads to the global failure of a system. Concrete is a typical material which shows such behavior under tensile loading – in this case, softening is related to the formation of

micro- and macro-cracks in the material. Often strain-softening is accompanied by the presence of narrow bands exhibiting highly localized deformations. A typical example is the formation of slip bands in soils. The thickness of these bands is several dimensions smaller than the characteristic diameter of the respective structure. As a result, such an effect can be understood as a multi-scale problem. This observation is crucial, since it implies some consequences for the development of efficient numerical models.

The importance of designing methods for the prediction of strain-softening is obvious, since classical continuum models are not objective in the presence of those local instabilities. Numerical results obtained by standard constitutive laws in conjunction with the finite element method thus show pathological mesh dependence. Consequently, the computed solutions are not meaningful. For this reason, one part of the present thesis deals with a new model suitable for the analysis of material failure. This approach fulfills, among other things, the following properties:

- The deformation is described in a geometrically exact manner.
- The model is fully three-dimensional.
- The results obtained by the model are independent of the finite element triangulation.
- It is multi-scale and accounts for the different length scales associated with the characteristic diameter of the structure and the thickness of the zones showing strain-softening.

The first three items ensure the objectivity of the numerical results for fully three-dimensional problems undergoing large deformations, while the fourth point is, as mentioned before, related to the efficiency of the implementation. Obviously, the third condition listed above can only be guaranteed asymptotically. More precisely, the space of deformations spanned by the finite element formulation must be large enough. One possible way of achieving this condition is classical (uniform) h-refinement, i. e., a discretization is generated in which the largest diameter of all finite elements is sufficiently small. This seemingly simple method shows two different problems. On the one hand, the term "sufficiently small" depends highly on the physical system under investigation. Consequently, this length scale cannot be computed a priori. On the other hand, uniform refinement strategies lead to a large number of finite elements and hence, they result in huge systems of equations. As a consequence, these approaches are relatively expensive.

As an alternative, an initially coarse triangulation can be locally refined. These models are referred to as adaptive finite element formulations. In contrast to uniform refinement, adaptive strategies enrich the space of deformations only where it is needed. For instance, if a notched beam is analyzed numerically, the vicinity of the notch requires finer

discretization compared to the remaining part of the body. Otherwise stress singularities cannot be captured adequately.

Nowadays, adaptive finite element methods are relatively well developed in the context of linearized elasticity theory. However, most physical phenomena require a geometrically exact description. If a linearized framework is used, the obtained results may be completely different compared to those predicted by the more exact theory. Unfortunately, the extension of adaptive methods originally derived for linearized models to the nonlinear case is by no means straightforward. This is mainly related to the fact that the theory of convergence is far from understood for nonlinear mechanics. Even the existence of the solution is often not known. However, the theory of convergence is required for the derivation of mathematically sound a posteriori error estimates which themselves represent the fundamentals of rigorous adaptive finite element formulations. The adaptive models for nonlinear problems which can be found in the literature are based on error indicators. Although some of them seem to give promising results, they are mostly introduced ad hoc.

The problems mentioned before point out the need of developing adaptive finite element formulations which can be applied to problems of nonlinear continuum mechanics. Therefore, the second part of the present thesis addresses a class of novel mesh adaptations. These new methods show the following properties:

- The deformation is described in a geometrically exact manner.
- The models are fully three-dimensional.
- Refinement is driven by the same principle which governs the underlying physical problem.
- It allows for refinement as well as for coarsening.

The first two items summarized above are identical to those fulfilled by the class of cohesive finite elements presented in this work. This is necessary to be able to couple both approaches. The canonical structure of the novel mesh adaptations is highlighted in the third point. More precisely, an error indicator is developed which guarantees a priori that the adaptively improved mesh leads to a better approximation of the underlying physical principle than the initial triangulation.

In many cases, the optimal mesh depends on the loading stage. For example, if crack propagation is analyzed numerically, the discretization in the vicinity of the crack tip has to be sufficiently fine. However, the position of this region changes due to crack growth. Hence, previously refined domains should be coarsened, while the vicinity of the new crack tip should be refined. Consequently, refinement has to be coupled with a de-refinement strategy.

## 1.2 State of the art review

As already mentioned, the first part of the present work is concerned with the development of a new class of finite elements suitable for the analysis of material failure resulting from strain-softening. Therefore, a state of the art review of such numerical approaches is given first. Since the number of different models is very large, attention is restricted to a special subset into which the newly proposed finite element formulation falls. Subsequently, a motivation for coupling those models with adaptive finite element methods is given and a state of the art review on mesh adaptations is addressed.

Nowadays, it is well known that numerical analyses based on standard (local) continuum models show a pathological mesh-dependence (see [DE BORST 1986]), if they are applied to the simulation of problems involving strain-localization. This is strongly related to the, by now classical, results on localization phenomena as studied for instance in [HADAMARD 1903; HILL 1958; THOMAS 1961; MANDEL 1966; RUDNICKI & RICE 1975]. In these works, the authors studied the transition of a smooth deformation field into one exhibiting weak discontinuities (the deformation field belongs to  $\mathcal{C}/\mathcal{C}^1$ ). In the static case, this transition is associated with the loss of ellipticity of the governing equations, see [MARSDEN & HUGHES 1994]. As a result, the respective Boundary Value Problem (BVP) is not well-posed anymore leading to non-uniqueness of the solution.

Unfortunately, the mesh-dependence corresponding to standard (local) continuum models as shown in [DE BORST 1986; DE BORST 2001] is not the only problem when dealing with problems involving strain-softening. As mentioned earlier, the width of the zones exhibiting localized deformations is often several orders of magnitude smaller than the characteristic diameter of the structure considered. Thus, the application of enhanced continuum models, such as non-local theories [PIJAUDIER-CABOT & BAŽANT 1987; BAŽANT & PIJAUDIER-CABOT 1988] or gradient enhanced models [MÜHLHAUS & AIFANTIS 1991; DE BORST & MÜHLHAUS 1992] (which involve a length scale related to the failure process) to the numerical analysis of a structural component requires a sufficiently fine resolution of the localization zone; the computational cost of which may be prohibitive.

According to [BELYTSCHKO, FISH & ENGELMANN 1988], an efficient approach suitable for the analysis of large-scale engineering structures should not only avoid the mesh dependence of the results computed numerically, but also account for the described multi-scale character of the underlying physical problem. Most approaches complying with both restrictions are based on the incorporation of the kinematics associated with the small-scale (the softening zone) into a large-scale macroscopic material model, cf. [SIMO, OLIVER & ARMERO 1993; GARIKIPATI & HUGHES 1998; ARMERO 1999; MOËS, DOLBOW & BELYTSCHKO 1999; ORTIZ & REPETTO 1999; CARSTENSEN, HACKL & MIELKE 2002; MIEHE & LAMBRECHT 2003]. In these works, small-scale kinematics are captured either by an enriched displacement field or a strain field.

One class of models fulfilling the conditions of [BELYTSCHKO, FISH & ENGELMANN 1988] is represented by approaches based on *strong discontinuities* (jumps in the deformation field), see [NEEDLEMAN 1990; DVORKIN, CUITIÑO & GIOIA 1990; KLISINSKI, RUNESSON & STURE 1991; SIMO, OLIVER & ARMERO 1993; CAMACHO & ORTIZ 1996; ORTIZ & PANDOLFI 1999; MOËS, DOLBOW & BELYTSCHKO 1999; SUKUMAR, MOËS, MORAN & BELYTSCHKO 2000]. These approaches can be understood as an extension of the cohesive zone models advocated in [DUGDALE 1960; BARENBLATT 1962] and further elaborated by [HILLERBORG, MODEER & PETERSSON 1976] who proposed the *Fictitious Crack Model*. In contrast to classical continuum theories, these models are based on cohesive laws connecting the traction vector with the displacement discontinuity. For example in [HILLERBORG, MODEER & PETERSSON 1976], the authors analyzed cracking in brittle materials and postulated the normal vector of the stress vector acting at the considered micro-crack to be a function of the crack-opening displacement.

The approaches using kinematics induced by strong discontinuities can be subdivided into two classes. The models which were proposed first fall into the range of *interface elements*, cf. [NEEDLEMAN 1990; CAMACHO & ORTIZ 1996; ORTIZ & PANDOLFI 1999]. That is, a jump in the deformation field is allowed to occur only at the boundary between neighboring elements. Within the second class of methods, the discontinuity can evolve arbitrarily. More precisely, displacement jumps are even accounted for in the interior of finite elements, see [DVORKIN, CUITIÑO & GIOIA 1990; KLISINSKI, RUNESSON & STURE 1991; SIMO, OLIVER & ARMERO 1993; MOËS, DOLBOW & BELYTSCHKO 1999; SUKUMAR, MOËS, MORAN & BELYTSCHKO 2000]. A further classification is possible, if the way of modeling the discontinuity is used as a criterion. In the numerical models [DVORKIN, CUITIÑO & GIOIA 1990; KLISINSKI, RUNESSON & STURE 1991; SIMO, OLIVER & ARMERO 1993], the displacement jump is approximated element-wise. Continuity of the field of the discontinuities is not guaranteed at the element boundaries. These implementations are often referred to as *Strong Discontinuity Approaches* (SDA). Since the work of [SIMO, OLIVER & ARMERO 1993], most of the SDAs are based on the *Enhanced Assumed Strain* (EAS) concept, cf. [SIMO & RIFAI 1990; SIMO & ARMERO 1992], i. e., the jump in the displacement field is not modeled directly. Instead, only the resulting strain field is taken into account. The other class of approaches accounting for discontinuities within finite elements is represented by the so-called *eXtended Finite Element Method* (X-FEM) or *Partition of Unity Finite Element Method* (PU-FEM), cf. [MOËS, DOLBOW & BELYTSCHKO 1999; SUKUMAR, MOËS, MORAN & BELYTSCHKO 2000]. As implied by the second name of this procedure, it is based on the *Partition of Unity* concept as introduced by [BABUŠKA & MELENK 1996; BABUŠKA & MELENK 1997]. Conceptually speaking, a given deformation approximation is locally enriched by functions showing a compact support. In contrast to the SDA, the displacement field itself is modified resulting in a continuous interpolation of the deformation jumps across element boundaries.

At present, many discussions on the advantages and drawbacks associated with each of the just described cohesive finite element approaches can be found in the scientific literature, cf. [JIRÁSEK 2000; JIRÁSEK & BELYTSCHKO 2002; MOSLER & MESCHKE 2004; DUMSTORFF, MOSLER & MESCHKE 2003; OLIVER, HUESPE, PULIDO & SAMANIEGO 2005]. From the discussions contained in these works, it follows that none of the cohesive element strategies published so far can be considered to be fully superior to the others. For instance, the possibility of modeling a crack arbitrarily crossing a finite element as allowed by using the SDA or the X-FEM sounds very promising. But this implies that the topology of the singular surface characterizing a crack or a shear band has to be stored, e. g. by using level sets cf. [STOLARSKA, CHOPP, MÖES & BELYTSCHKO 2001]. Clearly, even in the three-dimensional case, this does not represent a problem, if only few cracks are modeled. However, if complex crack patterns such as branching and intersecting cracks are to be simulated, the numerical costs are prohibitive. As a result, the SDA as well as the X-FEM have not been applied to such problems so far.

On the other hand, interface elements allow for computing complex crack paths and their implementation is relatively straightforward, see [ORTIZ & PANDOLFI 1999; PANDOLFI, KRYSL & ORTIZ 1999; PANDOLFI, KRYSL & ORTIZ 1999; CIRAK, ORTIZ & PANDOLFI 2005]. However, approximating the topology of a hyperplane by the facets of the finite elements contained in the respective discretization can lead to an overestimation of the dissipation, see [PAPOULIA, VAVASIS & GANGULY 2005]. More precisely, if a standard triangulation is considered and no adaptive techniques are applied, the area of the numerically computed crack surface cannot converge to the one corresponding to the analytical solution in general. Based on this observation [PAPOULIA, VAVASIS & GANGULY 2005] recently proposed to use so-called *pinwheel-based* discretizations, cf. [RADIN & SADUN 1996; GANGULY, VAVASIS & PAPOULIA 2005]. The interesting characteristic of those two-dimensional triangulations is the isoperimetric property. This property means that the length of the shortest path between two points ( $P$  and  $Q$ ) that uses only edges of the finite element mesh converges to the length of the EUCLIDIAN distance from  $P$  to  $Q$ . Consequently, the space of admissible crack paths spanned by the discretization is rich enough to guarantee convergence. Evidently, this property is not fulfilled for standard meshes. Although the results reported in [PAPOULIA, VAVASIS & GANGULY 2005] seem to be very promising, it should be pointed out that the proofs in [RADIN & SADUN 1996] are restricted to two-dimensional problems. Furthermore, even for plane triangulations, the rate of convergence is not known. Hence, the results are only asymptotical in nature and their extension to three dimensions is not straightforward.

As pointed out in the previous paragraphs, none of the cohesive element concepts is completely superior to the others. In the present work, a model which falls into the class of SDAs is advocated. In contrast to the interface elements and the X-FEM, the strong discontinuities are modeled element-wise, i. e., in an incompatible manner. By this means, the implementation is, conceptually speaking, restricted to the element level. Thus, in

contrast to X-FEM, the algorithmic formulation is not very expensive, cf. [OLIVER, HUESPE, PULIDO & SAMANIEGO 2005]. However, it should be noted that enforcing crack path continuity induces a nonlocal effect. More precisely, information of the neighboring elements are required, cf. [OLIVER 1996; OLIVER, HUESPE, SAMANIEGO & CHAVES 2002].

The Strong Discontinuity Approach (SDA) in its modern form has been advocated by [SIMO, OLIVER & ARMERO 1993; SIMO & OLIVER 1994]. Nowadays, the geometrically linearized SDA is relatively well developed. For a review article see [MOSLER 2004]. Most of the finite element formulations which are in line with [SIMO, OLIVER & ARMERO 1993] are based on the implementation known from the underlying EAS concept. More precisely, the additional degrees of freedom associated with the discontinuous deformation mapping are condensed out by employing the static condensation technique, see, e. g. References [SIMO & OLIVER 1994; OLIVER 1996; ARMERO & GARIKIPATI 1996; LARRSON & RUNESSON 1996; ARMERO 1999; WELLS & SLUYS 2001C; JIRÁSEK & ZIMMERMANN 2001]. Alternatively, [BORJA 2000; MOSLER & MESCHKE 2000; MOSLER & MESCHKE 2001] proposed an algorithm avoiding the use of the static condensation technique. In contrast to the classical EAS concept according to [SIMO & RIFAI 1990; SIMO & ARMERO 1992], the  $L_2$ -orthogonality condition between the stresses and the enhanced strain variations is not computed simultaneously with the weak form of equilibrium. Instead, a staggered solution scheme is applied. It turns out that the  $L_2$ -orthogonality condition can be interpreted as a consistency conditions known from classical plasticity theory formulated in stress-space. This observation is crucial, since on the one hand, it opens up the possibility of applying efficient integration algorithms originally designed for standard (continuous deformations) continuum models to cohesive finite element formulations, cf. [MOSLER & MESCHKE 2003; MOSLER 2005E]. On the other hand, the implementation as proposed in [BORJA 2000; MOSLER & MESCHKE 2000; MOSLER & MESCHKE 2001] can be regarded as the continuation of the work done by [SIMO, OLIVER & ARMERO 1993]. More specifically, the analogy as well as the link between material models for continuous deformations and interface laws such as traction-separation relations has been highlighted and extended to their numerical implementation.

According to [MOSLER 2004], the equivalence between SDAs based on the static condensation and models falling into the algorithmic framework advocated in [BORJA 2000; MOSLER & MESCHKE 2000; MOSLER & MESCHKE 2001] holds only for finite elements using a constant approximation of the strains. For higher order elements, both approaches lead to different results. Furthermore, and even more importantly, if the degrees of freedom corresponding to the discontinuous deformation field are already condensed out at the material point level, crack path continuity cannot be enforced for higher order elements. However, this is essential for computations being almost independent with respect to the mesh bias, cf. [JIRÁSEK & ZIMMERMANN 2001; OLIVER, HUESPE, SAMANIEGO

& CHAVES 2002; FEIST & HOFSTETTER 2005]. Without enforcing continuity of the crack surface, the results obtained from SDAs are almost identical to those predicted by smeared crack models, see [MOSLER & MESCHKE 2004]. That is, they show a dependence with respect to the given mesh bias. For this reason, a novel SDA was proposed in [MOSLER 2005B]. In this work, the  $L_2$ -orthogonality condition is re-written such that it is formally identical to the necessary condition for yielding known from standard plasticity theories. For higher order elements, this equation is formulated in terms of an average stress tensor. It can be shown that the resulting finite element formulation is fully equivalent to the one used in most SDAs, e. g. [SIMO & OLIVER 1994; OLIVER 1996; ARMERO & GARIKIPATI 1996; LARSSON & RUNESSON 1996; ARMERO 1999; WELLS & SLUYS 2001C; JIRÁSEK & ZIMMERMANN 2001]. However, the numerical implementation differs. Analogous to the previous works [BORJA 2000; MOSLER & MESCHKE 2000; MOSLER & MESCHKE 2001], subroutines developed for classical plasticity theory (continuous deformation) are applied to the integration of the internal variables. More precisely, a return-mapping algorithm is adopted. In summary, the SDA as suggested in [MOSLER 2005B] combines the advantages of the finite element models [BORJA 2000; MOSLER & MESCHKE 2000; MOSLER 2002; MOSLER & MESCHKE 2004] by leaving the original model itself (see [SIMO & OLIVER 1994; OLIVER 1996]) unaffected. As a consequence, it is possible to enforce crack path continuity.

It is well known that geometrical nonlinearities affect considerably the process of strain localization. More precisely, finite deformation effects do not only influence the time of bifurcation of a homogeneously distributed strain field into a highly localized one, but also the corresponding failure mode, cf. [STEINMANN, LARSSON & RUNESSON 1997]. Additionally, in many engineering applications, the response of the considered structure depends crucially on geometrical nonlinearities such as buckling. For instance, energy absorption in composite materials cannot be modeled adequately with linearized kinematics, cf. [JANSSON 2002]. Thus, neglecting finite deformation effects can lead to an overestimation of the ultimate load of the structural component analyzed. For this reason, the extension of the linearized kinematics of the SDA to finite strains was given by [ARMERO & GARIKIPATI 1996; GARIKIPATI 1996]. In these references, the authors proposed a SCHMID-type traction-separation law connecting the relative shear sliding displacement to the tangential component of the traction vector acting at the surface of strong discontinuities. The finite element model presented in the cited works was restricted to the two-dimensional case and based on a solution strategy almost identical to the one used for the geometrically linearized theory. More precisely, the standard implementation of the EAS concept was adopted, cf. [SIMO & ARMERO 1992; SIMO, ARMERO & TAYLOR 1993]. In contrast to [ARMERO & GARIKIPATI 1996; GARIKIPATI 1996], some authors approximate the displacement discontinuity by means of a ramp function. This leads to *regularized strong discontinuities*, cf. [LARSSON, STEINMANN & RUNESSON 1998; STEINMANN & BETSCH 2000; LARSSON & JANSSON 2002; OLIVER, HUESPE, PULIDO & SAMANIEGO 2003]. Since in this case, the deformation gradient is still bounded (in the

sense of the operator norm), standard continuum models can be applied. However, this approximation will not be considered throughout the rest of the present thesis. The ideas presented by [ARMERO & GARIKIPATI 1996; GARIKIPATI 1996] were further elaborated in [ARMERO 1999] in which the authors proposed a framework to embed a localized dissipative mechanism, i. e., a traction-separation law, into a large-scale problem (continuous deformation). By assuming the postulate of maximum dissipation, ARMERO derived the evolution laws of the model. Restricting to linearized kinematics, a similar concept has been presented in [MIEHE & SCHRÖDER 1994; OHLSSON & OLOFSSON 1997]. This concept is very appealing, since it allows the development of cohesive laws which are completely decoupled from the bulk material. For instance, [BORJA 2002] argues that the constitutive response associated with the continuous deformation would not be necessarily identical to that of the post-localization regime. His argumentation is based on the constitutive response of rocks.

The implementations of the geometrically exact SDA-based finite element formulations, which have been cited so far, are almost identical to those of the EAS concept. That is, the degrees of freedom characterizing the continuous, i. e., conforming, displacement field and those associated with the displacement jump are computed simultaneously from the weak form of equilibrium and the  $L_2$ -orthogonality condition, cf. [ARMERO & GARIKIPATI 1996; ARMERO 1999; LARSSON, STEINMANN & RUNESSON 1998; STEINMANN & BETSCH 2000; LARSSON & JANSSON 2002; OLIVER, HUESPE, PULIDO & SAMANIEGO 2003; GASSER & HOLZAPFEL 2003; CALLARI & ARMERO 2004]. The resulting stiffness matrix is computed by applying the static condensation technique. As an alternative, [BORJA 2002] proposed a SDA completely avoiding this technique. His model is a continuation of the ideas previously advocated for infinitesimal deformations, cf. [BORJA 2000; MOSLER & MESCHKE 2000; MOSLER & MESCHKE 2001]. In contrast to [ARMERO & GARIKIPATI 1996; ARMERO 1999; LARSSON, STEINMANN & RUNESSON 1998; STEINMANN & BETSCH 2000; LARSSON & JANSSON 2002; OLIVER, HUESPE, PULIDO & SAMANIEGO 2003; GASSER & HOLZAPFEL 2003; CALLARI & ARMERO 2004], BORJA followed the implementations in [BORJA 2000; MOSLER & MESCHKE 2000; MOSLER & MESCHKE 2001] and eliminated the additional degrees of freedom corresponding to the displacement jump on the material point level. The rate of the amplitude of the displacement jump was interpreted as a plastic multiplier. As mentioned earlier, this strategy shows the advantages that analogies with standard continuum theories can be observed leading to a better understanding of the model and standard integration algorithms such as the return-mapping algorithm can be applied.

Unfortunately, the numerical implementation in [BORJA 2002] has several limitations and has to be understood rather more as a prototype. It has been designed specifically for constant strain triangle elements and for the modeling of slip bands. The extensions necessary for higher order elements, three-dimensional problems or more complex traction-separation laws have not been discussed. However, they are crucial whenever engineering

problems are to be analyzed numerically in a realistic manner. To the best knowledge of the author, with the exception of the work [GASSER & HOLZAPFEL 2003] which is based on a specific damage-type traction-separation law and the static condensation technique, only two-dimensional geometrically exact SDAs can be found in the literature, cf. [ARMERO & GARIKIPATI 1996; ARMERO 1999; LARSSON, STEINMANN & RUNESSON 1998; STEINMANN & BETSCH 2000; LARSSON & JANSSON 2002; OLIVER, HUESPE, PULIDO & SAMANIEGO 2003; CALLARI & ARMERO 2004].

The ideas presented in [MOSLER 2005B] were generalized to a geometrically exact theory in [MOSLER 2005A]. In this paper, a novel numerical implementation of locally embedded strong discontinuities is suggested. In line with [BORJA 2000; MOSLER & MESCHKE 2000; MOSLER & MESCHKE 2001; BORJA 2002], the displacement jump is condensed out at the material point level. However, in contrast to [BORJA 2002], no specific assumption concerning the traction-separation law and the evolution equations of the displacement jump is made, i. e., this novel numerical framework holds for a broad range of different, fully three-dimensional, constitutive interface models. In contrast to previous works on the SDA accounting for finite strains, the finite element formulation in [MOSLER 2005A] is based on a return-mapping algorithm similar to that of standard plasticity theory. The conforming part of deformation and the part resulting from the displacement discontinuity are computed according to a predictor-corrector step procedure, cf. [SIMO 1998; SIMO & HUGHES 1998]. As a consequence, subroutines designed for classical (continuous displacement field) continuum models can be applied with only minor modifications necessary.

Although the X-FEM as well as the SDA allow for the modeling of material surfaces such as cracks crossing arbitrarily finite elements, the numerical results are, in general, not completely mesh independent. The reason for this is twofold. First, all criteria necessary for predicting the growth direction of the internal surface depend significantly on the quality of the numerical solution of the homogeneous deformation. For instance, if crack growth is modeled by the RANKINE criterion (the crack propagates orthogonal to the direction of the maximum principle stress), the direction of a new crack segment depends apparently on the stress field. As a consequence, even SDAs or X-FEMs have to be coupled with adaptive finite element methods. Otherwise, a sufficient quality of the stress field cannot be guaranteed. Second, the way of computing the topology of the internal surface is far from being understood. Usually strain-based (see [GEERS, PEIJS & BREKELMANS 1996; SIMONE, WELLS & SLUYS 2003]), stress-based (see [ERDOGAN & SIH 1963; MOËS, DOLBOW & BELYTSCHKO 1999; WELLS & SLUYS 2001B; JIRÁSEK & ZIMMERMANN 2001]), energy-based (see [NUISMER 1975; SIH 1974]), or criteria based on material bifurcation such as [SIMO, OLIVER & ARMERO 1993; SIMO & OLIVER 1994; OLIVER & SIMO 1994] are applied. Often these are used in a slightly different form. More specifically, they are computed by means of non-local stress or strain fields, cf. [SIMONE, WELLS & SLUYS 2003; FEIST & HOFSTETTER 2005; GASSER & HOLZAPFEL

2006]. However, according to [SIMONE, ASKES & SLUYS 2004], those modifications lead, in many cases, to non-physical results.

Obviously, the criterion best suited for the prediction of the growth direction of the internal surface depends on the underlying physical problem. For instance, the principle of energy-minimization, or dissipation-maximization cannot be applied to non-associative plasticity theories, since they do not obey such a variational structure. However, even if a reasonable criterion has been chosen, the computation of the resulting topology of the internal surface is not straightforward. Most of the approaches which can be found in the literature are based on geometrical smoothing techniques [OLIVER 1996; GASSER & HOLZAPFEL 2005; GASSER & HOLZAPFEL 2006] rather than on physical considerations. In any case, a new segment is connected with a previously existing one [OLIVER, HUESPE, SAMANIEGO & CHAVES 2002; FEIST & HOFSTETTER 2005; DUMSTORFF & MESCHKE 2005]. Those approaches work reasonably well if the internal surfaces do not cross each other, i. e., if the mapping between a new segment and its parent is unique. Unfortunately, many physical problems such as crack branching and intersecting cracks do not fulfill this condition. As mentioned before, interface elements do not show this problem. They can be applied to the analysis of complex crack patterns. However, since the results depend on the finite element discretization (cracks are allowed to propagate only between existing finite elements), they have to be coupled with adaptive strategies. In summary, the SDA or the X-FEM as well as interface elements have to be combined with adaptive methods. These concepts are needed in order to guarantee a sufficiently accurate computation of the growth direction of the internal surface and, if interface elements are used, to enrich the space of potential crack paths.

Nowadays, the mathematical theory of error estimates is relatively well understood and established in the case of linearized elasticity theory, cf. [VERFÜRTH 1996; VERFÜRTH 1999; AINSWORTH & ODEN 1997; AINSWORTH & ODEN 2000]. However, almost all mathematically rigorously derived estimates are restricted to isotropic meshes. More precisely, *shape regularity* of the finite elements is postulated a priori. Obviously, this excludes anisotropic meshes. Since it is well known that for many applications such as shock wave propagation and localized failure, discretizations with independent length scales in different spatial directions are significantly more efficient than their isotropic counterparts, this represents a serious restriction, cf. [FREY & ALAUZET 2005; LI, SHEPHARD & BEALL 2005]. Unfortunately, from a theoretical as well as from a practical point of view, the anisotropic case is much more complicated and hence, it is much less developed. For an overview, refer to [APEL 1999]. This is mainly related to interpolation theory and local interpolation errors which are, in general, restricted to isotropic meshes.

In addition to the just mentioned problems, most physical phenomena require a nonlinear description. In the case of cohesive element formulation presented in this work, those nonlinearities result from both geometrical as well as physical effects. However, according to [VERFÜRTH 1996; VERFÜRTH 1999], the extension of error estimates originally

derived for linearized models to the nonlinear case is by no means straightforward. One of the most serious problems associated with such a generalization is the dependence of a certain factor involved in the estimate on the unknown solution. Consequently, this factor cannot be computed a priori. Furthermore, for many problems, it is not even bounded.

A way to apply the well-known results of error estimates developed for linearized elasticity to strongly nonlinear problems was advocated by [RADOVITZKY & ORTIZ 1999] (see also [RADOVITZKY 1998; MOLINARI & ORTIZ 2002]). In this work the authors assumed a variational structure of the underlying physical problem. This property ensures the existence of a symmetric DIRICHLET form. As a result, the nonlinear problem decomposes locally (in time) into linear subproblems fully identical to those of linearized elasticity theory. By virtue of this observation, an efficient a posteriori error estimate resulting in an adaptive finite element method was derived. The adaptive strategy as proposed in [RADOVITZKY & ORTIZ 1999] is based on the assumption that the physical problem is driven by a variational structure. Although such a structure is not required by a physical law, it serves as a good approximation for many phenomena. For instance, the stable configurations of a hyperelastic body obey the principle of minimum potential energy. Even for a large class of dissipative materials a pseudo potential can be derived, cf. [ORTIZ & STAINIER 1999], cf. [COMI & PEREGO 1995]. More precisely, for all *standard dissipative media* (SDM) in the sense of [HALPHEN & NGUYEN 1975] (see also [MANDEL 1972; GERMAN, NGUYEN & SUQUET 1983; LEMAITRE 1985; HACKL 1997]) which obey the principle of maximum dissipation such a variational structure exists. The extension to fully thermomechanically coupled problems was given in [YANG, STAINIER & ORTIZ 2005]. The advantages resulting from those principles are twofold. First, they open up the possibility of analyzing the existence of a solution by using, by now classical, techniques known from hyperelasticity, cf. [BALL 1978] (see also [ORTIZ & REPETTO 1999; CARSTENSEN, HACKL & MIELKE 2002; MIEHE & LAMBRECHT 2003]). Furthermore, other promising mathematical theories such as  $\Gamma$ -convergence can be applied as well, see [DAL MASO 1983; BRAIDES 2002]. This theory of convergence is very powerful for analyzing the asymptotical behavior of numerical methods. For an investigation of the convergence of variational smeared crack approaches, cf. [NEGRI 2005A]. Second, and perhaps equally importantly, minimization principles provide a suitable basis for a posteriori error estimation and, consequently, for adaptive finite element methods. For example, if the potential to be minimized is denoted as  $I(\varphi)$ , and two different admissible candidates  $\varphi^{(1)}$  and  $\varphi^{(2)}$  with  $I(\varphi^{(1)}) < I(\varphi^{(2)})$  are considered, then  $I(\varphi^{(1)})$  is closer to the exact minimum and hence,  $\varphi^{(1)}$  is regarded as a better solution than  $\varphi^{(2)}$ , cf. [THOUTIREDDY 2003; THOUTIREDDY & ORTIZ 2004]. Based on this optimality criterion, different variational finite element mesh adaptations can be developed.

The concept of using the underlying variational principle to optimize the discretization enjoys a long tradition dating back, at least, to [MCNEICE & MARCAL 1973; FELIPPA 1976], in the special context of two-dimensional linearized elasticity. In these approaches,

also referred to as *variational r-adaptions*, the deformation and the optimal finite element discretization follow jointly from energy minimization. In contrast to the publications cited previously, the connection between mesh optimization and configurational or energetic forces [ESHELBY 1951; ESHELBY 1975] has only been recognized recently [BRAUN 1997; MUELLER & MAUGIN 2002; THOUTIREDDY 2003; THOUTIREDDY & ORTIZ 2004; KUHLE, ASKES & STEINMANN 2004; ASKES, KUHLE & STEINMANN 2004]. [BRAUN 1997] computed the forces associated with a variation of the nodal positions in the reference configuration in a finite element discretization and speculated on the possibility of computing such positions so as to attain configurational equilibrium. However, a full solution procedure was not proposed in that work. A variety of solution strategies have recently been proposed based on a steepest gradient algorithm [MUELLER & MAUGIN 2002]; conjugate gradients [THOUTIREDDY 2003; THOUTIREDDY & ORTIZ 2004]; and NEWTON's method [KUHLE, ASKES & STEINMANN 2004; ASKES, KUHLE & STEINMANN 2004]. [THOUTIREDDY & ORTIZ 2004] in addition to optimizing the positions of the nodes in the interior and on the boundary, allowed for changes in the connectivity of the mesh. In particular, the connectivity of the mesh was changed during the optimization of the nodal positions so as to maintain a DELAUNAY triangulation at all times.

Despite the conceptual appeal of variational r-adaptation, its robust numerical implementation is not without difficulty, cf. [MOSLER & ORTIZ 2005]. More precisely, the function to be minimized is nonconvex and its HESSIAN is highly singular. For this reason, [MOSLER & ORTIZ 2005] developed a solution strategy based on a viscous regularization of the configurational forces, i. e., the system of forces conjugate to the location of the nodes in the reference configuration. This method eliminates the just described problems by leaving the physical problem itself unaffected. As noted in [THOUTIREDDY 2003; THOUTIREDDY & ORTIZ 2004], in addition to optimizing the geometry of the mesh, i. e., the location of the nodes in the reference configuration, it is equally important to optimize the topology or connectivity of the mesh. Indeed, keeping the connectivity of the mesh fixed introduces strong topological or locking constraints which severely restrict the range of meshes that can be attained and, consequently, the quality of the solution. However, the determination of the energy-minimizing mesh connectivity for a fixed nodal set is a challenging discrete optimization problem. In two-dimensions, an upper bound on the number of different triangulation exists (cf. [AICHHOLZER, HURTADO & NOY 2004]) and, consequently, a global minimum is guaranteed. However, the number of different triangulations increases exponentially with the number of nodes [AICHHOLZER, HURTADO & NOY 2004], and the global minimum cannot be computed in practice. Instead, [MOSLER & ORTIZ 2005] proposed to modify the mesh topology by applying so-called LAWSON flips (cf. [LAWSON 1986; JOE 1989; JOE 1991]) based on an energy criterion. Specifically, a flip is accepted if it lowers the energy of the solution. The algorithm terminates when all flips raise or leave unchanged the energy of the solution.

In many cases, although variational r-adaption improves the numerically computed solution significantly, the space of interpolations has to be enlarged further. This can be achieved, for instance, by using *h-adaptivity* or *p-adaptivity*, cf. [SZABÓ & BABŮSKA 1991]. Since the final goal of the present work is the coupling of mesh adaption with cohesive finite elements for the analysis of localized material failure, the function to be approximated, i. e., the deformation mapping, is not very smooth. For this reason, attention is restricted to h-adaptive strategies.

A novel variational h-adaption was advocated in [MOSLER & ORTIZ 2006]. In line with [MOSLER & ORTIZ 2005], it is based on the assumed underlying minimization principle governing the physical problem. As a prototype, it has been applied to standard dissipative media. For refinement, an edge-bisection algorithm is adopted. Contrary to most previous numerical models, the energy represents the only refinement criterion in the presented algorithm. As a consequence, anisotropic meshes may evolve if they are energetically favorable. It is demonstrated that those meshes are superior compared to their isotropic counterparts. Unfortunately, if the elements are almost degenerate, the conditioning of the resulting stiffness matrix is relatively poor thereby resulting in a larger number of iteration cycles if indirect solvers are used. However, the energy-based h-adaption can be coupled with a criterion guaranteeing a small aspect ratio of the finite elements. In [MOSLER & ORTIZ 2006], a longest edge-bisection algorithm is employed, cf. [BÄNSCH 1991B; RIVARA 1991].

The coupling of mesh adaption with cohesive finite elements represents one of the ongoing research subjects. First ideas can be found in [NEGRI 2005B; MOSLER, ORTIZ & PANDOLFI 2006]. These works are in line with [FRANCFORT & MARIGO 1998; BOURDIN, FRANCFORT & MARIGO 2000; DAL MASO & ZANINI 2005]. The models in [NEGRI 2005B; MOSLER, ORTIZ & PANDOLFI 2006] are based on the assumption that crack growth is governed by a minimization principle. Roughly speaking, the idea is that the deformation mapping as well as the topology of the crack are computed from the same minimization principle simultaneously.

### 1.3 Structure of the present work

The present work is divided into two main parts. In Chapter 2, a short state of the art review concerning the modeling of dissipative materials is given. As a prototype, finite strain plasticity theory is considered. However, the modifications necessary for damage-induced stiffness degradation are briefly discussed as well. The main focus of this chapter is on standard dissipative media. For such constitutive models, the state variables, together with the deformation mapping, follow from a variational principle. More precisely, the respective finite element formulation takes the form of a minimum principle. This is a very significant aspect of the resulting approach, since it opens up the possibility of applying

standard optimization algorithms to the numerical implementation. Additionally, and even more importantly, a minimization principle provides a suitable foundation required for error estimation and mesh adaptation. The chapter closes with a canonical extension of standard dissipative media to fully thermomechanical coupled problems governed by a minimization principle.

The first main part of the present thesis is addressed in Chapter 3. It is concerned with a new class of cohesive elements suitable for the analyses of material failure such as cracking in brittle structures, the formation of slip bands in soils or the development of LÜDERS bands. From a macroscopic point of view, those phenomena are characterized by a discontinuity in the deformation mapping, since the width of the part of the structure showing localized strains is several dimensions smaller than the diameter of the system considered. For this reason, the new numerical model is based on the kinematics induced by strong discontinuities (jumps in the deformation mapping). Instead of classical stress-strain relationships, the dissipation is reflected by a cohesive law connecting the displacement jump with the traction vector. The advocated framework is relatively universal. It can be applied to a broad range of different cohesive interface laws and to any type of finite elements. In contrast to previously published models on cohesive approaches, the analogy between the novel numerical model and standard (continuous deformation mapping) finite element formulations is highlighted.

As already pointed out in the first section of this chapter, the results obtained by cohesive elements can only be accurate, if the diameter of the finite elements is sufficiently small. This condition can be achieved by applying either an expensive uniform refinement or by using a computationally efficient adaptive approach. For this reason, a class of novel adaptive finite element formulation is presented in the second main part of this thesis consisting of Chapters 4 – 6. Assuming the underlying physical problem is driven by an energy minimization principle such as that of standard dissipative media, three different mesh adaptations are advocated. The first of those represents a *Variational Arbitrary Lagrangian-Eulerian (VALE) formulation*. It is described in Chapter 4. In contrast to classical NEWTONIAN mechanics, this method seeks to minimize the energy function not only with respect to the finite element mesh over the deformed configuration of the body, but also over the undeformed triangulation. Since the corresponding space of interpolation functions is a superset of that associated with the classical NEWTONIAN approach, the predicted minimum is always closer to the analytical solution. Consequently, this method leads to an improvement of the numerically obtained results. If the mentioned VALE finite element formulation is applied and the connectivities of the elements are kept constant, strong topological constraints may evolve which severely restrict the range of meshes that can be attained and, consequently, the quality of the solution. Thus, it is important to improve the topology (connectivity) of the considered triangulation as well. In Chapter 5, an energy-driven re-triangulation is proposed. Based on local mesh transformations, the resulting discretization shows always a lower energy than the initial mesh. Hence, an

improvement of the solution is guaranteed a priori. In many cases, keeping the number of degrees of freedom as constant is not sufficient for getting accurate results. As a consequence, Chapter 6 deals with a method enriching further the space of admissible solutions. More specifically, a novel variational h-adaptation is suggested. Assuming an underlying physical minimization principle, the interpolation space is locally enlarged. Only if the resulting new triangulation improves the solution significantly, it is stored. Otherwise, the old discretization is used.

The present work closes with a summary and with some first ideas concerning the coupling of variational mesh adaptations with cohesive finite element formulations. Those ideas seem to be well-suited and very powerful for the numerical analyses of complex engineering problems showing localized material failure. As a prototype, cracking in brittle structures is considered.

# Chapter 2

## Constitutive modeling at finite strains

This chapter is concerned with a short state of the art review on the modeling of dissipative materials. Following standard restrictions of continuum mechanics, the deformation mapping is assumed to be sufficiently smooth. Weak or strong discontinuities are excluded. As a prototype dissipative material, a class of finite strain plasticity theories is discussed. However, the modifications necessary for damage-induced stiffness degradation are briefly presented as well. Special attention is turned on the variational structure of plasticity models governed by the postulate of maximum dissipation. This structure allows to formulate the constitutive update as a minimization problem. It represents the essential ingredient for the adaptive finite element formulations as described in Chapters 4 – 6. The present chapter closes with a canonical extension of variational constitutive updates for fully thermomechanically coupled general dissipative solids.

This chapter represents neither an introduction to continuum mechanics, nor to constitutive modeling. It only provides the fundamentals required for the following chapters. For further details on continuum mechanics, the interested reader is referred to the excellent works [TRUESDELL & TOUPIN 1960; TRUESDELL & NOLL 1965; MARSDEN & HUGHES 1994; ANTMAN 1995; STEIN & BARTHOLD 1995; OGDEN 1997; CHADWICK 2000; HAUPT 2000; ORTIZ 2003] and the references cited therein. In the case of modeling dissipative materials, the monographs [TRUESDELL & NOLL 1965; KRAWIETZ 1986; KRAJČINOVIC 1996; LUBLINER 1997; SIMO & HUGHES 1998; HAUPT 2000; ORTIZ 2002; NEMAT-NASSER 2004; BERTRAM 2005; XIAO, BRUHNS & MEYERS 2006] are comprehensive surveys.

## 2.1 Kinematics

In what follows, a domain  $\Omega \subset \mathbb{R}^3$ , that is, an open, bounded and connected set, is considered. It is assumed that this domain represents the reference configuration of a body. The material points  $P \in \Omega$  are identified by their position vectors  $\mathbf{X}(P)$  relative to a cartesian coordinate system with center  $O$ . Curvilinear coordinates will only be used when necessary. The body deforms under the action of applied body forces and tractions and prescribed displacements. The resulting deformation is described by the mapping  $\varphi : \Omega \rightarrow \mathbb{R}^3$ , which is sufficiently smooth, injective except possibly on the boundary and maps the position  $\mathbf{X} \in \Omega$  of material particles in the reference configuration to their position  $\mathbf{x} \in \varphi(\Omega)$  in the deformed configuration (cf. [CIARLET 1988]). With these assumptions, the local deformation is well defined and can be characterized by the deformation gradient

$$\mathbf{F} := \text{GRAD}\varphi, \quad \text{with} \quad \text{GRAD}(\bullet) := \frac{\partial(\bullet)}{\partial \mathbf{X}} =: \nabla_{\mathbf{X}}(\bullet). \quad (2.1)$$

Since  $\varphi|_{\Omega}$  is injective,  $\varphi^{-1}|_{\Omega}$  exists and by the inverse function theorem  $\det \mathbf{F} \neq 0 \forall \mathbf{X} \in \Omega$ . Taking into account that  $\varphi = \text{id}$  for an undeformed body,  $\det \text{id} > 0$ , together with the sufficient smoothness of  $\varphi$ , the local invertibility condition

$$\det \mathbf{F} > 0 \quad \forall \mathbf{X} \in \Omega \quad (2.2)$$

follows. Evidently, the global invertibility condition cannot be derived based on Eq. (2.2). Eq. (2.2) is only a necessary condition.

Since  $\mathbf{F} \in GL_+(3)$  with  $GL_+(n)$  denoting the general linear group of dimension  $n$  showing a positive determinant, a right and a left polar decomposition exist, i. e.,

$$\begin{aligned} \forall \mathbf{F} \in GL(n)_+ \quad \exists \mathbf{R}, \mathbf{U} \in GL(n) & : \mathbf{F} = \mathbf{R} \cdot \mathbf{U} \\ \forall \mathbf{F} \in GL(n)_+ \quad \exists \mathbf{R}, \mathbf{V} \in GL(n) & : \mathbf{F} = \mathbf{V} \cdot \mathbf{R}. \end{aligned} \quad (2.3)$$

Here and henceforth, the dot  $(\cdot)$  represents the simple contraction ( $F_{ij} = R_{ik} U_{kj}$ ). In Eq. (2.3),  $\mathbf{R}$  is a proper orthogonal tensor ( $\mathbf{R} \in SO(3)$ ) and  $\mathbf{U}$  as well as  $\mathbf{V}$  are symmetric and positive definite. Consequently, the spectral decomposition theorem can be applied to  $\mathbf{U}$  and  $\mathbf{V}$  leading to

$$\begin{aligned} \mathbf{U} &= \sum_{i=1}^3 \lambda_i^2 \mathbf{N}_i \otimes \mathbf{N}_i & \mathbf{N}_i \cdot \mathbf{N}_j &= \delta_{ij} \\ \mathbf{V} &= \sum_{i=1}^3 \lambda_i^2 \mathbf{n}_i \otimes \mathbf{n}_i & \mathbf{n}_i \cdot \mathbf{n}_j &= \delta_{ij} \end{aligned} \quad (2.4)$$

where  $\lambda_i^2$  are the eigenvalues ( $\lambda_i > 0$ ) and  $\mathbf{N}_i$  and  $\mathbf{n}_i$  are the eigenvectors of  $\mathbf{U}$  and  $\mathbf{V}$ , respectively. Based on this decomposition, a family of strain measures can be introduced.

According to [HILL 1968; HILL 1978], each HILL strain is defined by

$$\begin{aligned}\mathbf{A}(\mathbf{U}) &= \sum_{i=1}^3 f(\lambda_i^2) \mathbf{N}_i \otimes \mathbf{N}_i \\ \mathbf{a}(\mathbf{V}) &= \sum_{i=1}^3 f(\lambda_i^2) \mathbf{n}_i \otimes \mathbf{n}_i\end{aligned}\tag{2.5}$$

with  $f$  representing a scale function which is monotonically increasing and smooth and required to meet the normalizing condition  $f(1) = f'(1) - 1 = 0$ . For instance, setting  $f(\lambda_i^2) = 1/2(\lambda_i^2 - 1)$ ,  $\mathbf{A}$  equals the GREEN-LAGRANGE strain tensor.

## 2.2 Balance equations

This section summarizes briefly some of the balance equations of classical continuum mechanics which are used in the following chapters. A complete description will not be given here.

According to Section 2.1, the present thesis is exclusively concerned with BOLTZMANN continua. Additional rotational degrees of freedom are not considered. Furthermore, all problems discussed in this work fall into the range of *simple bodies* in the sense of [COLEMAN 1964; TRUESDELL & NOLL 1965; NOLL 1972]. It is well known that those assumptions impose some restrictions on the balance equations. The last assumption affecting the balance equations is that the systems under investigation are closed. As a result, the principle of conservation of mass is adopted.

### 2.2.1 Conservation of linear momentum

In what follows,  $\rho_0$ ,  $\mathbf{B}$  and  $\mathbf{T}$  represent the referential mass density per unit undeformed configuration  $\Omega$ , the referential material body-force per unit mass and the material traction per unit undeformed area, respectively. With respect to the deformed configuration  $\varphi(\Omega)$  those variables are denoted as  $\rho$ ,  $\mathbf{b}$  and  $\mathbf{t}$ . With these definitions, the resulting forces acting on a subset  $E \subset \Omega$ , are computed as

$$\mathbf{K} = \int_E \rho_0 \mathbf{B} \, dV + \int_{\partial E} \mathbf{T} \, dA.\tag{2.6}$$

Clearly, by using  $\rho$ ,  $\mathbf{b}$  and  $\mathbf{t}$ , Eq. (2.6) can be re-formulated in terms of variables defined on  $\varphi(\Omega)$ .

The balance law of conservation of linear momentum states that the rate of the linear momentum

$$\mathbf{L} = \frac{d}{dt} \int_E \rho_0 \varphi \, dV = \int_E \rho_0 \dot{\varphi} \, dV\tag{2.7}$$

equals the forces  $\mathbf{K}$ . In Eq. (2.7), the superposed dot represents the time derivative, i. e.,  $\dot{\boldsymbol{\varphi}} = d\boldsymbol{\varphi}/dt$ , with  $t$  being the time. For spatial fields, the superposed dot denotes the *material time derivative*, cf. [TRUEDELLE & NOLL 1965]. Applying the conservation law of mass for closed systems, i. e.,  $\dot{\rho}_0 = 0$ , the identity

$$\int_E \rho_0 \ddot{\boldsymbol{\varphi}} \, dV = \int_E \rho_0 \mathbf{B} \, dV + \int_{\partial E} \mathbf{T} \, dA \quad (2.8)$$

is obtained. This global- or integral-type of the balance law can be re-written into an equivalent local or differential form by using CAUCHY'S theorem, together with the divergence theorem and assuming sufficiently smooth solutions. The resulting equation yields

$$\text{DIV} \mathbf{P} + \rho_0 \mathbf{B} = \rho_0 \ddot{\boldsymbol{\varphi}} \quad \forall \mathbf{X} \in \Omega. \quad (2.9)$$

Here and henceforth,  $\mathbf{P}$  denotes the first PIOLA-KIRCHHOFF stress tensor and  $\text{DIV}(\bullet)$  is the divergence operator with respect to  $\mathbf{X}$ . Obviously, a corresponding equation formulated with respect to the deformed configuration can be derived similarly. According to Eq. (2.9), conservation of energy can be regarded as the extension of NEWTON'S axiom for discrete particles to continua.

**Remark 2.2.1.1** *Conservation of angular momentum is not considered in the present section. It requires the CAUCHY stresses, or equivalently, the second PIOLA-KIRCHHOFF stresses to be symmetric. However, by using appropriate material models, this symmetry is fulfilled a priori as shown in the following sections.*

## 2.2.2 Conservation of energy

The total energy of a body can be decomposed into four parts. The first of those is represented by the kinetic energy

$$K(E) = \frac{1}{2} \int_E \rho_0 \|\dot{\boldsymbol{\varphi}}\|_2^2 \, dV \quad (2.10)$$

being an extensive set function. Clearly,  $\|\bullet\|_2$  is the EUCLIDIAN norm. The second part contributing to change of the total energy is associated with heat. It shows the form

$$\dot{Q}(E) = \int_E \rho_0 R \, dV - \int_{\partial E} \mathbf{H} \cdot \mathbf{N} \, dA. \quad (2.11)$$

Here,  $R$  denotes the material heat-source density and  $\mathbf{H} \cdot \mathbf{N}$  depending on the normal vector  $\mathbf{N}$  of the hyperplane  $\partial E$  is the outward material heat flux. It should be emphasized that the variable  $\dot{Q}$  has to be understood as defined by Eq. (2.11). It is not necessarily

the time derivative of a function  $Q$ , cf. [STEIN & BARTHOLD 1995]. Finally, the power expended by the forces applied to the subbody  $E$  can be computed as

$$P_{\text{ext}} = \int_E \rho_0 \mathbf{B} \cdot \dot{\boldsymbol{\varphi}} \, dV + \int_{\partial E} \mathbf{T} \cdot \dot{\boldsymbol{\varphi}} \, dA. \quad (2.12)$$

With this notation, together with the introduction of the rate of the internal energy  $\dot{E}_{\text{int}}$ , conservation of energy reads

$$\dot{E}_{\text{int}} + \dot{K} = P_{\text{ext}} + \dot{Q}. \quad (2.13)$$

As a consequence, the sum of the rate of the internal energy and the rate of the kinetic energy must be equal to the power expended by the forces  $\mathbf{T}$  and  $\mathbf{B}$  and additional terms related to heat. Analogously to Eq. (2.11),  $\dot{E}_{\text{int}}$  has to be understood as defined by Eq. (2.13). However, according to observations made from experiments, the integral of  $\dot{E}_{\text{int}}$  over a time interval is almost independent of the respective path. For this reason, the existence of a material internal energy density  $U$  per unit mass can be justified and hence, its resulting energy yields

$$E_{\text{int}}(E) = \int_E \rho_0 U \, dV. \quad (2.14)$$

Thus, the rate of internal energy simplifies to the time derivative of Eq. (2.14), i. e.,

$$\dot{E}_{\text{int}} = \dot{E}_{\text{int}}. \quad (2.15)$$

Inserting Eq. (2.15) into Eq. (2.13), using the divergence theorem, conservation of linear momentum and assuming sufficiently smooth solutions, the balance law of energy results in

$$\rho_0 \dot{U} = \mathbf{P} : \dot{\mathbf{F}} + \rho_0 R - \text{DIV} \mathbf{H} \quad \forall \mathbf{X} \in \Omega. \quad (2.16)$$

As in the previous section, this equation can be re-written into an equivalent spatial form.

### 2.2.3 The second law of thermodynamics / Balance of entropy

In contrast to the conservation laws presented in the previous subsection, the balance of entropy represents only a conservation law, if reversible processes are considered. In general, the balance of entropy defines the direction of a thermodynamical process. It should be noted that different versions of this law can be found in the literature, cf. [HUTTER 1977]. In the present work, the second law is formulated according to rational mechanics, see [COLEMAN & GURTIN 1967; TRUESDELL & NOLL 1965].

Introducing the entropy  $S$  of a subbody  $E \subset \Omega$

$$S(E) = \int_E \rho_0 N \, dV \quad (2.17)$$

by the referential entropy density  $N$  per unit mass, together with the absolute temperature  $\theta$ , the second law of thermodynamics reads

$$\frac{d}{dt} \int_E \rho_0 N \, dV \geq \int_E \frac{\rho_0 R}{\theta} \, dV - \int_{\partial E} \frac{\mathbf{H} \cdot \mathbf{N}}{\theta} \, dA. \quad (2.18)$$

It states that the rate of the entropy is never smaller than the one associated with external entropy supply resulting from heat sources and fluxes, respectively. The entropy represents a measure for the amount of energy irreversibly transformed. For a more detailed motivation of the second law, the reader is referred to [COLEMAN & GURTIN 1967] (see also [ORTIZ 2002] for a collection of illustrative examples).

Assuming sufficiently smooth solutions, Eq. (2.18) can be transformed into the equivalent local counterpart

$$\rho_0 \dot{N} - \frac{\rho_0 R}{\theta} + \text{DIV} \frac{\mathbf{H}}{\theta} \geq 0. \quad (2.19)$$

This equation is the local statement of the CLAUSIUS-DUHEM inequality in material form. An alternative form can be derived by applying a LEGENDRE-transformation of the type

$$\psi_0(\bullet, \theta) = \inf_N \{U(\bullet, N) - \theta N\}. \quad (2.20)$$

Here,  $\psi_0$  is the HELMHOLTZ free energy. Using Eq. (2.20) and the law of energy conservation, the CLAUSIUS-DUHEM inequality reads

$$\mathbf{P} : \dot{\mathbf{F}} - \rho_0 \left( \dot{\theta} N + \dot{\psi}_0 \right) - \frac{1}{\theta} \mathbf{H} \cdot \text{GRAD}\theta \geq 0. \quad (2.21)$$

It is obvious that generally, one cannot resolve Ineq. (2.21) into an internal dissipation inequality  $\mathbf{P} : \dot{\mathbf{F}} - \rho_0 (\dot{\theta} N + \dot{\psi}_0) \geq 0$  holding for  $\text{GRAD}\theta \neq \mathbf{0}$  and a heat-conduction inequality  $\mathbf{H} \cdot \text{GRAD}\theta \geq 0$  holding for a nonzero rate of the internal variables (see Section 2.4), cf. [COLEMAN & GURTIN 1967]. However, according to [SIMO 1998], such a decomposition leading to the CLAUSIUS-PLANK form of the second law of thermodynamics

$$\mathbf{P} : \dot{\mathbf{F}} - \rho_0 \left( \dot{\theta} N + \dot{\psi}_0 \right) \geq 0 \quad (2.22)$$

is fulfilled for FOURIER-type models of heat conduction.

## 2.3 Hyperelasticity

In this section, a short review on non-dissipative materials is given. More precisely, special attention is restricted to standard (local) hyperelastic models. These models are characterized by the existence of a potential whose time derivative equals the stress power. In contrast to elastoplasticity, the concept of hyperelasticity is, nowadays, well accepted and understood from a mechanical point of view. However, many mathematical questions

such as existence of a solution and uniqueness are still unanswered, see [BALL 1978; CIARLET 1988]. Throughout the rest of this section thermal effects are neglected.

According to the definition of (local) elasticity (in the sense of CAUCHY), the stress tensor depends only on the deformation gradient, i. e.,  $\mathbf{P} = \mathbf{P}(\mathbf{F})$ . Here and henceforth, the dependence of the spatial position  $\mathbf{X}$  on  $\mathbf{P}$  is not explicitly highlighted.

Hyperelastic continua, also referred to as GREEN-elastic materials, are characterized by the additional property that the work of deformation  $\mathbf{P} : \dot{\mathbf{F}}$  is path independent. Consequently, a potential  $\Psi$  exists, with

$$\mathbf{P} = \frac{\partial \Psi(\mathbf{F})}{\partial \mathbf{F}} \quad \text{and} \quad \dot{\Psi} = \mathbf{P} : \dot{\mathbf{F}}. \quad (2.23)$$

Inserting Eq. (2.23) into Ineq. (2.22) and considering a mechanical process without dissipation, the identity

$$\dot{\Psi}(\mathbf{F}) = \rho_0 \dot{\psi}_0(\mathbf{F}) \quad (2.24)$$

follows. As a result, a hyperelastic material is defined uniquely by its HELMHOLTZ free energy. By virtue of the principle of material frame indifference (see also covariance requirement according to [MARSDEN & HUGHES 1994]), it must be possible to express  $\psi_0$  as a function of the right CAUCHY-GREEN tensor  $\mathbf{C} = \mathbf{F}^T \cdot \mathbf{F}$ . Thus,

$$\mathbf{P} = 2 \mathbf{F} \cdot \frac{\partial \Psi(\mathbf{C})}{\partial \mathbf{C}} = 2 \rho_0 \mathbf{F} \cdot \frac{\partial \psi_0(\mathbf{C})}{\partial \mathbf{C}}. \quad (2.25)$$

Often further restrictions on the form of the strain-energy density function follow from material symmetry. Mathematically, a material is said to be symmetric with respect to the symmetry group  $S \subset SO(3)$ , if its response is not affected by a rotation of an infinitesimal neighborhood with respect to the undeformed configuration. In mathematical terms,

$$\Psi(\mathbf{Q}^T \cdot \mathbf{C} \cdot \mathbf{Q}) = \Psi(\mathbf{C}) \quad \forall \mathbf{Q} \in S \subset SO(3). \quad (2.26)$$

If  $S = SO(3)$ , the material is referred to as isotropic. Clearly, in this case, the HELMHOLTZ free energy depends only on the eigenvalues  $\lambda_i^{\mathbf{C}}$  of  $\mathbf{C}$ , i. e.,

$$\Psi = \Psi(\lambda_1^{\mathbf{C}}, \lambda_2^{\mathbf{C}}, \lambda_3^{\mathbf{C}}). \quad (2.27)$$

It is obvious that instead of the eigenvalues  $\lambda_i^{\mathbf{C}}$ , different invariants of  $\mathbf{C}$  can be used as well.

For more complex symmetry groups ( $S \neq SO(3)$ ), the reader is referred to [SPENCER & RIVLIN 1962; SPENCER 1971] (see also [BETTEN 1993]). In the cited works, the authors derived *integrity bases* based on *structural tensors*. Those bases fulfill the symmetry condition (2.26). Clearly, for  $S = SO(3)$  the eigenvalues of  $\mathbf{C}$  represent an admissible set of integrity bases. In the case of more complex symmetry groups, the strain-energy density has to be formulated in terms of the respective basis.

**Remark 2.3.0.1** *The second PIOLA-KIRCHHOFF tensor  $\mathbf{S}$  resulting from a hyperelastic material law takes the form  $\mathbf{S} = 2 \partial_{\mathbf{C}}\Psi$ . Without loss of generality, this derivative can be represented by a symmetric tensor, since  $\mathbf{C}$  is symmetric. That is, the identity  $\mathbf{S} = \mathbf{S}^T$  is fulfilled a priori. As a consequence, conservation of angular momentum is guaranteed.*

### 2.3.1 Examples

In the present work, three different hyperelastic models will be applied. Each of them is isotropic. The respective strain-energy densities are:

- HENCKY's strain-energy function, cf. [BRUHNS, XIAO & MEYERS 2001]

$$\Psi = \frac{1}{2} \lambda [\varepsilon_1 + \varepsilon_2 + \varepsilon_3]^2 + \mu [(\varepsilon_1)^2 + (\varepsilon_2)^2 + (\varepsilon_3)^2], \quad \varepsilon_i = \log \sqrt{\lambda_i^{\mathbf{C}}} \quad (2.28)$$

- Neo-HOOKE, version I, cf. [SIMO & PISTER 1984]

$$\Psi = \frac{1}{2} \lambda \log^2 J + \frac{1}{2} \mu (\text{tr} \mathbf{C} - 3 - 2 \log J), \quad J = \det \mathbf{F}, \text{tr} \mathbf{C} = \mathbf{C} : \mathbf{1} \quad (2.29)$$

- Neo-HOOKE, version II, cf. [CIARLET 1988]

$$\Psi = \lambda \frac{J^2 - 1}{4} - \left( \frac{\lambda}{2} + \mu \right) \log J + \frac{1}{2} \mu (\text{tr} \mathbf{C} - 3) \quad (2.30)$$

In Eqs. (2.28)-(2.30),  $\lambda$  and  $\mu$  represent the LAMÉ constants. It should be noted that among the enumerated models only CIARLET's neo-HOOKEan function is polyconvex. It can easily be seen that the strain-energy density defining HENCKY's model as well as that of the first version of the neo-HOOKEan are not convex in  $J$ . Due to [BALL 1978] polyconvexity is very important from a mathematical point of view since it implies quasiconvexity of  $\psi_0$  and hence, under a few further conditions, the lower semicontinuity of the resulting potential of the system considered. This property is crucial for proving the existence of solutions.

### 2.3.2 Principle of minimum potential energy

In this subsection, the Boundary Value Problem (BVP) of a hyperelastic body is reformulated as a minimization problem. In what follows, thermal as well as dynamical effects are neglected. As a consequence, the resulting BVP reads

$$\begin{aligned} \text{DIV} \mathbf{P} + \rho_0 \mathbf{B} &= \mathbf{0} & \forall \mathbf{X} \in \Omega \\ \varphi &= \bar{\varphi} & \forall \mathbf{X} \in \partial_1 \Omega \\ \mathbf{P} \cdot \mathbf{N} &= \bar{\mathbf{T}} & \forall \mathbf{X} \in \partial_2 \Omega \end{aligned} \quad (2.31)$$

where  $\partial_1\Omega$  is the displacement boundary;  $\partial_2\Omega = \partial\Omega/\partial_1\Omega$  is the traction boundary;  $\bar{\varphi}$  is the prescribed value of the deformation mapping on  $\partial_1\Omega$ ; and  $\bar{\mathbf{T}}$  are the applied tractions.

Applying the principle of virtual work, together with a BUBNOV-GALERKIN method, the solution of the BVP can be re-written as

Find  $\varphi \in V$  such that

$$\int_{\Omega} \mathbf{P} : \text{GRAD}\boldsymbol{\eta} \, dV = \int_{\Omega} \rho_0 \mathbf{B} \cdot \boldsymbol{\eta} \, dV + \int_{\partial_2\Omega} \bar{\mathbf{T}} \cdot \boldsymbol{\eta} \, dA \quad \forall \boldsymbol{\eta} \in V. \quad (2.32)$$

Clearly,  $\varphi$  has to comply with the boundary conditions and the test functions  $\boldsymbol{\eta}$  must be zero on  $\partial_1\Omega$ . If  $V$  is large enough, Eq. (2.32) implies the local form Eq. (2.31). It is well known that if  $\mathbf{P}$  derives from a potential according to Eq. (2.25), Eq. (2.32) represents the stationarity condition of the equation

$$I(\varphi) = \int_{\Omega} \Psi(\text{GRAD}\varphi) \, dV - \int_{\Omega} \rho_0 \mathbf{B} \cdot \varphi \, dV + \int_{\partial_2\Omega} \bar{\mathbf{T}} \cdot \varphi \, dA. \quad (2.33)$$

More precisely,  $\varphi$  can be computed from the minimization principle

$$\inf_{\varphi \in V} I(\varphi). \quad (2.34)$$

The assumption that Problem (2.34) is the overriding principle (instead of just the stationarity condition of  $I$ ) originates from the presumption that the stable configurations are energy minimizers. Furthermore, in the case of isotropic linearized elasticity, Eq. (2.32) is, as well known, associated with a minimum.

**Remark 2.3.2.1** *From a mathematical point of view, a convex function  $\Psi(\mathbf{F})$  would be preferable, since it guarantees the existence of a unique minimizer (if a solution exists). Unfortunately, as pointed out for instance in [TRUESDELL & NOLL 1965; CIARLET 1988] such an assumption would violate fundamental physical observations. For example, a hydrostatic compression stress state could not be modeled.*

## 2.4 Plasticity theory

In this section, a class of finite strain plasticity models is presented. In contrast to elasticity, there exists a large number of different theories for plasticity accounting for finite strains. According to [XIAO, BRUHNS & MEYERS 2006], the most frequently applied ones can be subdivided into the following classes:

- *Classical EULERIAN rate formulations*, cf. [HILL 1958; LEHMANN 1960; BRUHNS, XIA & MEYERS 2001]. Those models are based on the additive decomposition of

the deformation rate  $\mathbf{d} := (\dot{\mathbf{F}} \cdot \mathbf{F}^{-1})^{\text{sym}}$  into an elastic part  $\mathbf{d}^e$  and a plastic part  $\mathbf{d}^p$ , i. e.,

$$\mathbf{d} = \mathbf{d}^e + \mathbf{d}^p. \quad (2.35)$$

- *Additive decomposition of LAGRANGIAN strains*, cf. [GREEN & NAGHDI 1965; PADOPOULOS & LI 1998; MIEHE, APEL & LAMBRECHT 2002]. The fundamental assumption of those approaches is the additive decomposition of a LAGRANGIAN strain measure  $\mathbf{A}$  into elastic and plastic parts, i. e.,

$$\mathbf{A} = \mathbf{A}^e + \mathbf{A}^p. \quad (2.36)$$

- *Multiplicative decomposition of the deformation gradient*, cf. [LEE 1969; SIMO & ORTIZ 1985]. The introduction of an unstressed configuration (locally) represents the basic principle for the models advocated by LEE. In mathematical terms, this postulate reads

$$\mathbf{F} = \mathbf{F}^e \cdot \mathbf{F}^p, \quad \text{with} \quad \det \mathbf{F}^e > 0, \det \mathbf{F}^p > 0. \quad (2.37)$$

See also [BERTRAM 1999; SVENDSON 1998] for models based on *material isomorphism*. They are related to theories using multiplicative kinematics. For further details, the reader is referred to [ITSKOV 2001; XIAO, BRUHNS & MEYERS 2006].

For a detailed overview and critical comments, refer to [NAGHDI 1990; NEMAT-NASSER 2004; XIAO, BRUHNS & MEYERS 2006]. It should be emphasized that in the case of linearized kinematics, all three methods are completely equivalent.

Since one focus of the present work is on the implementation of the mechanical models developed, computational issues are of great importance. For this reason, classical EULERIAN rate formulations are not considered. Although they are physically sound, they require, in general, expensive numerical integration schemes, even if the solid unloads purely elastically. Theories in the sense of [GREEN & NAGHDI 1965] show the problem that they are not well-motivated from a physical point of view, cf. [XIAO, BRUHNS & MEYERS 2006]. Furthermore, they may result in a questionable material response, see [ITSKOV 2004]. As a consequence, models based on the multiplicative decomposition of the deformation gradient will be used throughout the rest of this work. However, it is well-known that also those models are not completely unquestionable. One issue is the not uniquely defined intermediate configuration introduced by the split (2.37).

It should be noted that the material models used in this work are either fully isotropic, or the respective flow rule specifies  $\mathbf{F}^p$  completely. In the case of a fully isotropic response, the intermediate configuration is not important, see [SIMO & HUGHES 1998]. More precisely, a rotation with respect to the intermediate configuration does not affect any constitutive equation. On the other hand, if  $\mathbf{F}^p$  is determined completely by the constitutive model such as for single-crystal plasticity (cf. [ASARO 1983]), the intermediate configuration is defined uniquely, see [SIMO 1998].

### 2.4.1 Fundamentals

The fundamentals of finite strain plasticity theory based on a multiplicative decomposition of the deformation gradient in the sense of [LEE 1969] are briefly discussed in this subsection. Multisurface plasticity is not considered. For more details, the reader is referred to [LUBLINER 1997; MIEHE 1993; SIMO 1998; SIMO & HUGHES 1998]. In line with the previous section, isothermal static conditions are assumed. Additionally, for modeling a dissipative material response, a description with internal state variables is used, cf. [COLEMAN & GURTIN 1967]. Within this framework, a stored energy density of the type

$$\Psi = \Psi(\mathbf{F}^e, \mathbf{F}^p, \boldsymbol{\alpha}) \quad (2.38)$$

is considered with  $\boldsymbol{\alpha} \in \mathbb{R}^n$  being strain-like internal variables associated with hardening or softening. More specifically, an energy functional  $\Psi$  of the type

$$\Psi = \bar{\Psi}^e(\mathbf{F}^e) + \Psi^p(\boldsymbol{\alpha}). \quad (2.39)$$

is adopted. According to this equation, the elastic response modeled by  $\bar{\Psi}^e$  is assumed to be completely independent of the internal processes reproduced by  $\boldsymbol{\alpha}$ . Clearly, by the principle of material frame indifference,  $\bar{\Psi}^e(\mathbf{F}^e) = \Psi^e(\mathbf{C}^e)$  where  $\mathbf{C}^e := \mathbf{F}^{eT} \cdot \mathbf{F}^e$  is the elastic right CAUCHY-GREEN tensor. The second term in Eq. (2.39), denoted as  $\Psi^p$ , represents the stored energy due to plastic work. It is associated with isotropic/kinematic hardening/softening. For more details about energy functionals of the type (2.39), refer to [LUBLINER 1972]. It should be noted that in most applications, a functional of the type (2.39) is adopted.

**Remark 2.4.1.1** *In the case of damage-induced stiffness degradation, the material properties depend, apparently on the internal variables and hence, the assumption made before is wrong. For those models  $\Psi^e = \Psi^e(\mathbf{C}^e, \boldsymbol{\alpha})$ .*

Using Eq. (2.37), the CLAUSIUS-PLANK form (2.22) of the second law of thermodynamics for isothermal processes

$$\mathcal{D} = \mathbf{P} : \dot{\mathbf{F}} - \dot{\Psi} = \mathbf{S} : \frac{1}{2} \dot{\mathbf{C}} - \dot{\Psi} \geq 0 \quad (2.40)$$

yields

$$\mathcal{D} = \left( \mathbf{F}^p \cdot \mathbf{S} \cdot \mathbf{F}^{pT} - 2 \frac{\partial \Psi}{\partial \mathbf{C}^e} \right) : \frac{1}{2} \dot{\mathbf{C}}^e + \mathbf{S} : \left( \mathbf{F}^{pT} \cdot \mathbf{C}^e \cdot \dot{\mathbf{F}}^p \right) + \mathbf{Q} \cdot \dot{\boldsymbol{\alpha}} \geq 0. \quad (2.41)$$

In Eqs. (2.40) and (2.41),  $\mathbf{S} := \mathbf{F}^{-1} \cdot \mathbf{P}$  denotes the second PIOLA-KIRCHHOFF stress tensor and  $\mathbf{Q} := -\partial_{\boldsymbol{\alpha}} \Psi$  is the stress-like internal variable work conjugate to  $\boldsymbol{\alpha}$ . According to Eq. (2.41), the dissipation is decomposed additively into one part associated with the

elastic strain rate and a second part corresponding to plastic deformation. Since both parts are independent of one another, Ineq. (2.41) gives rise to

$$\mathbf{S} = 2 \frac{\partial \Psi}{\partial \mathbf{C}} = 2 \mathbf{F}^{\text{p}^{-1}} \cdot \frac{\partial \Psi}{\partial \mathbf{C}^{\text{e}}} \cdot \mathbf{F}^{\text{p}^{-T}} \quad (2.42)$$

and the reduced dissipation inequality

$$\mathcal{D} = \boldsymbol{\Sigma} : \mathbf{L}^{\text{p}} + \mathbf{Q} \cdot \dot{\boldsymbol{\alpha}} \geq 0. \quad (2.43)$$

Here and henceforth,  $\boldsymbol{\Sigma} = 2 \mathbf{C}^{\text{e}} \cdot \partial_{\mathbf{C}^{\text{e}}} \Psi$  are the MANDEL stresses (cf. [MANDEL 1972]) and  $\mathbf{L}^{\text{p}} = \dot{\mathbf{F}}^{\text{p}} \cdot \mathbf{F}^{\text{p}^{-1}}$  denotes the plastic velocity gradient.

Following geometrically linearized plasticity theory, the elastic domain has to be defined. For that purpose, the admissible stress space  $\mathbb{E}_{\boldsymbol{\sigma}}$  is introduced, cf. [LUBLINER 1997]. Since according to Ineq. (2.43), the reduced dissipation inequality depends naturally on the MANDEL stresses,  $\mathbb{E}_{\boldsymbol{\sigma}}$  is formulated in terms of  $\boldsymbol{\Sigma}$ , i. e.,

$$\mathbb{E}_{\boldsymbol{\sigma}} = \{(\boldsymbol{\Sigma}, \mathbf{Q}) \in \mathbb{R}^{9+n} \mid \phi(\boldsymbol{\Sigma}, \mathbf{Q}) \leq 0\}. \quad (2.44)$$

The boundary  $\partial \mathbb{E}_{\boldsymbol{\sigma}}$  represents a level set function measuring the elastic limit of the material considered. That is, if  $(\boldsymbol{\Sigma}, \mathbf{Q}) \in \text{int} \mathbb{E}_{\boldsymbol{\sigma}}$ , the solid deforms purely elastically. Only if  $(\boldsymbol{\Sigma}, \mathbf{Q}) \in \partial \mathbb{E}_{\boldsymbol{\sigma}}$ , a plastic response is possible. Clearly, the *yield function*  $\phi$  has to be derived from experimental observation. Additionally,  $\phi$  must be convex and sufficiently smooth, cf. [MAUGIN 1992].

**Remark 2.4.1.2** *The MANDEL stresses are defined by  $\boldsymbol{\Sigma} = 2 \mathbf{C}^{\text{e}} \cdot \partial_{\mathbf{C}^{\text{e}}} \Psi$ . Consequently, it is a mixed variant tensor operating on the intermediate configuration. More precisely, it maps cotangent vectors into cotangent vectors belonging to the same space. That is,  $\boldsymbol{\Sigma}$  can be interpreted as an endomorphism and hence, its eigenvalues are well defined (compare to [HACKL 1997]).*

The constitutive model is completed by evolution equations for  $\mathbf{L}^{\text{p}}$  and  $\boldsymbol{\alpha}$  and by loading/unloading conditions. They can be derived from the postulate of maximum dissipation. More precisely,

$$\max_{(\tilde{\boldsymbol{\Sigma}}, \tilde{\mathbf{Q}}) \in \mathbb{E}_{\boldsymbol{\sigma}}} \left[ \tilde{\boldsymbol{\Sigma}} : \mathbf{L}^{\text{p}} + \tilde{\mathbf{Q}} \cdot \dot{\boldsymbol{\alpha}} \right]. \quad (2.45)$$

This postulate leads to the evolution equations

$$\mathbf{L}^{\text{p}} = \lambda \partial_{\boldsymbol{\Sigma}} \phi \quad \dot{\boldsymbol{\alpha}} = \lambda \partial_{\mathbf{Q}} \phi, \quad (2.46)$$

together with the KARUSH-KUHN-TUCKER conditions

$$\lambda \geq 0 \quad \phi \lambda \geq 0. \quad (2.47)$$

As a result, plastic deformations require  $(\boldsymbol{\Sigma}, \mathbf{Q}) \in \partial \mathbb{E}_{\boldsymbol{\sigma}}$ . The plastic multiplier  $\lambda$  is obtained from the consistency condition

$$\dot{\phi} = 0. \quad (2.48)$$

Evolution laws of the type (2.46) are characterized by the property that the rates of the internal variables (together with  $\mathbf{L}^p$ ) are proportional to the gradient of the yield function. Such laws are referred to as *associated flow rules* or *normality rules*. They follow, as shown before, from the postulate of maximum dissipation. Although this postulate is mathematically and physically very appealing, it cannot be applied to the modeling of every material. That is, in contrast to the second law of thermodynamics, it is not a physical law. Hence, a generalization of the evolution Eqs. (2.46) is sometimes necessary. By analogy to Eq. (2.46), the generalized flow rules are postulated as

$$\mathbf{L}^p = \lambda \partial_{\Sigma} g \quad \dot{\boldsymbol{\alpha}} = \lambda \partial_{\mathbf{Q}} h. \quad (2.49)$$

Here, the plastic potential  $g$  and the hardening potential  $h$  define the directions of the rates of  $\mathbf{L}^p$  and  $\boldsymbol{\alpha}$ , respectively. Setting  $g = h = \phi$ , the associative case is recovered.

**Remark 2.4.1.3** *In the case of damage-induced stiffness degradation, similar evolution equations can be derived. However, since the respective internal variables are contained in  $\Psi^e$ , they result in a change of the elastic response, cf. [SIMO & JU 1989; MIEHE 1993; OLIVER, HUESPE, PULIDO & SAMANIEGO 2003].*

**Remark 2.4.1.4** *According to Eq. (2.46), the flow rule is nine-dimensional, since the yield function is formulated in terms of MANDEL stresses. Some researchers believe that this characteristic of the described model is not physically sound, cf. [LUBLINER 1997], page 460. Nevertheless, it should be noted that if an isotropic hyperelastic material model is applied (which is the case in this work), the MANDEL stresses are symmetric resulting in a six-dimensional flow rule.*

**Remark 2.4.1.5** *Introducing the characteristic function of  $\mathbb{E}_{\sigma}$*

$$J(\boldsymbol{\Sigma}, \mathbf{Q}) := \begin{cases} 0 & \forall (\boldsymbol{\Sigma}, \mathbf{Q}) \in \mathbb{E}_{\sigma} \\ \infty & \text{otherwise,} \end{cases} \quad (2.50)$$

*flow rules derived from the principle of maximum dissipation can be re-written into the form*

$$(\mathbf{L}^p, \dot{\boldsymbol{\alpha}}) \in \partial J(\boldsymbol{\Sigma}, \mathbf{Q}) \quad (2.51)$$

*where  $\partial J$  is the sub-differential of  $J$ , i. e.,*

$$\partial J(\boldsymbol{\Sigma}, \mathbf{Q}) := \left\{ (\bar{\mathbf{L}}^p, \dot{\bar{\boldsymbol{\alpha}}}) \in \mathbb{R}^{9+n} \mid \begin{aligned} & J(\boldsymbol{\Sigma} + \tilde{\boldsymbol{\Sigma}}, \mathbf{Q} + \tilde{\mathbf{Q}}) \geq \\ & J(\boldsymbol{\Sigma}, \mathbf{Q}) + \tilde{\boldsymbol{\Sigma}} : \bar{\mathbf{L}}^p + \tilde{\mathbf{Q}} \cdot \dot{\bar{\boldsymbol{\alpha}}}, \forall (\tilde{\boldsymbol{\Sigma}}, \tilde{\mathbf{Q}}) \in \mathbb{R}^{9+n} \end{aligned} \right\} \quad (2.52)$$

*For further details, the reader is referred to [MAUGIN 1992; ROCKAFELLAR 1970].*

**Remark 2.4.1.6** *A broad class of different plasticity models governed by the normality rule are defined by a yield function of the type*

$$\phi(\boldsymbol{\Sigma}, \mathbf{Q}) = \Sigma_{\text{eq}}(\boldsymbol{\Sigma}, \mathbf{Q}) - \Sigma_{\text{eq}}^{\text{ini}} \quad (2.53)$$

where  $\Sigma_{\text{eq}} : \mathbb{R}^{9 \times n} \rightarrow \mathbb{R}$  is an equivalent stress measure and  $\Sigma_{\text{eq}}^{\text{ini}} > 0$  is associated with the size of the elastic domain before plastic deformation occurs. Most of the yield functions applied in practice are based on an equivalent stress measure being a convex and positively homogeneous function of degree one, i. e.,

$$\Sigma_{\text{eq}}(c(\boldsymbol{\Sigma}, \mathbf{Q})) = c \Sigma_{\text{eq}}(\boldsymbol{\Sigma}, \mathbf{Q}) \quad \forall c \in \mathbb{R}_+ \quad (2.54)$$

cf. [SIMO 1998]. With this property, the dissipation can be re-written as

$$\mathcal{D} = \lambda \Sigma_{\text{eq}}^{\text{ini}} \geq 0. \quad (2.55)$$

Since  $\lambda \geq 0$  and  $\Sigma_{\text{eq}}^{\text{ini}} > 0$ , the second law of thermodynamics is fulfilled a priori. It should be noted that all yield functions used herein show the form (2.53) and (2.54).

## 2.4.2 Example: Single-crystal plasticity / single slip system

As an example, the yield function and the respective evolution equations of single-crystal plasticity theory are briefly presented in this subsection. It will be shown that if cohesive models are re-written according to the framework discussed in Chapter 3, they are formally identical to plasticity theories for a single slip system. More details about crystal-plasticity can be found in [ASARO 1983].

Since single-crystal plasticity (in the sense of SCHMID's law) is based on associative evolution equations, the model is defined completely by the respective yield function  $\phi$ . Introducing a slip plane by its corresponding normal vector  $\bar{\mathbf{n}}$  and the slip direction  $\bar{\mathbf{m}}$ ,  $\phi$  is given by

$$\phi(\boldsymbol{\Sigma}, \alpha) = |\boldsymbol{\Sigma} : (\bar{\mathbf{m}} \otimes \bar{\mathbf{n}})| - Q(\alpha) - \Sigma_{\text{eq}}^{\text{ini}}. \quad (2.56)$$

Evidently, the vectors  $\bar{\mathbf{n}}$  and  $\bar{\mathbf{m}}$  are objects that belong to the intermediate configuration. They are orthogonal to one another and time-independent, i. e.,

$$\bar{\mathbf{n}} \cdot \bar{\mathbf{m}} = 0 \quad \|\bar{\mathbf{n}}\|_2 = \|\bar{\mathbf{m}}\|_2 = 1. \quad (2.57)$$

Isotropic hardening/softening is taken into account by the yield stress  $Q$  depending on the strain-like internal variable  $\alpha$ . Applying Eq. (2.46), the plastic velocity gradient

$$\mathbf{L}^p = \tilde{\lambda} (\bar{\mathbf{m}} \otimes \bar{\mathbf{n}}), \quad \text{with} \quad \tilde{\lambda} = \lambda \text{sign} [\boldsymbol{\Sigma} : (\bar{\mathbf{m}} \otimes \bar{\mathbf{n}})] \quad (2.58)$$

is obtained.

**Remark 2.4.2.1** Eq. (2.56) can be re-written as

$$\phi = \Sigma_{\text{eq}}^{\text{ini}}(\boldsymbol{\Sigma}, \mathbf{Q}) - \Sigma_{\text{eq}}^{\text{ini}} \quad (2.59)$$

Obviously,  $\Sigma_{\text{eq}}^{\text{ini}}(\boldsymbol{\Sigma}, \mathbf{Q})$  is convex and positively homogeneous of degree one. Hence, the resulting dissipation is given by  $\mathcal{D} = \lambda \Sigma_{\text{eq}}^{\text{ini}}$ , cf. Remark 2.4.1.6.

### 2.4.3 Numerical implementation

The numerical implementation of finite strain plasticity models such as those discussed in the previous subsection can be found in [SIMO & HUGHES 1998; SIMO 1998; ORTIZ 2003]. For a more recent state of the art review, refer to [SCHMIDT-BALDASSARI & HACKL 2006]. The two fundamental ingredients required for the numerical computation of the problem defined in the previous subsection are:

- Integration of the evolution as defined by Eqs. (2.49)
- Operator split techniques allowing for decoupling the problem into fully elastic sub-problems and plastic corrector steps.

A comprehensive overview on integration algorithms can be found in [HAIRER & WANNER 2000]. For operator split methods, the reader is referred to [CHORIN, HUGHES, MCCrackEN & MARSDEN 1978]. An interesting comparison between different schemes is given in [SCHMIDT-BALDASSARI & HACKL 2006].

Herein, the backward-EULER integration is applied. More precisely, the by now classical return-mapping algorithm is adopted, cf. [SIMO & HUGHES 1998]. That is, based on an operator split method, the solution is computed first by assuming a fully elastic loading step (the *trial state*). If the stresses corresponding to this solution do not belong to  $\mathbb{E}_\sigma$ , a plastic corrector step is performed. Within this step the evolution equations are integrated by means of the backward-EULER scheme.

According to [HAIRER & WANNER 2000], the backward-EULER scheme is first order accurate. Clearly, more accurate methods are available, cf. [SCHMIDT-BALDASSARI & HACKL 2006]. Nevertheless, as mentioned in [SIMO 1998], if the long-term response is more important, the backward-EULER integration is often more accurate than algorithms showing a better short-term accuracy such as second order approaches. Furthermore, the numerical implementation presented in this subsection will be applied to problems like cracking. Consequently, the solution is not very smooth, in general.

In addition to the good long-term response of the backward-EULER scheme, the method is unconditional stable. More precisely, it possesses the linearized stability properties: *L*-stability (and hence, *A*-stability) and *B*-stability, cf. [SIMO 1998]. Those properties are needed in order to guarantee a bounded response of the integration algorithm.

In what follows, the numerical implementation of the class of material models described in the previous subsection is addressed. More specifically, the return-mapping algorithm is discussed.

Suppose the deformation gradient at time  $t_{n+1}$  is denoted as  $\mathbf{F}_{n+1}$ . Then, an elastic trial state is defined by

$$\mathbf{F}_{n+1}^p = \mathbf{F}_n^p, \quad \boldsymbol{\alpha}_{n+1} = \boldsymbol{\alpha}_n. \quad (2.60)$$

Evidently, this state is characterized by a purely elastic response. With those equations, the elastic right CAUCHY-GREEN tensor reads

$$\mathbf{C}_{n+1}^e = \mathbf{F}_{n+1}^{\text{p}-T} \cdot \mathbf{C}_{n+1} \cdot \mathbf{F}_{n+1}^{\text{p}-1}, \quad \text{with} \quad \mathbf{F}_{n+1}^{\text{p}} = \mathbf{F}_n^{\text{p}}. \quad (2.61)$$

Based on Eq. (2.61), the trial stresses  $\boldsymbol{\Sigma}_{n+1}$  and subsequently, the discrete loading condition

$$\phi(\boldsymbol{\Sigma}_{n+1}, \boldsymbol{\alpha}_n) > 0 \quad (2.62)$$

are computed. Clearly, if Ineq. (2.62) is not fulfilled, the loading state is fully elastic, and consequently, the solution of the trial state is already the solution of the problem considered.

On the other hand, if Ineq. (2.62) holds, a plastic corrector step is applied. For that purpose, the evolution Eqs. (2.49) are integrated numerically by using an implicit backward-EULER scheme leading to

$$\mathbf{F}_{n+1}^{\text{p}} = \mathbf{F}_n^{\text{p}} + \Delta\lambda \left. \partial_{\boldsymbol{\Sigma}} g \right|_{\boldsymbol{\Sigma}_{n+1}, \mathbf{Q}_{n+1}} \cdot \mathbf{F}_{n+1}^{\text{p}} \quad \boldsymbol{\alpha}_{n+1} = \boldsymbol{\alpha}_n + \Delta\lambda \left. \partial_{\mathbf{Q}} h \right|_{\boldsymbol{\Sigma}_{n+1}, \mathbf{Q}_{n+1}} \quad (2.63)$$

with  $\Delta\lambda = \lambda (t_{n+1} - t_n)$ . Here, it has been assumed that the internal variables are scalar-valued, since, obviously, the integration depends on the tensorial character of the evolution equation to be approximated, cf. [PINSKY, ORTIZ & PISTER 1983; SIMO & HUGHES 1998].

It should be noted that a modified exponential integration scheme of the type

$$\mathbf{F}_{n+1}^{\text{p}} = \exp \left( \Delta\lambda \left. \partial_{\boldsymbol{\Sigma}} g \right|_{\boldsymbol{\Sigma}_{n+1}, \mathbf{Q}_{n+1}} \right) \cdot \mathbf{F}_n^{\text{p}} \quad (2.64)$$

is often advantageous, see [WEBER & ANAND 1990; ETEROVIC & BATHE 1990; CUITINO & ORTIZ 1992]. For instance, this technique guarantees that isochronic constraints ( $\det \mathbf{F}^{\text{p}} = 1$ ) are preserved. For this reason, it will be used for the numerical implementation. For the computation of the derivatives of the exponential mapping necessary for the algorithmic formulation, the reader is referred to [ORTIZ, RADOVITZKY & REPETTO 2001; ITSKOV 2003].

The approximation of the evolution equations transforms the set of algebraic differential equations into the purely algebraic problem

$$\mathbf{R}_{n+1} = [\mathbf{R}_{n+1}^{\text{FP}}, \mathbf{R}_{n+1}^{\alpha}] = \mathbf{0} \quad \wedge \quad \phi(\boldsymbol{\Sigma}_{n+1}, \mathbf{Q}_{n+1}) = 0 \quad (2.65)$$

where the residuals are defined by

$$\begin{aligned} \mathbf{R}_{n+1}^{\text{FP}} &= -\mathbf{F}_{n+1}^{\text{p}} + \mathbf{F}_n^{\text{p}} + \Delta\lambda \left. \partial_{\boldsymbol{\Sigma}} g \right|_{\boldsymbol{\Sigma}_{n+1}, \mathbf{Q}_{n+1}} \cdot \mathbf{F}_{n+1}^{\text{p}} \\ \mathbf{R}_{n+1}^{\alpha} &= -\boldsymbol{\alpha}_{n+1} + \boldsymbol{\alpha}_n + \Delta\lambda \left. \partial_{\mathbf{Q}} h \right|_{\boldsymbol{\Sigma}_{n+1}, \mathbf{Q}_{n+1}}. \end{aligned} \quad (2.66)$$

Evidently, in the case of the exponential mapping, the first residual reads

$$\mathbf{R}_{n+1}^{\text{FP}} = -\mathbf{F}_{n+1}^{\text{p}} + \exp \left( \Delta\lambda \left. \partial_{\boldsymbol{\Sigma}} g \right|_{\boldsymbol{\Sigma}_{n+1}, \mathbf{Q}_{n+1}} \right) \cdot \mathbf{F}_n^{\text{p}}. \quad (2.67)$$

The solution of the nonlinear set of Eqs. (2.65) can be computed by means of different techniques. Herein, a classical NEWTON-type scheme guaranteeing an asymptotic quadratic convergence (for sufficiently smooth functions) is adopted. Linearizing this procedure at the solution point gives the *algorithmic tangent*  $\mathbb{C}_{n+1}^{\text{el}}$ , i. e.,

$$\mathbb{C}_{n+1}^{\text{el}} = \frac{d\mathbf{P}_{n+1}}{d\mathbf{F}_{n+1}} \quad (2.68)$$

Further details are omitted. They can be found in [SIMO & HUGHES 1998; SIMO 1998; ORTIZ 2002; SCHMIDT-BALDASSARI & HACKL 2006].

**Remark 2.4.3.1** *The nonlinear set of Eqs. (2.65) is a  $(9 + \dim \boldsymbol{\alpha} + 1)$ -dimensional problem. However, in many cases, this dimension can be reduced significantly. For instance, if the hyperelastic response as well as the plastic potential are isotropic tensor functions, the tensors  $\mathbf{C}^e$ ,  $\boldsymbol{\Sigma}$  and  $\partial_{\boldsymbol{\Sigma}}g$  are coaxial. Consequently, if the exponential mapping according to Eq. (2.67) is applied,  $\mathbf{C}_0^e$  and  $\mathbf{C}_{n+1}^e$  are coaxial with  $\mathbf{C}_0^e$  representing the trial elastic right CAUCHY-GREEN tensor. That is, all tensors involved in the algorithmic formulation are coaxial and hence, the algorithm can be performed in principle axes, leading to a  $(3 + \dim \boldsymbol{\alpha} + 1)$ -dimensional problem, cf. [SIMO 1992; SIMO 1998].*

**Remark 2.4.3.2** *If HENCKY's hyperelastic potential (2.28), together with an isotropic yield function (and associative evolution equations) are applied, the multiplicative decomposition of the deformation gradient results in an additive split of the HENCKY strain tensor. Since for HENCKY's potential the stresses depend linearly on the strain tensor, a decomposition formally identical to the one known from classical small strain theory can be derived. Hence, standard algorithms designed for the geometrically linear theory can be used, see [SIMO 1998; ORTIZ 2002].*

**Remark 2.4.3.3** *In the case of HENCKY's hyperelastic potential (2.28), together with the VON MISES yield function (and associative evolution equations), the set of equations (2.65) reduces to a single scalar-valued equation depending only on the integrated plastic multiplier  $\Delta\lambda$ , cf. [SIMO 1992; SIMO 1998]. Hence, the resulting numerical implementation is very efficient. This particular model is adopted for the numerical examples contained in Chapter 6.*

## 2.5 Standard dissipative media

If the evolution equations obey the normality rule (see Eq. (2.46)), they can be derived from a variational principle. More precisely, in this case, the solution of the algebraic differential equation characterizing the material response follows from a minimization principle. The advantages resulting from such a principle are manifold. On the one hand, the existence of solutions can be analyzed by using the same tools originally designed for hyperelastic material models, cf. [BALL 1978; ORTIZ & REPETTO 1999; CARSTENSEN,

HACKL & MIELKE 2002]. On the other hand, a minimum principle can be taken as a canonical basis for error estimation, cf. [RADOVITZKY & ORTIZ 1999; THOUTIREDDY & ORTIZ 2004; MOSLER & ORTIZ 2005]. In addition, from an implementational point of view, a minimization principle opens up the possibility to apply state of the art optimization algorithms. Particularly for multisurface plasticity models such as single-crystal plasticity this represents an interesting feature.

The concept of using the underlying variational principle for the constitutive update enjoys a relatively long tradition dating back, at least, to [COMI, CORIGLIANO & MAIER 1991; COMI & PEREGO 1995]. In those works, the authors, derived a HU-WASHIZU functional whose minimum corresponds to the solution of the discretized algebraic differential equations defining the material model. In the respective numerical implementation, the constitutive model was enforced in a weak sense. That is, the resulting finite element formulation is different compared to the one usually applied in computational plasticity, cf. [SIMO & HUGHES 1998; SIMO 1998]. According to the previous section, most frequently, the constitutive law is strongly enforced pointwise (usually at the integration points).

Probably inspired by the works [COMI, CORIGLIANO & MAIER 1991; COMI & PEREGO 1995], ORTIZ advocated a constitutive update based on a minimization principle as well, cf. [ORTIZ & STAINIER 1999; ORTIZ 2002]. Nevertheless, in contrast to the previous works, the proposed algorithmic formulation coincides with the structure of standard finite element codes. That is, the update is performed pointwise, i. e., at the integration points. The ideas suggested by ORTIZ are briefly discussed in this section. They represent the fundamental ingredient for the adaptive finite element schemes presented in Chapters 4 – 6. Similar numerical procedure and further elaborations can be found, for instance, in [CARSTENSEN, HACKL & MIELKE 2002]. For models based on linearized kinematics, the reader is referred to [MIEHE 2002].

### 2.5.1 Fundamentals

The goal of this section is the derivation of a potential of the type (2.33), from which the unknown deformation mapping can be computed by minimization. Evidently, for path dependent problems such as plasticity theory, this potential is defined pointwise (with respect to the (pseudo) time). As in the previous sections, isothermal conditions are assumed and dynamical effects are neglected.

Following [ORTIZ & STAINIER 1999; ORTIZ 2002; CARSTENSEN, HACKL & MIELKE 2002], the functional

$$\tilde{\mathcal{E}}(\dot{\varphi}, \dot{\mathbf{F}}^p, \dot{\alpha}, \Sigma, \mathbf{Q}) = \Psi(\dot{\varphi}, \dot{\mathbf{F}}^p, \dot{\alpha}) + \mathcal{D}(\dot{\mathbf{F}}^p, \dot{\alpha}, \Sigma, \mathbf{Q}) + J(\Sigma, \mathbf{Q}) \quad (2.69)$$

is introduced. According to Eq. (2.69), for admissible stress states, i. e.,  $(\Sigma, \mathbf{Q}) \in \mathbb{E}_\sigma$ ,  $\tilde{\mathcal{E}}$  represents the sum of the rate of the free energy and the dissipation, cf. Remark 2.4.1.5.

Clearly, if  $(\boldsymbol{\Sigma}, \mathbf{Q}) \in \mathbb{E}_\sigma$ ,

$$\tilde{\mathcal{E}}(\dot{\boldsymbol{\varphi}}, \dot{\mathbf{F}}^p, \dot{\boldsymbol{\alpha}}, \boldsymbol{\Sigma}, \mathbf{Q}) = \mathbf{P} : \dot{\mathbf{F}} =: \mathcal{P}, \quad (2.70)$$

cf. Eq. (2.21). That is,  $\tilde{\mathcal{E}}$  equals the deformation power denoted as  $\mathcal{P}$ . Inadmissible stress states are penalized by  $J = \infty$ . The interesting properties of the functional (2.69) become apparent, if the stationarity conditions are computed. A variation of  $\tilde{\mathcal{E}}$  with respect to  $(\boldsymbol{\Sigma}, \mathbf{Q})$  leads to

$$(\mathbf{L}^p, \dot{\boldsymbol{\alpha}}) \in \partial J. \quad (2.71)$$

The respective equation associated with  $\dot{\boldsymbol{\alpha}}$  reads

$$\mathbf{Q} = -\frac{\partial \Psi}{\partial \boldsymbol{\alpha}}. \quad (2.72)$$

Finally, a variation with respect to  $\dot{\mathbf{F}}^p$  yields

$$\boldsymbol{\Sigma} = \mathbf{F}^{eT} \cdot \frac{\partial \Psi}{\partial \mathbf{F}^e} = 2 \mathbf{C}^e \cdot \frac{\partial \Psi}{\partial \mathbf{C}^e}. \quad (2.73)$$

As a consequence, the stationarity condition of  $\tilde{\mathcal{E}}$  results in the flow rule (2.71), the constitutive relation for the internal stress-like variables (2.72) and the constitutive relation for the MANDEL stresses  $\boldsymbol{\Sigma}$ . The remaining variation of  $\tilde{\mathcal{E}}$  with respect to  $\dot{\boldsymbol{\varphi}}$  will be discussed in the next paragraph.

According to [ORTIZ & STAINIER 1999; ORTIZ 2002; CARSTENSEN, HACKL & MIELKE 2002], it is possible to derive a reduced functional, denoted as  $\mathcal{E}$ , which only depends on the rate of the deformation and the strain-like internal variables  $\boldsymbol{\alpha}$  and  $\mathbf{F}^p$ . For that purpose,  $\mathcal{E}$  is re-written by applying the LEGENDRE transformation

$$J^*(\bar{\mathbf{L}}^p, \dot{\boldsymbol{\alpha}}) = \sup \{ \boldsymbol{\Sigma} : \bar{\mathbf{L}}^p + \mathbf{Q} \cdot \dot{\boldsymbol{\alpha}} \mid (\boldsymbol{\Sigma}, \mathbf{Q}) \in \mathbb{E}_\sigma \} \quad (2.74)$$

of  $J$ . Since  $J^*$  is positively homogeneous of degree one, a maximization of  $\tilde{\mathcal{E}}$  with respect to  $(\boldsymbol{\Sigma}, \mathbf{Q})$ , results in

$$\mathcal{E}(\dot{\boldsymbol{\varphi}}, \dot{\mathbf{F}}^p, \dot{\boldsymbol{\alpha}}) = \dot{\Psi}(\dot{\boldsymbol{\varphi}}, \dot{\mathbf{F}}^p, \dot{\boldsymbol{\alpha}}) + J^*(\dot{\mathbf{L}}^p, \dot{\boldsymbol{\alpha}}). \quad (2.75)$$

Hence, the only remaining variables are  $\dot{\boldsymbol{\varphi}}$ ,  $\dot{\mathbf{F}}^p$  and  $\dot{\boldsymbol{\alpha}}$ . Even more importantly, the strain-like internal variables  $\mathbf{F}^p$  and  $\boldsymbol{\alpha}$  follow jointly from the minimization principle

$$\overset{\circ}{\Psi}_{\text{red}}(\dot{\boldsymbol{\varphi}}) := \inf_{\dot{\mathbf{F}}^p, \dot{\boldsymbol{\alpha}}} \mathcal{E}(\dot{\boldsymbol{\varphi}}, \dot{\mathbf{F}}^p, \dot{\boldsymbol{\alpha}}) \quad (2.76)$$

which, itself, gives rise to the introduction of the reduced functional  $\overset{\circ}{\Psi}_{\text{red}}$  depending only on the deformation mapping. It is interesting to note that for hyperelastic continua,  $\overset{\circ}{\Psi}_{\text{red}}$  equals the rate of the strain-energy density, i. e.,

$$\overset{\circ}{\Psi}_{\text{red}}(\dot{\boldsymbol{\varphi}}) = \dot{\Psi}(\boldsymbol{\varphi}). \quad (2.77)$$

As a result, in this case,  $\overset{\circ}{\Psi}_{\text{red}}$  represents the time derivative of a potential. This identity leads to the presumption that the time integration of Eq. (2.76) or Eq. (2.77) defines an incremental functional, denoted as  $I_{\text{inc}}$ , which extends the principle of minimum potential energy according to Subsection 2.3.2 to standard dissipative continua, i. e.,

$$I_{\text{inc}}(\boldsymbol{\varphi}) = \inf_{\mathbf{F}^{\text{p}}, \boldsymbol{\alpha}} \left[ \int_{\Omega} \int_{t_n}^{t_{n+1}} \mathcal{E}(\dot{\boldsymbol{\varphi}}, \dot{\mathbf{F}}^{\text{p}}, \dot{\boldsymbol{\alpha}}) dt dV - \int_{\Omega} \rho_0 \mathbf{B} \cdot \boldsymbol{\varphi} dV - \int_{\partial_2 \Omega} \bar{\mathbf{T}} \cdot \boldsymbol{\varphi} dA \right] \quad (2.78)$$

and

$$\boldsymbol{\varphi} = \arg \inf_{\boldsymbol{\varphi}} I_{\text{inc}}(\boldsymbol{\varphi}). \quad (2.79)$$

It should be pointed out that the minimization path of the internal variables according to Problem (2.78) can only be computed analytically for selected, relatively simple examples, cf. [CARSTENSEN, HACKL & MIELKE 2002].

**Remark 2.5.1.1** *The extension of the method described in this subsection necessary for rate-sensitivity (for the inelastic deformations) as well as for viscous material models is relatively straightforward, see [ORTIZ & STAINIER 1999; ORTIZ 2002]. For further details concerning the implementation of non-linear finite viscoelasticity, refer to [FANCELLO, PONTHOT & STAINIER 2005].*

## 2.5.2 Numerical implementation

As mentioned before, the analytical solution of the minimization path of the internal variables required in Eq. (2.78) can only be computed for simple problems. For more complex systems, the time integration is approximated by the following methods

$$\mathbf{L}^{\text{p}} \Delta t \approx \left[ \mathbf{1} - \mathbf{F}_n^{\text{p}} \cdot \mathbf{F}_{n+1}^{\text{p}-1} \right], \quad \text{or} \quad \mathbf{L}^{\text{p}} \Delta t \approx \log \left[ \mathbf{F}_{n+1}^{\text{p}} \cdot \mathbf{F}_n^{\text{p}-1} \right] \quad (2.80)$$

and

$$\dot{\boldsymbol{\alpha}} \Delta t \approx [\boldsymbol{\alpha}_{n+1} - \boldsymbol{\alpha}_n]. \quad (2.81)$$

Here,  $\Delta t = t_{n+1} - t_n$  is the length of the time interval considered. The numerical schemes (2.80) and (2.81) are equivalent to the time integrations (2.63) and (2.64). Applying these approximations, time integration of Eq. (2.75) leads to

$$\begin{aligned} \int_{t_n}^{t_{n+1}} \mathcal{E} dt &\approx \Psi(\boldsymbol{\varphi}_{n+1}, \mathbf{F}_{n+1}^{\text{p}}, \boldsymbol{\alpha}_{n+1}) - \Psi(\boldsymbol{\varphi}_n, \mathbf{F}_n^{\text{p}}, \boldsymbol{\alpha}_n) + J^*(\mathbf{L}^{\text{p}} \Delta t, \boldsymbol{\alpha}_{n+1} - \boldsymbol{\alpha}_n) \\ &=: \Psi_{\boldsymbol{\varphi}, \mathbf{F}^{\text{p}}, \boldsymbol{\alpha}}(\boldsymbol{\varphi}_{n+1}, \mathbf{F}_{n+1}^{\text{p}}, \boldsymbol{\alpha}_{n+1}) \end{aligned} \quad (2.82)$$

where the assumption that  $J^*$  is positively homogeneous of degree one was introduced and  $\Delta t > 0$ . Obviously, the functional  $\Psi_{\boldsymbol{\varphi}, \mathbf{F}^{\text{p}}, \boldsymbol{\alpha}}$  is not unique. It depends on the time

integration applied, cf. [ORTIZ & STAINIER 1999; ORTIZ 2002; CARSTENSEN, HACKL & MIELKE 2002]. Since Eq. (2.82) represents an approximation (time discretization) of Eq. (2.75), the strain-like internal variables are obtained by minimizing  $\Psi_{\varphi, \mathbf{F}^p, \boldsymbol{\alpha}}$  with respect to  $\mathbf{F}_{n+1}^p$  and  $\boldsymbol{\alpha}_{n+1}$ . That is,

$$(\mathbf{F}_{n+1}^p, \boldsymbol{\alpha}_{n+1}) = \arg \inf_{\mathbf{F}_{n+1}^p, \boldsymbol{\alpha}_{n+1}} \Psi_{\varphi, \mathbf{F}^p, \boldsymbol{\alpha}}(\varphi_{n+1}, \mathbf{F}_{n+1}^p, \boldsymbol{\alpha}_{n+1}). \quad (2.83)$$

It is noteworthy that  $\mathbf{F}^p$  and  $\boldsymbol{\alpha}$  are defined pointwise. Consequently, the optimization problem (2.83) is restricted to the integration points, if standard finite element formulations are used. For the computation of the tuple  $(\mathbf{F}_{n+1}^p, \boldsymbol{\alpha}_{n+1})$  classical numerical procedures such as NEWTON's method can be applied. Inserting the solution  $(\mathbf{F}_{n+1}^p, \boldsymbol{\alpha}_{n+1})$  into  $\Psi_{\varphi, \mathbf{F}^p, \boldsymbol{\alpha}}$  gives rise to the definition of the reduced potential

$$\Psi_{\text{inc}}(\varphi_{n+1}) = \inf_{\mathbf{F}_{n+1}^p, \boldsymbol{\alpha}_{n+1}} \Psi_{\varphi, \mathbf{F}^p, \boldsymbol{\alpha}}(\varphi_{n+1}, \mathbf{F}_{n+1}^p, \boldsymbol{\alpha}_{n+1}). \quad (2.84)$$

According to Eq. (2.84),  $\Psi_{\text{inc}}$  depends on the state variables at time  $t_n$  and hence, it is incremental in nature. If now the hyperelastic functional  $\Psi$  in Eq. (2.33) is replaced by  $\Psi_{\text{inc}}(\varphi_{n+1})$ ,  $I(\varphi_{n+1})$  reads

$$I(\varphi_{n+1}) = \int_{\Omega} \Psi_{\text{inc}}(\varphi_{n+1}) \, dV - \int_{\Omega} \rho_0 \mathbf{B} \cdot \varphi_{n+1} \, dV - \int_{\partial_2 \Omega} \bar{\mathbf{T}} \cdot \varphi_{n+1} \, dA. \quad (2.85)$$

The interesting property of this function becomes apparent if the respective stationarity condition is computed. It gives

$$\text{DIV} \mathbf{P} + \rho_0 \mathbf{B} = \mathbf{0}, \quad \mathbf{P} \cdot \mathbf{N} = \bar{\mathbf{T}}, \quad \text{with} \quad \mathbf{P} = \frac{\partial \Psi_{\text{inc}}}{\partial \mathbf{F}_{n+1}^p}. \quad (2.86)$$

Consequently conservation of linear momentum, together with the NEUMANN boundary conditions, are obtained by a variation of  $I$  with respect to  $\varphi$ . More precisely and fully analogously to hyperelastic materials, the deformation mapping follows from the minimization principle

$$\varphi_{n+1} = \arg \inf_{\varphi_{n+1}} I(\varphi_{n+1}) \quad (2.87)$$

and the reduced functional  $\Psi_{\text{inc}}$  acts like a potential for the first PIOLA-KIRCHHOFF stresses  $\mathbf{P}$ . The only difference between hyperelastic continua and standard dissipative solids is the specific form of  $\Psi$  and  $\Psi_{\text{inc}}$ . In summary, the strain-like internal variables  $\mathbf{F}^p$  and  $\boldsymbol{\alpha}$  as well as the deformation mapping are governed by the variational formulation (2.83) and (2.87), respectively. Further details about variational constitutive updates can be found in [COMI, CORIGLIANO & MAIER 1991; COMI & PEREGO 1995; ORTIZ & STAINIER 1999; ORTIZ 2002; CARSTENSEN, HACKL & MIELKE 2002; MIEHE 2002].

**Remark 2.5.2.1** *Clearly, the algorithmic tangent obtained by linearizing the variational update described in this section is always symmetric. Consequently, the resulting stiffness matrix is also symmetric leading to an increase in computational efficiency.*

**Remark 2.5.2.2** *It should be pointed out that in contrast to conventional plasticity theories, the variational formulation as advocated in [ORTIZ & STAINIER 1999] is not based on the introduction of a yield function. Instead of that, the flow rule represents the primitive postulate. The yield function depending on this rule follows from the variational update. This procedure is sometimes advantageous, cf. [ORTIZ & PANDOLFI 2004].*

### 2.5.3 Example: VON MISES plasticity model

In this subsection, the previously discussed variational update is applied to VON MISES plasticity theory. The resulting numerical implementation is used in the examples in Chapter 6. The particular model addressed in this subsection follows to a large extent [ORTIZ & STAINIER 1999], see also [ORTIZ 2002]. However, in contrast to the original work, a yield function in terms of MANDEL stresses is introduced a priori.

The space of admissible stresses corresponding to classical VON MISES plasticity model can be defined by the yield function

$$\phi(\boldsymbol{\Sigma}, Q) = \|\text{dev}[\boldsymbol{\Sigma}]\|_2 - \Sigma_{\text{eq}}^{\text{ini}} - Q(\varepsilon^{\text{P}}). \quad (2.88)$$

Here,  $\varepsilon^{\text{P}}$  is the VON MISES effective plastic strain, and  $\text{dev}[\boldsymbol{\Sigma}]$  denotes the deviatoric part of  $\boldsymbol{\Sigma}$ . It should be noted that the entire model is isotropic and hence, the MANDEL stress tensor  $\boldsymbol{\Sigma}$  is symmetric. Since  $\phi$  is positively homogeneous of degree one (in  $\boldsymbol{\Sigma}$  and  $Q$ ),  $J^*$  reads

$$J^* = \dot{\varepsilon}^{\text{P}} \Sigma_{\text{eq}}^{\text{ini}} \quad (2.89)$$

(cf. Remark 2.4.1.6), if the plastic deformations are admissible, i. e.,

$$\dot{\mathbf{F}}^{\text{P}} \cdot \mathbf{F}^{\text{P}-1} = \dot{\varepsilon}^{\text{P}} \mathbf{M}, \quad \text{with} \quad \text{tr} \mathbf{M} = 0, \quad \mathbf{M} = \mathbf{M}^T, \quad \frac{2}{3} \mathbf{M} : \mathbf{M} = 1, \quad \dot{\varepsilon}^{\text{P}} \geq 0. \quad (2.90)$$

Otherwise,  $J^* = \infty$ . Further details may be found in [ORTIZ & STAINIER 1999; ALBERTY, CARSTENSEN & ZARRABI 1999; ORTIZ 2002; CARSTENSEN, HACKL & MIELKE 2002]. Clearly, since  $\boldsymbol{\Sigma}$  is symmetric, the plastic spin  $\mathbf{W}^{\text{P}} = \text{skew}[\dot{\mathbf{F}}^{\text{P}} \cdot \mathbf{F}^{\text{P}-1}]$  (relative to the intermediate configuration) cannot be computed by Eq. (2.90)<sub>1</sub>. However, as mentioned before, the reason for the symmetry of  $\mathbf{M}$  is that the model proposed here is fully isotropic. For such theories the orientation of the intermediate configuration is irrelevant. More precisely, the plastic spin remains arbitrary. The model as described has to be supplemented by an energy density. As a result of the different volumetric and deviatoric material response associated with metals which are often modeled by VON MISES plasticity theory, an energy functional of the type

$$\Psi(\mathbf{C}^{\text{e}}, \varepsilon^{\text{P}}) = \Psi^{\text{vol}}(J^{\text{e}}) + \mu \|e^{\text{e}}\|_2^2 + \Psi^{\text{P}}(\varepsilon^{\text{P}}), \quad J^{\text{e}} = \det \mathbf{F}^{\text{e}} \quad (2.91)$$

represents a reasonable choice. Here,  $\mathbf{e}^e$  denotes the deviatoric part of the HENCKY strains  $\boldsymbol{\varepsilon}^e$ , i. e.,

$$\mathbf{e}^e := \boldsymbol{\varepsilon}^e - \frac{1}{3} \operatorname{tr}[\boldsymbol{\varepsilon}^e] \mathbf{1}, \quad \boldsymbol{\varepsilon}^e := \frac{1}{2} \log \mathbf{C}^e. \quad (2.92)$$

Alternatively, by using the properties of the exponential mapping,  $\mathbf{e}^e$  can be re-written as

$$\mathbf{e}^e := \frac{1}{2} \log \mathbf{C}^{e(\text{dev})} \quad (2.93)$$

with  $\mathbf{C}^{e(\text{dev})}$  being the elastic right CAUCHY-GREEN tensor corresponding to a volume preserving deformation, i. e.,

$$\mathbf{C}^{e(\text{dev})} = \mathbf{F}^{e(\text{dev})T} \cdot \mathbf{F}^{e(\text{dev})}, \quad \text{with } \mathbf{F}^{e(\text{dev})} = J^{e^{1/3}} \mathbf{F}^e, \quad \det \mathbf{F}^{e(\text{dev})} = 1, \quad (2.94)$$

cf. [SIMO & TAYLOR 1991]. With those identities, the elastic isochoric part of the energy density (2.91) reads

$$\mu \|\mathbf{e}^e\|_2^2 = \mu \sum_{A=1}^3 \log^2 \lambda_A^{\text{dev}} \quad (2.95)$$

where  $\lambda_A^{\text{dev}}$  are the principal stretches associated with  $\mathbf{F}^{e(\text{dev})}$ . Clearly, by specifying the elastic dilatant material response by setting

$$\Psi^{\text{vol}}(J^e) = \frac{1}{2} \kappa \log^2 J^e, \quad \kappa = \lambda + \frac{2}{3} \mu, \quad (2.96)$$

HENCKY's model is obtained, cf. [SIMO 1998], page 391. The interesting property of the density (2.91) is that the resulting deviatoric stresses

$$\operatorname{dev}[\bar{\mathbf{S}}] := \frac{\partial \Psi}{\partial \mathbf{e}^e} = 2 \mu \mathbf{e}^e \quad (2.97)$$

governing inelastic deformations depend linearly on the strains  $\mathbf{e}^e$ , cf. [CUITI NO & ORTIZ 1992; ORTIZ 2002]. This fact leads, as it will be shown, to a numerical implementation formally identical to that of standard small strain plasticity models.

If the exponential time integration scheme according to Eq. (2.64) is used, the computed inelastic deformations are purely deviatoric, i. e.,  $\operatorname{tr}[\mathbf{M}] = 0$  and  $\det \mathbf{F}_{n+1}^p = 1$ . Furthermore, in the case of the model adopted, the direction of the plastic flow is constant within the return-mapping algorithm. That is,  $\mathbf{M}|_{n+1} = \mathbf{M} = \text{const.}$  Considering those identities, the deviatoric part of the stresses takes the form

$$\operatorname{dev}[\bar{\mathbf{S}}]|_{n+1} = 2 \mu \mathbf{e}_{n+1}^e, \quad \text{with } \mathbf{e}_{n+1}^e = \mathbf{e}_{\text{tr}}^e - \Delta \varepsilon_{n+1}^p \mathbf{M}. \quad (2.98)$$

Clearly, here  $\mathbf{e}_{\text{tr}}^e$  are the elastic trial strains. By inserting Eq. (2.98)<sub>2</sub> into the energy density, the incremental potential (2.82) simplifies to

$$\Psi_{\boldsymbol{\varphi}, \mathbf{F}^p, \varepsilon^p} = \Psi_{\boldsymbol{\varphi}, \mathbf{F}^p, \varepsilon^p}(\boldsymbol{\varphi}_{n+1}, \Delta \varepsilon_{n+1}^p, \mathbf{M}, \boldsymbol{\varphi}_n, \mathbf{F}_n^p, \varepsilon_n^p). \quad (2.99)$$

As a result, this potential depends only on the deformation mapping and the plastic multiplier at time  $t_{n+1}$  and on the flow direction  $\mathbf{M}$  being constant within the return-mapping algorithm. Minimization of Eq. (2.99) with respect to  $\mathbf{M}$  yields

$$\mathbf{M} = \frac{3}{2} \frac{\text{dev}[\bar{\mathbf{S}}_{\text{tr}}]}{\|\text{dev}[\bar{\mathbf{S}}_{\text{tr}}]\|_2} = \frac{3}{2} \frac{\mathbf{e}_{\text{tr}}^e}{\|\mathbf{e}_{\text{tr}}^e\|_2}. \quad (2.100)$$

Finally, inserting this equation and minimizing with respect to  $\Delta\varepsilon_{n+1}^p$  defines the reduced potential  $\Psi_{\text{inc}}$ . Further details are omitted. They may be found in [ORTIZ & STAINIER 1999; ORTIZ 2002].

According to Remark 2.5.3.1, the flow direction can be re-written alternatively as

$$\mathbf{M} = \frac{3}{2} \frac{\text{dev}[\boldsymbol{\Sigma}_{\text{tr}}]}{\|\text{dev}[\boldsymbol{\Sigma}_{\text{tr}}]\|_2} \quad (2.101)$$

in terms of MANDEL stresses. Interestingly, since  $\phi$  is a positively homogeneous function of degree one, the minimum problem governing the internal variables (2.83), together with the flow rule (2.101), is equivalent to the discrete yield condition, i. e.,

$$\arg \inf_{\Delta\varepsilon_{n+1}^p} \Psi_{\boldsymbol{\varphi}, \mathbf{F}^p, \varepsilon^p} \iff \Delta\varepsilon_{n+1}^p \geq 0 : \phi(\boldsymbol{\Sigma}, Q(\Delta\varepsilon^p))|_{n+1} = 0 \quad (2.102)$$

This problem is solved locally (for each integration point) by applying NEWTON's scheme. The consistent linearization of the algorithm necessary for an asymptotic quadratic convergence can be derived in a relatively straightforward manner, cf. [ORTIZ 2002]. It requires the derivative of the exponential and logarithmic mapping, cf. [ORTIZ, RADOVITZKY & REPETTO 2001; ITSKOV 2003]. Details are omitted.

**Remark 2.5.3.1** *Here, it is shown that the discrete flow rule (2.100) can alternatively be re-written as*

$$\mathbf{M} = \frac{2}{3} \frac{\text{dev}[\boldsymbol{\Sigma}_{\text{tr}}]}{\|\text{dev}[\boldsymbol{\Sigma}_{\text{tr}}]\|_2}. \quad (2.103)$$

*From the assumed potential (2.91) the KIRCHHOFF stresses are obtained as*

$$\boldsymbol{\tau} = \frac{\partial \Psi^{\text{vol}}}{\partial J^e} \mathbf{1} + \mu \log \mathbf{b}^{e(\text{dev})} \quad (2.104)$$

*with  $\mathbf{b}^{e(\text{dev})}$  being the left CAUCHY-GREEN tensor defined by the volume preserving deformation gradient (2.94)<sub>2</sub>. Using this equation, the deviatoric part of the MANDEL stresses is defined by*

$$\text{dev}[\boldsymbol{\Sigma}] = \mu \text{dev} \left[ \mathbf{F}^{e^T} \cdot \log \mathbf{b}^{e(\text{dev})} \cdot \mathbf{F}^{e^{-T}} \right] = 2 \mu \sum_{A=1}^3 \log \lambda_A^{\text{dev}} \mathbf{N}_A \otimes \mathbf{N}_A. \quad (2.105)$$

*where  $\mathbf{N}_A$  represent the eigenvectors of  $\mathbf{C}^e$  and  $\mathbf{C}^{e(\text{dev})}$ , respectively. Furthermore, applying Eq. (2.93), the strain tensor  $\mathbf{e}^e$  yields*

$$\mathbf{e}^e = \frac{1}{2} \log[\text{dev} \mathbf{C}^e] = \sum_{A=1}^3 \log \lambda_A^{\text{dev}} \mathbf{N}_A \otimes \mathbf{N}_A. \quad (2.106)$$

*Consequently  $\text{dev} \boldsymbol{\Sigma} = \text{dev} \bar{\mathbf{S}}$  and thus, the equivalence (2.103) holds.*

## 2.6 Variational, thermomechanically coupled formulation

The extension of the variational constitutive formulation, as described previously, which is necessary for thermodynamically coupled problems, is briefly discussed in this section. Although the variational coupling of mechanical and thermal processes enjoys a relatively long tradition (dating back at least to [BIOT 1956; BIOT 1958] in the case of thermoelasticity) a consistent framework taking into account large deformations and dissipation resulting from plasticity or material damage, rate sensitivity and viscosity has been proposed only recently, [YANG 2004; YANG, STAINIER & ORTIZ 2005], see also [HACKL 1997].

Since a naive coupling of the purely mechanical problem with heat conduction does not lead to a variational structure and consequently, it does not lead to a symmetric stiffness matrix, most of the previous implementations were based on staggered solution schemes consisting of two subproblems, each of them showing a symmetric tangent matrix. A state of the art review concerning those models can be found in [SIMO 1998]. Despite this ad hoc decoupling, those models require additional constitutive assumptions. For instance, usually the TAYLOR-QUINNEY *factor* is introduced (see [TAYLOR & QUINNEY 1937]) measuring the fraction of plastic power converted to heat.

With a variational constitutive update as proposed in [YANG 2004; YANG, STAINIER & ORTIZ 2005], those drawbacks can be avoided. Additionally, as mentioned in the previous sections, a variational structure opens up the possibility to analyze the existence of solutions by using, nowadays, standard techniques originally designed for hyperelastic continua. Furthermore, such a structure can be taken as a basis for canonical error estimation. This will be shown in Chapters 4 – 6.

Conceptually speaking, the extension of the variational formulation advocated in [ORTIZ & STAINIER 1999] to the fully thermodynamically coupled problem as proposed in [YANG 2004; YANG, STAINIER & ORTIZ 2005] requires three modifications.

- Thermal effects have to be added to the dissipation. For the sake of clarity and simplicity, a fully uncoupled plasticity, viscosity and heat conduction is assumed. The more general case does not cause any additional problems. With this postulate, the dissipation resulting from plastic deformations is reflected by  $J^*$  according to Eq. (2.74). Introducing a viscous-type dissipation pseudo-potential  $\phi^*$  in the sense of [ORTIZ & STAINIER 1999] and a FOURIER-type dissipation pseudo-potential  $\chi$  (cf. [SIMO 1998], page 437), such that

$$\mathbf{P}_{\text{visco}} = \partial_{\dot{\mathbf{F}}}\phi^* \quad (2.107)$$

and

$$\mathbf{H} = \partial_{\mathbf{G}}\chi, \quad \text{with} \quad \mathbf{G} = -\frac{1}{\theta} \text{GRAD}\theta, \quad (2.108)$$

a positive dissipation is guaranteed a priori, if  $J^*$  and  $\phi^*$  are convex and  $\chi$  is a concave function. Here,  $\mathbf{P}_{\text{visco}}$  is the viscous or non-equilibrium stress of first PIOLA-KIRCHHOFF type.

- The second step necessary to obtain a variational structure is the distinction between the *equilibrium temperature* and the *external temperature*, cf. [YANG, STAINIER & ORTIZ 2005]. While the external temperature  $\theta$  is the standard one, the equilibrium temperature  $\tilde{\theta}$  is given by the equilibrium condition, i. e.,

$$\tilde{\theta} = \partial_N U(\mathbf{F}, \mathbf{F}^p, \boldsymbol{\alpha}, N) \quad (2.109)$$

with  $U$  denoting the internal energy density and  $N$  is the entropy, see Subsections 2.2.2 and 2.2.3. Clearly, at equilibrium those two temperature are equal. However, this condition is only enforced in a weak form by applying a HU-WASHIZU formulation. That is,  $\theta$  and  $N$  can be varied independently of one another.

- If the standard field equations governing the thermomechanical problem are rewritten into a corresponding weak form, they do not represent the EULER-LAGRANGE equations of a potential. In [YANG, STAINIER & ORTIZ 2005], this problem is solved by using integrating factors obtained by a time rescaling. More specifically, the integration factor derived from the symmetry condition of the DIRICHLET form of the rescaled weak form reads

$$f(\theta, \tilde{\theta}) = \frac{\theta}{\tilde{\theta}}. \quad (2.110)$$

Evidently, at equilibrium,  $f = 1$  and hence, no rescaling occurs. Further details are omitted. They can be found in [YANG 2004; YANG, STAINIER & ORTIZ 2005].

Applying the three steps listed above, [YANG 2004; YANG, STAINIER & ORTIZ 2005] finally derived the variational problem

$$\inf_{\dot{\boldsymbol{\varphi}}, \dot{\boldsymbol{\alpha}}, \dot{\mathbf{F}}^p, \dot{N}} \sup_{\theta} I(\dot{\boldsymbol{\varphi}}, \theta, \dot{N}, \dot{\boldsymbol{\alpha}}, \dot{\mathbf{F}}^p) \quad (2.111)$$

with

$$\begin{aligned} I(\dot{\boldsymbol{\varphi}}, \theta, \dot{N}, \dot{\boldsymbol{\alpha}}, \dot{\mathbf{F}}^p) &= \int_{\Omega} \left[ \dot{U} - \theta \dot{N} + \Delta \left( \frac{\theta}{\tilde{\theta}} (\dot{\mathbf{F}}, \dot{\mathbf{F}}^p, \dot{\boldsymbol{\alpha}}), -\frac{1}{\theta} \text{GRAD}\theta \right) \right] dV \\ &- \int_{\Omega} \rho_0 \mathbf{B} \cdot \dot{\boldsymbol{\varphi}} dV - \int_{\partial_2 \Omega} \bar{\mathbf{T}} \cdot \dot{\boldsymbol{\varphi}} dA \\ &+ \int_{\Omega} \rho_0 R \log \frac{\theta}{\theta_0} dV - \int_{\partial_{\mathbf{H}} \Omega} \mathbf{H} \cdot \mathbf{N} \frac{\theta}{\theta_0} dA. \end{aligned} \quad (2.112)$$

Here,  $\theta_0$  is the temperature of the referential state 0,  $\partial_{\mathbf{H}}\Omega$  is the boundary with prescribed heat fluxes and

$$\Delta = J^* + \phi^* - \chi. \quad (2.113)$$

It can be shown in a relatively straightforward manner that the EULER-LAGRANGE equations associated with Eq. (2.112) are equivalent to the field equations governing the coupled thermomechanical problem. For further details, the reader is referred to [YANG 2004; YANG, STAINIER & ORTIZ 2005].

Similarly to the purely mechanical formulation, the variational constitutive update is based on an approximation of Eq. (2.112). More specifically, a time discretization of Eq. (2.112) leads to the incremental functional

$$\Psi_{\boldsymbol{\varphi}, \mathbf{F}^p, \boldsymbol{\alpha}, \theta, N}(\boldsymbol{\varphi}_{n+1}, \theta_{n+1}, N_{n+1}, \mathbf{F}_{n+1}^p, \boldsymbol{\alpha}_{n+1}) \approx \int_{t_n}^{t_{n+1}} I(\dot{\boldsymbol{\varphi}}, \dot{\theta}, \dot{N}, \dot{\boldsymbol{\alpha}}, \dot{\mathbf{F}}^p) dt. \quad (2.114)$$

Clearly, the stationarity conditions of Eq. (2.114) represent consistent approximations of the field equations of the thermomechanically coupled problem. Following Section 2.5, the internal variables and the entropy are computed from the minimization principle

$$\Psi_{\text{inc}}(\boldsymbol{\varphi}_{n+1}, \theta_{n+1}) = \inf_{N_{n+1}, \mathbf{F}_{n+1}^p, \boldsymbol{\alpha}_{n+1}} \Psi_{\boldsymbol{\varphi}, \mathbf{F}^p, \boldsymbol{\alpha}, \theta, N} \quad (2.115)$$

which defines the reduced pseudo-potential  $\Psi_{\text{inc}}$ . Finally, the deformation mapping and the temperature follow from the variational problem

$$(\boldsymbol{\varphi}_{n+1}, \theta_{n+1}) = \arg \inf_{\boldsymbol{\varphi}_{n+1}} \sup_{\theta_{n+1}} \Psi_{\text{inc}}. \quad (2.116)$$

It should be noted that for many material models the minimization problem (2.115) can be simplified significantly.

## 2.7 Range of application of classical local continuum theories

Since the early work of [HADAMARD 1903] it is known that classical local continuum theories may lead to non-physical solutions. More precisely, [HADAMARD 1903] showed that the wave propagation speed depending on the constitutive relation can become complex-valued. This phenomenon is strongly linked to the loss of ellipticity of the governing equations, cf. [HILL 1958; THOMAS 1961; MANDEL 1966; RUDNICKI & RICE 1975; RANIECKI & BRUHNS 1981; MARSDEN & HUGHES 1994]. That is, the partial differential equation corresponding to the respective physical problem may change from the elliptic to the hyperbolic type (in the static case). Hence, it is possible that the considered

Boundary Value Problem (BVP) becomes ill-posed (see [BRAESS 1997]). If this transition occurs, the solution of the BVP is not unique anymore. Clearly, applying the finite element method to the numerical analysis of such problems, the described mathematical implications result in a lack of invariance of the computed solution with respect to the spatial discretization, cf. [DE BORST 1986; DE BORST 2001].

The just mentioned ill-posedness of the governing equations characterizing the considered physical problem is often activated by strain-softening. This type of softening is defined as the effect of decreasing stresses while the respective strains are increasing. For instance, the macroscopic material response due to cracking in brittle materials, slip bands in soils or LÜDER's bands shows strain-softening. As a consequence, those physical phenomena cannot be modeled by applying a standard local continuum theory.

The mesh dependency of the numerical results is not the only problem when dealing with strain-softening. Often, the regions showing inelastic deformations are highly localized. More precisely, the characteristic diameter of those regions is several orders of magnitude smaller than the respective engineering structure under investigation. As a consequence, strain-softening can be understood as a multi-scale problem. According to [BELYTSCHKO, FISH & ENGELMANN 1988], an efficient approach suitable for the analysis of strain-softening should not only avoid the mesh dependence of the numerically computed solutions resulting from the ill-posedness of the governing equations, but it should also account for the multi-scale character of the underlying physical problem. In the next chapter, a model falling into the range of such multi-scale approaches will be proposed.

## Chapter 3

# Modeling of localized material failure by strong discontinuities

In this chapter, a finite element formulation suitable for numerical analyses of highly localized material failure such as cracking in concrete or shear bands in ductile metals is presented. The model is based on the so-called *Strong Discontinuity Approach* (SDA). Within this framework, the final failure kinematics of solids are approximated by means of a discontinuous displacement field (jumps in the deformation mapping). Following the *Enhanced Assumed Strain concept* (EAS), an additive decomposition of the displacement gradient into a conforming and an enhanced part is employed. While the conforming part is represented in a standard manner by using classical LAGRANGIAN interpolations, the enhanced part is derived from a discontinuous displacement field reflecting the kinematics induced by localized material failure. Referring to the displacement jump, no special assumption, such as purely mode-I or mode-II failure, is made. The same holds for the class of interface laws considered which govern the evolution of the displacement discontinuity in terms of the traction vector acting at the surface of strong discontinuities. Consequently, the suggested numerical framework can be applied to a broad range of different interface laws, including damage-based models. In contrast to previous works, the presented finite element formulation does not require the static condensation technique to be employed. More precisely, instead of computing the conforming part of deformation and the displacement jump simultaneously from the weak form of equilibrium and the weak form of traction continuity, the different parts of the local deformation are decomposed according to a predictor-corrector algorithm. The proposed predictor and the corrector step are formally identical to those of classical computational plasticity models. Hence, subroutines originally designed for standard models (continuous deformation) can be applied with only minor modifications necessary. The applicability as well as the performance of the resulting finite element formulation are demonstrated by means of selected numerical examples.

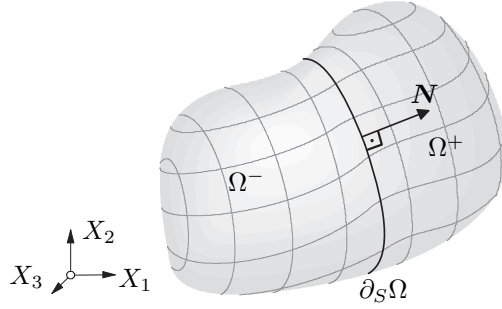


**Figure 3.1:** Body  $\Omega \subset \mathbb{R}^3$  separated into two parts  $\Omega^-$  and  $\Omega^+$  by a two-dimensional submanifold  $\partial_s \Omega$  of class  $\mathcal{C}^1$

## 3.1 Kinematics induced by strong discontinuities

A review on the kinematics associated with the Strong Discontinuity Approach (SDA) is given. At first, discontinuous deformation mappings are described in a general format. Subsequently, the characteristic assumptions concerning the SDA are incorporated. This section follows to a large extent [MOSLER 2004; MOSLER 2005B; MOSLER 2005A].

### 3.1.1 Fundamentals

According to [OLIVER & SIMO 1994; OLIVER & SIMO 1994; OLIVER 1995A; OLIVER 1995B], a domain  $\Omega \subset \mathbb{R}^3$  (more precisely, an open bounded set) is assumed to be separated into two parts  $\Omega^-$  and  $\Omega^+$  by means of a surface  $\partial_s \Omega$  (see Fig. 3.1). In what follows, it is sufficient to postulate that  $\partial_s \Omega$  is a piecewise  $\mathcal{C}^1$  hyperplane. From a physical point of view, this hyperplane represents a crack surface or a slip plane, respectively. Since  $\partial_s \Omega$  is of class  $\mathcal{C}^1$ , the normal vector  $\mathbf{N} \in N_{\mathbf{X}_0}$  of the submanifold  $\partial_s \Omega$  at the point  $\mathbf{X}_0 \in \partial_s \Omega$  is well-defined, i. e.,  $\dim N_{\mathbf{X}_0} = 1$ . Clearly, the introduction of a surface  $\partial_s \Omega$  induces a partition, i. e.,

$$\Omega = \Omega^+ \dot{\cup} \Omega^- \dot{\cup} \partial_s \Omega. \quad (3.1)$$

Next, a discontinuous deformation mapping  $\varphi$  is considered. This mapping connects each point  $\mathbf{X}$  in the reference configuration  $\Omega$  to the corresponding point  $\mathbf{x}$  in the current placement  $\varphi(\Omega)$ . Since  $\Omega$  is assumed as connected and  $\varphi = \text{id}_\Omega + \mathbf{u}$ , a discontinuous deformation mapping is equivalent to a discontinuous displacement field  $\mathbf{u}$ . In what follows, a displacement mapping of the type

$$\mathbf{u}|_{\Omega^\pm} \in \mathcal{C}^\infty(\Omega^\pm, \mathbb{R}^3), \quad \Omega^\pm := \Omega^+ \cup \Omega^- \quad (3.2)$$

is considered, i. e.,  $\mathbf{u}$  may be discontinuous at  $\partial_s \Omega$  while it is smooth on  $\Omega^\pm$ . This restriction is reasonable, since the finite element kinematics as proposed in Section 3.1.3 are based on a polynomial approximation of the displacement field  $\mathbf{u}|_{\Omega^\pm}$ . Applying condition (3.2), the left hand limit  $\mathbf{u}^-(\mathbf{X}_0)$  and the right hand limit  $\mathbf{u}^+(\mathbf{X}_0)$  of the displacement

mapping  $\mathbf{u} : \Omega \rightarrow \mathbb{R}^3$  at  $\mathbf{X}_0 \in \partial_s \Omega$  are obtained as

$$\mathbf{u}^\pm(\mathbf{X}_0) := \lim_{n \rightarrow \infty} \mathbf{u}(\mathbf{X}_n^\pm), \quad (\mathbf{X}_n^\pm)_{n \in \mathbb{N}} \in (\Omega^\pm)^\mathbb{N}, \quad \mathbf{X}_n^\pm \rightarrow \mathbf{X}_0 \quad (n \rightarrow \infty). \quad (3.3)$$

Hence, the discontinuity of  $\mathbf{u}$  at  $\mathbf{X}_0$  is computed as

$$\llbracket \mathbf{u}(\mathbf{X}_0) \rrbracket := \mathbf{u}^+(\mathbf{X}_0) - \mathbf{u}^-(\mathbf{X}_0) \quad \forall \mathbf{X}_0 \in \partial_s \Omega. \quad (3.4)$$

Introducing the HEAVISIDE function with respect to the singular surface  $\partial_s \Omega$ , i. e., the indicating function of the subset  $\Omega^+$ , a displacement field of the type (3.2) can be rewritten into the form

$$\mathbf{u}(\mathbf{X}) = \mathbf{u}_-(\mathbf{X}) + H_s (\mathbf{u}_+(\mathbf{X}) - \mathbf{u}_-(\mathbf{X})), \quad \mathbf{u}_-, \mathbf{u}_+ \in \mathcal{C}^\infty(\Omega, \mathbb{R}^3). \quad (3.5)$$

Since  $\mathbf{u}_-$  and  $\mathbf{u}_+$  are completely independent of one another,  $\mathbf{u}|_{\Omega^-} = \mathbf{u}_-|_{\Omega^-}$  and  $\mathbf{u}|_{\Omega^+} = \mathbf{u}_+|_{\Omega^+}$  are independent as well. As a consequence, the jump of the deformation gradient  $\mathbf{F}$  computed from Eq. (3.5) is not zero, in general, i. e.,

$$\llbracket \mathbf{F}(\mathbf{X}_0) \rrbracket \neq 0, \quad \mathbf{X}_0 \in \partial_s \Omega. \quad (3.6)$$

All numerical models based on the incorporation of strong discontinuities into finite elements are based on a deformation mapping characterized by Eq. (3.5), see [SIMO & OLIVER 1994; ARMERO & GARIKIPATI 1995; LARSSON, RUNESSON & ÅKESSON 1995; LARRSON & RUNESSON 1996; OLIVER 1996; ORTIZ & PANDOLFI 1999; ARMERO 1999; BORJA & REGUEIRO 2001; WELLS & SLUYS 2001C; WELLS & SLUYS 2001B; DOLBOW, MOËS & BELYTSCHKO 2002; MOSLER & MESCHKE 2003; MOSLER & BRUHNS 2004]. In some approaches, an additional term associated with the stress singularity at the crack tip is added to the displacement field (3.5), cf. [BELYTSCHKO & BLACK 1999; MOËS, GRAVOUIL & BELYTSCHKO 2002B; MOËS, GRAVOUIL & BELYTSCHKO 2002A].

**Remark 3.1.1.1** *The displacement field (3.5) and its corresponding deformation mapping are piecewise continuous. More precisely,  $\mathbf{u}$  belongs to the space of special functions with bounded variations (SBV), cf. [AMBROSIO, FUSCO & PALLARA 2000]. This space is spanned by all functions having bounded deformations (BD) in the sense of [MATTHIES, STRANG & CHRISTIANSEN 1979; TEMAN & STRANG 1980] and a singular CANTOR-part. According to [NEGRI 2005B], the space SBV is large enough for most free discontinuity problems but significantly more regular than BD.*

### 3.1.2 The strong discontinuity approach

After having presented the general kinematics induced by a discontinuous deformation mapping, attention is turned to the displacement field characteristic for the strong discontinuity approach in the sense of [SIMO, OLIVER & ARMERO 1993; SIMO & OLIVER

1994; OLIVER 1996]. According to [OLIVER 1996], a displacement field of the format

$$\mathbf{u} = \hat{\mathbf{u}} + \llbracket \mathbf{u} \rrbracket (H_s - \varphi), \quad \text{with} \quad \hat{\mathbf{u}} \in C^\infty(\Omega, \mathbb{R}^3), \quad \varphi \in C^\infty(\Omega, \mathbb{R}) \quad (3.7)$$

is assumed. By comparing Eq. (3.7) to Eq. (3.5),

$$\mathbf{u}_- = \hat{\mathbf{u}} - \llbracket \mathbf{u} \rrbracket \varphi \quad \text{and} \quad \mathbf{u}_+ = \hat{\mathbf{u}} + \llbracket \mathbf{u} \rrbracket (1 - \varphi) \quad (3.8)$$

is obtained. The smooth ramp function  $\varphi$  allows to prescribe the Dirichlet boundary conditions in terms of  $\bar{\mathbf{u}}$  (see [SIMO & OLIVER 1994; OLIVER 1996]). This will be described in Subsection 3.1.3.

Applying the generalized derivative  $D$  to the Heaviside function which results in the identity  $DH_s = \mathbf{N} \delta_s$  the deformation gradient is computed from Eq. (3.7) as

$$\mathbf{F} = \mathbf{1} + \frac{\partial \hat{\mathbf{u}}}{\partial \mathbf{X}} + \frac{\partial \llbracket \mathbf{u} \rrbracket}{\partial \mathbf{X}} (H_s - \varphi) + \llbracket \mathbf{u} \rrbracket \otimes \mathbf{N} \delta_s - \llbracket \mathbf{u} \rrbracket \otimes \frac{\partial \varphi}{\partial \mathbf{X}}. \quad (3.9)$$

Here,  $\delta_s$  represents the DIRAC-delta distribution with respect to  $\partial_s \Omega$ . Clearly, Eq. (3.9) has to be understood in a distributional sense, cf. [STAKGOLD 1967; STAKGOLD 1998]. According to Eq. (3.9),  $\mathbf{F}$  consists of three parts: An absolutely continuous part  $\mathbf{1} + \partial \hat{\mathbf{u}} / \partial \mathbf{X} - \partial \llbracket \mathbf{u} \rrbracket / \partial \mathbf{X} \varphi - \llbracket \mathbf{u} \rrbracket \otimes \partial \varphi / \partial \mathbf{X}$ , a jump part  $\partial \llbracket \mathbf{u} \rrbracket / \partial \mathbf{X} H_s$  and a singular distribution  $\llbracket \mathbf{u} \rrbracket \otimes \mathbf{N} \delta_s$ .

**Remark 3.1.2.1** *Restricting attention to the one-dimensional case for now and applying the partial derivative to Eq. (3.7), the non-vanishing component  $F$  of the deformation gradient in  $\Omega^\pm := \Omega^+ \cup \Omega^-$  is computed as*

$$F = 1 + \frac{\partial \hat{u}}{\partial X} - \llbracket u \rrbracket \frac{\partial \varphi}{\partial X}. \quad (3.10)$$

Consequently, the limits according to Eq. (3.3) yield

$$F^\pm = \lim_{X^\pm \rightarrow X_0} \left( 1 + \frac{\partial \hat{u}}{\partial X} - \llbracket u \rrbracket \frac{\partial \varphi}{\partial X} \right), \quad \text{with} \quad X_0 = \partial_s \Omega. \quad (3.11)$$

Since  $\hat{u}, \varphi \in C^\infty$ , the equivalence

$$F^+ = F^- = \left( \frac{\partial \bar{u}}{\partial X} - \llbracket u \rrbracket \frac{\partial \varphi}{\partial X} \right) \Big|_{X_0} \quad (3.12)$$

holds. Hence, in contrast to the displacement field (3.5), the kinematics corresponding to  $\Omega^-$  and  $\Omega^+$  are not completely independent of one another, cf. Eq. (3.6). For further details refer to [JIRÁSEK & BELYTSCHKO 2002; MOSLER & BRUHNS 2004]. As it will be shown, for the SDA, the identity (3.12) is also fulfilled in the three-dimensional case.

### 3.1.3 Numerical implementation

The approaches using kinematics induced by strong discontinuities can be subdivided into two classes:

- *Interface elements* as proposed in [NEEDLEMAN 1990; CAMACHO & ORTIZ 1996; ORTIZ & PANDOLFI 1999]. For such models, a jump in the deformation field is allowed to occur only at the boundary between neighboring finite elements.
- Approaches accounting for displacement jumps in the interior of finite elements. A further classification is possible, if the way of modeling the discontinuity is used as a criterion.
  - The deformation discontinuity is approximated element-wise (SDA). Continuity of the field of the discontinuities is not guaranteed at the element boundaries, cf. [DVORKIN, CUITIÑO & GIOIA 1990; KLISINSKI, RUNESSON & STURE 1991; SIMO, OLIVER & ARMERO 1993].
  - *eXtended Finite Element Method* (X-FEM) or *Partition of Unity Finite Element Method* (PU-FEM), cf. [MOËS, DOLBOW & BELYTSCHKO 1999; SUKUMAR, MOËS, MORAN & BELYTSCHKO 2000]. Conceptually speaking, a given deformation approximation is locally enriched by functions showing a compact support.

More detailed comparisons between numerical models based on strong discontinuity kinematics are given in [JIRÁSEK 2000; JIRÁSEK & BELYTSCHKO 2002; MOSLER & MESCHKE 2004; DUMSTORFF, MOSLER & MESCHKE 2003; MOSLER 2004; OLIVER, HUESPE, PULIDO & SAMANIEGO 2005]. From the discussions contained in these works follows that at present, it is not clear which of those approaches is more promising.

On the one hand, finite element formulations accounting for deformation jumps within the interior of the elements show the advantage that the space of admissible discontinuities (the geometry of  $\partial_s\Omega$ ) is very large. However, those approaches imply that the topology of  $\partial_s\Omega$  has to be stored, e. g. by using level, cf. [STOLARSKA, CHOPP, MÖES & BELYTSCHKO 2001]. Consequently, the resulting numerical costs are very expensive. To the best knowledge of the author, neither the SDA nor the X-FEM have been applied to the simulation of complex material failure with  $\partial_s\Omega$  modeled in a continuous manner.

On the other hand interface elements allow for computing complex material failure. In the case of cracking in brittle structures, the reader is referred to [ORTIZ & PANDOLFI 1999; PANDOLFI, KRYSL & ORTIZ 1999; PANDOLFI, KRYSL & ORTIZ 1999; CIRAK, ORTIZ & PANDOLFI 2005]. However, by approximating  $\partial_s\Omega$  by the facets of the finite elements, the space of admissible discontinuities is relatively small. Hence, this method can lead to an overestimation of the dissipation, see [PAPOULIA, VAVASIS & GANGULY 2005].

In the present work, a finite element formulation based on the Enhanced Assumed Strain concept (EAS), cf. [SIMO & RIFAI 1990; SIMO & ARMERO 1992; SIMO, ARMERO & TAYLOR 1993], is proposed. It falls into the framework advocated by [SIMO, OLIVER & ARMERO 1993; SIMO & OLIVER 1994; OLIVER 1996]. The numerical comparison between the SDA and the X-FEM contained in [OLIVER, HUESPE, PULIDO & SAMANIEGO 2005] leads to the conjecture that the SDA is, in many cases, more efficient than the X-FEM.

Following the EAS concept, the enhanced part of the deformation gradient is modeled in an incompatible fashion. In what follows, only the displacement field  $\hat{\mathbf{u}}$  is approximated globally (conforming), i. e.,

$$\hat{\mathbf{u}} = \sum_{i=1}^{n_{\text{node}}} N_i \hat{\mathbf{u}}_i^e, \quad (3.13)$$

with the nodal displacements  $\hat{\mathbf{u}}_i^e$  at node  $i$ . Eq. (3.13) gives rise to the introduction of the deformation gradient

$$\hat{\mathbf{F}} := \mathbf{1} + \text{GRAD}\hat{\mathbf{u}}, \quad \text{GRAD}\hat{\mathbf{u}} := \frac{\partial \hat{\mathbf{u}}}{\partial \mathbf{X}} \quad (3.14)$$

corresponding to the conforming part of the deformation.

Assuming the jump  $[[\mathbf{u}]]$  is known, only the ramp function  $\varphi$  has to be specified in order to define the kinematics (3.9) uniquely. In line with [OLIVER 1996],  $\varphi$  is designed by using the standard shape functions  $N_i$ . More precisely,

$$\phi = \sum_{i=1}^{n_{\overline{\Omega}^+}} N_i. \quad (3.15)$$

Here,  $\sum_{i=1}^{n_{\overline{\Omega}^+}}$  denotes the summation over all nodes of the respective finite element belonging to  $\overline{\Omega}^+$ . Owing to the properties of the shape functions,

$$\mathbf{u}(\mathbf{X}_i^e) = \hat{\mathbf{u}}(\mathbf{X}_i^e) \quad \forall \mathbf{X}_i^e, \quad (3.16)$$

i. e., the displacement field is identical to the globally conforming one at the nodes  $\mathbf{X}_i^e$  of the finite element  $e$  and hence, the DIRICHLET boundary conditions can be formulated in terms of  $\hat{\mathbf{u}}$ . Most of the finite element formulations dealing with strong discontinuities are based on an element-wise plane surface  $\partial_s \Omega$ . This approximation is used for the numerical model presented in this chapter as well. If  $\partial_s \Omega$  is plane, it can be checked efficiently, if a node belongs to  $\Omega^+$  or  $\Omega^-$ .

Interpolating only  $\hat{\mathbf{u}}$  in a compatible manner, the incompatible enhanced displacement gradient results in

$$\mathbf{H} = \frac{\partial [[\mathbf{u}]]}{\partial \mathbf{X}} (H_s - \varphi) + [[\mathbf{u}]] \otimes \mathbf{N} \delta_s - [[\mathbf{u}]] \otimes \frac{\partial \varphi}{\partial \mathbf{X}}, \quad (3.17)$$

cf. Eq. (3.9). Since  $\mathbf{H}$  does not need to represent the derivative of a conforming discontinuous deformation field, it is admissible to neglect the gradient of the displacement discontinuity, i. e.,  $\partial \llbracket \mathbf{u} \rrbracket / \partial \mathbf{X} = \mathbf{0}$  and to consider a deformation gradient of the type

$$\mathbf{F} = \mathbf{1} + \frac{\partial \hat{\mathbf{u}}}{\partial \mathbf{X}} + \llbracket \mathbf{u} \rrbracket \otimes \mathbf{N} \delta_s - \llbracket \mathbf{u} \rrbracket \otimes \frac{\partial \varphi}{\partial \mathbf{X}}. \quad (3.18)$$

The assumption  $\partial \llbracket \mathbf{u} \rrbracket / \partial \mathbf{X} = \mathbf{0}$  is characteristic for the SDA, see e. g. [SIMO & OLIVER 1994; OLIVER 1996; ARMERO & GARIKIPATI 1996; LARRSON & RUNESSON 1996; ARMERO 1999; BORJA 2000; WELLS & SLUYS 2001c; JIRÁSEK & ZIMMERMANN 2001]. Clearly, only in the case  $\partial \llbracket \mathbf{u} \rrbracket / \partial \mathbf{X} = \mathbf{0}$ , Eq. (3.18) represents the generalized derivative of the deformation mapping (3.7). However,  $\mathbf{F}$  captures the highly localized displacements and complies with the restrictions of the EAS concept. It should be noted that the more general case  $\partial \llbracket \mathbf{u} \rrbracket / \partial \mathbf{X} \neq \mathbf{0}$  does not lead to any problems, cf. [ALFAIATE, SIMONE & SLUYS 2003].

The additive decomposition (3.18) of the deformation gradient is not well-suited for the development of constitutive equations. Following [GARIKIPATI 1996; ARMERO & GARIKIPATI 1996], Eq. (3.18) is re-written into a multiplicative decomposition as

$$\mathbf{F} = \bar{\mathbf{F}} \cdot \tilde{\mathbf{F}}, \quad \text{with} \quad \begin{aligned} \bar{\mathbf{F}} &= \mathbf{1} + \text{GRAD} \hat{\mathbf{u}} - \llbracket \mathbf{u} \rrbracket \otimes \text{GRAD} \varphi \\ \tilde{\mathbf{F}} &= \mathbf{1} + \mathbf{J} \otimes \mathbf{N} \delta_s, \quad \mathbf{J} := \bar{\mathbf{F}}^{-1} \cdot \llbracket \mathbf{u} \rrbracket. \end{aligned} \quad (3.19)$$

As a consequence,  $\bar{\mathbf{F}}$  represents the regularly distributed part of the deformation gradient, while  $\tilde{\mathbf{F}}$  is associated with the singular distribution resulting from the generalized derivative of the displacement jump. In Eq. (3.19),  $\mathbf{J}$  denotes the material counterpart of the displacement discontinuity, i. e.,  $\mathbf{J}$  is the pull-back of  $\llbracket \mathbf{u} \rrbracket$  with respect to the mapping represented by  $\bar{\mathbf{F}}$  in a differential geometry framework. Therefore,  $\mathbf{J}$  can be interpreted as a vector on the intermediate configuration induced by the multiplicative decomposition (3.19)<sub>1</sub>. However, since

$$\mathbf{F}|_{\Omega^\pm} = \bar{\mathbf{F}}|_{\Omega^\pm}, \quad (3.20)$$

the pull-back of tensors (with  $\bar{\mathbf{F}}$ ) defined on  $\varphi(\Omega^\pm)$  leads to objects on the undeformed configuration. More precisely, the multiplicative decomposition (3.19)<sub>1</sub> holds only for  $\mathbf{X}_0 \in \partial_s \Omega$ . For  $\mathbf{X} \in \Omega^\pm$  it reduces to  $\mathbf{F} = \bar{\mathbf{F}}$ .

Analogous to standard multiplicative plasticity theory, the spatial velocity gradient  $\mathbf{l} := \dot{\mathbf{F}} \cdot \mathbf{F}^{-1}$  is computed as

$$\mathbf{l} = \bar{\mathbf{l}} + \tilde{\mathbf{l}}, \quad \text{with} \quad \begin{aligned} \bar{\mathbf{l}} &= \dot{\bar{\mathbf{F}}} \cdot \bar{\mathbf{F}}^{-1} \\ \tilde{\mathbf{l}} &= \bar{\mathbf{F}} \cdot \dot{\tilde{\mathbf{F}}} \cdot \tilde{\mathbf{F}}^{-1} \cdot \bar{\mathbf{F}}^{-1}. \end{aligned} \quad (3.21)$$

According to Eq. (3.21),  $\mathbf{l}$  is decomposed additively. It consists of a part  $\bar{\mathbf{l}}$ , associated with the continuous deformation mapping and a second term  $\tilde{\mathbf{l}}$ , resulting from the rate

of the displacement discontinuity. Since  $\bar{\mathbf{F}}$  is regularly distributed,  $\bar{\mathbf{l}}$  can be computed in standard manner. However, to obtain  $\tilde{\mathbf{l}}$ , an inversion of a singular distribution is necessary. To the best knowledge of the author,  $\tilde{\mathbf{l}}$  was computed in [GARIKIPATI 1996; ARMERO & GARIKIPATI 1996] for the first time. For that purpose,  $\hat{\mathbf{F}}$  was interpreted as a linear mapping between two vector spaces. Alternatively, it is possible to approximate the DIRAC-delta function by using an  $h$ -sequence, that is,

$$\delta_s^h := \frac{\chi_{\partial_s \Omega}}{h}, \quad \delta_s^h \rightarrow \delta_s \quad (h \rightarrow \infty), \quad (3.22)$$

applying the well-known SHERMAN-MORRISON formula and computing the limiting value, i. e.,  $h \rightarrow \infty$ , cf. [LARSSON, STEINMANN & RUNESSON 1998]. Both procedures result in

$$\tilde{\mathbf{l}} = \mathcal{L}_\nu [\mathbf{u}] \otimes \mathbf{N} \cdot \bar{\mathbf{F}}^{-1} \delta_s \quad (3.23)$$

where  $\mathcal{L}_\nu [\mathbf{u}]$  represents a LIE-type derivative according to

$$\mathcal{L}_\nu [\mathbf{u}] = \bar{\mathbf{F}} \cdot \frac{\partial}{\partial t} \left\{ \bar{\mathbf{F}}^{-1} \cdot [\mathbf{u}] \right\} = [\dot{\mathbf{u}}] + \bar{\mathbf{l}} \cdot [\mathbf{u}]. \quad (3.24)$$

Here,  $\chi_{\partial_s \Omega}$  denotes the indicating function of the subset  $\partial_s \Omega$ .

**Remark 3.1.3.1** According to Eqs. (3.13) and (3.15),  $\hat{\mathbf{u}} \in \mathcal{C}^\infty(\Omega, \mathbb{R}^3)$  and  $\varphi \in \mathcal{C}^\infty(\Omega, \mathbb{R})$ . As a result,

$$[\mathbf{F}] = [\bar{\mathbf{F}}] = \mathbf{0} \quad \forall \mathbf{X} \in \partial_s \Omega \quad (3.25)$$

Hence, as in the one-dimensional case, the kinematics in  $\Omega^+$  and  $\Omega^-$  are not completely independent of one another, cf. Remark 3.1.2.1.

**Remark 3.1.3.2** Note that for functions belonging to SBV, boundary conditions or the definition of the displacement jump require the trace of  $\mathbf{u}$ , cf. [NEGRI 2005B]. However, most finite element formulations, including the one presented in this work, are based on piecewise smooth deformation approximations. As a consequence, the trace operation reduces to the standard evaluation of  $\mathbf{u}$  or  $\varphi$ , respectively.

**Remark 3.1.3.3** The kinematics, as well as the finite element implementation proposed in this chapter are based on only one localization surface  $\partial_s \Omega$  within the body  $\Omega$  (the finite element). For the case of multiple strong discontinuities, see [MOSLER 2004; MOSLER 2005D].

**Remark 3.1.3.4** Since in what follows, an evolution equation for  $\mathbf{J}$  will be applied,  $\tilde{\mathbf{F}}$  can be computed. As a consequence, the intermediate configuration induced by the multiplicative decomposition (3.19) of the deformation gradient is defined uniquely.

### 3.1.4 Comparison to other SDA-based finite element formulations

Many different numerical methods based on embedded strong discontinuities can be found in the literature. In this section, it will be shown that some of them are equivalent, cf. [MOSLER 2004]. Since most of the approaches are restricted to a geometrically linearized theory, the small strain tensor  $\boldsymbol{\varepsilon}$  is required. From the kinematics described in the previous subsection  $\boldsymbol{\varepsilon}$  results in

$$\boldsymbol{\varepsilon} = (\nabla \mathbf{u})^{\text{sym}} = (\nabla \hat{\mathbf{u}})^{\text{sym}} - \underbrace{([\mathbf{u}] \otimes \nabla \varphi)^{\text{sym}}}_{=: \tilde{\boldsymbol{\varepsilon}}} + ([\mathbf{u}] \otimes \mathbf{N})^{\text{sym}} \delta_s. \quad (3.26)$$

Restricting attention to constant strain triangle elements and using VOIGT notation (the conversion between a tensor  $\mathbf{A}$  and its corresponding matrix is indicated by brackets, i. e.,  $[\mathbf{A}]$ ), [JIRÁSEK & ZIMMERMANN 2001] considered a strain field of the type

$$[\boldsymbol{\varepsilon}] = \mathbf{B} \mathbf{d} - \mathbf{B} \mathbf{H} \mathbf{e}, \quad \forall \mathbf{X} \in \Omega^\pm, \quad \text{with} \quad \mathbf{d} = \begin{bmatrix} \hat{\mathbf{u}}_1^e \\ \hat{\mathbf{u}}_2^e \\ \hat{\mathbf{u}}_3^e \end{bmatrix}. \quad (3.27)$$

Here,  $\mathbf{B}$  represents the B-operator,  $\mathbf{d}$  the vector of nodal displacements (see [BATHE 1995]),  $\mathbf{e}$  the vector of the displacement jump with respect to a local cartesian coordinate system defined by the normal  $\mathbf{N}$  and  $\mathbf{H}$  a matrix which reflects the effect of the displacement discontinuity on the nodal displacements, respectively. The B-operator is decomposed into a differential operator  $\mathbf{D}_\boldsymbol{\varepsilon}$  and the interpolation matrix  $\mathbf{N}$  according to [BATHE 1995]

$$\mathbf{B} := \mathbf{D}_\boldsymbol{\varepsilon} \mathbf{N}, \quad \mathbf{N} := \begin{bmatrix} N_1 & 0 & \cdots & 0 \\ 0 & N_1 & \cdots & N_3 \end{bmatrix}. \quad (3.28)$$

Clearly,  $\mathbf{B} \mathbf{d} = [\nabla^{\text{sym}} \hat{\mathbf{u}}]$  (compare Eqs. (3.27) and (3.28) to Eqs. (3.26) and (3.13)). Hence, to show the equivalence of Eq. (3.27) and Eq. (3.26),

$$[\tilde{\boldsymbol{\varepsilon}}] \stackrel{!}{=} \mathbf{B} \mathbf{H} \mathbf{e}. \quad (3.29)$$

Without loss of generality, it is assumed that  $\mathbf{X}_3^e \in \Omega^+$  while  $\mathbf{X}_1^e, \mathbf{X}_2^e \in \Omega^-$ . In this case, the matrix  $\mathbf{H}$  is of the type (see [JIRÁSEK & ZIMMERMANN 2001])

$$\mathbf{H}^T = [\mathbf{H}_1^T, \mathbf{H}_2^T, \mathbf{H}_3^T] \quad \text{with} \quad \mathbf{H}_1 = \mathbf{H}_2 = \begin{bmatrix} 0 & 0 \\ 0 & 0 \end{bmatrix}, \quad \mathbf{H}_3 = \begin{bmatrix} \cos \alpha & \sin \alpha \\ -\sin \alpha & \cos \alpha \end{bmatrix}. \quad (3.30)$$

With Eq. (3.15) and applying the differential operator  $\mathbf{D}_\boldsymbol{\varepsilon}$ , the left hand side of Eq. (3.29) yields

$$[\tilde{\boldsymbol{\varepsilon}}] = \mathbf{D}_\boldsymbol{\varepsilon} (\varphi [\mathbf{u}]), \quad \text{with} \quad \varphi = N_3. \quad (3.31)$$

Inserting Eq. (3.31) into Eq. (3.29) and computing the product  $\mathbf{N} \mathbf{H}$ , Eq. (3.29) is re-written as

$$N_3 \llbracket \mathbf{u} \rrbracket \stackrel{!}{=} N_3 \mathbf{H}_3^T \mathbf{e}. \quad (3.32)$$

Since  $\llbracket \mathbf{u} \rrbracket = \mathbf{H}_3^T \mathbf{e}$ , i. e., the matrix  $\mathbf{H}_3^T$  transforms the local components of the displacement discontinuity denoted as  $\mathbf{e}$  to the global counterparts  $\llbracket \mathbf{u} \rrbracket$ , both strain fields (Eq. (3.26) and Eq. (3.27)) are fully equivalent.

In contrast to [JIRÁSEK & ZIMMERMANN 2001], [DVORKIN, CUITIÑO & GIOIA 1990] proposed an enhanced strain field of the type

$$\llbracket \tilde{\boldsymbol{\varepsilon}} \rrbracket = \mathbf{B} \boldsymbol{\phi} \mathbf{U}^c. \quad (3.33)$$

In Eq. (3.33),  $\mathbf{U}^c$  denotes the displacement discontinuity with respect to a global coordinate system, i. e.,  $\mathbf{U}^c = \llbracket \mathbf{u} \rrbracket$ , and the matrix  $\boldsymbol{\phi}$  is defined as

$$\boldsymbol{\phi}^T = [\boldsymbol{\phi}_1^T, \dots, \boldsymbol{\phi}_{n_{\text{node}}}^T], \quad \text{with} \quad \boldsymbol{\phi}_i = \begin{cases} \mathbf{0} & \text{if } \mathbf{X}_i^e \in \Omega^- \\ \mathbf{1} & \text{if } \mathbf{X}_i^e \in \Omega^+ \end{cases} \quad \mathbf{0}, \mathbf{1} \in M_{2 \times 2}(\mathbb{R}). \quad (3.34)$$

As a consequence, the identity  $\boldsymbol{\phi} \mathbf{U}^c = \mathbf{H} \mathbf{e}$  holds. Hence, the kinematics suggested by [JIRÁSEK & ZIMMERMANN 2001] are fully equivalent to those presented in [DVORKIN, CUITIÑO & GIOIA 1990].

Independently of the work [DVORKIN, CUITIÑO & GIOIA 1990], [KLISINSKI, RUNESSON & STURE 1991; OLOFSSON, KLISINSKI & NEDAR 1994; KLISINSKI, OLOFSSON & TANO 1995] suggested an enhanced strain field of the type

$$\llbracket \tilde{\boldsymbol{\varepsilon}} \rrbracket = \mathbf{B} \mathbf{A} \mathbf{H}_3^T \mathbf{e}. \quad (3.35)$$

In Eq. (3.35),  $\mathbf{A}$  represents the so-called *redistribution matrix*, cf. [KLISINSKI, OLOFSSON & TANO 1995]. It should be noted that in the original work [KLISINSKI, OLOFSSON & TANO 1995],  $\llbracket \tilde{\boldsymbol{\varepsilon}} \rrbracket = \mathbf{B} \mathbf{A} \mathbf{q} \mathbf{e}$ , with  $\mathbf{q} \neq \mathbf{H}_3^T$ . This difference ( $\mathbf{q} \neq \mathbf{H}_3^T$ ) between [KLISINSKI, OLOFSSON & TANO 1995] and [JIRÁSEK & ZIMMERMANN 2001] results from different local coordinates. However, by applying the same local cartesian coordinate system,  $\mathbf{q} = \mathbf{H}_3^T$ . Restricting attention to constant strain triangles and assuming that  $\mathbf{X}_3^e \in \Omega^+$  while  $\mathbf{X}_1^e, \mathbf{X}_2^e \in \Omega^-$ ,  $\mathbf{A}$  is specified by (see [KLISINSKI, OLOFSSON & TANO 1995])

$$\mathbf{A}^T = \begin{bmatrix} -\xi & 0 & -\xi & 0 & 1-\xi & 0 \\ 0 & -\xi & 0 & \xi & 0 & 1-\xi \end{bmatrix}, \quad \xi \in [0, 1]. \quad (3.36)$$

The parameter  $\xi$  defines the relative distance of the discontinuity within the finite element. However, it can be shown directly that the product  $\mathbf{B} \mathbf{A}$  is independent of  $\xi$ . Hence, without loss of generality,  $\xi$  is set to  $\xi = 0$ . Applying the product of  $\mathbf{A}(\xi = 0) \mathbf{H}_3^T$ , the equivalence

$$\mathbf{H} = \mathbf{A}(\xi = 0) \mathbf{H}_3^T \quad (3.37)$$

is verified. As a consequence,  $\mathbf{B} \mathbf{A} \mathbf{H}_3^T \mathbf{e} = \mathbf{B} \mathbf{H} \mathbf{e}$ , and the kinematics proposed by KLISINSKI and co-workers are fully equivalent to those presented in the previous Subsection. It should be noted that the works of [DVORKIN, CUITIÑO & GIOIA 1990] and [KLISINSKI, RUNESSON & STURE 1991] were published earliest; three (two) years earlier than the paper [SIMO, OLIVER & ARMERO 1993].

## 3.2 Constitutive equations

### 3.2.1 Constitutive Equations for $\mathbf{X} \in \Omega^\pm$ :

#### Stress-strain laws

According to Section 3.1.3,  $\mathbf{F}|_{\Omega^\pm}$  is regularly distributed. As a consequence, standard stress-strain relationship based continuum models such as those presented in Chapter 2 can be applied. Since the main focus of this chapter is on the modeling of localized inelastic deformations, the homogeneously distributed part of deformation is assumed as purely elastic. More precisely, the existence of a stored-energy functional  $\Psi_{\text{reg}} = \Psi_{\text{reg}}(\bar{\mathbf{F}})$  is postulated. Following Section 2.3, the KIRCHHOFF stresses  $\boldsymbol{\tau}$  and the second PIOLA-KIRCHHOFF stress tensor are obtained as

$$\boldsymbol{\tau} = 2 \bar{\mathbf{F}} \cdot \partial_{\bar{\mathbf{C}}} \Psi_{\text{reg}} \cdot \bar{\mathbf{F}}^T \quad \text{and} \quad \mathbf{S} = 2 \partial_{\bar{\mathbf{C}}} \Psi_{\text{reg}}, \quad (3.38)$$

with the right CAUCHY-GREEN tensor

$$\bar{\mathbf{C}} := \bar{\mathbf{F}}^T \cdot \bar{\mathbf{F}}. \quad (3.39)$$

Note that the identity  $\bar{\mathbf{C}}|_{\Omega^\pm} = \mathbf{C}|_{\Omega^\pm}$  holds. It should be emphasized that other constitutive models such as plasticity-based formulations can be easily applied as well.

**Remark 3.2.1.1** *Since the stress tensors are only defined for  $\mathbf{X} \in \Omega^\pm$ , and for those points the identity  $\bar{\mathbf{F}}|_{\Omega^\pm} = \mathbf{F}|_{\Omega^\pm}$  holds, the bar over the second PIOLA-KIRCHHOFF stress tensor  $\mathbf{S}$  is omitted.*

### 3.2.2 Constitutive Equations for $\mathbf{X} \in \partial_s \Omega$ :

#### Traction-separation laws

As shown in Section 3.1.3, the kinematics depend on two independent fields, namely  $\hat{\mathbf{u}}$  and  $[\![\mathbf{u}]\!]$ . As a consequence,  $\bar{\mathbf{F}}$  and  $\tilde{\mathbf{F}}$  as defined by Eq. (3.19) are independent from one another as well. Therefore, two constitutive laws can be introduced: one as a function of  $\bar{\mathbf{F}}$  and an additional model formulated in terms of  $\tilde{\mathbf{F}}$ . The first of those has already been given in Subsection 3.2.1. Hence, a second material law connecting  $\tilde{\mathbf{F}}$  with its conjugate variable is presented here.

According to Eq. (3.19),  $\tilde{\mathbf{F}}$  depends only on the displacement discontinuity ( $\mathbf{N}$  is time invariant). Consequently, it is convenient to derive the new constitutive law in terms of the deformation jump. By analyzing Eq. (3.19), it is evident that a complete decoupling of  $\tilde{\mathbf{F}}$  and  $\tilde{\mathbf{F}}$  requires the new law to be a function of the spatial displacement discontinuity  $\mathbf{J}$ . Clearly, in principle, the true deformation jump  $[[\mathbf{u}]]$  can be used as well.

Following [SIMO & OLIVER 1994] it can be shown that the displacement discontinuity  $[[\mathbf{u}]]$  is conjugated to the traction vector  $\mathbf{T} = \mathbf{P} \cdot \mathbf{N}$  acting within the surface  $\partial_s \Omega$ . Laws connecting  $[[\mathbf{u}]]$  with  $\mathbf{T}$  are referred to as *traction-separation laws* or *cohesive laws*. They are based on the pioneering works by [DUGDALE 1960; BARENBLATT 1962], see also [HILLERBORG, MODEER & PETERSSON 1976].

For the development of those laws two different concepts can be found in the literature. [SIMO, OLIVER & ARMERO 1993] proposed to project a standard stress-strain relationship onto a surface leading to a traction-separation law. SIMO and co-workers were the first who recognized that the singular DIRAC-delta distribution connects classical stress-strain relationship-based continuum mechanics to discrete phenomena such as cracking or shear sliding. See References [OLIVER, CERVERA & MANZOLI 1999; OLIVER 2000; OLIVER, HUESPE, PULIDO & SAMANIEGO 2003] for more details concerning the discrete constitutive models induced by strong discontinuities and classical continuum models.

Despite the considerable progress made by SIMO and co-workers and OLIVER and co-workers in the field of modeling of strain localization, constitutive equations based on the described projection concept are not totally indisputable. For instance, [BORJA 2002] argues that the constitutive response associated with the continuous deformation is not necessarily identical to that of the post-localization regime. His argumentation is based on the constitutive response of rocks. In line with BORJA, many authors derive a specific traction-separation law which is completely independent of that corresponding to the homogeneous deformation, cf. [SNYMAN, BIRD & MARTIN 1991; MIEHE & SCHRÖDER 1994; ARMERO & GARIKIPATI 1996; ARMERO 1999; MOSLER 2004]. It should be emphasized that a decoupled material response for  $\Omega^\pm$  and  $\partial_s \Omega$  is equivalent to an additive decomposition of the HELMHOLTZ free energy. Such a split is mathematically sound and often applied, if convergence of cohesive formulations is analyzed, see [FRANCFORT & MARIGO 1998; NEGRI 2005B; DAL MASO & ZANINI 2005]. Furthermore, the projection method by [SIMO, OLIVER & ARMERO 1993] leads to an additive decomposition of the energy as well, cf. [OLIVER 1996]. As a result and without loss of generality, in the following, only interface laws which are completely independent of the bulk response are considered.

A decoupling of the material models for  $\Omega^\pm$  and  $\partial_s \Omega$  is equivalent to a HELMHOLTZ free energy of the type

$$\Psi(\bar{\mathbf{C}}, \mathbf{J}, \boldsymbol{\alpha}) = \Psi_{\text{reg}}(\bar{\mathbf{C}}) + \Psi_{\text{sing}}(\mathbf{J}, \boldsymbol{\alpha}) \delta_s. \quad (3.40)$$

Here, purely elastic deformations in  $\Omega^\pm$  have been assumed. However, the more general

case does not lead to any further problems. Integration of Eq. (3.40) yields

$$\int_{\Omega} \Psi(\bar{\mathbf{C}}, \mathbf{J}, \boldsymbol{\alpha}) \, dV = \int_{\Omega} \Psi_{\text{reg}}(\bar{\mathbf{C}}) \, dV + \int_{\partial_s \Omega} \Psi_{\text{sing}}(\mathbf{J}, \boldsymbol{\alpha}) \, dA. \quad (3.41)$$

Hence, the HELMHOLTZ free energy of the whole system is decomposed into a bulk part and a surface part. In Eq. (3.40) and (3.41),  $\boldsymbol{\alpha}$  represents displacement-like internal variables. Based on an energy of the type (3.40) a novel thermodynamically consistent procedure for developing traction-separation laws is presented in this section.

For deriving cohesive models, attention is restricted to purely inelastic localized deformations, i. e., the displacement jump  $\mathbf{J}$  corresponds to fully inelastic deformations. In this case,  $\mathbf{J}$  can also be interpreted as a displacement-like internal variable. Hence,  $\Psi_{\text{sing}}(\mathbf{J}, \boldsymbol{\alpha})$  reduces to  $\Psi_{\text{sing}}(\boldsymbol{\alpha}(\mathbf{J}))$ . Evidently, a decomposition of  $\mathbf{J}$  into an elastic and an inelastic part can be easily applied as well, cf. [MIEHE & SCHRÖDER 1994; ARMERO 1999].

So far, the mechanical problem describing the material response in  $\Omega^{\pm}$  and that corresponding to  $\mathbf{X} \in \partial_s \Omega$  are uncoupled. The coupling is provided by the condition of continuity of the traction vector  $\mathbf{T} := \mathbf{P} \cdot \mathbf{N}$  where  $\mathbf{P}$  denotes the first PIOLA-KIRCHHOFF stress tensor:

$$\mathbf{T}^{-}(\mathbf{X}_0) = \mathbf{T}^{+}(\mathbf{X}_0) = \mathbf{T}(\mathbf{X}_0), \quad \mathbf{X}_0 \in \partial_s \Omega, \quad (3.42)$$

with  $\mathbf{T}^{\pm}$  denoting the left hand and the right hand limits of the traction vector  $\mathbf{T}$  according to Eq. (3.3). This canonical condition follows from the extension of the principle of virtual work to continua with internal surfaces  $\partial_s \Omega$ , if the space of admissible test functions is chosen as that spanned by the displacement field (3.7), i. e., BUBNOV-GALERKIN-type. For further details, refer to [SIMO & OLIVER 1994]. Condition (3.42) allows to compute the stress vector  $\mathbf{T}(\mathbf{X}_0)$  by means of the hyperelastic material law associated with  $\mathbf{X} \in \Omega^{\pm}$ .

Now, the dissipation  $\mathcal{D}$  in  $\partial_s \Omega$  can be calculated. Combining Condition (3.42) and the hyperelastic law (3.38), together with the spatial velocity gradient (3.21),  $\mathcal{D}$  is obtained as

$$\mathcal{D} = \boldsymbol{\tau} : \mathbf{l} - \dot{\Psi} = \left[ \left( \boldsymbol{\tau} \cdot \bar{\mathbf{F}}^{-T} \cdot \mathbf{N} \right) \cdot \mathcal{L}_{\nu} [\mathbf{u}] + \mathbf{q} \cdot \dot{\boldsymbol{\alpha}} \right] \delta_s \geq 0. \quad (3.43)$$

In Eq. (3.43), the internal stress-like variables  $\mathbf{q} := -\partial_{\boldsymbol{\alpha}} \Psi_{\text{sing}}$  conjugate to  $\boldsymbol{\alpha}$  have been introduced. Hence, the scalar product  $\mathbf{q} \cdot \dot{\boldsymbol{\alpha}}$  depends on the order of the tensor  $\boldsymbol{\alpha}$ . Alternatively, the dissipation can be re-written as

$$\mathcal{D} = \left[ (\bar{\mathbf{C}} \cdot \mathbf{S} \cdot \mathbf{N}) \cdot \dot{\mathbf{J}} + \mathbf{q} \cdot \dot{\boldsymbol{\alpha}} \right] \delta_s \geq 0. \quad (3.44)$$

Note that Ineq. (3.44) is formally identical to its counterpart of standard multiplicative plasticity. To show this equivalence more explicitly, the pull-back (with respect to the intermediate configuration) of  $\tilde{\mathbf{l}}$  resulting in

$$\tilde{\mathbf{L}} = \dot{\mathbf{J}} \otimes \mathbf{N} \delta_s \quad (3.45)$$

is introduced. With Eq. (3.45), the dissipation yields

$$\mathcal{D} = (\bar{\mathbf{C}} \cdot \mathbf{S}) : \tilde{\mathbf{L}} + \mathbf{q} \cdot \dot{\boldsymbol{\alpha}} \delta_s \geq 0. \quad (3.46)$$

Fully analogously to standard continuum models, the dissipation which is now computed with respect to the intermediate configuration depends on the MANDEL stresses  $\bar{\mathbf{C}} \cdot \mathbf{S}$  (compare Eq. (3.45) to Subsection 2.4.2, Eq. (2.58)<sub>1</sub>). Note that  $\boldsymbol{\alpha} = \boldsymbol{\alpha}(\mathbf{J})$ . Hence,  $\boldsymbol{\alpha}$  and  $\mathbf{q}$  are also defined on the intermediate configuration and thus,  $\dot{\boldsymbol{\alpha}}$  represents an objective time derivative.

The evolution equations, i. e.,  $\dot{\mathbf{J}}$  and  $\dot{\boldsymbol{\alpha}}$ , are computed from the postulate of maximum dissipation under the constraint imposed by the condition of traction continuity. Following [MOSLER 2005B; MOSLER 2004] and using the positive definiteness of a norm  $\|\bullet\|$ , the constraint (3.42) is re-written as

$$\phi := \|\mathbf{T}^+(\mathbf{X}_0) - \mathbf{T}(\mathbf{X}_0)\| = 0. \quad (3.47)$$

Alternatively, a pull-back yields

$$\phi := \|\bar{\mathbf{T}}^+(\mathbf{X}_0) - \bar{\mathbf{T}}(\mathbf{X}_0)\| = 0, \quad \text{with} \quad \bar{\mathbf{T}} := \bar{\mathbf{C}} \cdot \mathbf{S} \cdot \mathbf{N}. \quad (3.48)$$

Evidently, this equation is fully equivalent to the necessary condition of yielding known from standard plasticity models. By this equivalence, the definition of the space of admissible stresses

$$\mathbb{E}_{\bar{\mathbf{T}}} := \left\{ (\bar{\mathbf{T}}^+, \mathbf{q}) \in \mathbb{R}^3 \times \mathbb{R}^n \mid \phi(\bar{\mathbf{T}}^+, \mathbf{q}) \leq 0 \right\} \quad (3.49)$$

is motivated. Restricting to the geometrically linearized theory, further details are addressed in [MOSLER 2005B; MOSLER 2004]. For the special choice,  $\mathbf{q} = \bar{\mathbf{T}}(\mathbf{X}_0)$  and  $\phi(\bar{\mathbf{T}}^+, \mathbf{q}) = \|\bar{\mathbf{T}}^+ - \mathbf{q}\|$ ,  $\phi = 0$  is equivalent to the condition of traction continuity.

However, the condition  $\mathbf{T}^+ = \mathbf{T}_s := \mathbf{T}|_{\partial_s \Omega}$  has only to be enforced to compute the inelastic part of the deformation, i. e.,  $\dot{\mathbf{J}}$  and  $\dot{\boldsymbol{\alpha}}$ . In the case of fully elastic loading, the stress response is defined uniquely by Eq. (3.38). As a consequence, the condition of traction continuity has only to be enforced to those components of the traction vector  $\bar{\mathbf{T}}$  which are conjugated to non-vanishing components of the material displacement jump  $\mathbf{J}$ . Hence,  $\phi(\bar{\mathbf{T}}^+, \mathbf{q})$  needs not necessarily to be identical to  $\|\bar{\mathbf{T}}^+(\mathbf{X}_0) - \bar{\mathbf{T}}(\mathbf{X}_0)\|$ . For instance, plastic deformations occurring in slip bands in ductile materials such as metals depend exclusively on the resultant of the shear components of  $\bar{\mathbf{T}}$ . Furthermore, the material response associated with metals does not distinguish between compressive or tensile loading (approximately). Hence,

$$\phi = \|\bar{\mathbf{T}}_m^+\|_2 - q(\alpha), \quad \text{with} \quad \bar{\mathbf{T}}_m^+ := \bar{\mathbf{T}}^+ - (\bar{\mathbf{T}}^+ \cdot \mathbf{N}) \mathbf{N} \quad (3.50)$$

represents a suitable choice. In the context of linearized kinematics, this yield function was proposed in [MOSLER 2005B]. It will be used in the numerical analysis presented in Section 3.6.

In summary, the postulate of maximum dissipation subjected to the condition of traction continuity can be written as

$$\max_{(\bar{\mathbf{T}}^+, \mathbf{q}) \in \mathbb{E}_{\bar{\mathbf{T}}}} \mathcal{D}(\bar{\mathbf{T}}^+, \mathbf{q}) \quad (3.51)$$

Consequently, the evolution equation are obtained as

$$\dot{\mathbf{J}} = \lambda \partial_{\bar{\mathbf{T}}^+} \phi, \quad \dot{\boldsymbol{\alpha}} = \lambda \partial_{\mathbf{q}} \phi. \quad (3.52)$$

The plastic multiplier  $\lambda$  as introduced in Definition (3.52) is computed from the consistency condition  $\dot{\phi} = 0$ . Analogous to standard plasticity theory, the evolution laws are defined completely by means of the yield function, if the postulate of maximum dissipation is enforced. Non-associative material models can be derived in a similar manner. For that purpose, two additional potentials  $g = g(\bar{\mathbf{T}}^+, \mathbf{q})$  and  $h = h(\bar{\mathbf{T}}^+, \mathbf{q})$  are introduced and the evolution equations are specified by

$$\dot{\mathbf{J}} = \lambda \partial_{\bar{\mathbf{T}}^+} g, \quad \dot{\boldsymbol{\alpha}} = \lambda \partial_{\mathbf{q}} h. \quad (3.53)$$

For the yield function (3.50), the respective associative evolution equations are contained in [MOSLER 2005B].

The singular surface  $\partial_s \Omega$  has been postulated to be time invariant, i. e.,  $\dot{\mathbf{N}} = \mathbf{0}$ . Consequently,

$$\phi(\bar{\mathbf{T}}^+, \mathbf{q}) = \phi^*(\bar{\mathbf{C}} \cdot \mathbf{S}, \mathbf{q}), \quad \text{with} \quad \phi^*(\mathbf{A}, \mathbf{b}) := \phi(\mathbf{A} \cdot \mathbf{N}, \mathbf{b}). \quad (3.54)$$

Hence, equivalently to Eq. (3.53)<sub>1</sub>, the evolution law

$$\dot{\mathbf{J}} \otimes \mathbf{N} = \lambda \partial_{\bar{\mathbf{C}} \cdot \mathbf{S}} g^* \quad (3.55)$$

can be derived. Thus, the space of admissible stresses is formulated in terms of MANDEL-stresses and the evolution law associated with inelastic deformations governs the inelastic velocity gradient  $\tilde{\mathbf{L}}$ . As a result, the constitutive equations describing the localized inelastic part of the deformation are formally identical to those known from standard plasticity (compare to Section 2.4).

In the following sections, the condition of traction continuity will be replaced by the more general type of equations  $\phi(\bar{\mathbf{T}}^+, \mathbf{q})$  or  $\phi^*(\bar{\mathbf{C}} \cdot \mathbf{S}, \mathbf{q})$ . Consequently,  $\mathbf{T}|_{\partial_s \Omega}$  is included in the stress-like variable  $\mathbf{q}$ . Hence, without risk of confusion, the + sign indicating the right hand side limit is omitted, i. e.,  $\bar{\mathbf{T}} := \bar{\mathbf{T}}^+$ .

**Remark 3.2.2.1** *The inelastic displacements  $\mathbf{J}$  can be of plastic nature or damage-induced. Thus, the presented constitutive framework holds also for a broad range of damage-type models. If damage accumulation is to be modeled, one part of the inelastic strains has to be connected to the elastic material properties, cf. [MOSLER & BRUHNS 2004; MOSLER 2005E].*

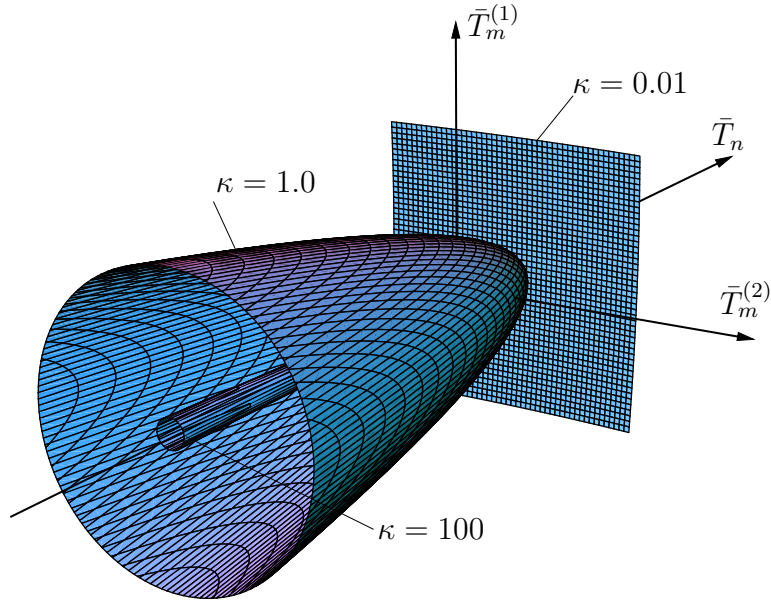


**Figure 3.2:** 3-D constitutive model for the analysis of mixed-mode material failure ( $n = 2$ ): yield surface  $\phi = 0$  in the  $\bar{T}_n$ - $\bar{T}_m^{(1)}$ - $\bar{T}_m^{(2)}$ -space for different values of  $\kappa$  (see Eq. (3.59))

**Remark 3.2.2.2** Introducing an equivalent stress measure denoted as  $\bar{T}_{\text{eq}}(\bar{\mathbf{T}})$  isotropic hardening/softening can be modeled by

$$\phi(\bar{\mathbf{T}}, \mathbf{q}) = \bar{T}_{\text{eq}}(\bar{\mathbf{T}}) - \bar{T}_{\text{eq}}^{\text{ini}} - q(\alpha), \quad (3.56)$$

cf. Eq. (3.50). Kinematic hardening/softening can be accounted for by using

$$\phi(\bar{\mathbf{T}}, \mathbf{q}) = \bar{T}_{\text{eq}}(\bar{\mathbf{T}} - \mathbf{q}) - \bar{T}_{\text{eq}}^{\text{ini}}, \quad (3.57)$$

where  $\mathbf{q}$  is a back-stress vector and  $\bar{T}_{\text{eq}}^{\text{ini}}$  is associated with the elastic space of the virgin material. If  $\bar{T}_{\text{eq}}$  is a positively homogeneous function of degree one and associative evolution equations are assumed, both models (Eq. (3.56) and (3.57)) yield a positive dissipation, i. e.,

$$\mathcal{D} = \lambda \bar{T}_{\text{eq}}^{\text{ini}} \delta_s. \quad (3.58)$$

**Remark 3.2.2.3** A class of mixed mode models suitable for the analysis of cracking in brittle structures is defined by the yield function

$$\phi(\bar{\mathbf{T}}, \mathbf{q}) = (\bar{\mathbf{T}} \cdot \mathbf{N}) + \kappa \|\bar{\mathbf{T}}_m\|^{2n} - q(\alpha), \quad (3.59)$$

cf. [MOSLER 2005D]. The material parameter  $\kappa$  controls the interaction between normal and shear stresses. Introducing a cartesian coordinate system by its defining vectors  $\mathbf{N}$   $\mathbf{M}^{(1)}$  and  $\mathbf{M}^{(2)}$ , the yield surface  $\phi = 0$  is illustrated in Fig. 3.2.

### 3.3 Numerical implementation

This section contains the numerical implementation of the kinematics as proposed in Section 3.1.3 as well as the constitutive equations presented in Section 3.2. Referring to the yield function  $\phi$ , the evolution equations and the type of finite elements, no special assumption has to be made. Hence, the model as described in this section holds for a broad range of different constitutive models and can be applied to a variety of different problems.

To the best knowledge of the author, with the exception of the work [BORJA 2002], all other geometrically exact embedded strong discontinuity models in the sense of [SIMO, OLIVER & ARMERO 1993; SIMO & OLIVER 1994] such as [ARMERO & GARIKIPATI 1996; LARSSON, STEINMANN & RUNESSON 1998; ARMERO 1999; OLIVER, HUESPE, PULIDO & SAMANIEGO 2003; GASSER & HOLZAPFEL 2003; CALLARI & ARMERO 2004] are based on the static condensation technique. In contrast to this procedure, [BORJA 2002] proposed a finite element formulation in which the degrees of freedom characterizing the displacement discontinuity are condensed out at the material level. In the case of infinitesimal deformations, this approach was presented in [BORJA 2000; MOSLER & MESCHKE 2000; MOSLER & MESCHKE 2001]. However, the work [BORJA 2002] is restricted to constant strain triangle elements. Furthermore, the displacement jump is assumed to represent a purely sliding deformation, i. e.,  $\mathbf{J} = \zeta \mathbf{M}$ , with  $\mathbf{N} \cdot \mathbf{M} = 0$  and  $\zeta$  denoting the amplitude of the displacement discontinuity. Evidently, the underlying kinematics cannot capture mode-I or mixed-mode failure. In the two-dimensional case, these kinematics result in  $\dot{\mathbf{M}} = \mathbf{0}$ . Consequently, the scalar  $\zeta$  is the only unknown variable associated with the displacement jump. Additionally, for a purely sliding deformation in 2D, the identity

$$\frac{\bar{\mathbf{F}} \cdot \mathbf{M}}{\|\bar{\mathbf{F}} \cdot \mathbf{M}\|_2} = \frac{\hat{\mathbf{F}} \cdot \mathbf{M}}{\|\hat{\mathbf{F}} \cdot \mathbf{M}\|_2} \quad (3.60)$$

holds, cf. Eq. (3.14). Hence, the tangential vector which defines the direction of the displacement jump depends only on the known (in the case of displacement-based finite elements) compatible deformation field  $\hat{\mathbf{u}}$ . Both simplifications, i. e.,  $\dot{\mathbf{M}} = \mathbf{0}$  and Eq. (3.60), have been included in the numerical model as proposed in [BORJA 2002]. However, even for a vanishing normal component of the displacement jump ( $\mathbf{J} \cdot \mathbf{N} = 0$ ), which is a very restrictive assumption,  $\dot{\mathbf{M}} = \mathbf{0}$  is not fulfilled in 3D in general. As a consequence, the extension of the model [BORJA 2002] to a fully three-dimensional framework is not a straightforward task.

In this section a novel geometrically exact three-dimensional finite element formulation based on the SDA is presented. The approach is characterized by the following properties:

- A broad range of different constitutive interface models can be applied. Arbitrary yield functions and non-associative evolution equations can be implemented consistently.

- The model is not restricted to a certain type of finite elements. Higher-order three-dimensional formulations can be used as well.
- The implementation is formally identical to that of standard multiplicative plasticity and hence, existing subroutines can be employed.
- The proposed method is equivalent to the original SDA by [SIMO, OLIVER & ARMERO 1993] (see also [ARMERO & GARIKIPATI 1996]). Only the algorithmic formulation is different.

For the geometrically linearized theory, a finite element model showing the enumerated properties was proposed in [MOSLER 2005B]. In this respect, the implementation of the SDA as explained in this section can be understood as the generalization of the framework advocated in [MOSLER 2005B].

In what follows, the fundamentals concerning the novel numerical model are described first. For that purpose, the finite element formulation in [GARIKIPATI 1996; ARMERO & GARIKIPATI 1996] which represents the first published work on embedded strong discontinuities within a finite strain setting is summarized briefly. Subsequently, the new finite element formulation will be explained.

### 3.3.1 Fundamentals

The additive decomposition of the deformation gradient according to Eq. (3.18) is formally identical to that of the well-known EAS concept [SIMO & RIFAI 1990; SIMO, ARMERO & TAYLOR 1993]. Hence, the implementation of most finite element models dealing with embedded strong discontinuities such as [SIMO, OLIVER & ARMERO 1993; SIMO & OLIVER 1994; ARMERO & GARIKIPATI 1996; LARSSON, STEINMANN & RUNESSON 1998; ARMERO 1999; OLIVER, HUESPE, PULIDO & SAMANIEGO 2003; GASSER & HOLZAPFEL 2003; CALLARI & ARMERO 2004] is identical to that applied in the original EAS concept. More specifically, the stationarity conditions of the respective two field functional

$$\int_{\Omega^e} \text{GRAD}\boldsymbol{\eta}_0 : \mathbf{P} \, dV = \int_{\Omega^e} \rho_0 \mathbf{B} \cdot \boldsymbol{\eta}_0 \, dV + \int_{\partial_2\Omega} \mathbf{T}^* \cdot \boldsymbol{\eta}_0 \, dA \quad (3.61)$$

and

$$\int_{\Omega^e} \hat{\mathbf{H}} : \mathbf{P} \, dV = 0 \quad (3.62)$$

depending on the displacement fields  $\hat{\mathbf{u}}$  and  $[[\mathbf{u}]]$  build the starting point of the numerical model. In Eqs. (3.61) and (3.62),  $\boldsymbol{\eta}_0$ ,  $\rho_0 \mathbf{B}$  and  $\mathbf{T}^*$  denote a continuous test function, body forces and prescribed traction vectors acting on the NEUMANN boundary  $\partial_2\Omega$ , respectively.

The approximations of the kinematics are those contained in Subsection 3.1.3. Following the EAS concept, the test functions are chosen as

$$\boldsymbol{\eta}_0 = \sum_i^{n_{\text{node}}} N_i \boldsymbol{\eta}_i^e. \quad (3.63)$$

By designing the variation  $\hat{\mathbf{H}}$  of the enhanced displacement gradient according to [GARIKIPATI 1996; ARMERO & GARIKIPATI 1996], namely

$$\hat{\mathbf{H}} := -\frac{1}{V^e} \boldsymbol{\beta} \otimes \mathbf{N} + \frac{1}{A_s} \boldsymbol{\beta} \otimes \mathbf{N} \delta_s, \quad (3.64)$$

the  $L_2$ -orthogonality condition (3.62) is equivalent to the weak form of traction continuity

$$\frac{1}{V^e} \int_{\Omega^e} \mathbf{P} \cdot \mathbf{N} \, dV = \frac{1}{A_s} \int_{\partial_s \Omega} \mathbf{T}_s \, dA \quad (3.65)$$

where  $V^e$ ,  $A_s$  and  $\boldsymbol{\beta}$  represent the volume of the finite element  $e$ , the volume of the localization surface, i. e.,  $A_s := \int_{\partial_s \Omega} dA$ , and the variations of the displacement jump  $[[\mathbf{u}]]$ , respectively. For further details, refer to [SIMO & OLIVER 1994; OLIVER 1996] (see also Remark 3.3.1.1). Since the material displacement jump  $\mathbf{J}$  does not appear explicitly in the formulation, but the displacement jump  $[[\mathbf{u}]]$ , a material law of the type  $\mathbf{T}_s = \mathbf{T}_s([[ \mathbf{u} ]])$  is frequently applied, see [GASSER & HOLZAPFEL 2003] and [GARIKIPATI 1996] (Appendix). The implementation of an interface law in terms of  $\mathbf{J}$  and  $\bar{\mathbf{T}}$  was suggested in [LARSSON & JANSSON 2002]. However, the model proposed in the cited paper is based on an interface element with regularized strong discontinuities. Following the EAS concept, the solution associated with Eqs. (3.61) and (3.62) is computed by solving both equation simultaneously, cf. [SIMO & ARMERO 1992].

In the present work, a different solution strategy is proposed. For the development of this model, the average value of  $\mathbf{T} = \mathbf{P} \cdot \mathbf{N}$  is introduced via

$$\text{ave}(\mathbf{T}) := \frac{1}{V^e} \int_{\Omega^e} \mathbf{P} \cdot \mathbf{N} \, dV. \quad (3.66)$$

Since  $\mathbf{T}_s = \mathbf{T}_s([[ \mathbf{u} ]])$  and  $[[\mathbf{u}]]$  has been assumed spatially constant within the respective finite element (GRAD  $[[\mathbf{u}]] = \mathbf{0}$ ), the right hand side of Eq. (3.65) simplifies to

$$\frac{1}{A_s} \int_{\partial_s \Omega} \mathbf{T}_s \, dA = \mathbf{T}_s. \quad (3.67)$$

As a consequence, Eq. (3.65) can be re-written as

$$\phi = ||\text{ave}(\mathbf{T}) - \mathbf{T}_s|| = 0. \quad (3.68)$$

For further details, refer to [MOSLER 2005B; MOSLER 2004]. Clearly, Eq. (3.68) is equivalent to

$$\phi = \|\text{ave}(\bar{\mathbf{T}}) - \bar{\mathbf{T}}_s\| = 0 \quad (3.69)$$

depending on vectors defined on the intermediate configuration. According to Subsection 3.2.2, this equation results in

$$\phi(\text{ave}(\bar{\mathbf{T}}), \mathbf{q}) \leq 0. \quad (3.70)$$

In the case of constant strain elements, i. e.,  $\text{GRAD}\hat{\mathbf{u}} = \text{const}$  (with respect to  $\mathbf{X}$ ), which will be considered in Subsections 3.3.2 – 3.3.4,  $\text{GRAD}\varphi = \text{const}$ , and consequently,  $\bar{\mathbf{F}} = \text{const}$ . Hence,  $\bar{\mathbf{C}} = \text{const}$  and  $\mathbf{S} = \text{const}$  as well, leading to  $\bar{\mathbf{T}} = \text{const}$ . As a result,  $\text{ave}(\bar{\mathbf{T}}) = \bar{\mathbf{T}}$  and the weak form of traction continuity is equivalent to the strong form

$$\phi(\bar{\mathbf{T}}, \mathbf{q}) \leq 0. \quad (3.71)$$

Consequently, in the case of loading ( $\lambda > 0$ ), the stationarity conditions (3.61) and (3.62) are equivalent to the set of equations

$$\begin{aligned} \int_{\Omega^e} \text{GRAD}\boldsymbol{\eta}_0 : \mathbf{P} \, dV &= \int_{\Omega^e} \mathbf{B} \cdot \boldsymbol{\eta}_0 \, dV + \int_{\partial_2\Omega} \mathbf{T}^* \cdot \boldsymbol{\eta}_0 \, dA \\ \phi(\bar{\mathbf{T}}, \mathbf{q}) &= 0. \end{aligned} \quad (3.72)$$

The extensions necessary for the more general case, i. e., non constant strain elements, are discussed in Subsection 3.3.5.

Evidently, Eqs. (3.72) show the structure of standard (local) finite element models for finite strain plasticity theory. Thus, according to computational plasticity [SIMO 1998; SIMO & HUGHES 1998], the problem defined by means of Eqs. (3.72) is solved in two steps. At first, if inelastic loading is signaled, the condition of traction continuity (3.72)<sub>2</sub> is solved (for fixed  $\hat{\mathbf{u}}$ ). Subsequently, the solution of Eq. (3.72)<sub>1</sub> is computed. It should be noted that despite the procedure described is not standard in finite element formulations based on the EAS concept, a similar strategy, namely a staggered solution scheme, has been successfully applied before, cf. [SIMO, ARMERO & TAYLOR 1993]. However, with the exception that one of the algorithms proposed in [SIMO, ARMERO & TAYLOR 1993] is based on a staggered solution scheme as well, the numerical implementation presented in this work is significantly different.

**Remark 3.3.1.1** *By construction, the incompatible part of the displacement gradient belongs to the space*

$$\mathbb{H} = \{[\mathbf{u}] \otimes \mathbf{N} \delta_s - [\mathbf{u}] \otimes \text{GRAD}\varphi \mid [\mathbf{u}] \cdot \mathbf{N} \geq 0\}. \quad (3.73)$$

Clearly, since  $\hat{\mathbf{H}}$  has been designed such that the  $L_2$ -orthogonality condition is equivalent to the strong form of the traction continuity for the average stresses,  $\hat{\mathbf{H}} \notin \mathbb{H}$ , cf. Eq. (3.64).

Consequently, the proposed model is a PETROV-GALERKIN approach. As a result, even if the evolution equations are governed by the postulate of maximum dissipation, a variational structure such as described in Section 2.5 cannot be derived for the models presented in this subsection.

However, according to [SIMO & OLIVER 1994], a standard BUBNOV-GALERKIN approximation of the type

$$\mathbf{u} = \bar{\mathbf{u}} + \llbracket \mathbf{u} \rrbracket (H_s - \varphi) \quad \boldsymbol{\eta}_0 = \bar{\boldsymbol{\eta}}_0 + \boldsymbol{\beta} (H_s - \varphi) \quad (3.74)$$

implies the equilibrium conditions and the traction continuity, as well. Hence, it is reasonable to assume that the solution obtained from the standard BUBNOV-GALERKIN approximation converges to the one predicted by the PETROV-GALERKIN method. This educated guess is verified by the numerical results in [OLIVER, HUESPE, BLANCO & LINERO 2006]. Obviously, if a BUBNOV-GALERKIN formulation is applied, a material model based on the postulate of maximum dissipation can be recast into a minimization problem such as that described in Section 2.5. Hence, the adaptive strategies presented in Chapters 4 – 6 which crucially depend on the variational structure of the underlying physical problem can be used for the SDA as well.

It should be noted that the convergence rate of the PETROV-GALERKIN-type SDA is, in many cases, significantly better than that of the BUBNOV-GALERKIN approach, cf. [OLIVER, HUESPE, BLANCO & LINERO 2006]. Consequently, the numerical implementation advocated in this section is based on a PETROV-GALERKIN concept. However, only minor modifications are necessary for the fully variationally consistent model.

### 3.3.2 Elastic unloading

At first, the solution associated with an elastic load step is computed, i. e., the inequality  $\phi(\bar{\mathbf{T}}, \mathbf{q}) \leq 0$  is assumed to hold within the considered time interval  $[t_n, t_{n+1}]$ . Thus,

$$\mathbf{J}_{n+1} = \mathbf{J}_n, \quad \text{with} \quad (\bullet)_n := (\bullet)|_{t_n}. \quad (3.75)$$

Consequently, the elastic solution is computed from the weak form of equilibrium (3.72)<sub>1</sub> subjected to the Constraint (3.75). Since the left hand side of Eq. (3.72)<sub>1</sub> does not represent the best choice for computational purposes, a standard transformation leading to

$$\int_{\Omega^e} \text{GRAD} \boldsymbol{\eta}_0 : \mathbf{P} \, dV = \int_{\Omega^e} \overline{\text{grad}} \boldsymbol{\eta}_0 : \boldsymbol{\tau} \, dV, \quad \text{with} \quad \overline{\text{grad}}(\bullet) := \frac{\partial(\bullet)}{\partial \mathbf{X}} \cdot \bar{\mathbf{F}}^{-1} \quad (3.76)$$

is applied. Hence, the solution corresponding to an elastic load step is given by the procedure

compute:  $\hat{\mathbf{u}}_{n+1}$  under the constraints:

$$\int_{\Omega^e} \overline{\text{grad}} \boldsymbol{\eta}_0 : \boldsymbol{\tau} \, dV = \int_{\Omega^e} \mathbf{B} \cdot \boldsymbol{\eta}_0 \, dV + \int_{\partial_2 \Omega} \mathbf{T}^* \cdot \boldsymbol{\eta}_0 \, dA \quad (3.77)$$

$$\mathbf{J}_{n+1} = \mathbf{J}_n.$$

Analogous to standard displacement-based finite element formulations,  $\hat{\mathbf{u}}_{n+1}$  is computed by using a NEWTON-type iteration. For that purpose, the interpolations (3.63)<sub>1</sub> resulting in

$$\overline{\text{grad}} \boldsymbol{\eta}_0 = \sum_{i=1}^{n_{\text{node}}} \boldsymbol{\eta}_{0i}^e \otimes \text{GRAD} N_i \cdot \bar{\mathbf{F}}^{-1} \quad (3.78)$$

are inserted into Eq. (3.77)<sub>1</sub> and the residual

$$\mathbf{R}_I = \mathbf{A} \int_{\Omega^e} \left[ \text{GRAD} N_i \cdot \bar{\mathbf{F}}^{-1} \right] \cdot \boldsymbol{\tau} \, dV \quad (3.79)$$

$$- \int_{\Omega^e} N_i \mathbf{B} \, dV - \int_{\partial_2 \Omega} N_i \mathbf{T}^* \, dA$$

is introduced. Following standard conventions in finite element methods,  $\mathbf{A}$  denotes the assembly of all element contributions at the local element node  $i$  to the global residual at the global node  $I \in \{1, \dots, n_{\text{gl}}\}$ . According to NEWTON's method, the solution  $\hat{\mathbf{u}}_{n+1}$  (more precisely, the increment  $\Delta \hat{\mathbf{u}}$ ) associated with  $\mathbf{R}_I = \mathbf{0}$  (for all global node points  $I$ ) is obtained from the iterative scheme

$$\mathbf{R}_I|_n + \mathbf{K}^{IJ}|_n \Delta \hat{\mathbf{u}}_J|_{n+1} = \mathbf{0} \quad \forall I = 1, \dots, n_{\text{gl}} \quad (3.80)$$

where  $\mathbf{K}^{IJ}$  denotes the components of the global stiffness matrix, i. e.,

$$\mathbf{K}^{IJ} = \frac{\partial \mathbf{R}_I}{\partial \hat{\mathbf{u}}_J}, \quad (3.81)$$

and  $\hat{\mathbf{u}}_J$  represents the conforming part of the displacement field at global node  $J$ . Within each iteration cycle,  $\hat{\mathbf{u}}$  is updated as  $\hat{\mathbf{u}}_{n+1} = \hat{\mathbf{u}}_n + \Delta \hat{\mathbf{u}}_{n+1}$ .

The residual  $\mathbf{R}_I$  depends on the regularly distributed part of the deformation gradient. However,  $\bar{\mathbf{F}}$  is not given explicitly. More precisely, it follows from the implicit equation

$$\bar{\mathbf{F}}_{n+1} = \mathbf{1} + \text{GRAD} \hat{\mathbf{u}}_{n+1} - \bar{\mathbf{F}}_{n+1} \cdot \mathbf{J}_n \otimes \text{GRAD} \varphi, \quad (3.82)$$

cf. Eq. (3.19). Since Eq. (3.82) is linear in  $\bar{\mathbf{F}}_{n+1}$  and the tuple  $(\mathbf{J}_n, \hat{\mathbf{u}}_{n+1})$  is given (in displacement-based finite element formulations), the exact solution of Eq. (3.82) yields

$$\bar{\mathbf{F}}_{n+1} = \mathbb{A}^{-1} : [\mathbf{1} + \text{GRAD} \hat{\mathbf{u}}_{n+1}], \quad (3.83)$$

with the fourth-order tensor  $\mathbb{A}$  defined as

$$\mathbb{A}_{ikpq} := \mathbb{I}_{ikpq} + [\mathbb{I}_{ijpq} J_j \text{GRAD}\varphi_k]_{|t_n}. \quad (3.84)$$

Next, the components of the stiffness matrix  $\mathbf{K}$  are derived. Starting with the rate form of Eq. (3.72)<sub>1</sub>,

$$\int_{\Omega^e} \text{GRAD}\boldsymbol{\eta}_0 : \dot{\mathbf{P}} \, dV = \int_{\Omega^e} \dot{\mathbf{B}} \cdot \boldsymbol{\eta}_0 \, dV + \int_{\partial_2\Omega} \dot{\mathbf{T}}^* \cdot \boldsymbol{\eta}_0 \, dA = 0, \quad (3.85)$$

together with the identity

$$\int_{\Omega^e} \text{GRAD}\boldsymbol{\eta}_0 : \dot{\mathbf{P}} \, dV = \int_{\Omega^e} \overline{\text{grad}}\boldsymbol{\eta}_0 : [\bar{\mathbf{l}} \cdot \boldsymbol{\tau} + \mathcal{L}_\nu \boldsymbol{\tau}] \, dV \quad (3.86)$$

which follows from standard algebraic manipulations, the rate form of the principle of virtual work is re-written as

$$\int_{\Omega^e} \overline{\text{grad}}\boldsymbol{\eta}_0 : [\bar{\mathbf{l}} \cdot \boldsymbol{\tau} + \mathcal{L}_\nu \boldsymbol{\tau}] \, dV = \int_{\Omega^e} \dot{\mathbf{B}} \cdot \boldsymbol{\eta}_0 \, dV + \int_{\partial_2\Omega} \dot{\mathbf{T}}^* \cdot \boldsymbol{\eta}_0 \, dA = 0. \quad (3.87)$$

In Eq. (3.87), the LIE-type derivative

$$\mathcal{L}_\nu \boldsymbol{\tau} := \bar{\mathbf{F}} \cdot \dot{\mathbf{S}} \cdot \bar{\mathbf{F}}^T \quad (3.88)$$

has been introduced. Using the rate form of the hyperelastic material law (3.38), i. e.,

$$\dot{\mathbf{S}} = \frac{1}{2} \mathbb{C} : \dot{\mathbf{C}}, \quad \text{with} \quad \mathbb{C} = 4 \frac{\partial^2 \Psi_{\text{reg}}}{\partial \bar{\mathbf{C}} \otimes \partial \bar{\mathbf{C}}} \quad (3.89)$$

and applying the well-known identity

$$\mathcal{L}_\nu \boldsymbol{\tau} = \mathbf{c} : \bar{\mathbf{l}}, \quad \text{with} \quad c_{abcd} = \bar{F}_{aA} \bar{F}_{bB} \bar{F}_{cC} \bar{F}_{dD} \mathbb{C}_{ABCD}, \quad (3.90)$$

Eq. (3.87) yields

$$\int_{\Omega^e} \overline{\text{grad}}\boldsymbol{\eta}_0 : [\bar{\mathbf{l}} \cdot \boldsymbol{\tau} + \mathbf{c} : \bar{\mathbf{l}}] \, dV = \int_{\Omega^e} \dot{\mathbf{B}} \cdot \boldsymbol{\eta}_0 \, dV + \int_{\partial_2\Omega} \dot{\mathbf{T}}^* \cdot \boldsymbol{\eta}_0 \, dA = 0. \quad (3.91)$$

Clearly, the only tensor in Eq. (3.91) which depends on the rate of the conforming displacement field  $\hat{\mathbf{u}}$  is the regularly distributed part of the spatial velocity gradient  $\bar{\mathbf{l}}$ . In the context of the iterative solution scheme according to Eq. (3.80),  $\bar{\mathbf{l}}$  leads to

$$\bar{\mathbf{l}} = d\bar{\mathbf{F}} \cdot \bar{\mathbf{F}}^{-1}, \quad (3.92)$$

with the linearization

$$d\bar{\mathbf{F}} = \frac{\partial \bar{\mathbf{F}}}{\partial \hat{\mathbf{u}}} \cdot \Delta \hat{\mathbf{u}}. \quad (3.93)$$

By differentiating Eq. (3.83) for fixed  $\mathbf{J}$  which results in

$$d\bar{\mathbf{F}}_{n+1} = \mathbb{A}^{-1} : \text{GRAD}\Delta\hat{\mathbf{u}}_{n+1}, \quad (3.94)$$

Eq. (3.92) is re-written as

$$\bar{\mathbf{l}} = (\mathbb{A}^{-1} : \text{GRAD}\Delta\hat{\mathbf{u}}_{n+1}) \cdot \bar{\mathbf{F}}^{-1} \quad (3.95)$$

or equivalently,

$$\bar{\mathbf{l}} = \mathbb{L}^e : \text{GRAD}\Delta\hat{\mathbf{u}}_{n+1}, \quad \text{with} \quad \mathbb{L}_{ijkl}^e = \mathbb{A}_{ipkl}^{-1} \bar{F}_{pj}^{-1}. \quad (3.96)$$

Based on Eq. (3.96), the rate form of the principle of virtual work (3.91), and consequently, the stiffness matrix  $\mathbf{K}^{IJ}$  can be computed. It is obtained as

$$\mathbf{K}^{IJ} = \mathbf{K}_{\text{geo}}^{IJ} + \mathbf{K}_{\text{mat}}^{IJ}. \quad (3.97)$$

In Eq. (3.97),  $\mathbf{K}_{\text{geo}}^{IJ}$  denotes the geometric stiffness matrix defined as

$$\mathbf{K}_{\text{geo}}^{IJ} = \mathbf{A} \int_{\Omega^e}^{n_{\text{ele}}} \left[ \text{GRAD}N_i \cdot \bar{\mathbf{F}}^{-1} \right] \cdot \boldsymbol{\tau}^{(2)} \cdot \mathbb{L}^e \cdot \text{GRAD}N_j dV, \quad (3.98)$$

and  $\mathbf{K}_{\text{mat}}^{IJ}$  represents the material tangent. It is computed according to

$$\mathbf{K}_{\text{mat}}^{IJ} = \mathbf{A} \int_{\Omega^e}^{n_{\text{ele}}} \left[ \text{GRAD}N_i \cdot \bar{\mathbf{F}}^{-1} \right] \cdot \mathbf{c}^{(2)} : \mathbb{L}^e \cdot \text{GRAD}N_j dV. \quad (3.99)$$

The contractions applied in Eq. (3.98) and (3.99) are defined according to Remark 3.3.2.1. It is obvious that now the operator  $\mathbf{A}$  denotes the assembly of all element contributions ( $e = 1, \dots, n_{\text{ele}}$ ) at the local element nodes ( $i, j = 1, \dots, n_{\text{node}}$ ) to the components of the global stiffness matrix  $\mathbf{K}^{IJ}$ . Clearly, in the case of linearized kinematics,  $\mathbf{K}_{\text{geo}}^{IJ} = \mathbf{0}$ .

**Remark 3.3.2.1** The notations  $\overset{(i)}{\cdot}$  and  $\overset{(i)}{\vdots}$  represent different type of contractions.  $i$  indicates the first component of the tensor on the right hand side of  $\overset{(i)}{\cdot}$  or  $\overset{(i)}{\vdots}$  over which the summation has to be performed, i. e.,  $[\mathbf{a} \overset{(2)}{\cdot} \mathbb{C}]_{jkl} = a_i \mathbb{C}_{jikl}$  and  $[\mathbf{A} \overset{(2)}{\vdots} \mathbb{C}]_{il} = A_{jk} \mathbb{C}_{ijkl}$ . Clearly, for  $i = 1$  the standard contractions are obtained.

### 3.3.3 Inelastic loading

Next, the solution corresponding to an inelastic loading step, i. e.,  $\lambda > 0$  is addressed. At first, according to the return-mapping algorithm [SIMO 1998; SIMO & HUGHES 1998]

(compare also to Subsection 2.4.3), a trial step characterized by purely elastic deformation is defined as

$$\begin{aligned} \lambda = 0 &\iff \dot{\mathbf{J}} = \mathbf{0}, \quad \dot{\boldsymbol{\alpha}} = \mathbf{0}, \quad \dot{\mathbf{q}} = \mathbf{0} \\ &\implies \bar{\mathbf{F}}_{n+1}^{\text{tr}} = \mathbf{1} + \text{GRAD}\hat{\mathbf{u}}_{n+1} - \bar{\mathbf{F}}_{n+1}^{\text{tr}} \cdot \mathbf{J}_n \otimes \text{GRAD}\varphi. \end{aligned} \quad (3.100)$$

Clearly,  $\bar{\mathbf{F}}_{n+1}^{\text{tr}}$  is computed by applying Eq. (3.83). With  $\bar{\mathbf{F}}_{n+1}^{\text{tr}}$  the right CAUCHY-GREEN trial tensor  $\bar{\mathbf{C}}_{n+1}^{\text{tr}}$  and the second PIOLA-KIRCHHOFF trial stresses  $\mathbf{S}_{n+1}^{\text{tr}}$  are introduced in standard manner. This leads to the trial stress vector

$$\bar{\mathbf{T}}_{n+1}^{\text{tr}} = \bar{\mathbf{C}}_{n+1}^{\text{tr}} \cdot \mathbf{S}_{n+1}^{\text{tr}} \cdot \mathbf{N}. \quad (3.101)$$

As a consequence, the discrete loading condition is given as

$$\phi^{\text{tr}} := \phi(\bar{\mathbf{T}}_{n+1}^{\text{tr}}, \mathbf{q}_{n+1}^{\text{tr}}) > 0, \quad \text{with } \mathbf{q}_{n+1}^{\text{tr}} = \mathbf{q}_n. \quad (3.102)$$

In the case  $\phi^{\text{tr}} \leq 0$ , i. e., a purely elastic loading step, the material response is computed according to Subsection 3.3.2. Otherwise, if inelastic loading is signaled by  $\phi^{\text{tr}} > 0$ , a return-mapping algorithm is performed, cf. Subsection 2.4.3. At first, a backward-EULER integration is applied to the evolution Eqs. (3.53). Hence, the displacement jump (more precisely, its material counterpart) and the internal displacement-like variable  $\boldsymbol{\alpha}$  at time  $t_{n+1}$  are computed as

$$\mathbf{J}_{n+1} = \mathbf{J}_n + \Delta\lambda_{n+1} \partial_{\bar{\mathbf{T}}}g|_{n+1}, \quad \boldsymbol{\alpha}_{n+1} = \boldsymbol{\alpha}_n + \Delta\lambda_{n+1} \partial_{\mathbf{q}}h|_{n+1}, \quad (3.103)$$

with  $\Delta\lambda_{n+1} := \lambda_{n+1} (t_{n+1} - t_n)$ . Evidently, by using a backward-EULER integration, the differential equations characterizing the solution of an inelastic load step are transformed into a set of nonlinear algebraic equation. This is solved by means of NEWTON's method. For that purpose, the residuals

$$\mathbf{R} := \begin{Bmatrix} \mathbf{R}^J \\ \mathbf{R}^\alpha \end{Bmatrix} := \begin{Bmatrix} -\mathbf{J}_{n+1} + \mathbf{J}_n + \Delta\lambda_{n+1} \partial_{\bar{\mathbf{T}}}g|_{n+1} \\ -\boldsymbol{\alpha}_{n+1} + \boldsymbol{\alpha}_n + \Delta\lambda_{n+1} \partial_{\mathbf{q}}h|_{n+1} \end{Bmatrix} \quad (3.104)$$

are introduced. As a consequence, the solution associated with an inelastic load step is computed from the algebraic problem

$$\mathbf{R} = \mathbf{0} \quad \wedge \quad \phi_{n+1} = 0. \quad (3.105)$$

According to NEWTON's method, the linearizations of Eqs. (3.105) are required. After some algebraic manipulations, they result in

$$d\mathbf{R} = \mathbf{A}^{-1} \boldsymbol{\Delta} + d\Delta\lambda_{n+1} \boldsymbol{\nabla}M, \quad d\phi = \boldsymbol{\nabla}\phi \cdot \boldsymbol{\Delta} \quad (3.106)$$

where the notations

$$\mathbf{A}^{-1} := \left[ \begin{array}{cc} \mathbf{A}^{J^{-1}} + \Delta\lambda \partial_{\bar{\mathbf{T}} \otimes \bar{\mathbf{T}}}^2 g & \Delta\lambda_{n+1} \partial_{\bar{\mathbf{T}} \otimes \mathbf{q}}^2 g \\ \Delta\lambda \partial_{\mathbf{q} \otimes \bar{\mathbf{T}}}^2 h & \mathbf{D}^{-1} + \Delta\lambda \partial_{\mathbf{q} \otimes \mathbf{q}}^2 h \end{array} \right] \Big|_{n+1}, \quad \mathbf{D} := -\frac{\partial \mathbf{q}}{\partial \boldsymbol{\alpha}} \quad (3.107)$$

and

$$\Delta^T := [\mathrm{d}\bar{\mathbf{T}}; \mathrm{d}\mathbf{q}]|_{n+1}, \quad \nabla M^T := [\partial_{\bar{\mathbf{T}}}g; \partial_{\mathbf{q}}h]|_{n+1}, \quad \nabla \phi^T := [\partial_{\bar{\mathbf{T}}}\phi; \partial_{\mathbf{q}}\phi]|_{n+1} \quad (3.108)$$

have been used. The second-order tensor  $\mathbf{A}^J$  connects the rate of the material displacement jump  $\mathbf{J}$  to the rate of the traction vector  $\bar{\mathbf{T}}$  for a fixed compatible displacement field  $\hat{\mathbf{u}}$ . The identity  $\mathrm{d}\bar{\mathbf{T}} = -\mathbf{A}^J \cdot \mathrm{d}\mathbf{J}$  is derived in [MOSLER 2005A].

Based on Eqs. (3.105) and (3.106), the increment of the plastic multiplier during an iteration cycle is computed in matrix notation as

$$\mathrm{d}\Delta\lambda_{n+1} = \frac{\phi_{n+1} - \nabla\phi^T \mathbf{A} \mathbf{R}}{\nabla\phi^T \mathbf{A} \nabla M} \Rightarrow \Delta\lambda_{n+1} = \Delta\lambda_n + \mathrm{d}\Delta\lambda_{n+1}. \quad (3.109)$$

Note that the updated deformation gradient  $\bar{\mathbf{F}}$  ( $\Delta\hat{\mathbf{u}} = \mathbf{0}$  during an iteration cycle) follows from Eq. (3.83).

**Remark 3.3.3.1** *According to Section 3.2.2, the constitutive laws governing cohesive models can be re-written into a format fully identical to classical (local) continuum models as those discussed in Chapter 2. In the present paragraph it has been shown that this analogy holds for the numerical implementation as well, cf. Subsection 2.4.3. Due to this similarity, subroutines originally designed for standard continuum models can be used for cohesive finite element formulations with only minor modifications necessary.*

**Remark 3.3.3.2** *According to Eq. (3.106), the linearizations have been computed with respect to  $\bar{\mathbf{T}}$ ,  $\mathbf{q}$  and  $\Delta\lambda$ . Clearly, instead of choosing  $\bar{\mathbf{T}}$  as an independent variable, the MANDEL-type stresses  $\bar{\mathbf{C}} \cdot \mathbf{S}$  may be used. That way, the proposed return-mapping algorithm becomes formally identical to that of classical multiplicative plasticity theory. However, in this case, the dimension of the residuals increases from  $\dim \bar{\mathbf{T}} + \dim \mathbf{q} + \dim \Delta\lambda = n + 4$  to  $\dim(\bar{\mathbf{C}} \cdot \mathbf{S}) + \dim \mathbf{q} + \dim \Delta\lambda = 10 + n$ . Particularly, for isotropic softening ( $\dim \mathbf{q} = 1$ ) which is considered in the numerical example presented in Section 3.6, the number of algebraic equations increases by more than a factor of 2. As a consequence, this alternative formulation has not been chosen.*

### 3.3.4 Linearization

This subsection contains the consistent linearization of the algorithm necessary for an asymptotic quadratic convergence, cf. [SIMO & HUGHES 1998]. For fully elastic unloading, this linearization has been given in Subsection 3.3.2. Next, attention is restricted to an inelastic loading step, i. e.,  $\lambda > 0$ .

By applying the return-mapping algorithm as proposed in Subsection 3.3.3, the regularly distributed part of the deformation gradient  $\bar{\mathbf{F}}$ , the stresses  $\boldsymbol{\tau}$  or  $\mathbf{S}$  and the elastic moduli  $\mathbf{c}$  (see Eq. (3.90)) are computed. Hence, with the exception of the spatial velocity gradient  $\bar{\mathbf{l}}$ , all variables appearing in the rate form of equilibrium (3.91) are known. More precisely,

only the fourth-order tensor  $\mathbb{L}^e$  which is necessary for the computation of the stiffness matrices (3.98) and (3.99) has to be derived. All other variables involved in Eqs. (3.98) and (3.99) are already well defined. Since now attention is restricted to an inelastic loading step, the fourth-order tensor  $\mathbb{L}^e$  is renamed as  $\mathbb{L}^i$ .

According to Eq. (3.82), the linearization of the regularly distributed part of the deformation gradient yields

$$d\bar{\mathbf{F}} = \text{GRAD}\Delta\hat{\mathbf{u}} - d\bar{\mathbf{F}} \cdot \mathbf{J} \otimes \text{GRAD}\varphi - \bar{\mathbf{F}} \cdot d\mathbf{J} \otimes \text{GRAD}\varphi. \quad (3.110)$$

Consequently,  $d\bar{\mathbf{F}}$  is obtained as

$$\begin{aligned} d\bar{\mathbf{F}} &= d\bar{\mathbf{F}}|_{\mathbf{J}=\text{const}} + d\bar{\mathbf{F}}|_{\hat{\mathbf{u}}=\text{const}} \\ &= \mathbb{A}^{-1} : [\text{GRAD}\Delta\hat{\mathbf{u}} - \bar{\mathbf{F}} \cdot d\mathbf{J} \otimes \text{GRAD}\varphi]. \end{aligned} \quad (3.111)$$

Clearly,  $d\bar{\mathbf{F}}|_{\mathbf{J}=\text{const}}$  represents the linearization associated with a fully elastic load step, cf. Subsection 3.3.2. However, the linearization  $d\mathbf{J}$  defining  $d\bar{\mathbf{F}}|_{\hat{\mathbf{u}}=\text{const}}$  is unknown so far. It follows from the return-mapping algorithm.

At a converged state of the return-mapping algorithm, characterized by  $\mathbf{R} = \mathbf{0}$  and  $\phi = 0$  (cf. Subsection 3.3.3) the linearization of  $\mathbf{J}$  with respect to  $\bar{\mathbf{T}}$ ,  $\mathbf{q}$  and  $\Delta\lambda$  results from  $d\mathbf{R} = \mathbf{0}$  and  $d\phi = 0$  (see Eq. (3.106)). Evidently, the goal of this paragraph is to linearize  $\mathbf{J}$  with respect to the primary variable  $\hat{\mathbf{u}}$ . For that purpose, the standard procedure known from computational plasticity theory is borrowed, cf. [SIMO 1998; SIMO & HUGHES 1998].

By applying the chain rule

$$d\bar{\mathbf{T}} = \frac{\partial \bar{\mathbf{T}}}{\partial \bar{\mathbf{C}}} : \frac{\partial \bar{\mathbf{C}}}{\partial \bar{\mathbf{F}}} : [d\bar{\mathbf{F}}|_{\mathbf{J}=\text{const}} + d\bar{\mathbf{F}}|_{\hat{\mathbf{u}}=\text{const}}] \quad (3.112)$$

and inserting the linearization of  $\mathbf{J}$  with respect to  $\bar{\mathbf{T}}$ ,  $\mathbf{q}$  and  $\Delta\lambda$ , together with  $\mathcal{A}^C := \partial \bar{\mathbf{T}} / \partial \bar{\mathbf{C}}$ ,  $\mathbb{T} := \partial \bar{\mathbf{C}} / \partial \bar{\mathbf{F}}$  and  $\mathbf{A}^J := -\partial \bar{\mathbf{T}} / \partial \mathbf{J}$  according to [MOSLER 2005A], Eq. (3.112) is re-written as

$$\begin{aligned} d\bar{\mathbf{T}} &= \mathcal{A}^C : \mathbb{T} : \mathbb{A}^{-1} : \text{GRAD}\Delta\hat{\mathbf{u}} - \mathbf{A}^J \cdot d\mathbf{J} \\ &= \mathcal{A}^C : \mathbb{T} : \mathbb{A}^{-1} : \text{GRAD}\Delta\hat{\mathbf{u}} - \mathbf{A}^J \cdot [\Delta\lambda \partial_{\bar{\mathbf{T}}} g + \Delta\lambda \partial_{\bar{\mathbf{T}} \otimes \bar{\mathbf{T}}}^2 g : d\bar{\mathbf{T}} \\ &\quad + \Delta\lambda \partial_{\bar{\mathbf{T}} \otimes \mathbf{q}}^2 g : d\mathbf{q}]. \end{aligned} \quad (3.113)$$

With the matrix  $\mathbf{A}$  according to Eq. (3.107), the increment of the stress vector  $\bar{\mathbf{T}}$  and that of the internal variables  $\mathbf{q}$  are re-written in matrix notation as

$$\mathbf{A}^{-1} \Delta = \begin{bmatrix} \mathbf{A}^{J^{-1}} \cdot \mathcal{A}^C : \mathbb{T} : \mathbb{A}^{-1} : \text{GRAD}\Delta\hat{\mathbf{u}} \\ 0 \end{bmatrix} - \Delta\lambda \nabla M. \quad (3.114)$$

Pre-multiplying Eq. (3.114) by  $\nabla\phi^T \mathbf{A}$  and considering  $d\phi = \nabla\phi^T \Delta = 0$ , the linearization of the plastic multiplier with respect to the primary variable  $\hat{\mathbf{u}}$  is obtained as

$$\begin{aligned} d\Delta\lambda &= \frac{\nabla\phi^T \mathbf{A} \begin{bmatrix} \mathbf{A}^{J^{-1}} \cdot \mathcal{A}^C : \mathbb{T} : \mathbb{A}^{-1} : \text{GRAD}\Delta\hat{\mathbf{u}} \\ 0 \end{bmatrix}}{\nabla\phi^T \mathbf{A} \nabla M} \\ &= \frac{[\partial_{\bar{\mathbf{T}}}\phi \cdot \mathbf{A}_{[11]} + \partial_{\mathbf{q}}\phi \cdot \mathbf{A}_{[21]}] \cdot \mathbf{A}^{J^{-1}} \cdot \mathcal{A}^C : \mathbb{T} : \mathbb{A}^{-1}}{\nabla\phi^T \mathbf{A} \nabla M} : \text{GRAD}\Delta\hat{\mathbf{u}} \end{aligned} \quad (3.115)$$

where  $\mathbf{A}_{[ij]}$  denotes the submatrix  $ij$  of the hypermatrix  $\mathbf{A}$ . Clearly, this equation is formally identical to that of the standard return-mapping algorithm, cf. [SIMO 1998; SIMO & HUGHES 1998].

Next, the linearizations of  $\bar{\mathbf{T}}$  and  $\mathbf{q}$  with respect to the primary variable  $\hat{\mathbf{u}}$  are computed. By inserting Eq. (3.115) into Eq. (3.114) and pre-multiplying Eq. (3.114) by  $\mathbf{A}$ , these linearizations are given as

$$\begin{aligned} d\bar{\mathbf{T}} &= \mathbf{A}_{[11]} \cdot \mathbf{A}^{J^{-1}} \cdot \mathcal{A}^C : \mathbb{T} : \mathbb{A}^{-1} : \text{GRAD}\Delta\hat{\mathbf{u}} \\ &\quad - \left( \frac{[\partial_{\bar{\mathbf{T}}}\phi \cdot \mathbf{A}_{[11]} + \partial_{\mathbf{q}}\phi \cdot \mathbf{A}_{[21]}] \cdot \mathbf{A}^{J^{-1}} \cdot \mathcal{A}^C : \mathbb{T} : \mathbb{A}^{-1}}{\nabla\phi^T \mathbf{A} \nabla M} : \text{GRAD}\Delta\hat{\mathbf{u}} \right) \\ &\quad \left( \mathbf{A}_{[11]} \cdot \partial_{\bar{\mathbf{T}}}g + \mathbf{A}_{[12]} \cdot \partial_{\mathbf{q}}h \right) \end{aligned} \quad (3.116)$$

and

$$\begin{aligned} d\mathbf{q} &= \mathbf{A}_{[21]} \cdot \mathbf{A}^{J^{-1}} \cdot \mathcal{A}^C : \mathbb{T} : \mathbb{A}^{-1} : \text{GRAD}\Delta\hat{\mathbf{u}} \\ &\quad - \left( \frac{[\partial_{\bar{\mathbf{T}}}\phi \cdot \mathbf{A}_{[11]} + \partial_{\mathbf{q}}\phi \cdot \mathbf{A}_{[21]}] \cdot \mathbf{A}^{J^{-1}} \cdot \mathcal{A}^C : \mathbb{T} : \mathbb{A}^{-1}}{\nabla\phi^T \mathbf{A} \nabla M} : \text{GRAD}\Delta\hat{\mathbf{u}} \right) \\ &\quad \left( \mathbf{A}_{[21]} \cdot \partial_{\bar{\mathbf{T}}}g + \mathbf{A}_{[22]} \cdot \partial_{\mathbf{q}}h \right). \end{aligned} \quad (3.117)$$

Finally, the linearization of  $\mathbf{J}$  with respect to the primary variable  $\hat{\mathbf{u}}$  is obtained by inserting Eqs. (3.115)-(3.117) into

$$d\mathbf{J} = d\Delta\lambda \partial_{\bar{\mathbf{T}}}g + \Delta\lambda \partial_{\bar{\mathbf{T}} \otimes \bar{\mathbf{T}}}^2 g \cdot d\bar{\mathbf{T}} + \Delta\lambda \partial_{\bar{\mathbf{T}} \otimes \mathbf{q}}^2 g \cdot d\mathbf{q}. \quad (3.118)$$

This leads to

$$d\mathbf{J} = \mathcal{J} : \text{GRAD}\Delta\hat{\mathbf{u}}. \quad (3.119)$$

The third-order tensor  $\mathcal{J}$  is given in the [MOSLER 2005A].

Now, the linearization of  $\bar{\mathbf{F}}$  can be computed. With Eq. (3.119), Eq. (3.111) is re-written as

$$d\bar{\mathbf{F}} = \underbrace{\left[ \mathbb{A}^{-1} - (\mathbb{A}^{-1} \cdot \text{GRAD}\varphi) \cdot \bar{\mathbf{F}} \cdot \mathcal{J} \right]}_{=: \mathbb{P}} : \text{GRAD}\Delta\hat{\mathbf{u}}. \quad (3.120)$$

Hence,  $\mathbb{L}^i$  is obtained as

$$\bar{\mathbf{l}} = \mathbb{L}^i : \text{GRAD}\Delta\hat{\mathbf{u}}_{n+1}, \quad \text{with} \quad \mathbb{L}_{ijkl}^i = \mathbb{P}_{ipkl} \bar{F}_{pj}^{-1}, \quad (3.121)$$

cf. Eq. (3.96). As a consequence, the geometric stiffness matrix results in

$$\mathbf{K}_{\text{geo}}^{IJ} = \mathbf{A} \int_{\Omega^e} \left[ \text{GRAD}N_i \cdot \bar{\mathbf{F}}^{-1} \right] \cdot \boldsymbol{\tau}^{(2)} \mathbb{L}^i \cdot \text{GRAD}N_j dV \quad (3.122)$$

and the material tangent is given as

$$\mathbf{K}_{\text{mat}}^{IJ} = \mathbf{A} \int_{\Omega^e} \left[ \text{GRAD}N_i \cdot \bar{\mathbf{F}}^{-1} \right] \cdot \mathbf{c}^{(2)} \mathbb{L}^i \cdot \text{GRAD}N_j dV \quad (3.123)$$

(compare Eqs. (3.122) and (3.123) to Eqs. (3.98) and (3.99)).

**Remark 3.3.4.1** *In the case of a constant direction of the material displacement jump, i. e., an evolution equation of the type*

$$\dot{\mathbf{J}} = \lambda \mathbf{M}, \quad \text{with} \quad \dot{\mathbf{M}} = \mathbf{0}, \quad (3.124)$$

*together with an isotropic softening response, the algorithmic formulation presented can be significantly simplified, cf. [MOSLER 2005A].*

### 3.3.5 Extension to higher order elements

In Subsections 3.3.2 – 3.3.4, the numerical implementation associated with constant strain elements has been presented. Now, the more general case is discussed. However, since the extensions necessary for higher order elements are relatively straightforward, the respective modifications of the algorithm are described in a brief manner. In the case of linearized kinematics, more details can be found in [MOSLER 2005B].

According to Subsection 3.3.1, for non constant strain elements, the restriction imposed by the weak form of traction continuity across  $\partial_s\Omega$  reads

$$\phi(\text{ave}(\bar{\mathbf{T}}), \mathbf{q}) \leq 0 \quad (3.125)$$

with the average operator  $\text{ave}(\bullet)$  defined by Eq. (3.66). Following the arguments as presented in Subsection 3.2.2, the evolution equations corresponding to the traction-separation law are obtained as

$$\begin{aligned} \dot{\mathbf{J}} &= \lambda \partial_{\text{ave}(\bar{\mathbf{T}})} g \\ \dot{\boldsymbol{\alpha}} &= \lambda \partial_{\mathbf{q}} h. \end{aligned} \quad (3.126)$$

Analogous to the yield function, the two potentials  $g(\text{ave}(\bar{\mathbf{T}}), \mathbf{q})$  and  $h(\text{ave}(\bar{\mathbf{T}}), \mathbf{q})$  depend now on the average stress vector  $\text{ave}(\bar{\mathbf{T}})$ , see [MOSLER 2005B]. Clearly, the identity

$$\text{ave}(\bar{\mathbf{T}}) = \text{ave}(\bar{\mathbf{C}} \cdot \mathbf{S}) \cdot \mathbf{N} \quad (3.127)$$

holds.

Next, the modifications of the kinematics necessary for higher order elements are explained. All finite element formulations based on the strong discontinuity approach are based on the assumption  $\partial \llbracket \mathbf{u} \rrbracket / \partial \mathbf{X} = \mathbf{0}$ , cf. [SIMO & OLIVER 1994; OLIVER 1996; ARMERO & GARIKIPATI 1996; LARRSON & RUNESSON 1996; ARMERO 1999; BORJA 2000; WELLS & SLUYS 2001C; JIRÁSEK & ZIMMERMANN 2001]. This condition is enforced for higher order elements as well. Clearly, instead of describing the kinematics in terms of  $\llbracket \mathbf{u} \rrbracket$  one can alternatively use its material counterpart  $\mathbf{J}$ . In this case, it is canonical to enforce the equivalent constraint  $\partial \mathbf{J} / \partial \mathbf{X} = \mathbf{0}$ . Combining these assumptions and computing the push forward of  $\mathbf{J}$  in an average form, results in the transformation

$$\llbracket \mathbf{u} \rrbracket = \text{ave}(\bar{\mathbf{F}}) \cdot \mathbf{J}. \quad (3.128)$$

A similar argument leading to Eq. (3.128) was recently proposed by [CALLARI & ARMERO 2004]. Using Eq. (3.128), the trial state of the deformation gradient at time  $t_{n+1}$  is computed as

$$\bar{\mathbf{F}}_{n+1}^{\text{tr}} = \mathbf{1} + \text{GRAD} \hat{\mathbf{u}}_{n+1} - \underbrace{\text{ave} \left( \bar{\mathbf{F}}_{n+1}^{\text{tr}} \right) \cdot \mathbf{J}_n \otimes \text{GRAD} \varphi}_{\llbracket \mathbf{u} \rrbracket_{n+1}^{\text{tr}}}, \quad (3.129)$$

compare to Eq. (3.82). From the average counterpart of Eq. (3.129), the average trial deformation gradient is obtained as

$$\text{ave}(\mathbf{F}_{n+1}^{\text{tr}}) = \text{ave}(\mathbb{A})^{-1} : [\mathbf{1} + \text{ave}(\text{GRAD} \hat{\mathbf{u}}_{n+1})], \quad (3.130)$$

with  $\text{ave}(\mathbb{A})$  according to Eq. (3.84) ( $\hat{\mathbf{u}}_{n+1}$  and  $\mathbf{J}_n$  are known). By inserting Eq. (3.130) into Eq. (3.129), the local trial deformation gradient can be computed. As a consequence, the local trial stresses and the discrete loading condition  $\phi(\text{ave}(\bar{\mathbf{T}}_{n+1}^{\text{tr}}, \mathbf{q}_n)$  are well defined. For the neo-HOOKEan hyperelastic material according to Potential (2.30), the average MANDEL stresses are computed as

$$\text{ave}(\bar{\mathbf{C}} \cdot \mathbf{S}) = \lambda \frac{\text{ave}(J^2) - 1}{2} \mathbf{1} + \mu (\text{ave}(\bar{\mathbf{C}}) - \mathbf{1}). \quad (3.131)$$

### 3.3.5.1 Elastic unloading

Clearly, if  $\phi(\text{ave}(\bar{\mathbf{T}}_{n+1}^{\text{tr}}, \mathbf{q}_n) \leq 0$ , the solution corresponding to the trial state is already the final solution. In this case, the residuals  $\mathbf{R}_I$  according to Eq. (3.79) can be computed directly.

Except for the regularly distributed part of the spatial velocity gradient  $\bar{\mathbf{l}}$ , all other variables necessary to obtain the stiffness matrix are known, compare to Eq. (3.91). Hence, the linearization of  $\bar{\mathbf{F}}$  with respect to  $\hat{\mathbf{u}}$  is required. By linearizing Eq. (3.130) and inserting the result into the linearization of Eq. (3.129), the final solution reads

$$d\bar{\mathbf{F}}_{n+1} = \text{GRAD}\Delta\hat{\mathbf{u}}_{n+1} - [\text{ave}(\mathbb{A})^{-1} : \text{ave}(\text{GRAD}\Delta\hat{\mathbf{u}}_{n+1})] \cdot \mathbf{J}_n \otimes \text{GRAD}\varphi. \quad (3.132)$$

### 3.3.5.2 Inelastic loading

If an inelastic load step is signaled by  $\phi(\text{ave}(\bar{\mathbf{T}}_{n+1}^{\text{tr}}, \mathbf{q}_n) > 0$ , a backward-EULER integration is applied to Eqs. (3.126) and the solution of the resulting nonlinear set of algebraic Eqs. (3.105) is computed by means of NEWTON's method. However, in contrast to constant strain elements, the independent variables are now  $\text{ave}(\bar{\mathbf{T}})$ ,  $\mathbf{q}$ ,  $\Delta\lambda$ . Hence, all partial derivatives with respect to  $\bar{\mathbf{T}}$  in Subsection (3.3.3) have to be replaced by derivatives with respect to  $\text{ave}(\bar{\mathbf{T}})$ . Since the potentials  $g$  and  $h$  and the yield function  $\phi$  are formulated in terms of  $\text{ave}(\bar{\mathbf{T}})$  (instead of the local stress vector  $\bar{\mathbf{T}}$ ), these derivatives can be computed easily.

The only significant difference between the return-mapping algorithm for constant strain elements and that for higher order elements results from the linearization of the average traction vector with respect to  $\mathbf{J}$  (instead of  $d\bar{\mathbf{T}} = -\mathbf{A}^{\mathbf{J}} : d\mathbf{J}$ , for constant strain elements). However, since

$$d[\text{ave}(\bar{\mathbf{T}})] = \frac{1}{V^e} \int_{\Omega^e} d(\bar{\mathbf{C}} \cdot \mathbf{S}) \cdot \mathbf{N} dV, \quad (3.133)$$

only the local linearization  $d(\bar{\mathbf{C}} \cdot \mathbf{S})$  is required. Hence, by applying the equations presented in [MOSLER 2005A], the identity

$$d(\bar{\mathbf{C}} \cdot \mathbf{S}) \cdot \mathbf{N} = \mathcal{A}^{\mathbf{C}} : \mathbb{T} : d\bar{\mathbf{F}} \quad (3.134)$$

with  $\mathcal{A}^{\mathbf{C}} = \partial\bar{\mathbf{T}}/\partial\mathbf{C}$  and  $\mathbb{T} = \partial\bar{\mathbf{C}}/\partial\bar{\mathbf{F}}$  is derived. Unfortunately, the linearization of  $\bar{\mathbf{F}}$  with respect to  $\mathbf{J}$  for constant strain elements differs from that for higher order elements. However, linearizing the average counterpart of Eq. (3.129) with respect to  $\mathbf{J}$  (for fixed  $\hat{\mathbf{u}}$ ), leads to

$$d[\text{ave}(\bar{\mathbf{F}})] = -\tilde{\mathcal{G}} \cdot d\mathbf{J}, \quad (3.135)$$

with

$$\tilde{\mathcal{G}} = \text{ave}(\mathbb{A})^{-1} : \tilde{\mathcal{P}}, \quad \tilde{\mathcal{P}}_{ijk} = \text{ave}(\bar{F}_{ik}) \text{ave}(\text{GRAD}\varphi_j) \quad (3.136)$$

(compare to Step 3 in the Appendix of [MOSLER 2005A]). Finally, the linearization of the local deformation gradient with respect to  $\mathbf{J}$  is obtained as

$$d\bar{\mathbf{F}} = (\tilde{\mathcal{G}} \cdot d\mathbf{J}) \cdot \mathbf{J} \otimes \text{GRAD}\varphi - \text{ave}(\bar{\mathbf{F}}) \cdot d\mathbf{J} \otimes \text{GRAD}\varphi =: \hat{\mathcal{G}} \cdot d\mathbf{J}. \quad (3.137)$$

As a consequence, Eq. (3.133) yields

$$d [\text{ave}(\bar{\mathbf{T}})] = \text{ave} \left[ \mathcal{A}^C : \mathbb{T} : \hat{\mathcal{G}} \right] \cdot d\mathbf{J}. \quad (3.138)$$

Now, all linearizations necessary for the return-mapping algorithm have been derived.

**Remark 3.3.5.1** *The computation of the stiffness matrix for higher order elements is not presented in detail in this work. However, all linearizations necessary for that purpose have been given in this subsection.*

**Remark 3.3.5.2** *According to Eq. (3.132), the linearization of a variable with respect to the conforming displacement field  $\hat{\mathbf{u}}$  consists, in general, of two parts. One is associated with the local displacement gradient and one corresponds to its average counterpart. Hence, the resulting stiffness matrix shows a similar decomposition. For linearized kinematics, details can be found in [MOSLER 2004; MOSLER 2005B].*

## 3.4 Computation of the normal vector

In the previous sections, the kinematics as well as the constitutive equations associated with the SDA, together with their implementation, have been presented. However, the topology, or more precisely, the orientation of the surface  $\partial_s\Omega$  has been regarded as known. Hence, in this subsection, the normal vector  $\mathbf{N}$  will be computed.

In the literature, different criteria for the prediction of the formation and the orientation of a surface at which the displacement field or its derivatives are not continuous can be found. Such surfaces are called *singular surfaces*, cf. [FETECAU, MARSDEN & WEST 2003]. In this connection, the order of a singular surface is defined by the lowest order of the derivatives of the deformation map that suffer a non-zero jump across this surface. Hence, discontinuous displacement fields, i. e., strong discontinuities, belong to the set of singular surfaces of order zero. For a singular surface of order one the deformation mapping, i. e., the displacement field, is continuous, but its first-order derivatives (the velocity or the deformation gradient) are discontinuous. In the case of jumps in the field of the deformation gradient, these surfaces are referred to as weak discontinuities. Further details are addressed in [MOSLER 2005C].

The problem discussed in this section is closely related to the classical bifurcation analysis in the sense of [HADAMARD 1903], cf. [RUDNICKI & RICE 1975; RICE 1976; MAIER & HUECKEL 1979; RANIECKI & BRUHNS 1981; MARSDEN & HUGHES 1994]. The questions of interest are: 1.) When does a continuous deformation map bifurcate into a discontinuous one? 2.) What is the orientation of the resulting surface of discontinuous displacements?

In the literature, different methods of resolution can be found. They may be classified according to:

- Energy-based criteria such as the maximum energy release rate criterion suggested by [NUISMER 1975] or the minimum strain-energy density criterion presented by [SIH 1974]. For a modified GRIFFITH's criterion, refer to [FRANCFORT & MARIGO 1998].
- Stress-based criteria such as the maximum circumferential stress criterion proposed by [ERDOGAN & SIH 1963], cf. [MOËS, DOLBOW & BELYTSCHKO 1999], or the maximum principal stress direction, see [WELLS & SLUYS 2001B], [JIRÁSEK & ZIMMERMANN 2001]. These concepts are closely related to linear fracture mechanics.
- Strain-based criteria such as that presented by [GEERS, PEIJS & BREKELMANS 1996] which is based on the direction of maximum accumulation of the non-local equivalent strain, cf. [SIMONE, WELLS & SLUYS 2003].
- Transition from weak to strong discontinuities: [OLIVER 1998; OLIVER, CERVERA & MANZOLI 1999; OLIVER, HUESPE, PULIDO & SAMANIEGO 2003] embedded a weak discontinuity (jump in the strain field) into the respective finite element when the classical bifurcation criterion was fulfilled. By assuming an evolution law for the width of the softening zone, the transition to a strong discontinuity was achieved.
- Bifurcation analysis according to [SIMO, OLIVER & ARMERO 1993; SIMO & OLIVER 1994; OLIVER & SIMO 1994]. In these references, the authors analyzed the condition necessary for a formation of a strong discontinuity in a classical rate-independent (local) continuum.

It should be noted that the given list is not exhaustive. Since this chapter deals exclusively with the formation and propagation of strong discontinuities, the idea proposed by SIMO and co-workers seems to be most canonical. It will be described briefly in the following subsection.

### 3.4.1 Formation of discontinuities in rate independent media

In [SIMO, OLIVER & ARMERO 1993], the authors derived conditions associated with the transition of a continuous deformation mapping into a discontinuous one. The analysis presented in the cited work is restricted to the geometrically linearized theory. For finite strains and arbitrary material symmetries, the generalizations may be found in [MOSLER 2005C]. It will be shown that the equations characterizing the aforementioned transition are formally identical to the LEGENDRE-HADAMARD conditions dating back to the early

20th century, cf. [HADAMARD 1903]. For this reason, the classical conditions are briefly discussed first.

According to [RUDNICKI & RICE 1975; RICE & RUDNICKI 1980; RANIECKI & BRUHNS 1981], the classical localization condition corresponds to the development of weak discontinuities, i. e., the transition of a deformation mapping showing a continuous deformation gradient into one with  $\mathbf{F} \notin \mathcal{C}$  is considered. Consequently, the local deformation at the time of bifurcation is of the type

$$\mathbf{F} \in \mathcal{C}, \quad \dot{\mathbf{F}} \notin \mathcal{C}. \quad (3.139)$$

Assuming  $\dot{\mathbf{F}}$  is only discontinuous on the material surface  $\partial_s \Omega$ , the HADAMARD compatibility condition states that  $\mathbf{F}^+$  and  $\mathbf{F}^-$  defined by Eq. (3.3) have to map all vectors tangent to  $\partial_s \Omega$  into the same spatial vectors. Clearly, this requires

$$\llbracket \dot{\mathbf{F}} \rrbracket = \mathbf{m} \otimes \mathbf{N} \quad (3.140)$$

with  $\mathbf{N}$  denoting the normal vector of  $\partial_s \Omega$  and  $\mathbf{m}$  defines the jump direction, cf. [ORTIZ 2003]. With Eq. (3.140), the equilibrium condition at the interface reads

$$\llbracket \dot{\mathbf{T}} \rrbracket = \dot{\mathbf{T}}^+ - \dot{\mathbf{T}}^- = \left( \dot{\mathbf{P}}^+ - \dot{\mathbf{P}}^- \right) \cdot \mathbf{N} = \underbrace{\left( \mathbf{N} \stackrel{(2)}{\cdot} \mathbb{C}_T \cdot \mathbf{N} \right)}_{=: \mathbf{Q}} \cdot \mathbf{m} = \mathbf{0}. \quad (3.141)$$

Here, the contraction according to Remark 3.3.2.1 has been applied,  $\mathbb{C}_T = d\mathbf{P}/d\mathbf{F}$  and  $\mathbf{Q}$  represents the *acoustic tensor*. Additionally, it has been assumed that  $\llbracket \mathbb{C}_T \rrbracket = \mathbf{0}$ . This constraint is reasonable, since a discontinuity based on the condition  $\llbracket \mathbb{C}_T \rrbracket \neq 0$  cannot form before one with  $\llbracket \mathbb{C}_T \rrbracket = 0$ , [RICE & RUDNICKI 1980]. The non-trivial solution of Eq. (3.141) yields

$$\det \mathbf{Q}(\mathbf{N}) = 0. \quad (3.142)$$

The normal vector  $\mathbf{N}$  follows from the localization condition (3.142). Once  $\mathbf{N}$  is known,  $\mathbf{m}$  can be computed according to

$$\mathbf{m} \in \ker \mathbf{Q}(\mathbf{N}). \quad (3.143)$$

In the case of the bifurcation condition in the sense of [SIMO, OLIVER & ARMERO 1993], the transition of  $\varphi \in \mathcal{C}$  into  $\varphi \notin \mathcal{C}$  is considered (strong discontinuities). Analogous as before, the singular surface where the jump occurs is denoted as  $\partial_s \Omega$ . The crucial observation made by [SIMO, OLIVER & ARMERO 1993] is that the stress vector acting in  $\partial_s \Omega$  is not allowed to be a singular distribution, if traction continuity across  $\partial_s \Omega$  is postulated. This restriction is obvious, since the stresses in  $\Omega^\pm$  result from continuous deformation mappings and hence, they are regular distributions. Following [MOSLER 2005c], this restriction can be written into the format

$$\text{dirac} \left[ \dot{\mathbf{T}}^+ - \dot{\mathbf{T}}^- \Big|_{\partial_s \Omega} \right] = \mathbf{0}, \quad \text{with } \varphi \in \mathcal{C}, \quad \dot{\varphi} \notin \mathcal{C}. \quad (3.144)$$

Here, the DIRAC mapping is defined as

$$\text{dirac} : \begin{array}{ll} (\mathbb{R}^3)^\Omega & \rightarrow (\mathbb{R}^3)^\Omega \\ \mathbf{f} & \mapsto \chi_{\mathcal{DIR}} \mathbf{f} \end{array} \quad (3.145)$$

and  $\chi_{\mathcal{DIR}}$  represents the characteristic mapping of the set of singular distributions, cf. [MOSLER 2005C]. Note that condition (3.144) and (3.141) look formally identical, although they are associated with different physical problems. Clearly, since  $\mathbf{T}^+$  is regularly distributed, Eq. (3.144) is equivalent to  $\text{dirac}[\dot{\mathbf{T}}|_{\partial_s\Omega}] = \mathbf{0}$ .

The computation of the condition  $\text{dirac}[\dot{\mathbf{T}}|_{\partial_s\Omega}] = \mathbf{0}$  depends, apparently, on the material model considered. In [MOSLER 2005C], a GREEN-NAGHDI-type finite strain plasticity theory (cf. page 26) allowing for the modeling of arbitrary material symmetries is considered. For the derivation of the localization condition the following properties are of utmost importance:

- At the time of bifurcation,  $\text{dirac}[\dot{\mathbf{F}}] = \llbracket \dot{\mathbf{u}} \rrbracket \otimes \mathbf{N} \delta_s$ , cf. Eq. (3.9).
- The internal stress-like variables are bounded and hence,  $\text{dirac}[\mathbf{Q}] = \mathbf{0}$ .
- In the case of plasticity theories formulated in stress space,  $\phi$  is stress-like and consequently,  $\text{dirac}[\dot{\phi}] = 0$ .

Without going too much into detail, the enumerated properties require the plastic multiplier to be a singular distribution, i. e.,  $\text{dirac}[\lambda] \neq 0$ . It should be noted that the regularly distributed part of  $\lambda$  is not important for the bifurcation analysis. More precisely, the assumption that the regular part of  $\lambda$  is zero, as postulated in [SIMO, OLIVER & ARMERO 1993], is not necessary, cf. [MOSLER 2005C]. Inserting the singular part of the plastic multiplier into Eq. (3.144) leads finally to the localization condition

$$\mathbf{Q}^{\text{perf}}(\mathbf{N}) \cdot \llbracket \mathbf{u} \rrbracket = \mathbf{0}, \quad \text{with} \quad \mathbf{Q}^{\text{perf}}(\mathbf{N}) = \mathbf{N} \overset{(2)}{\cdot} \mathbb{C}_T^{\text{perf}} \cdot \mathbf{N}. \quad (3.146)$$

Here  $\mathbf{Q}^{\text{perf}}$  denotes the acoustic tensor corresponding to the perfect plastic material. Further details are omitted. They are contained in [MOSLER 2005C]. Analogous to the classical LEGENDRE-HADAMARD condition, the non-trivial solution of Eq. (3.146) gives rise to

$$\det \mathbf{Q}^{\text{perf}}(\mathbf{N}) = 0. \quad (3.147)$$

Interestingly, condition (3.147) is formally identical to the classical one (3.142). However, it depends now on the tangent  $\mathbb{C}_T^{\text{perf}}$  of the perfect plastic material.

**Remark 3.4.1.1** *According to [ORTIZ 1987; ORTIZ, LEROY & NEEDLEMAN 1987], a condition of the type (3.142) or (3.147) is not well-suited for computational purpose. In fact, it is more appropriate to consider the optimization problem*

$$\mathbf{N} = \arg \left( \min_{\mathbf{N}} \det \mathbf{Q}(\mathbf{N}) \right) \quad (3.148)$$

under the constraints

$$\det \mathbf{Q} \leq 0 \quad \wedge \quad \|\mathbf{N}\|_2 = 1. \quad (3.149)$$

**Remark 3.4.1.2** *Non-local criteria for the prediction of the normal vector  $\mathbf{N}$  as applied for instance in [FEIST & HOFSTETTER 2005] are not considered in this work. Although they seem to give often good numerical results, they can lead to a completely unphysical initiation and propagation of failure, cf. [SIMONE, ASKES & SLUYS 2004].*

### 3.4.2 Uniqueness of the solution

Based on the localization criterion presented in the previous subsection, or one of the methods enumerated on page 77, the normal vector of  $\partial_s \Omega$  can be computed. However, in general, the solution concerned with  $\det \mathbf{Q}(\mathbf{N}) = 0$  or a similar concept is not unique. Consequently, it is convenient to introduce the set of all candidates

$$\mathbb{J}_{\mathbf{N}} := \{ \mathbf{N} \in \mathcal{S}^2 \mid 0 \geq \det \mathbf{Q}(\mathbf{N}) \leq \det \mathbf{Q}(\mathbf{N}^*), \forall \mathbf{N}^* \in \mathcal{S}^2 \} \quad (3.150)$$

with  $\mathcal{S}^2$  being the 2-sphere. Even if load cases which are invariant with respect to a rotation applied to special axes such as uniaxial stress states or hydrostatic stress states are neglected, not any element of  $\mathbb{J}_{\mathbf{N}}$  has a physical relevance (see [SIMO & OLIVER 1994; BORJA 2000]). Hence, the "correct" bifurcation mode has to be chosen from  $\mathbb{J}_{\mathbf{N}}$ . For that purpose, different solution strategies have been developed.

For instance, restricting to the geometrically linearized plane strain state, together with an associative VON MISES plasticity theory, condition (3.147) applied to a simple shear deformation, i. e.,  $\mathbf{u} = u_1 X_2 \mathbf{e}_1$  and  $\boldsymbol{\sigma} = \sigma_{12} (\mathbf{e}_1 \otimes \mathbf{e}_2 + \mathbf{e}_2 \otimes \mathbf{e}_1)$ , yields  $\mathbb{J}_{\mathbf{N}} = \{\mathbf{e}_1, \mathbf{e}_2\}$ . However, according to the displacement field, only  $\mathbf{e}_2$  is admissible, cf. [BORJA 2000].

In this chapter, only local criteria for determining the "correct" vector  $\mathbf{N} \in \mathbb{J}_{\mathbf{N}}$  are considered. They are in contrast to methods based on geometrical smoothing techniques such as [GARIKIPATI 1996; GASSER & HOLZAPFEL 2006]. Most frequently, the following local criteria are applied, cf. [MOSLER 2005C]:

- In [ARMERO & GARIKIPATI 1996; GARIKIPATI 1996; BORJA 2000], the vector  $\mathbf{N}$  which results in a failure mode more closely aligned with the smooth deformation field is chosen. Locally, this idea can be re-written into the format (at the onset of bifurcation  $\mathbf{F} = \bar{\mathbf{F}} = \hat{\mathbf{F}}$ , see Eq. (3.18))

$$\mathbf{N} = \arg \max_{\tilde{\mathbf{N}}} [\mathbf{F} : (\mathbf{m} \otimes \tilde{\mathbf{N}})] \quad (3.151)$$

with  $\mathbf{m}$  denoting the jump direction fulfilling  $\mathbf{m} \in \ker \mathbf{Q}^{\text{perf}}$  and  $\|\mathbf{m}\|_2 = 1$ .

- In [WELLS & SLUYS 2001A], the criterion

$$\mathbf{N} = \arg \max_{\tilde{\mathbf{N}}} \left\| \left[ \dot{\mathbf{u}}(\tilde{\mathbf{N}}) \right] \right\|_2 \quad (3.152)$$

has been applied. Hence, the vector  $\mathbf{N}$  maximizing the inelastic deformations is chosen.

- $\mathbf{N}$  follows from the principle of maximum dissipation

$$\mathbf{N} = \arg \max_{\tilde{\mathbf{N}}} \mathcal{D}(\tilde{\mathbf{N}}), \quad (3.153)$$

cf. [MOSLER 2005C].

In what follows, it will be shown that the enumerated criteria are equivalent for many different material models. The next paragraph follows to a large extent [MOSLER 2005C].

First, the straightforward equivalence between criteria (3.152) and (3.153) is pointed out. Clearly, the proof requires the evolution equations of the internal variables and the displacement jump to be governed by the postulate of maximum dissipation. Assuming a cohesive law defined by a free HELMHOLTZ energy of the type (3.40) and a yield function according to Eq. (3.49) depending on a positively homogeneous yield function  $\phi$  of degree one, the dissipation reads

$$\mathcal{D} = \lambda \bar{T}_{\text{eq}}^{\text{ini}} \delta_s \quad (3.154)$$

cf. Remark. (3.2.2.2). Since the plastic multiplier represents a measure for the amount of plastic deformations and

$$\lambda(\mathbf{N}) \geq \lambda(\tilde{\mathbf{N}}) \quad \Leftrightarrow \quad \mathcal{D}(\mathbf{N}) \geq \mathcal{D}(\tilde{\mathbf{N}}) \quad \forall \tilde{\mathbf{N}} \in \mathbb{J}_{\mathbf{N}}. \quad (3.155)$$

the equivalence between criteria (3.152) and (3.153) follows directly.

Next, it is shown that  $\mathbf{N}$  predicted by the compatibility condition (3.151) is identical to the one obtained from the postulate of maximum dissipation. Again, associative evolution equation and a positively homogeneous yield function of degree one are considered. Since Eqs. (3.152) and (3.153) are rate equations, but Eq. (3.151) does not involve a time derivative, the different criteria cannot be compared directly to each other. For this reason, the discrete counterparts induced by a time integration are analyzed.

Assuming a sufficiently small load step, principle (3.153) can be re-written as

$$\phi^{\text{tr}}((\bar{\mathbf{C}} \cdot \mathbf{S}) \cdot \mathbf{N}, (\mathbf{J}, \boldsymbol{\alpha}) = \mathbf{0})|_{n+1} \geq \phi^{\text{tr}}((\bar{\mathbf{C}} \cdot \mathbf{S}) \cdot \tilde{\mathbf{N}}, (\mathbf{J}, \boldsymbol{\alpha}) = \mathbf{0})|_{n+1}, \quad \forall \tilde{\mathbf{N}} \in \mathbb{J}_{\mathbf{N}} \quad (3.156)$$

( $\phi^{\text{tr}} \leq 0$  implies a zero dissipation). Since the stress-like internal variables are zero before the deformation localizes, Ineq. (3.156) is equivalent to

$$\bar{T}_{\text{eq}}^{\text{tr}}((\bar{\mathbf{C}} \cdot \mathbf{S}) \cdot \mathbf{N}, (\mathbf{J}, \boldsymbol{\alpha}) = \mathbf{0})|_{n+1} \geq \bar{T}_{\text{eq}}^{\text{tr}}((\bar{\mathbf{C}} \cdot \mathbf{S}) \cdot \tilde{\mathbf{N}}, (\mathbf{J}, \boldsymbol{\alpha}) = \mathbf{0})|_{n+1}, \quad \forall \tilde{\mathbf{N}} \in \mathbb{J}_{\mathbf{N}}, \quad (3.157)$$

cf. Remark. (3.2.2.2). With  $\bar{T}_{\text{eq}}$  being a positively homogeneous function of degree one, Ineq. (3.157) reads

$$(\bar{\mathbf{C}} \cdot \mathbf{S}) : (\mathbf{M} \otimes \mathbf{N})|_{n+1} \geq (\bar{\mathbf{C}} \cdot \mathbf{S}) : (\tilde{\mathbf{M}} \otimes \tilde{\mathbf{N}})|_{n+1}, \quad \forall \tilde{\mathbf{N}} \in \mathbb{J}_{\mathbf{N}}, \quad (3.158)$$

Here,  $\mathbf{M}$  denotes the flow direction, i. e.,  $\mathbf{M} = \partial_{\mathbf{T}}\phi$ . Applying a pull back to Eq. (3.151), the equivalence between criterion (3.151) and the one based on the principle of maximum dissipation (3.153) simplifies to

$$\begin{aligned} & (\bar{\mathbf{C}} \cdot \mathbf{S}) : (\mathbf{M} \otimes \mathbf{N})|_{n+1} \geq (\bar{\mathbf{C}} \cdot \mathbf{S}) : (\tilde{\mathbf{M}} \otimes \tilde{\mathbf{N}})|_{n+1} \\ \iff & \bar{\mathbf{C}} : (\mathbf{M} \otimes \mathbf{N})|_{n+1} \geq \bar{\mathbf{C}} : (\tilde{\mathbf{M}} \otimes \tilde{\mathbf{N}})|_{n+1}. \end{aligned} \quad (3.159)$$

Obviously, those inequalities are not equivalent for arbitrary material symmetries. More precisely, a comparison between the deformation-based criterion (3.151) and the stress-based criterion (3.157) makes only sense for isotropic materials. In this case, the elastic part of the energy  $\Psi_{\text{reg}}$  depends only on the invariants of  $\bar{\mathbf{C}}$  denoted as  $I_i$  and the MANDEL stresses show the form

$$\bar{\mathbf{C}} \cdot \mathbf{S} = 2 \bar{\mathbf{C}} \cdot \partial_{\bar{\mathbf{C}}} \Psi_{\text{reg}} = 2 \left[ \frac{\partial \Psi_{\text{reg}}}{\partial I_1} + \frac{\partial \Psi_{\text{reg}}}{\partial I_2} I_1 \right] \bar{\mathbf{C}} - 2 \frac{\partial \Psi_{\text{reg}}}{\partial I_2} \bar{\mathbf{C}}^2 + 2 \frac{\partial \Psi_{\text{reg}}}{\partial I_3} I_3 \mathbf{1}. \quad (3.160)$$

Additionally, it is assumed that  $\Psi_{\text{ref}}$  is independent of the second invariant of  $\bar{\mathbf{C}}$ . This restriction is fulfilled for many materials. For instance, neo-HOOKE-type material models which will be applied in Section 3.6 are characterized by this assumption, cf. [CIARLET 1988; BAŞAR & WEICHERT 2000]. Using this postulate, the equivalence (3.159) reduces to

$$\begin{aligned} & \left[ \frac{\partial \Psi_{\text{reg}}}{\partial I_1} \bar{\mathbf{C}} + \frac{\partial \Psi_{\text{reg}}}{\partial I_3} I_3 \mathbf{1} \right] : (\mathbf{M} \otimes \mathbf{N}) \geq \left[ \frac{\partial \Psi_{\text{reg}}}{\partial I_1} \bar{\mathbf{C}} + \frac{\partial \Psi_{\text{reg}}}{\partial I_3} I_3 \mathbf{1} \right] : (\tilde{\mathbf{M}} \otimes \tilde{\mathbf{N}}) \\ \iff & \bar{\mathbf{C}} : (\mathbf{M} \otimes \mathbf{N})|_{n+1} \geq \bar{\mathbf{C}} : (\tilde{\mathbf{M}} \otimes \tilde{\mathbf{N}})|_{n+1}. \end{aligned} \quad (3.161)$$

Since all vectors  $\mathbf{N} \in \mathbb{J}_{\mathbf{N}}$  show the same localization mode characterized by the absolute value  $|\mathbf{N} \cdot \mathbf{M}|$  (if  $\mathbf{M}$  is normalized,  $|\mathbf{N} \cdot \mathbf{M}| = 1 \Leftrightarrow$  mode-I failure,  $|\mathbf{N} \cdot \mathbf{M}| = 0 \Leftrightarrow$  mode-II failure and  $|\mathbf{N} \cdot \mathbf{M}| \in (0, 1) \Leftrightarrow$  mixed-mode failure), without loss of generality,

$$\mathbf{N} \cdot \mathbf{M} = \tilde{\mathbf{N}} \cdot \tilde{\mathbf{M}}. \quad (3.162)$$

Applying Eq. (3.162), the equivalence (3.161) requires

$$\frac{\partial \Psi_{\text{reg}}}{\partial I_1} \geq 0. \quad (3.163)$$

For isotropic material laws depending only on the first and the third invariant of  $\bar{\mathbf{C}}$ , Ineq. (3.163) is a direct consequence of the so-called *empirical inequalities*, cf. [WANG & TRUESDELL 1973; TRUESDELL & NOLL 1965] (see also Remark 3.4.2.1). In summary, for isotropic elastic materials invariant with respect to  $I_2$ , together with associative evolution equations designed by means of a positively homogeneous yield function of degree one, the criteria (3.151)-(3.153) are equivalent.

**Remark 3.4.2.1** *The empirical inequalities state that*

$$\psi_0 \leq 0, \quad \psi_1 > 0, \quad \psi_{-1} \leq 0. \quad (3.164)$$

Here,  $\psi_i$  depending on the invariants of  $\bar{\mathbf{C}}$  defines the response function of the CAUCHY stresses, i. e.,

$$\boldsymbol{\sigma} = \psi_0 \mathbf{1} + \psi_1 \bar{\mathbf{b}} + \psi_{-1} \bar{\mathbf{b}}^{-1}, \quad \text{with } \bar{\mathbf{b}} := \bar{\mathbf{F}} \cdot \bar{\mathbf{F}}^T. \quad (3.165)$$

According to [WANG & TRUESDELL 1973; TRUESDELL & NOLL 1965], Ineqs. (3.164) imply the so-called ordered forces inequalities as well as the BAKER-ERICKSEN inequalities. It can be shown in a relatively straightforward manner that for materials invariant with respect to the second invariant of  $\bar{\mathbf{C}}$ ,

$$\psi_1 > 0 \iff \frac{\partial \Psi_{\text{reg}}}{\partial I_1} > 0. \quad (3.166)$$

### 3.5 Computation of the topology of the singular surface $\partial_s\Omega$

The methods described in the previous sections can be applied to compute the topology of the singular surface  $\partial_s\Omega$ . More precisely, only the local topology, namely the normal vector  $\mathbf{N}$ , is predicted. However, if  $\partial_s\Omega$  is to be modeled continuously as necessary in the case of numerical analyses of cracks, the position of  $\partial_s\Omega$  is required additionally. Unfortunately, this is not a trivial issue. For instance, if constant strain finite elements are used, the strain and the resulting stress fields are constant within the elements and hence, a local criterion cannot define the position of  $\partial_s\Omega$ .

It should be pointed out that enforcing continuity of the singular surface  $\partial_s\Omega$  is essential for computations being almost independent with respect to the mesh bias, cf. [JIRÁSEK & ZIMMERMANN 2001; OLIVER, HUESPE, SAMANIEGO & CHAVES 2002; FEIST & HOFSTETTER 2005]. Without enforcing continuity, the results obtained from SDAs are almost identical to those predicted by standard smeared crack models, see [MOSLER & MESCHKE 2004].

Several different methods for computing the global topology of  $\partial_s\Omega$  can be found in the literature. Conceptually, they can be grouped into the following two types of approaches:

- When localization is detected, the normal vector  $\mathbf{N}$  of a singular surface  $\partial_s\Omega$  is computed first. If no neighboring finite elements are localized,  $\partial_s\Omega$  is assumed to cross the centroid of the respective element. On the other side, if a slip band has already formed in one of the neighboring elements, the new band  $\partial_s\Omega$  is connected with the existing one, cf. [OLIVER 1996; GARIKIPATI 1996; BORJA 2000]. The method just described is applied most frequently. It should be noted that the

extension of this band tracking algorithm to the fully three-dimensional case is, in general, not trivial. If  $\partial_s\Omega$  is assumed to propagate element-wise (the tip of  $\partial_s\Omega$  is restricted to the element boundary), the cut set of a planar localization surface  $\partial_s\Omega$  and one surface of a three-dimensional finite element (linear approximation of the geometry) is represented by a straight line. Consequently, in general, it is impossible to connect two neighboring surfaces  $\partial_s\Omega$  in a continuous fashion (at this cut set). For this reason, some authors propose to apply smoothing techniques, cf. [GASSER & HOLZAPFEL 2006].

- Global band tracking algorithms according to OLIVER and co-workers, cf. [OLIVER, HUESPE, SAMANIEGO & CHAVES 2002; CHAVES 2003]. Conceptually speaking, OLIVER suggests to compute the solution of an auxiliary PDE. This PDE is designed such that the isolines of its primary, scalar-valued, variable define possible globally continuous localization surfaces. Since  $\partial_s\Omega$  may change each load step, the solution of the auxiliary PDE has to be determined every step as well. Hence, the resulting numerical costs are relatively high. For this reason, [FEIST & HOFSTETTER 2005] suggested to apply OLIVER's method to certain neighborhoods (close to the tip of  $\partial_s\Omega$ ).

Although some of the described algorithms sound promising, complex failure modes such as crack branching and multiple cracks crossing each other cannot be modeled yet. Very recently, a new class of algorithms has been proposed, [NEGRI 2005B; MOSLER, ORTIZ & PANDOLFI 2006]. It will be presented in a more detailed way in Chapter 7.2. Here, only a short description is given. Different from the two approaches discussed before, the novel numerical formulation can be applied, in principle, to arbitrarily complex problems.

In contrast to the numerical models discussed in this chapter, the novel method according to [NEGRI 2005B; MOSLER, ORTIZ & PANDOLFI 2006] is based on interface elements, cf. page 49. The overriding principle of this approach is energy minimization. More precisely, assuming the physical problem is governed by the postulate of maximum dissipation, an incremental potential  $I$  can be derived such that the continuous and the discontinuous displacement field follow from a minimization problem, i. e.,

$$(\hat{\mathbf{u}}, \llbracket \mathbf{u} \rrbracket) = \arg \inf_{\hat{\mathbf{u}}, \llbracket \mathbf{u} \rrbracket} I(\hat{\mathbf{u}}, \llbracket \mathbf{u} \rrbracket), \quad (3.167)$$

cf. Section 2.5. Such a method has been applied for instance in [YANG, MOTA & ORTIZ 2005]. Evidently, the solution associated with problem (3.167) depends on the topology of  $\partial_s\Omega$ . As a consequence, a canonical extension of the problem (3.167) yields

$$(\hat{\mathbf{u}}, \llbracket \mathbf{u} \rrbracket, \partial_s\Omega) = \arg \inf_{\hat{\mathbf{u}}, \llbracket \mathbf{u} \rrbracket, \partial_s\Omega} I(\hat{\mathbf{u}}, \llbracket \mathbf{u} \rrbracket, \partial_s\Omega). \quad (3.168)$$

It is obvious that by thermodynamical considerations,  $\partial_s\Omega$  is not allowed to shrink, i. e.,  $\partial_s\Omega|_{t_n} \subseteq \partial_s\Omega|_{t_{n+1}}$ . An approximation of problem (3.168) can be found in [NEGRI 2005B;

MOSLER, ORTIZ & PANDOLFI 2006]. For instance in [MOSLER, ORTIZ & PANDOLFI 2006] the authors optimize the mesh in order to capture the crack path better by applying variational mesh adaptations as presented in Chapters 4 – 6. Further details will be given in Chapter 7.2.

## 3.6 Numerical examples

The applicability and performance of the strong discontinuity approach as proposed in the previous sections are investigated by means of a 2D as well as by two different 3D numerical analyses. While in Subsection 3.6.1, a steel made strip with a hole is analyzed numerically, a uniaxial tension test is investigated in Subsection 3.6.2.1. Again, a ductile material model is applied. Finally, a debinding problem is computed in Subsection 3.6.2.2. In contrast to the other examples, the interface problem is characterized by mode-I failure.

In the numerical examples presented in this section, continuity of  $\partial_s \Omega$  is enforced by applying the purely geometrical procedure as adopted by [OLIVER 1996; GARIKIPATI 1996; BORJA 2000], cf. page 83. If the localization criterion leads to more than one admissible vector  $\mathbf{N}$ , the physically relevant one is determined by means of the postulate of maximum dissipation (see criterion (3.153)).

### 3.6.1 Two-dimensional problem:

#### Extension of a strip with a circular hole

In this section, the extension of the SDA to higher order elements as described in Section 3.3.5 is shown. As a prototype, a 4-node, purely displacement-based, plane stress element is used. This element is analyzed by a numerical computation of the extension of a steel made strip with a circular hole (see Fig. 3.3). A similar problem has been investigated numerically by several authors, see e. g. [SIMO & HUGHES 1998]. For the modeling of slip bands in ductile materials, the VON MISES yield function according to Eq. (3.50) is adopted. A shear band is assumed to propagate, when the condition  $\phi > 0$  (a loading step) is fulfilled.

To demonstrate the independence of the numerically computed results on the spatial discretization, three different finite element meshes are used. According to Fig. 3.4, mesh I and mesh II are aligned with the expected slip band path. They contain 192 and 834 4-node plane stress elements, respectively. In addition to these meshes, an unstructured discretization (mesh III) is considered as well. It has been designed automatically by applying an overlay procedure and consists of 176 elements. It is noteworthy that the stress field associated with the problem illustrated in Fig. 3.3 is highly inhomogeneous even in the elastic regime. As a consequence, no imperfections are necessary to activate

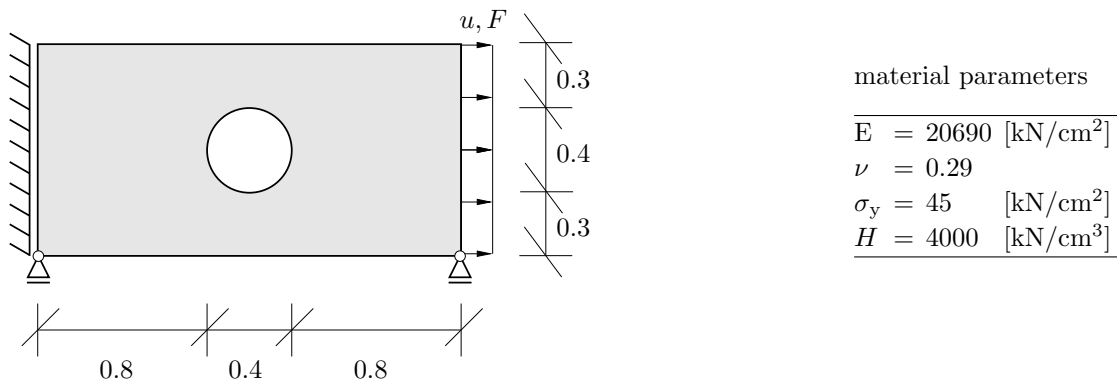


**Figure 3.3:** Numerical study of the extension of a strip with a circular hole: dimensions (in [cm]) and material parameters; thickness of the strip  $t = 0.1$  cm

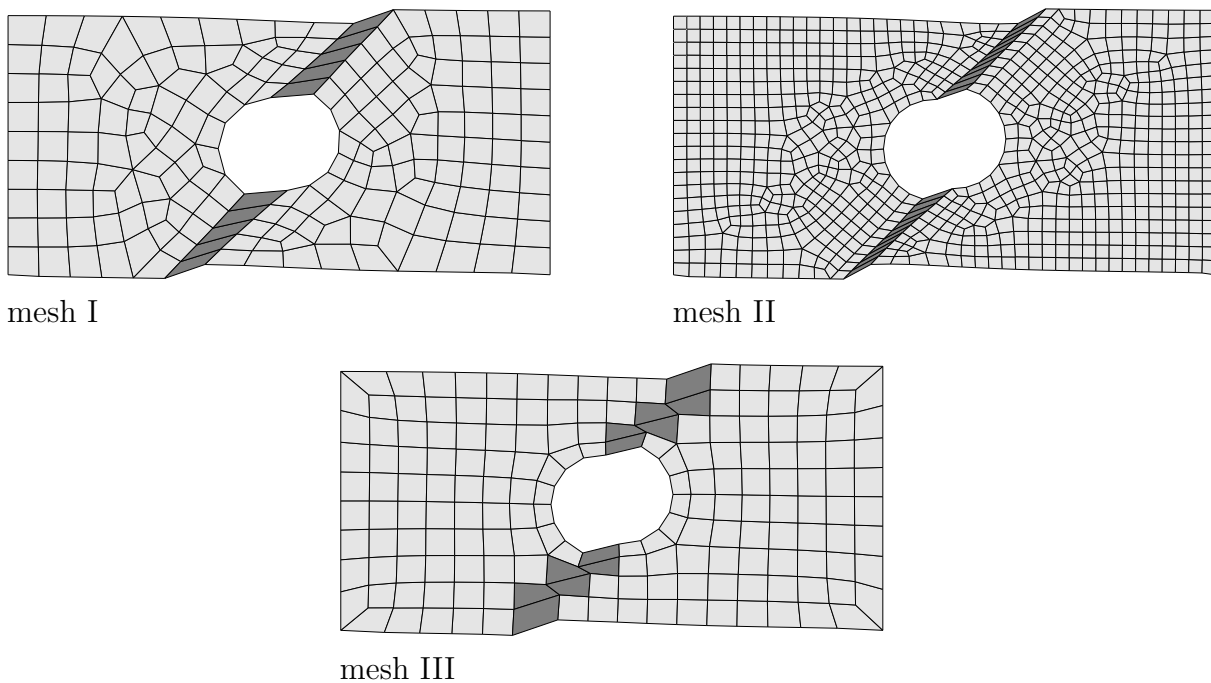


**Figure 3.4:** Numerical study of the extension of a strip with a circular hole: distribution of the internal variable  $\alpha$  representing the relative shear sliding displacement as obtained from discretizations mesh I-III (8-fold magnifications of displacements)

localization. Since the resulting deformations are, as it will be shown, relatively small, linearized kinematics are used.

In Fig. 3.4, the distribution of the internal variable  $\alpha$  representing the relative shear sliding displacement obtained from the numerical analyses is illustrated. The plots are associated with a displacement  $u$  of magnitude  $u = 0.008835$  cm. As expected, the slip bands computed are almost completely independent of the spatial discretization. The

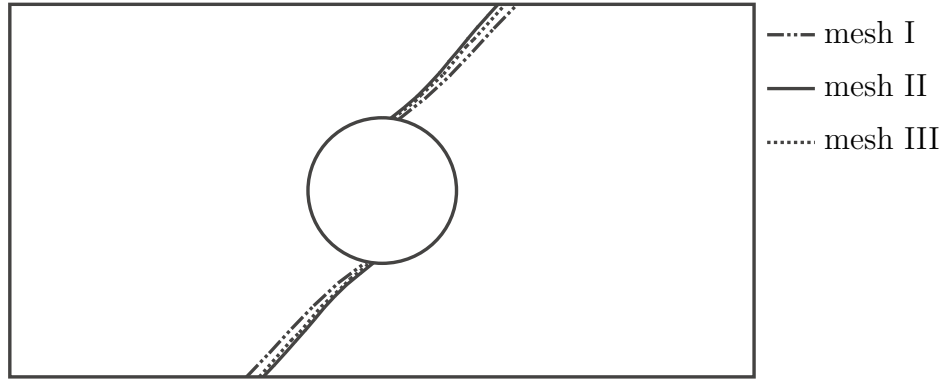


**Figure 3.5:** Numerical study of the extension of a strip with a circular hole: topology of the primary slip band as computed from discretizations mesh I-III

angle between these bands and the horizontal is about  $45^\circ$ . It should be noted that in Fig. 3.4 only the primary slip bands are shown. Secondary bands, i. e., those exhibiting a relative shear sliding displacement several orders of magnitude less than that of the primary localization surfaces are not presented.

Although the topology of the slip bands computed numerically can be estimated by means of Fig. 3.4, a more precise analysis of the topology is not realizable. For a more detailed investigation, the primary localization surfaces are illustrated in Fig. 3.5. As expected from Fig. 3.4, the slip bands obtained from the finite element analyses based on mesh I-III are almost identical. They are nearly independent of the size of the finite elements and the bias induced by the discretization. According to Fig. 3.5, the slip band orientations are not constant. They vary between  $\theta \in [37.44^\circ, 47.55^\circ]$ ,  $\theta \in [38.74^\circ - 49.71^\circ]$  and  $\theta \in [38.67^\circ, 51.25^\circ]$  for meshes I, II and III, respectively. Here,  $\theta$  denotes the angle between the slip band and the horizontal. The slip bands start to form at the hole under a relatively small angle  $\theta$ . If loading is further increased, these bands propagate. At the same time, the angle  $\theta$  at the tip of the band increases. After reaching the maximum value,  $\theta$  decreases in the vicinity of the upper and the lower boundary of the strip. Consequently, the slip bands computed numerically are slightly curved.

The load-displacement diagrams computed from the numerical analyses are shown in Fig. 3.6. Each of the three discretizations predicts an almost identical structural response. According to Fig. 3.6, a maximum loading of  $F_{\max} = 5.36$  kN,  $F_{\max} = 5.27$  kN and  $F_{\max} = 5.44$  kN is obtained from meshes I-III. By comparing the load-displacement curves to that of the linear solution, it is seen that localization is activated significantly before the maximum loading  $F_{\max}$  is reached. Not until the slip band separates the steel made strip completely, an overall softening response is observed. However, the differences between the post-peak behavior computed from meshes I-III are marginal.

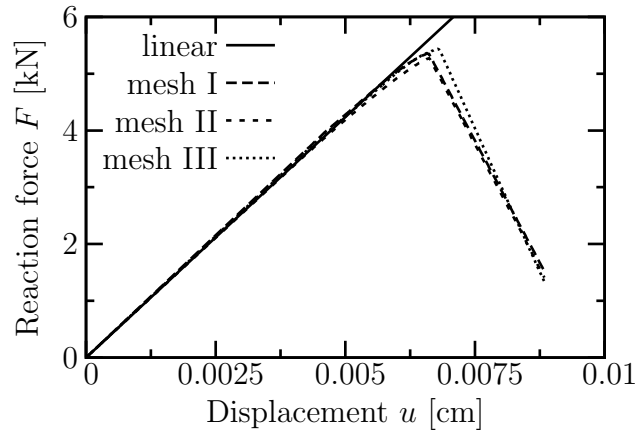
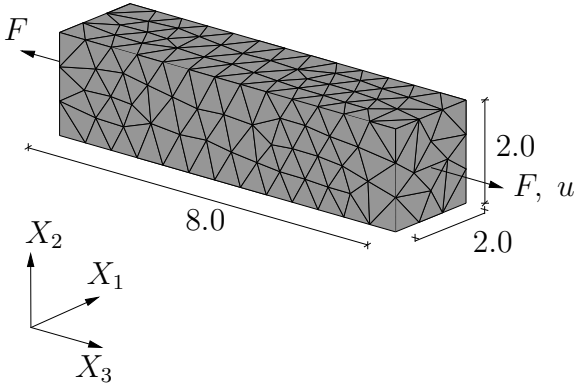


**Figure 3.6:** Numerical study of the extension of a strip with a circular hole: load-displacement diagrams as computed from discretizations mesh I-III

### 3.6.2 Three-dimensional problems using geometrically exact kinematics

Next, the applicability of the novel finite element formulation and its numerical performance are investigated by means of fully three-dimensional examples. In contrast to the previous subsection, a geometrically exact theory is used.

To the best knowledge of the author, two different benchmarks are most frequently applied to the analysis of strong discontinuity approaches at finite strains: the uniaxial tension or compression test as studied in [GARIKIPATI 1996; ARMERO & GARIKIPATI 1996; LARSSON, STEINMANN & RUNESSON 1998; ARMERO 1999; BORJA 2002] or a mode-I type debinding problem, cf. [OLIVER, HUESPE, PULIDO & SAMANIEGO 2003; GASSER & HOLZAPFEL 2003]. For the fully three-dimensional case, only one numerical analysis based on the SDA at finite strains has been presented in [GASSER & HOLZAPFEL 2003] so far. Both numerical examples, that is, the uniaxial tension/compression test as well as the mode-I type debinding problem are relatively simple. However, they are reasonable and meaningful for the analysis of the numerical model. The reasons for this are manifold. First, even in the case of the uniaxial compression or tension test, the stress field computed is inhomogeneous due to the initial imperfection set to activate localization. Thus, the localization surface  $\partial_s\Omega$  does not form at once, but an evolution of  $\partial_s\Omega$  during the numerical analysis can be observed. However, the most important property of these benchmarks is that the topology of the localization surface can be computed analytically. Furthermore, if an additional assumption concerning the activation of  $\partial_s\Omega$  is made, the complete structural response, i. e., the load-displacement curve, can be calculated analytically as well. Consequently, the results obtained numerically can be compared to the analytical solution. Particularly, for the uniaxial tension/compression test the analytical solution can be computed very easily. As a result, the applicability and the performance of the finite element formulation proposed will be demonstrated by means of the uniaxial



material parameters

|            |           |                           |
|------------|-----------|---------------------------|
| $E$        | $= 20690$ | $[\text{kN}/\text{cm}^2]$ |
| $\nu$      | $= 0.29$  |                           |
| $\sigma_y$ | $= 45$    | $[\text{kN}/\text{cm}^2]$ |
| $H$        | $= 200$   | $[\text{kN}/\text{cm}^3]$ |

**Figure 3.7:** Numerical study of the tension test: dimensions (in [cm]) and material parameters

tension test and the debinding problem.

### 3.6.2.1 Uniaxial tensile test of a ductile bar

In this paragraph, the formation and propagation of shear bands occurring in a steel made bar are analyzed numerically. The geometry is illustrated in Fig. 3.7. The bar is subjected to a prescribed displacement field  $u$  at its face side. Other boundary conditions are chosen such that stresses occur only in one direction (uniaxial tension test).

For the analysis of slip band formation in ductile materials, a VON MISES-type yield function

$$\phi(\bar{\mathbf{T}}, q) = \|\bar{\mathbf{T}}_m\|_2 - q(\alpha), \quad \text{with} \quad \bar{\mathbf{T}}_m := \bar{\mathbf{T}} - [\bar{\mathbf{T}} \cdot \mathbf{N}] \mathbf{N} \quad (3.169)$$

is adopted, i. e., only the shear stresses  $\bar{\mathbf{T}}_m$  govern the evolution of the slip sliding displacements. Following the postulate of maximum dissipation, associative evolution equations are assumed. According to Eq. (3.169), the softening response characterized by the internal variable  $q$  is modeled as isotropic. Analogous to [GARIKIPATI 1996; ARMERO & GARIKIPATI 1996; ARMERO 1999], a linear evolution of  $q$  of the type

$$q(\alpha) = \sigma_y - H \alpha \quad (3.170)$$

is chosen. In the case of linearized kinematics, the three-dimensional VON MISES-type model described was proposed in [MOSLER 2005B]. In this reference, further details concerning this specific model are available. The bulk material is modeled by applying a hyperelastic material law. The respective free energy functional is given in Eq. (2.30).

The model is completed by a criterion necessary for the computation of the normal vector  $\mathbf{N}$  of the localization surface. For that purpose, it assumed that the angle between the vector  $\mathbf{N}$  and the direction of the maximum principle stress at the time of localization is about  $45^\circ$ . This represents a widely accepted criterion, cf. [GARIKIPATI 1996; ARMERO & GARIKIPATI 1996]. In the case of linearized kinematics, it follows from

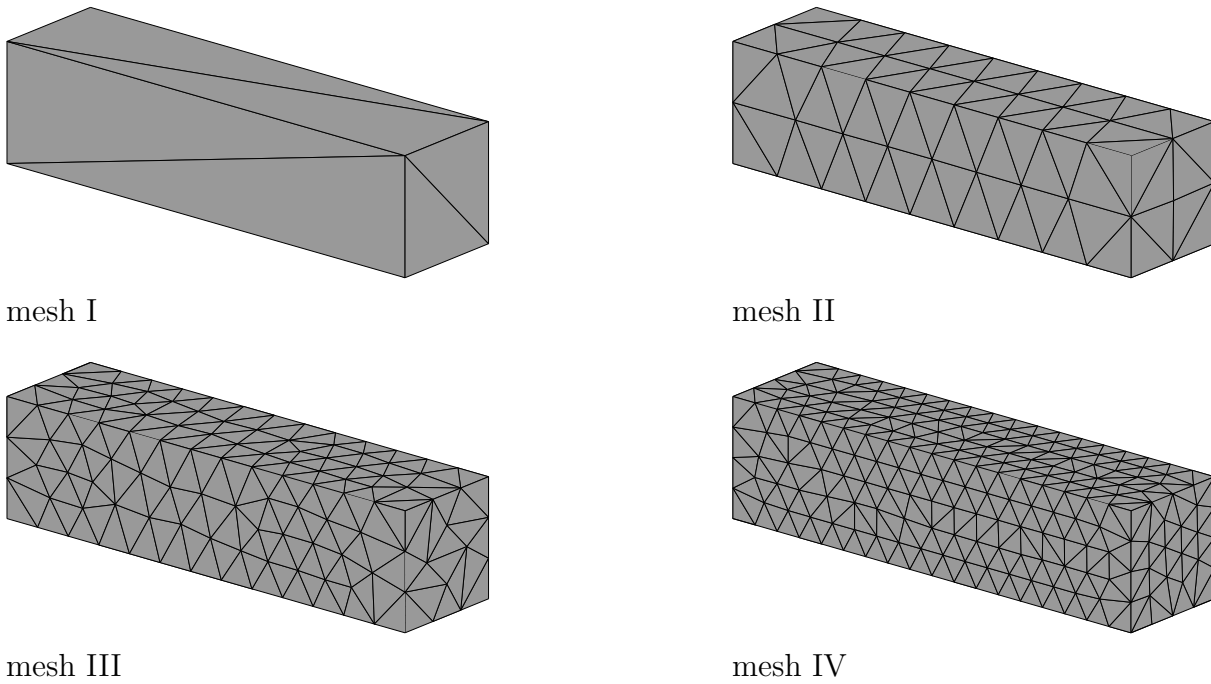


**Figure 3.8:** Numerical study of the tension test: finite element discretizations; mesh I, II, III and IV contain 6, 454, 1405 and 3361 constant strain tetrahedral elements, respectively

a bifurcation analysis in the sense of [SIMO, OLIVER & ARMERO 1993]. Clearly, the normal vector  $\mathbf{n}$  in the deformed configuration transforms as  $\mathbf{n} = \bar{\mathbf{F}}^{-1} \cdot \mathbf{N}$ . In contrast to the localization condition proposed in [SIMO, OLIVER & ARMERO 1993], the shear band is assumed to propagate when the condition  $\phi_{n+1} > 0$  is fulfilled (i. e., a loading step), cf. [MOSLER 2005B]. Of course, other criteria can be easily applied as well. The adopted criterion shows an important advantage compared to other models. According to [MOSLER 2005B], in the case of small displacements, the load displacement curve can be computed analytically. More precisely, the maximum loading is calculated as

$$F_{\max} = 8.0 \sigma_y \quad \text{at} \quad u = \frac{16.0 \sigma_y}{E} \quad (3.171)$$

and the ultimate displacement ( $q = 0$ , a completely softened material) as

$$u = \frac{1}{\sqrt{2}} \frac{\sigma_y}{H}. \quad (3.172)$$

For further details, refer to [MOSLER 2005B].

For the assessment of mesh dependence of the results computed numerically, three different discretizations are used. The unstructured meshes II, III and IV contain 454, 1405 and 3361 constant strain tetrahedral elements, respectively, see Fig. 3.8. Localization is induced by slightly reducing the initial yield stress  $\sigma_y$  of one element. Since an infinite number of possible slip band orientation exists, the normal vector of the first localized

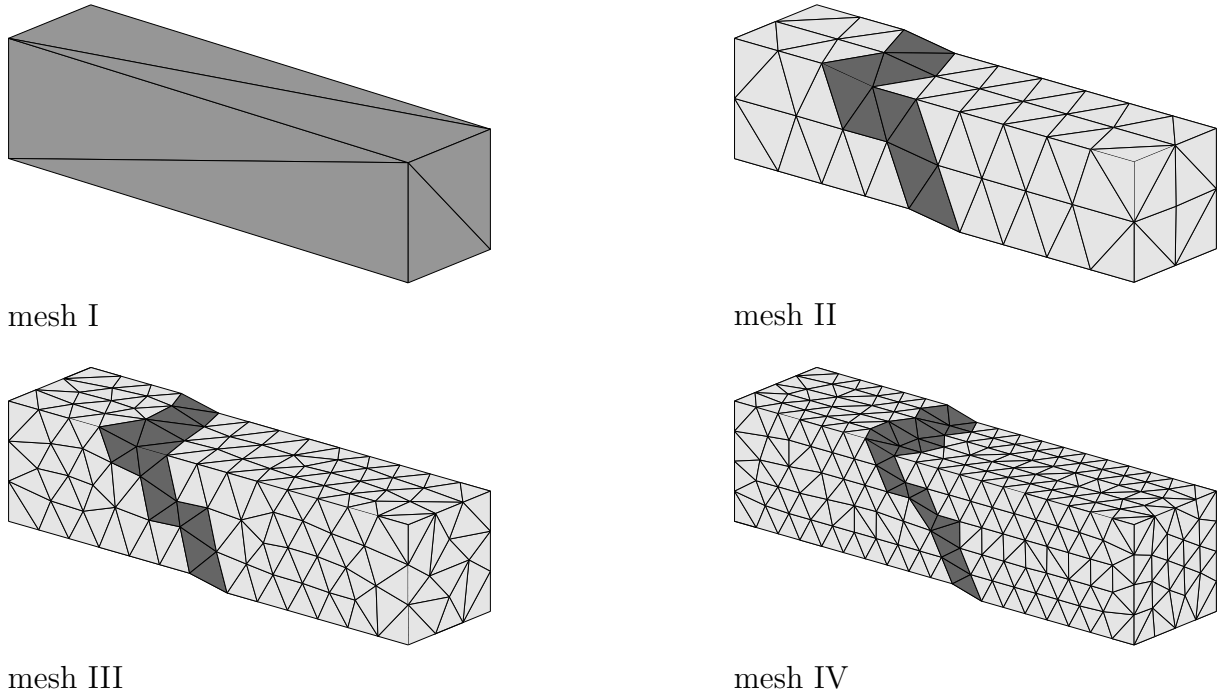


**Figure 3.9:** Numerical study of the tension test: distribution of the internal variable  $\alpha$  representing the relative shear sliding displacement as obtained from the proposed finite element formulation (1-fold magnification of the displacements); solution corresponding to the final stage of deformation ( $\mathbf{q}(\alpha) = 0$ )

element is explicitly prescribed as  $\mathbf{N}^T = [0; 1/\sqrt{2}; 1/\sqrt{2}]$ . Again, the numerical analyses are performed with enforcing slip band path continuity.

Additional to meshes II-IV, another discretization is considered for the sake of comparison. In contrast to the numerical analyses based on mesh II-IV, no imperfection has to be prepared for mesh I. As a result, the localization surface forms at once. Furthermore, the orientation of  $\partial_s \Omega$  is accounted for a priori. Hence, contrary to the numerical analyses based on mesh II-IV, the computation performed by means of mesh I is semi numerical.

**Set of material parameters I** First, the material parameters  $E$ ,  $\nu$ ,  $\sigma_y$  and  $H$ , used for the numerical analysis are assumed according to [GARIKIPATI 1996], see Fig. 3.7.

Fig. 3.9 contains the distribution of the internal variable  $\alpha$  representing the relative shear sliding displacement as obtained from the proposed finite element formulation. As expected, independent of the respective discretization, a mode-II failure is observed. Analogous to the analytical solution, the angle between the normal vector of the predicted shear band and that of the maximum principle stress direction is about  $45^\circ$ .

The resulting load-displacement diagrams are shown in Fig. 3.10. For the purpose of comparison, the structural response computed from the geometrically linearized model as presented in [MOSLER 2005B] is illustrated as well. As shown in Fig. 3.10, the results ob-

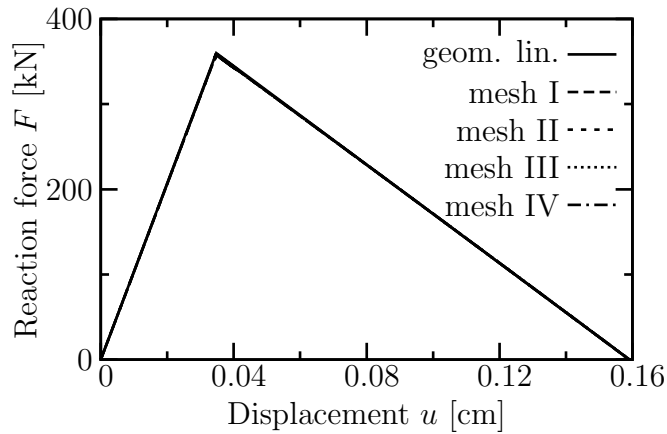


**Figure 3.10:** Numerical study of the tension test: load-displacement diagram as obtained from the proposed finite element formulation; material parameters according to Fig. 3.7

tained from the finite strain model are independent with respect to the spatial discretization. Furthermore, since the maximum displacement is relatively small ( $u = 0.159099$  cm), the load-displacement diagrams computed from the geometrically exact model are almost identical to that predicted by the linearized finite element formulation. In summary, all results obtained numerically are identical to the small strain analytical solution as defined by means of Eqs. (3.171) and (3.172).

The convergence profiles for the global NEWTON-type iteration are shown in Table 3.1. The load step considered corresponds to a displacement of the face side of  $u = 0.1527$  cm.

| Iteration $i$ | Relative error of the residuals $\mathbf{R}_I$ |           |           |
|---------------|--|-----------|-----------|
|               | mesh II  | mesh III  | mesh IV   |
| 1             | 7.074E+00                                      | 1.561E+00 | 1.922E+00 |
| 2             | 2.041E+00                                      | 3.738E-02 | 2.002E-01 |
| 3             | 1.947E-02                                      | 4.318E-07 | 1.125E-05 |
| 4             | 1.471E-06                                      | 1.168E-12 | 2.594E-12 |
| 5             | 4.979E-12                                      |           |           |

**Table 3.1:** Numerical study of the tension test: convergence profile of the global NEWTON-type iteration; magnitude of the load step  $\Delta u = 0.01$  cm; relative error of the residuals in the maximum norm; convergence tolerance for all computations  $\text{TOL} = 10^{-8}$

Although the prescribed increment of the nodal displacement  $\Delta u = 0.01$  cm is relatively large, a rapid rate of the convergence is observed. The asymptotic quadratic convergence shows the exact linearization of the finite element formulation presented.

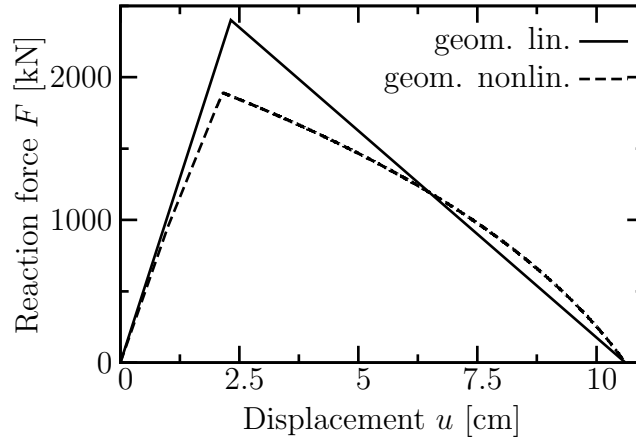


**Figure 3.11:** Numerical study of the tension test: load-displacement diagram as obtained from the proposed finite element formulation; material parameters:  $E = 2.069 \cdot 10^3$  kN/cm<sup>2</sup>,  $\nu = 0.29$ ,  $\sigma_y = 300$  kN/cm<sup>2</sup>,  $H = 20$  kN/cm<sup>3</sup>

**Set of material parameters II** In the previous subsection, the applicability as well as the efficiency of the proposed finite element model have been demonstrated. However, the material parameters which have been chosen according to [GARIKIPATI 1996] lead to a maximum displacement of the front size of the bar of  $u = 0.159099$  cm. Hence, only relatively small strains occur and consequently, geometrical nonlinearities do not play an important role.

In this subsection, a re-analysis of the tension test as analyzed in the previous subsection is performed. In contrast to Subsection 3.6.2.1 the material parameters according to Table 3.2 are assumed.

| $E$                        | $\nu$    | $\sigma_y$                | $H$                      |
|----------------------------|----------|---------------------------|--------------------------|
| 2069 [kN/cm <sup>2</sup> ] | 0.29 [-] | 300 [kN/cm <sup>2</sup> ] | 20 [kN/cm <sup>3</sup> ] |

**Table 3.2:** Numerical study of the tension test: material parameters

Evidently, the direction of the slip band, that is, the vector  $\mathbf{N}$  is not influenced by the change of the material parameters. Only the vector  $\mathbf{n}$  is affected.

The computed load-displacement diagram is illustrated in Fig. 3.11. Even before localization occurs, the elastic response as predicted from the linearized model using HOOKE's law differs from that obtained by means of the energy functional (2.30).

The deviation of the maximum load computed from the linearized model to that associated with the fully nonlinear algorithmic formulation is relatively large. With an ultimate load of 1891 kN (geometrically exact) and 2400 kN (geometrically linearized), the relative difference follows to 27%, i. e., the results obtained from the SDA model based on the assumption of small strains are clearly non conservative.

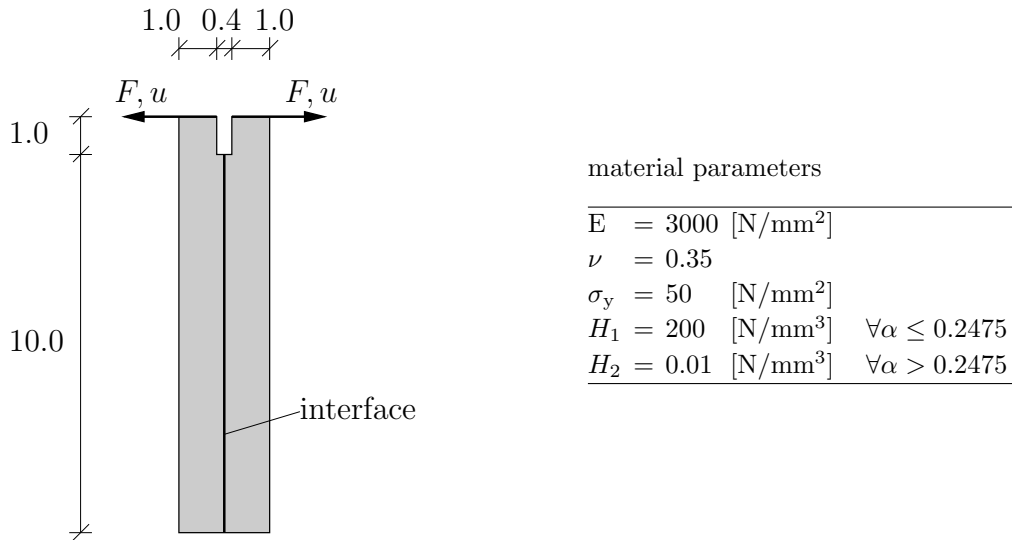


**Figure 3.12:** Numerical study of a debinding problem: dimensions (in [mm]) and material parameters; thickness of the strip  $t = 0.5$  mm

After the shear band has formed completely, a global softening response is observed. However, although a linear softening evolution of the type (3.170) has been adopted, a nonlinear load-displacement diagram is computed. It is obvious that these nonlinearities result from the finite strain kinematics. In summary, the structural response as obtained by assuming small displacements (and strains) differs significantly from that associated with the finite strain SDA finite element formulation as presented in this work.

It is interesting to note that the face side displacement  $u$  corresponding to a completely softened bar is independent of geometrically exact kinematics. However, this is quite evident. According to Eq. (3.170),  $\alpha_{\max} = \sigma_y/H$ . Hence, at the time when the structure fails ( $q = 0$ ), the material displacement jump  $\mathbf{J}$  is computed as  $\mathbf{J} = \sigma_y/H [0; 1/\sqrt{2}; 1/\sqrt{2}]$ . Since a stress free, completely softened bar is locally characterized by  $\mathbf{S} = \mathbf{0} \iff \bar{\mathbf{F}} = \mathbf{1}$ , the displacement jump  $[[\mathbf{u}]]$  is equivalent to its material counterpart  $\mathbf{J}$ , i. e.,  $[[\mathbf{u}]] = \mathbf{J}$  (in general,  $[[\mathbf{u}]] = \bar{\mathbf{F}} \cdot \mathbf{J}$ ). As a consequence, the maximum displacement in the direction of the axis of the bar is computed as  $[[[\mathbf{u}]]]_3 = 1/\sqrt{2} \sigma_y/H$ . Clearly, this result is identical to that predicted by the geometrically linearized model.

### 3.6.2.2 Debinding problem: Mode-I failure

The last example is a debinding problem taken from [OLIVER, HUESPE, PULIDO & SAMANIEGO 2003]. However, in contrast to the cited work which deals exclusively with constant strain triangle elements, a fully three-dimensional analysis is given in this paragraph. The geometry and the material parameters defining the mechanical problem are depicted in Fig. 3.12. It should be noted that the corners of the notch are slightly rounded. While the bulk material is modeled by the polyconvex energy functional (2.30), the in-

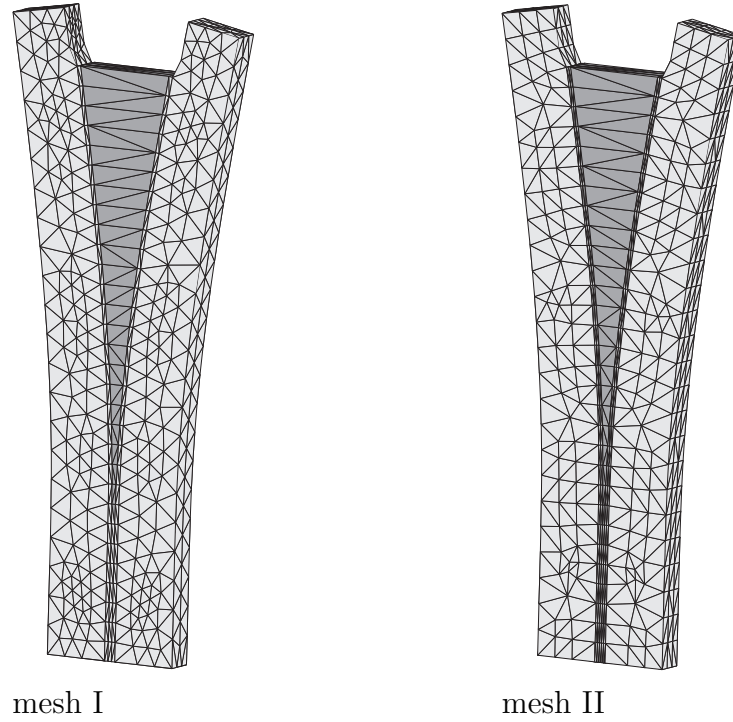


**Figure 3.13:** Numerical study of a debinding problem: Dark grey colored elements are those with active embedded discontinuities (1-fold magnification of the displacements); solution corresponding to  $u = 1.0$  mm.

terface law is chosen according to Eq. (3.59). Hence, a mixed-mode model is adopted. In contrast to the examples presented previously, the singular surface  $\partial_s\Omega$  is assumed to exist a priori. More precisely, the interface is located as illustrated in Fig. 3.12. As a consequence, using a cartesian coordinate system, the normal vector  $\mathbf{N}$  is  $\mathbf{N}^T = (1; 0; 0)$ . Due to the symmetry of the problem the shear stresses vanish at the interface. As a result, the mixed-mode cohesive law (3.59) reduces to the classical RANKINE criterion and, without loss of generality, the material parameter  $\kappa$  is set to  $\kappa = 0$ . Consequently, the mechanical problem is characterized by a pure mode-I failure. Softening is accounted for by the bi-linear function

$$q(\alpha) = \begin{cases} \sigma_y - H_1 \alpha & \forall \alpha \leq 0.2475 \text{ mm} \\ (\sigma_y - H_1 \cdot 0.2475) - H_2 (\alpha - 0.2475) & \forall \alpha > 0.2475 \text{ mm}. \end{cases} \quad (3.173)$$

For the assessment of mesh dependence of the numerically computed results, two different discretizations are analyzed. It can be seen that the elements of Mesh II which cross the interface  $\partial_s\Omega$  are 3/5 times smaller than those of Mesh I (in the direction orthogonal to  $\partial_s\Omega$ ).

The deformed configurations are shown in Fig. 3.13. The dark grey colored elements are those with active embedded discontinuities. According to Fig. 3.13 both triangulations predict an identical structural response.

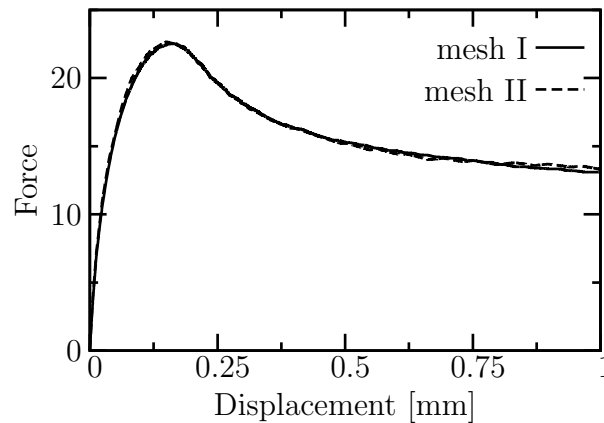


**Figure 3.14:** Numerical study of a debinding problem: load-displacement diagrams computed from mesh I and II

This is verified by the load-displacement diagrams given in Fig. 3.14. The  $F - u$  diagrams are only marginally affected by the discretization.

### 3.7 Open problems concerning strong discontinuity approaches

Although finite element formulations based on kinematics induced by strong discontinuities represent, nowadays, one of the most powerful techniques for analyzing problems exhibiting strain-localization and additionally, these models are relatively well developed, several questions are still unanswered. One of those is associated with the computation of the topology of  $\partial_s \Omega$ . This subject has been discussed briefly in Section 3.5. Although some of the methods described in Section 3.5 seem to be very promising, neither the SDA nor the X-FEM have been applied to the simulation of complex material failure such as fully three-dimensional problems showing crack branching and intersecting cracks (to the best knowledge of the author).

Any physically well-motivated method suitable for computing the topology of  $\partial_s \Omega$  requires a sufficiently fine resolution of the continuous deformation field. This is obvious, since all criteria necessary for predicting the growth direction of the internal surface depend significantly on the quality of the continuous deformation. An effective way for guaranteeing such a sufficiently fine resolution is represented by adaptive finite element methods. Particularly for complex three-dimensional simulations, those methods are essential. Three of them will be presented in the next chapters.

# Chapter 4

## A variational $r$ -adaptive finite element formulation

This chapter is concerned with the implementation of *Variational Arbitrary Lagrangian-Eulerian* (VALE) formulations, also known as variational  $r$ -adaptation methods. These methods seek to minimize the energy function governing the underlying physical problem with respect to the finite element mesh over the reference configuration of the body. A solution strategy is proposed which is based on a viscous regularization of the configurational forces. This procedure eliminates the ill-posedness of the optimization problem without changing its solutions, i. e., the minimizers of the regularized problems are also minimizers of the original functional. Selected numerical examples demonstrate the robustness of the solution procedures and their ability to produce highly anisotropic mesh refinement in regions of high energy density.

### 4.1 Introduction to Arbitrary Lagrangian-Eulerian (VALE) formulations

If the finite element method is applied to the analysis of mechanical problems, the solutions depend on the approximation of the primary variables resulting from the triangulation and the shape functions within the finite elements. As a consequence, the quality of an initial computation can be improved either by modifying the spatial discretization, or by using higher order interpolations. The latter is referred to as *p-adaptive method*, cf. [SZABÓ & BABŮSKA 1991]. In the present work, such approaches will not be considered. The reasons for this are twofold. First, the problems analyzed numerically here are, in many cases, highly non-smooth such as cracking in brittle structures. Second, if finite deformations are to be analyzed, the geometry of the deformed triangulation can be highly distorted which may lead eventually to ill-defined interpolations. This problem cannot be eliminated by using higher order elements, cf. [BELYTSCHKO, LIU & MORAN 2000].

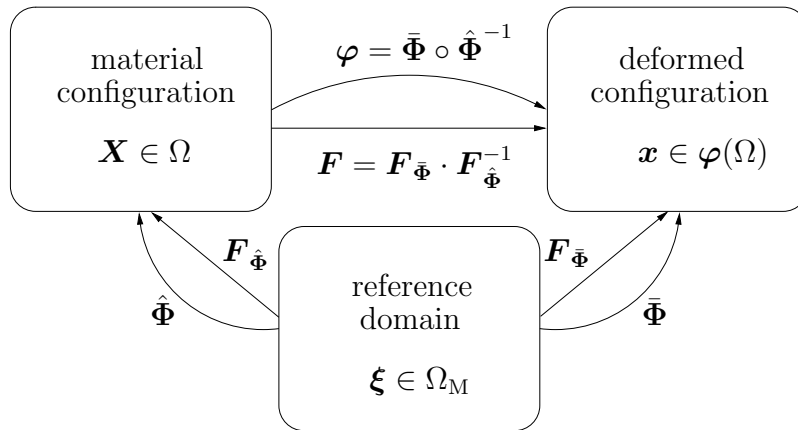


**Figure 4.1:** Different configurations and mappings characterizing the ALE kinematics

The method advocated in this chapter falls into the class of *r-adaption*, cf. Chapter 7 in [BELYTSCHKO, LIU & MORAN 2000]. Such models are often referred to as *Arbitrary Lagrangian Eulerian formulations* (ALE). Within this framework, the positions of the nodes defining the reference configuration are modified such that the resulting finite element mesh predicts the response of the mechanical system under investigation better than the initial triangulation. More specifically, two independent mappings are introduced. According to Fig. 4.1,  $\hat{\Phi} : \Omega_M \rightarrow \Omega$  connects points belonging to the reference domain  $\Omega_M$  to their counterparts in the material configuration  $\Omega$ , while the motion of the deformed triangulation is described by the mapping  $\bar{\Phi} : \Omega_M \rightarrow \varphi(\Omega)$ . As a result, the deformation  $\varphi$  follows from the composition of both mappings. Clearly, by setting  $\hat{\Phi}$  constant, the classical LAGRANGIAN description is obtained. In contrast,  $\bar{\Phi} = \text{const}$  is equivalent to an EULERIAN formulation.

Usually, the LAGRANGIAN framework is adopted when dealing with problems in solid mechanics. However, sometimes this framework is inappropriate. For instance, for problems showing large deformations and hence, highly distorted deformed meshes, LAGRANGIAN approaches often lead to ill-defined interpolations. Typically, this can be observed in fluid mechanics where an EULERIAN setting is more suitable. But even in solid mechanics, LAGRANGIAN formulations are sometimes not applicable. The interesting feature of ALE methods is that they combine the advantages of both LAGRANGIAN as well as EULERIAN finite element methods. In the present chapter, a novel ALE formulation for analyzing problems in solid mechanics is proposed. The EULERIAN part of the finite element model is used to modify the triangulation such that the interpolations are well-defined and the initial numerical solution is improved.

Although ALE formulations enjoy a relatively long tradition, dating back, at least, to [BELYTSCHKO & KENNEDY 1978; HUGHES, LIU & ZIMMERMANN 1981], first ideas for combining them with hyperelastoplasticity based on a multiplicative decomposition of the deformation gradient have been just recently presented, for instance in [RODRIGUEZ-

FERRAN, PÉREZ-FOGUET & HUERTA 2002; ARMERO & LOVE 2003]. As a consequence, many questions are still open and ALE formulations represent one of the active research areas. For example, if the triangulation of the reference or the deformed configuration is highly distorted, smoothing algorithms are usually adopted, cf. [ARMERO & LOVE 2003]. However, according to [DONEA 1983], most of those techniques are entirely based on heuristic developments. In contrast to the references on ALE finite element methods cited before, *Variational Arbitrary Lagrangian-Eulerian formulations* (VALE) do not require such smoothing algorithms. VALE methods will be discussed in the remaining part of this chapter. It follows to a large extent [MOSLER & ORTIZ 2005].

## 4.2 Introduction to Variational Arbitrary Lagrangian-Eulerian (VALE) formulations

According to Section 2.3.2, the stable configurations of a hyperelastic body obey the principle of minimum potential energy. For dynamical and general dissipative materials, the incremental problem can also be recast as a minimization problem by recourse to time discretization, cf. Subsection 2.5.2 and [RADOVITZKY 1998; RADOVITZKY & ORTIZ 1999]. The corresponding finite element approximations then follow from a constrained minimization of the (pseudo) potential energy over the space of interpolants. However, strongly nonlinear problems, e. g., involving finite deformations or unstable material behavior, may lack uniqueness – or even existence –, e. g., as a consequence of buckling or material instabilities. In addition, the space of solutions may not have a natural linear space – much less normed space – structure, and the usual framework of error estimation fails to apply in general. By virtue of this variational structure, the quality of two solutions can be compared simply by their respective energies. Based on this optimality criterion, a class of Variational Arbitrary Eulerian Lagrangian (VALE) methods can be formulated. In these approaches, the deformation and the optimal finite-element discretization follow jointly from energy minimization. The resulting energy is the lowest – and, therefore, the attendant solution is the best – among all allowed discretizations, e. g., of a prescribed number of nodes.

One of the first VALE formulations can be found in [MCNEICE & MARCAL 1973; FELIPPA 1976]. In these works, the nodal positions of a two-dimensional triangulation are computed from the variational principle governing the mechanical problem under investigation. More specifically, the principle of potential energy of linearized elasticity theory was considered. However, at that state, the authors could not give a physical interpretation of a variation with respect to the nodal positions of the undeformed mesh. It seems that [BRAUN 1997] was the first who realized that this variation is associated with equilibrium of configurational or energetic forces in the sense of [ESHELBY 1951; ESHELBY 1975]. Furthermore, BRAUN speculated on the possibility of computing such

nodal positions of the undeformed mesh so as to attain configurational equilibrium. Probably inspired by BRAUN's work, several authors proposed VALE finite methods recently. More precisely, [MUELLER & MAUGIN 2002; THOUTIREDDY 2003; THOUTIREDDY & ORTIZ 2004; KUHLE, ASKES & STEINMANN 2004] computed the nodal positions of the undeformed  $\mathbf{X}_h$  as well as the deformed  $\mathbf{x}_h$  configuration by applying the principle of potential energy corresponding to finite hyperelasticity. In contrast to classical methods in which energy is expressed in terms of  $\mathbf{x}_h$  only ( $\mathbf{X}_h$  is assumed as constant), the formulations advocated in the just cited references are based on an energy functional depending on both  $\mathbf{x}_h$  and  $\mathbf{X}_h$ . Although the ideas of the VALE methods in the citations share the same underlying idea, the respective solution strategies vary significantly. [MUELLER & MAUGIN 2002] proposed a steepest gradient algorithm without a line search. Since the convergence rate of such a method is relatively low, it has to be understood rather more as a prototype. More efficient implementations were advocated in [THOUTIREDDY 2003; THOUTIREDDY & ORTIZ 2004; ASKES, KUHLE & STEINMANN 2004]. While the algorithms adopted in the first two works are based on conjugate gradient methods, a classical NEWTON iteration (without damping or line search) was employed in [ASKES, KUHLE & STEINMANN 2004].

### 4.3 ALE approximation of the deformed and the undeformed configuration

Within the variational framework discussed in Sections 2.3.2, 2.5.2 and 2.6, finite-element approximations may be conveniently characterized as constrained minimizers of the (pseudo) potential energy. While this connection is standard and well-understood, it may stand a brief review in the interest of completeness.

Before a finite element analysis can be performed, the domain of analysis must be defined. It is assumed that the domains of interest are triangulable topological polyhedra [HOFFMANN 1989]. This assumption allows bodies to be described by their boundaries, a representational paradigm known as *Boundary Representation of Solids* (B-Rep) in the solid modeling literature [HOFFMANN 1989; MANTYLA 1988; REQUICHA 1980; RADOVITZKY & ORTIZ 2000]. A boundary representation consists of: a topological description of the connectivity, incidence and adjacency of the vertices, edges, and faces that constitute the boundary of the body, together with a consistent orientation leading to an unambiguous determination of the interior and exterior of the domain of analysis; and a geometrical description of the surface of the domain. The boundary representation of the domain is particularly important in the present context, since the motion of the nodes in the reference configuration must ensure that the integrity of the boundary representation is preserved.

In addition to the geometrical description of the domain, a *discretization* ( $\mathbf{X}_h, \mathcal{T}_h$ ) is

considered. It consists of: an abstract simplicial complex  $\mathcal{T}_h$ , or triangulation (cf, e. g., [HOFFMANN 1989]); and an array of nodal coordinates  $\mathbf{X}_h := \{\mathbf{X}_a, a = 1, \dots, n_{\text{node}}\}$ . It should be noted that the information encoded by  $\mathcal{T}_h$  is strictly topological. The node set is required to contain the vertex set of  $\mathcal{T}_h$ , but it may be larger than the latter. For instance, for ten-node quadratic tetrahedra the node set contains the mid-side nodes in addition to the vertex nodes. In general the node set will be attached to the cells of  $(\mathbf{X}_h, \mathcal{T}_h)$ , e. g., vertex nodes to vertices, mid-side nodes to edges, and so on. This constraint has the consequence that changes in  $\mathcal{T}_h$ , e. g., edge swaps, induces changes in  $\mathbf{X}_h$ , e. g., redefinition of mid-side nodes. For every element  $e$  in the triangulation the standard isoparametric framework conveniently supplies the local embeddings

$$\hat{\Phi}_h^e(\boldsymbol{\xi}) = \sum_{a=1}^{n_{\text{node}}^e} N_a(\boldsymbol{\xi}) \mathbf{X}_a^e \quad (4.1)$$

$$\bar{\Phi}_h^e(\boldsymbol{\xi}) = \sum_{a=1}^{n_{\text{node}}^e} N_a(\boldsymbol{\xi}) \mathbf{x}_a^e \quad (4.2)$$

of the standard element domain  $\Omega_M$  into  $\mathbb{R}^3$ , cf. Fig. 4.1. In the above representations  $\boldsymbol{\xi}$  are the natural coordinates over  $\Omega_M$ ;  $N_a$  are the standard element shape functions over  $\Omega_M$ ;  $n_{\text{node}}^e$  is the number of nodes in element  $e$  (e. g.,  $n_{\text{node}}^e = 4$  for simplicial tetrahedral elements and  $n_{\text{node}}^e = 10$  for quadratic tetrahedral elements); and  $\{\mathbf{X}_a^e, e = 1, \dots, n_{\text{node}}^e\}$  and  $\{\mathbf{x}_a^e, e = 1, \dots, n_{\text{node}}^e\}$  are the undeformed and deformed nodal coordinates of element  $e$ , respectively. It should be noted that ALE formulations are, obviously, not restricted to an isoparametric framework i. e.,  $\hat{\Phi}_h^e$  and  $\bar{\Phi}_h^e$  may be interpolated differently. The mappings  $\hat{\Phi}_h^e$  and  $\bar{\Phi}_h^e$  are required to be diffeomorphisms, i. e., bijective, differentiable, and with differentiable inverse; and  $\{\Omega^e = \hat{\Phi}_h^e(\Omega_M), e = 1, \dots, n_{\text{element}}\}$  and  $\{\varphi(\Omega^e) = \bar{\Phi}_h^e(\Omega_M), e = 1, \dots, n_{\text{element}}\}$  are required to define a partition of  $\Omega$  and  $\varphi(\Omega)$ , respectively, cf. Fig. 4.1. The deformation mapping for element  $e$  then reads

$$\varphi_h^e = \bar{\Phi}_h^e \circ \hat{\Phi}_h^{e-1} \equiv \sum_{a=1}^{n_{\text{node}}^e} N_a^e \mathbf{x}_a \quad (4.3)$$

where

$$N_a^e = N_a \circ \hat{\Phi}_h^{e-1} \quad (4.4)$$

are the element shape functions over  $\Omega^e$ . Clearly, the usual requirement of conformity is appended, i. e.,  $\varphi_h^e$  is the restriction to  $\Omega^e$  of a continuous mapping  $\varphi_h$ . This places topological restrictions on the triangulation and constraints on the standard shape functions. By virtue of the linearity of the interpolation it follows that

$$\varphi_h = \sum_{a=1}^{n_{\text{node}}} \hat{N}_a \mathbf{x}_a \quad (4.5)$$

where  $\hat{N}_a$  are the nodal shape functions over  $\Omega$ . For the coordinates  $\mathbf{x}_h$  to be admissible, they must additionally be consistent with the displacement boundary conditions. Finally, the deformation gradient  $\mathbf{F}$  can be computed. From Eq. (4.3), the element-wise approximation of  $\mathbf{F}$  reads

$$\mathbf{F}_h^e = \mathbf{F}_{\bar{\Phi}} \cdot \mathbf{F}_{\hat{\Phi}}^{-1}, \quad (4.6)$$

with

$$\mathbf{F}_{\bar{\Phi}} = \frac{\partial \bar{\Phi}_h^e}{\partial \boldsymbol{\xi}} \quad \text{and} \quad \mathbf{F}_{\hat{\Phi}} = \frac{\partial \hat{\Phi}_h^e}{\partial \boldsymbol{\xi}}. \quad (4.7)$$

Since  $\bar{\Phi}_h^e$  and  $\hat{\Phi}_h^e$  are diffeomorphisms, the inverses of  $\mathbf{F}_{\bar{\Phi}}$  and  $\mathbf{F}_{\hat{\Phi}}$  exist and consequently, the deformation gradient  $\mathbf{F}$  is well-defined.

## 4.4 Fundamentals of VALE formulations

By virtue of the preceding representations, the (pseudo) potential energy of the discretized solid reads

$$I_h(\mathbf{x}_h, \mathbf{X}_h, \mathcal{T}_h) = I(\boldsymbol{\varphi}_h). \quad (4.8)$$

Thus, in addition to being a function of deformation,  $I_h$  is also a function of the discretization of the domain. The principle of minimum potential energy compels to minimize  $I_h$  over its entire domain of definition and thus leads to the discrete minimum problem

$$\inf_{(\mathbf{x}_h, \mathbf{X}_h, \mathcal{T}_h) \in X_h} I_h(\mathbf{x}_h, \mathbf{X}_h, \mathcal{T}_h) \quad (4.9)$$

where  $X_h$  is the discrete configuration space of the solid. Clearly, in classical finite element formulations, the optimization problem

$$\inf_{\mathbf{x}_h} I_h(\mathbf{x}_h, \mathbf{X}_h, \mathcal{T}_h) \Big|_{(\mathbf{X}_h, \mathcal{T}_h) = \text{const}} \quad (4.10)$$

is considered. Consequently, principle (4.9) can be understood as the canonical extension of the classical formulation. It is obvious that  $X_h|_{(\mathbf{X}_h, \mathcal{T}_h) = \text{const}} \subset X_h$ . As a result,

$$\inf_{(\mathbf{x}_h, \mathbf{X}_h, \mathcal{T}_h) \in X_h} I_h(\mathbf{x}_h, \mathbf{X}_h, \mathcal{T}_h) \leq \inf_{\mathbf{x}_h} I_h(\mathbf{x}_h, \mathbf{X}_h, \mathcal{T}_h) \Big|_{(\mathbf{X}_h, \mathcal{T}_h) = \text{const}}. \quad (4.11)$$

Hence, the generalized optimization principle (4.9) leads indeed to an improvement of the solution.

For ease of reference, the constraints that define the discrete configuration space  $X_h$  of the solid are enumerated:

C1  $\mathcal{T}_h$  is an abstract simplicial complex.

C2 The embeddings  $\hat{\Phi}_h^e : \Omega_M \rightarrow \mathbb{R}^3$  and  $\bar{\Phi}_h^e : \Omega_M \rightarrow \mathbb{R}^3$  are diffeomorphic.

- C3  $\{\Omega^e = \Phi_h^e(\hat{\Omega}), e = 1, \dots, n_{\text{element}}\}$  defines a partition of  $\Omega$ .
- C4 The discretization is conforming, i. e.,  $\varphi_h^e = \bar{\Phi}_h^e \circ \hat{\Phi}_h^{e-1}$  is the restriction to  $\Omega^e$  of a continuous mapping  $\varphi_h$ .
- C5 The deformations are admissible, i. e.,  $\varphi_h = \bar{\varphi}$  on  $\partial\Omega_1$ .

The solution of the minimum problem (4.9) is not without difficulty. Thus, the constraint C3 that the triangulation spans  $\Omega$  introduces an interplay between discretization and geometry of the domain; the function  $I_h(\mathbf{x}_h, \mathbf{X}_h, \mathcal{T}_h)$  may be strongly nonconvex in the first two variables; and the minimization of  $I_h(\mathbf{x}_h, \mathbf{X}_h, \mathcal{T}_h)$  with respect to the triangulation is an exceedingly complex discrete minimization problem. The remainder of this chapter is devoted to the formulation of solution procedures that effectively address the optimization of the (pseudo) energy with respect to the nodal coordinates  $\mathbf{x}_h$  and  $\mathbf{X}_h$ . An adaptive strategy based on varying the connectivity  $\mathcal{T}_h$  will be presented in the next chapter.

## 4.5 Optimization of the positions of the nodal coordinates

In this section, the subproblem of minimizing  $I_h(\mathbf{x}_h, \mathbf{X}_h, \mathcal{T}_h)$  with respect to  $(\mathbf{x}_h, \mathbf{X}_h)$  while keeping the triangulation  $\mathcal{T}_h$  unchanged is considered. In order to preserve the boundary representation of the domain the following constraints are enforced:

1. Vertices are fixed points of the reference configuration.
2. Edge nodes are required to remain within their edges.
3. Face nodes are required to remain within their faces.

These constraints introduce boundary conditions in the minimization of  $I_h(\mathbf{x}_h, \mathbf{X}_h, \mathcal{T}_h)$  with respect to  $\mathbf{X}_h$ . In particular, the number of nodes in each surface edge and face remains unchanged. The general minimization problem, including the optimization of the connectivity of the mesh, is considered subsequently in Chapter 5. A more general implementation that relaxes the constraints on the number of surface nodes is presented in Section 4.7.

### 4.5.1 Fundamentals

Provided that  $I_h$  is sufficiently differentiable, whenever  $\mathbf{x}_h$  and  $\mathbf{X}_h$  are independent, a necessary condition for  $(\mathbf{x}_h, \mathbf{X}_h)$  being a minimum is

$$\begin{aligned}\mathbf{r} &:= \frac{\partial I_h}{\partial \mathbf{x}_h} = \mathbf{0} \\ \mathbf{R} &:= \frac{\partial I_h}{\partial \mathbf{X}_h} = \mathbf{0}.\end{aligned}\tag{4.12}$$

On the displacement boundary  $\partial\Omega_1$ ,  $\mathbf{x}_h$  and  $\mathbf{X}_h$  are related according to

$$\delta \mathbf{x}_h = \frac{\partial \bar{\varphi}}{\partial \mathbf{X}_h} \delta \mathbf{X}_h,\tag{4.13}$$

and hence, are not independent. By virtue of this constraint, at  $\partial\Omega_1$  the stationarity condition of the functional  $I_h$  with respect to  $\mathbf{X}_h$  is

$$\frac{\partial I_h}{\partial \mathbf{X}_h} + \frac{\partial I_h}{\partial \mathbf{x}_h} \frac{\partial \bar{\varphi}}{\partial \mathbf{X}_h} = \mathbf{0},\tag{4.14}$$

instead of Eqs. (4.12).

#### 4.5.1.1 Computation of the first derivatives

Explicit expressions for the residuals  $(\mathbf{r}, \mathbf{R})$  can be derived in a straightforward manner, cf. [THOUTIREDDY 2003; THOUTIREDDY & ORTIZ 2004; KUHLE, ASKES & STEINMANN 2004]. For the sake of completeness they are given in this paragraph.

Clearly, the variation of  $I_h$  with respect to  $\mathbf{x}_h$  by keeping  $\mathbf{X}_h$  constant is identical to the discretized principle of virtual work known from classical (LAGRANGIAN) finite element methods. More specifically,

$$\mathbf{r}_I = \mathbf{A} \int_{\Omega} \text{GRAD} N_i \cdot \mathbf{P} \, dV - \int_{\Omega} \rho_0 N_i \mathbf{B} \, dV - \int_{\partial\Omega_2} N_i \bar{\mathbf{T}} \, dA.\tag{4.15}$$

Analogous to Eq. (3.79),  $\mathbf{A}$  denotes the assembly of all element contributions at the local element node  $i$  to the global residual at the global node  $I \in \{1, \dots, n_{\text{node}}\}$ . The non-standard derivative  $\partial I_h / \partial \mathbf{X}_h$  can be derived in a similar manner,

$$\begin{aligned}\mathbf{R}_I &= \mathbf{A} \int_{\Omega} \text{GRAD} N_i \cdot \mathbf{M} \, dV - \int_{\Omega} \rho_0 \text{GRAD} N_i [\mathbf{B} \cdot \varphi] \, dV \\ &\quad - \int_{\Omega} [\text{GRAD} N_i (\mathbf{F} : \bar{\mathbf{P}} + \varphi \cdot \text{DIV} \bar{\mathbf{P}}) - \mathbf{F}^T \cdot \bar{\mathbf{P}} \cdot \text{GRAD} N_i] \, dV.\end{aligned}\tag{4.16}$$

Here,  $\mathbf{M}$  denotes the ESHELBY momentum tensor, i. e.,

$$\mathbf{M} := \Psi \mathbf{1} - \mathbf{F}^T \cdot \mathbf{P} \quad (4.17)$$

and  $\bar{\mathbf{P}}$  is an arbitrary tensor-valued function such that

$$\begin{aligned} \bar{\mathbf{P}} \cdot \mathbf{N} &= \bar{\mathbf{T}} \quad \forall \mathbf{X} \in \partial\Omega_2 \\ \bar{\mathbf{P}} \cdot \mathbf{N} &= \mathbf{0} \quad \forall \mathbf{X} \in \partial\Omega_1. \end{aligned} \quad (4.18)$$

For further details, refer to [THOUTIREDDY & ORTIZ 2004]. While  $\mathbf{r} = \mathbf{0}$  corresponds to classical NEWTONIAN equilibrium,  $\mathbf{R} = \mathbf{0}$  is associated with equilibrium of the so-called *configurational forces* or *material forces*. Since the latter are not standard in finite element implementations (yet), a short physical interpretation is given in Subsection 4.5.1.3.

#### 4.5.1.2 Computation of the second derivatives

Since the proposed VALE implementation is based on a NEWTON-type iteration, the second derivatives of the (pseudo) potential  $I_h$  are required. After some straightforward algebraic transformations they are obtained as

$$\begin{aligned} \frac{\partial \mathbf{r}_a^e}{\partial \mathbf{x}_b^e} &= \int_{\Omega} \text{GRAD}N_a \stackrel{(2)}{\cdot} \frac{\partial^2 \Psi}{\partial \mathbf{F}^2} \cdot \text{GRAD}N_b \, dV \\ \frac{\partial \mathbf{R}_a^e}{\partial \mathbf{X}_b^e} &= \int_{\Omega} \text{GRAD}N_a \stackrel{(2)}{\cdot} \mathbb{C} \cdot \text{GRAD}N_b \, J \, dV \\ \frac{\partial \mathbf{r}_a}{\partial \mathbf{X}_b} &= \int_{\Omega} \text{GRAD}N_a \stackrel{(2)}{\cdot} \frac{\partial \mathbf{M}}{\partial \mathbf{F}} \cdot \text{GRAD}N_b \, dV, \end{aligned} \quad (4.19)$$

with

$$\mathbb{C}_{ijkl} = \mathbf{F}^{-T} \stackrel{(2)}{\cdot} \frac{d^2(\Psi J)}{d[\mathbf{F}^{-1}]^2} \cdot \mathbf{F}^{-T}. \quad (4.20)$$

Clearly, for sufficiently smooth  $I_h$ ,  $\nabla^2 I_h$  is symmetric resulting in

$$\frac{\partial \mathbf{R}_a}{\partial \mathbf{x}_b} = \left( \frac{\partial \mathbf{r}_b}{\partial \mathbf{X}_a} \right)^T. \quad (4.21)$$

Further details can be found in [THOUTIREDDY 2003; THOUTIREDDY & ORTIZ 2004; ASKES, KUHL & STEINMANN 2004]. For the hyperelastic material model characterized by the energy functional (2.29), the respective derivatives are summarized in Appendix B.

#### 4.5.1.3 Comment on equilibrium of configurational forces

In classical mechanics, forces in the sense of NEWTON are considered, i. e., these forces cause positional changes relative to the ambient space. In contrast to this viewpoint,

material forces or configurational forces are closely related to ESHELBY mechanics, cf. [ESHELBY 1951; ESHELBY 1975]. More specifically, configurational forces are the driving forces for positional changes relative to the ambient material. For instance, in fracture mechanics, the force driving crack propagation is important. It is obvious that such a force cannot be interpreted in the classical NEWTONIAN framework.

Although comprehensive overviews on ESHELBY mechanics and material forces can be found in [MAUGIN 1993; GURTIN 2000; MAUGIN 2001; STEINMANN 2002], the computation of these forces by applying the finite element method has only been proposed recently, cf. [BRAUN 1997]. This is relatively surprising, since according to Eq. (4.16), once the deformation mapping is determined, the configurational forces can be computed by a simple postprocessing step. Unfortunately, these so-called *discrete configurational forces* do not possess all properties of their continuous counterparts. This can be shown by a relatively simple example. Following [ESHELBY 1951; ESHELBY 1975], the material force acting on a defect can be obtained from

$$\mathbf{R} = \int_S \mathbf{M} \cdot \mathbf{N} \, dA \quad (4.22)$$

where  $S$  is a closed surface containing the defect and  $\mathbf{N}$  is the normal vector of the hyperplane  $S$ . As a result, without a defect  $\mathbf{R}$  vanishes. However, this is only true for the analytical solution. If the finite element method is applied, the discretization leads to additional configurational forces, cf. [BRAUN 1997]. As a consequence, physical and numerical phenomena superpose. This is, of course, a serious problem, since those forces cannot be interpreted anymore. For instance, in [DENZER, BARTH & STEINMANN 2003] this effect can be observed. These authors applied the material force method to the computation of the J-integral.

However, with the proposed VALE formulation this drawback can be avoided completely. According to the variational principle governing the presented ALE method, the discretization is modified such that  $\mathbf{R} = \mathbf{0}$  for all nodes which are allowed to move (relative to the ambient material). Consequently, the non-vanishing discrete configurational forces are exclusively associated with a positional change of physical defects. The excellent agreement between the analytical solution and discrete configurational forces computed from the proposed VALE formulation has been pointed out in [THOUTIREDDY 2003; THOUTIREDDY & ORTIZ 2004]. In these works the authors compared the J-integral predicted by the VALE formulation to the analytical solution.

## 4.5.2 Numerical ill-posedness of the optimization problem

Based on the linearizations (4.15), (4.16) and (4.19), several optimization strategies have been implemented and applied to compute the solution of the minimum problem

$$\inf_{\mathbf{x}_h, \mathbf{X}_h} I_h(\mathbf{x}_h, \mathbf{X}_h, \mathcal{T}_h) \Big|_{\mathcal{T}_h = \text{const}}. \quad (4.23)$$

More specifically, the following schemes have been employed:

- a NEWTON iteration
- different types of conjugate gradient methods such as the POLAK-RIBIÉRE method with different preconditioners
- limited memory LBFGS approaches, cf. [LIU & NOCEDAL 1989].

Each of the enumerated optimization algorithms has been adopted for solving problem (4.23) monolithically. In addition, staggered, i. e., nested, schemes have been analyzed as well. The global convergence behavior of the schemes has been improved by line search strategies. Further details are omitted. An excellent overview on optimization methods is given in [GEIGER & KANZOW 1999].

Although for relatively simple problems some of the algorithms find a local minimum, the iterations fail to converge in general. A careful analysis of the optimization problem reveals the following essential difficulties:

1. The minimizers can be vastly non-unique. For instance, for constant strain deformations, the discrete energy  $I_h$  is independent of the nodal coordinates  $\mathbf{X}_h$ .
2. The HESSIAN matrix can be singular. By way of illustration, consider the linearized problem near the undeformed configuration. In this case one finds

$$\frac{\partial^2 I_h}{\partial \mathbf{X}_h^2} = \frac{\partial^2 I_h}{\partial \mathbf{x}_h^2} = -\frac{\partial^2 I_h}{\partial \mathbf{x}_h \otimes \partial \mathbf{X}_h} = -\frac{\partial^2 I_h}{\partial \mathbf{X}_h \otimes \partial \mathbf{x}_h} \quad (4.24)$$

which is clearly singular. Additional examples of this source of degeneracy are given in Subsection 4.6.1.

3. The minimization problem is nonconvex in general. This lack of convexity is illustrated by the examples presented in Subsection 4.6.1, for which the HESSIAN matrix is found to have a number of negative eigenvalues.

[ASKES, KUHL & STEINMANN 2004] have proposed a dynamic constraint for eliminating the rank-deficiency of the system of equations. The procedure consists of checking if the absolute value of a component of the residual  $\mathbf{R}$  associated with  $\mathbf{X}_h$  is lower than a numerical tolerance. If so, the corresponding equation is eliminated from the NEWTON step. However, the rank-deficiency of the HESSIAN is not necessarily equal to the number of vanishing components of  $\mathbf{R}$ , i. e., the null subspace of the HESSIAN  $\nabla^2 I_h$  needs not to coincide with the space spanned by the degrees of freedom in configurational equilibrium, and the rank-deficiency of the system is not eliminated by constraining the latter space. In addition, the modes corresponding to negative eigenvalues are not stabilized by the procedure.

For the elimination of the rank-deficiency, three different concepts have been implemented. The first is based on a pseudo-inverse, i. e., with the spectral decomposition of the HESSIAN

$$\nabla^2 I_h = \sum_{i=1}^{n_{\text{DOF}}} \lambda_i \mathbf{n}_i \otimes \mathbf{n}_i \quad (4.25)$$

the pseudo-inverse

$$\text{inv}(\nabla^2 I_h) := \sum_{i=1}^{n_{\text{DOF}}} \text{inv}(\lambda_i) \mathbf{n}_i \otimes \mathbf{n}_i, \quad (4.26)$$

with

$$\text{inv}(\lambda_i) := \begin{cases} 1/\lambda_i & \forall |\lambda_i| > \text{TOL} \\ 0 & \forall |\lambda_i| \leq \text{TOL}, \end{cases} \quad (4.27)$$

has been used. Additionally, the modified inverse

$$\text{inv}(\lambda_i) := \begin{cases} 1/\lambda_i & \forall \lambda_i > \text{TOL} \\ 0 & \forall \lambda_i \leq \text{TOL} \end{cases} \quad (4.28)$$

has been applied as well. The third alternative is the modified CHOLESKY decomposition according to [SCHNABEL & ESKOW 1990]. In this concept, the HESSIAN is approximated by means of a symmetric and positive definite matrix. These methods have been combined with a NEWTON iteration. That is, instead of the standard search direction

$$\mathbf{d} = -[\nabla^2 I_h]^{-1} \nabla I_h, \quad (4.29)$$

$\mathbf{d}$  is replaced by

$$\mathbf{d} = -[\mathbf{A}]^{-1} \nabla I_h, \quad (4.30)$$

with  $\mathbf{A}$  representing one of the three different approximations of the HESSIAN. Since for the second and third method  $\mathbf{A}$  is symmetric and positive definite, they result in a descent direction, cf. [GEIGER & KANZOW 1999].

The modified NEWTON's methods improve significantly the robustness of the proposed VALE formulation. However, for several problems convergence is not attained. For this reason, a novel solution scheme is developed in the next subsection.

**Remark 4.5.2.1** *All NEWTON-type iterations briefly discussed in this subsection show the following properties:*

- *The criterion*

$$\nabla I_h(x_k) \cdot \mathbf{d}_k \leq -\rho \|\mathbf{d}_k\|^p \quad (4.31)$$

*is checked. If it is not fulfilled,  $\mathbf{d}_k$  is set to  $\mathbf{d}_k = -\nabla I_h(x_k)$ . Obviously, this criterion ensures that the direction  $\mathbf{d}_k$  is a descent direction.*

- *An ARMIJO line search is applied, i. e.,*

$$t_k = \max\{\beta^l \mid l \in \mathbb{N}_0\} \quad : \quad I_h(x_k + t_k \mathbf{d}_k) \leq f(x_k) + \sigma \nabla I_h(x_k) \cdot \mathbf{d}_k. \quad (4.32)$$

Here, for the sake of brevity, the notation  $x = (\mathbf{x}_h, \mathbf{X}_h)$  has been introduced. The number  $k$  indicates the  $k$ -th iteration. The numerical parameters  $\rho$ ,  $p$ ,  $\beta$  and  $\sigma$  have to be chosen such that  $\rho > 0$ ,  $p > 2$ ,  $\beta \in (0, 1)$ ,  $\sigma \in (0, 1/2)$ . According to [GEIGER & KANZOW 1999], for any function  $I_h \in \mathcal{C}^2$ , the enumerated properties guarantee that every cluster point generated by the sequence  $(x_k)_{k \in \mathbb{N}}$  is a stationarity point of  $I_h$ . As a result, if  $I_h$  is bounded below, the algorithm converges. Clearly, this property does not imply that convergence is attained in practice.

### 4.5.3 Viscous regularization of the configurational forces

In this subsection, an alternative stabilization strategy based on a *viscous regularization* of the configurational forces is proposed. To this end, problem (4.9) is replaced by the following sequence of problems:

$$\inf_{(\mathbf{x}_{n+1}, \mathbf{X}_{n+1}) \in X_h} I_n(\mathbf{x}_{n+1}, \mathbf{X}_{n+1}) \quad (4.33)$$

where  $n = 0, \dots$ ,  $(\mathbf{x}_0, \mathbf{X}_0)$  is given, and

$$I_n(\mathbf{x}_{n+1}, \mathbf{X}_{n+1}) := I_h(\mathbf{x}_{n+1}, \mathbf{X}_{n+1}) + \alpha \|\mathbf{X}_{n+1} - \mathbf{X}_n\|^2 \quad (4.34)$$

is a regularized incremental energy function in which  $\alpha \geq 0$  is a numerical parameter and  $\|\cdot\|$  is the EUCLIDEAN norm. The function  $I_n(\mathbf{x}_{n+1}, \mathbf{X}_{n+1})$  is the potential for the equations resulting from a backward-Euler time discretization of the gradient flow

$$\frac{\partial I_h}{\partial \mathbf{x}_h} = \mathbf{0} \quad (4.35a)$$

$$\frac{d\mathbf{X}_h}{dt} + \frac{\partial I_h}{\partial \mathbf{X}_h} = \mathbf{0}. \quad (4.35b)$$

The stationarity conditions are now

$$\frac{\partial I_n}{\partial \mathbf{x}_{n+1}} = \frac{\partial I_h}{\partial \mathbf{x}_h} \Big|_{\mathbf{x}_{n+1}, \mathbf{X}_{n+1}} = \mathbf{r}_{n+1} = \mathbf{0} \quad (4.36a)$$

$$\frac{\partial I_n}{\partial \mathbf{X}_{n+1}} = \frac{\partial I_h}{\partial \mathbf{X}_h} \Big|_{\mathbf{x}_{n+1}, \mathbf{X}_{n+1}} = \mathbf{R}_{n+1} + 2\alpha (\mathbf{X}_{n+1} - \mathbf{X}_n) = \mathbf{0}, \quad (4.36b)$$

and the corresponding HESSIAN is

$$\frac{\partial^2 I_n}{\partial \mathbf{x}_{n+1}^2} = \frac{\partial^2 I_h}{\partial \mathbf{x}_h^2} \Big|_{\mathbf{x}_{n+1}, \mathbf{X}_{n+1}} \quad (4.37a)$$

$$\frac{\partial^2 I_n}{\partial \mathbf{x}_{n+1} \otimes \partial \mathbf{X}_{n+1}} = \frac{\partial^2 I_h}{\partial \mathbf{x}_h \otimes \partial \mathbf{X}_h} \Big|_{\mathbf{x}_{n+1}, \mathbf{X}_{n+1}} \quad (4.37b)$$

$$\frac{\partial^2 I_n}{\partial \mathbf{X}_{n+1}^2} = \frac{\partial^2 I_h}{\partial \mathbf{X}_h^2} \Big|_{\mathbf{x}_{n+1}, \mathbf{X}_{n+1}} + 2\alpha \mathbf{1}. \quad (4.37c)$$

From Eq. (4.37c) follows that the regularized HESSIAN can be made positive definite by choosing  $\alpha$  sufficiently large. In addition, if the iteration converges, it follows that  $\|\mathbf{X}_{n+1} - \mathbf{X}_n\| \rightarrow 0$ . Consequently, the viscous term in (4.36b) becomes negligibly small as convergence is attained.

In calculations, a NEWTON iteration according to Remark 4.5.2.1 is used. The resulting stabilized iterative procedure can be summarized as follows:

1. Initialize  $\mathbf{x}_h = \mathbf{x}_0$ ,  $\mathbf{X}_h = \mathbf{X}_0$ , set  $n = 0$ .
2. Compute the solution  $(\mathbf{x}_{n+1}, \mathbf{X}_{n+1})$  of the regularized problem (4.33) by a NEWTON iteration.
3. If  $\|\mathbf{x}_{n+1} - \mathbf{x}_n\| < \text{TOL}$  and  $\|\mathbf{X}_{n+1} - \mathbf{X}_n\| < \text{TOL}$  exit.
4. Reset  $n$  to  $n + 1$ , go to 2.

According to Remark 4.5.3.1, the iterative procedure generates a monotonically decreasing sequence of energies. As a consequence, under displacement control, the energy is bounded below and consequently, the energy is guaranteed to converge.

It should be carefully noted that the choice of  $\alpha$  influences the rate of convergence. In particular, a large  $\alpha$  tends to slow down convergence. Hence, in calculations  $\alpha$  is set to the smallest value resulting in a strictly convex incremental energy function  $I_n$ . More specifically,  $\alpha$  is chosen such that the spectrum of  $\nabla^2 I_n$  is minorized by a prespecified tolerance TOL. It is noteworthy that, by this criterion, if the original problem is strictly convex,  $\alpha$  equals zero and the problem is not regularized, cf. Remark 4.5.3.2.

**Remark 4.5.3.1** *In this paragraph, it is shown that the sequence  $(I_h(\mathbf{x}_n, \mathbf{X}_n))_{n \in \mathbb{N}}$  generated by the proposed algorithm is monotonically decreasing. In what follows,  $\mathbf{x}_{n+1}^{(k)}$  and  $\mathbf{X}_{n+1}^{(k)}$  denote the solution of the  $k$ -th iteration step predicted by the advocated NEWTON's method. According to Remark 4.5.2.1, the proposed solution strategy guarantees that*

$$I_n(\mathbf{x}_{n+1}^{(k)}, \mathbf{X}_{n+1}^{(k)}, \mathcal{T}_h) \geq I_n(\mathbf{x}_{n+1}^{(k+1)}, \mathbf{X}_{n+1}^{(k+1)}, \mathcal{T}_h). \quad (4.38)$$

Applying this inequality leads to

$$\begin{aligned} I_h(\mathbf{x}_n, \mathbf{X}_n, \mathcal{T}_h) &= I_h(\mathbf{x}_n, \mathbf{X}_n, \mathcal{T}_h) + \alpha \underbrace{\|\mathbf{X}_{n+1}^{(0)} - \mathbf{X}_n\|^2}_{= 0} \\ &= I_n(\mathbf{x}_{n+1}^{(0)}, \mathbf{X}_{n+1}^{(0)}, \mathcal{T}_h) \\ &\geq I_n(\mathbf{x}_{n+1}^{(k)}, \mathbf{X}_{n+1}^{(k)}, \mathcal{T}_h) \\ &= I_h(\mathbf{x}_{n+1}^{(k)}, \mathbf{X}_{n+1}^{(k)}, \mathcal{T}_h) + \alpha \underbrace{\|\mathbf{X}_{n+1}^{(k)} - \mathbf{X}_n\|^2}_{\geq 0} \\ &\geq I_h(\mathbf{x}_{n+1}^{(k)}, \mathbf{X}_{n+1}^{(k)}, \mathcal{T}_h) \geq I_h(\mathbf{x}_{n+1}, \mathbf{X}_{n+1}, \mathcal{T}_h). \end{aligned} \quad (4.39)$$

Hence, the sequence  $(I_h(\mathbf{x}_n, \mathbf{X}_n))_{n \in \mathbb{N}}$  generated by the viscous-type relaxation is indeed monotonically decreasing.

**Remark 4.5.3.2** *The relaxation parameter  $\alpha$  is obtained from*

$$\alpha = \inf\{\alpha \in \mathbb{R}_+ \mid \lambda_{\min}(\nabla^2 I_n(\alpha)) > TOL\}, \quad (4.40)$$

with  $\lambda_{\min}$  denoting the smallest eigenvalue. In practice, the condition  $\lambda_{\min}(\nabla^2 I_n(\alpha)) > TOL$  is only checked for certain values of  $\alpha$ .

## 4.6 Numerical examples

In this section, the applicability, performance and robustness of the proposed viscous-type relaxation are demonstrated by means of two numerical examples. Stretching of a slab is analyzed in Subsection 4.6.1. This example highlights two important facts. First, without a relaxation, the mechanical minimization problem is ill-posed. Second, allowing the nodes to move on the boundaries is essential. Otherwise, these boundary conditions induce topological constraints that limit the range of attainable meshes. The second example presented in Subsection 4.6.2 is a VALE computation of a uniaxial tensile test of a notched specimen. It illustrates that anisotropic meshes are, in general, superior to their isotropic counterparts.

### 4.6.1 Stretching of a slab

The first example concerns the stretching of a slab of dimensions  $L \times L \times L/4$ . The slab is clamped on two opposite sides and is subjected to prescribed extensional displacements. The nominal stretch ratio is 1.5 and the entire deformation is applied in one step. The discretization of the domain is coarse and contains 80 elements. In all examples, the material is neo-HOOKEAN with strain-energy density

$$\Psi(\mathbf{F}) = \frac{1}{2}\lambda \log^2 J + \frac{1}{2}\mu (\mathbf{F} : \mathbf{F} - 3 - 2 \log J). \quad (4.41)$$

In calculations the LAMÉ constants are set to  $\lambda = 12115.38 \text{ MN/m}^2$  and  $\mu = 8071.92 \text{ MN/m}^2$ , respectively. A similar problem was analyzed in [MUELLER & MAUGIN 2002] and [ASKES, KUHLE & STEINMANN 2004]. However, in contrast to those references, three-dimensional tetrahedral elements are used here and the nodes are allowed to move within the boundary.

The undeformed and the computed deformed configuration in the absence of mesh adaptation are shown in Fig. 4.2. The energy  $I_h$  corresponding to this solution is  $I_h^{(1)} = 577.859 \text{ MNm}$ . By way of comparison, the results obtained by means of the variational  $r$ -adaptive scheme are shown in Fig. 4.3. As may be observed in this figure, the

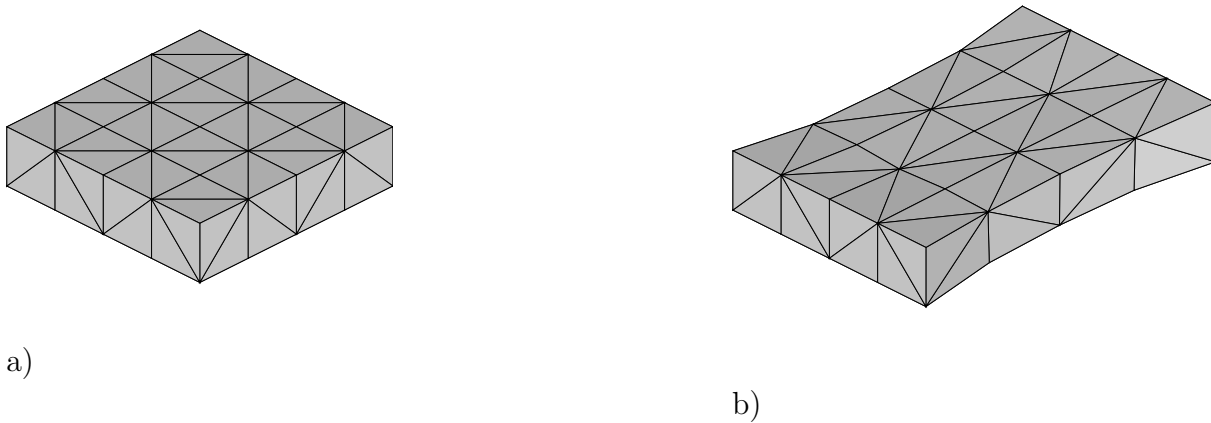


**Figure 4.2:** Stretching of a neo-HOOKEan hyperelastic block. Fixed-mesh solution: a) undeformed configuration; b) deformed configuration

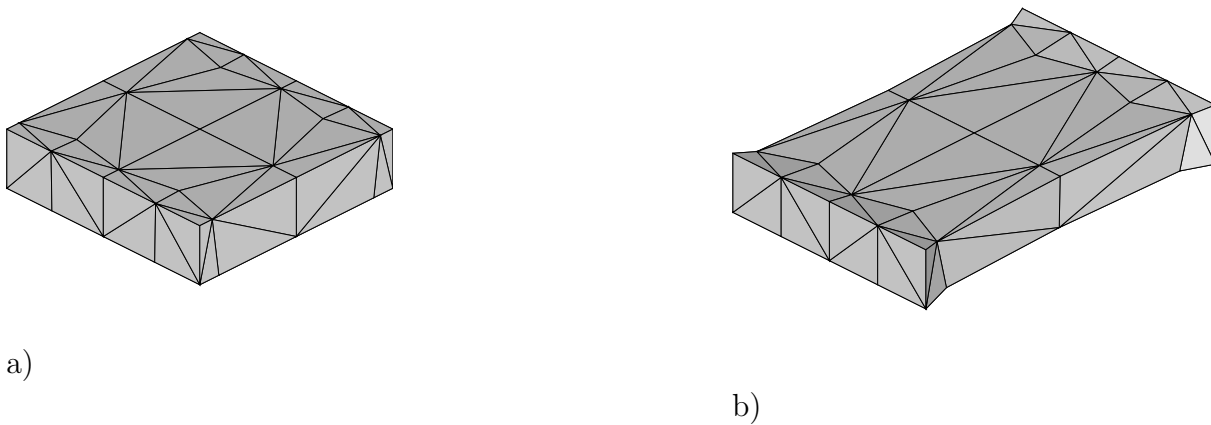


**Figure 4.3:** Stretching of a neo-HOOKEan hyperelastic block.  $r$ -adapted solution: a) undeformed configuration; b) deformed configuration

nodes move towards the clamped sides. The energy resulting from the adaptive scheme is  $I_h^{(2)} = 562.300$  MNm, or a 2.8% reduction with respect to the non-adaptive scheme. In order to gage the effect of the motion of the nodes on the boundary, an additional computation is performed by constraining the respective degrees of freedom on two boundary faces. The optimized undeformed and deformed configurations are shown in Fig. 4.4. The resulting energy is now  $I_h^{(3)} = 569.678$  MNm, which represents a 1.4% reduction from the non-adaptive energy  $I_h^{(1)}$ . As expected,  $I_h^{(1)} \geq I_h^{(3)} \geq I_h^{(2)}$  and the addition of constraints on the motion of boundary nodes wipes out about half the energy gain due to adaption. This test suggests that the motion of the boundary nodes is important and cannot be neglected in general.

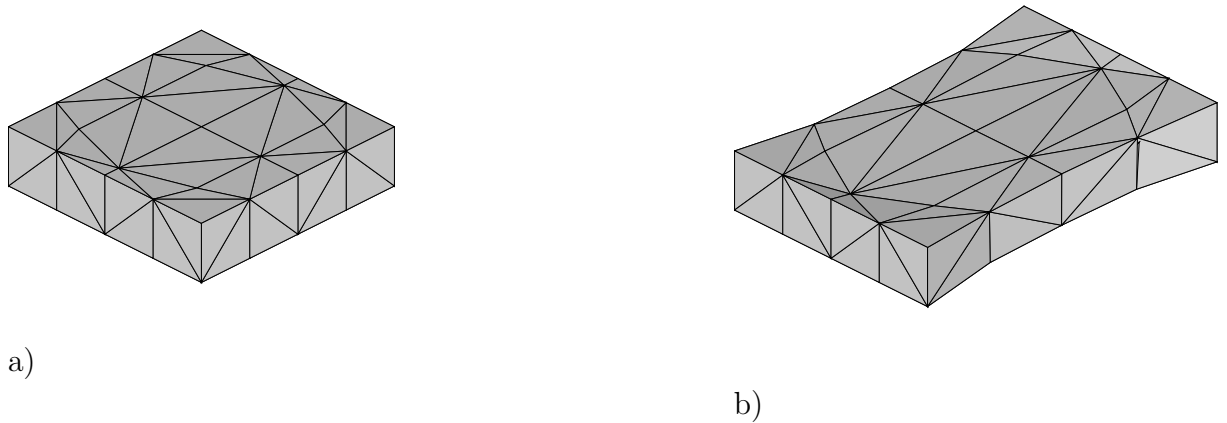


**Figure 4.4:** Stretching of a neo-HOOKEan hyperelastic block.  $r$ -adapted solution with surface nodes constrained on two boundary faces: a) undeformed configuration; b) deformed configuration

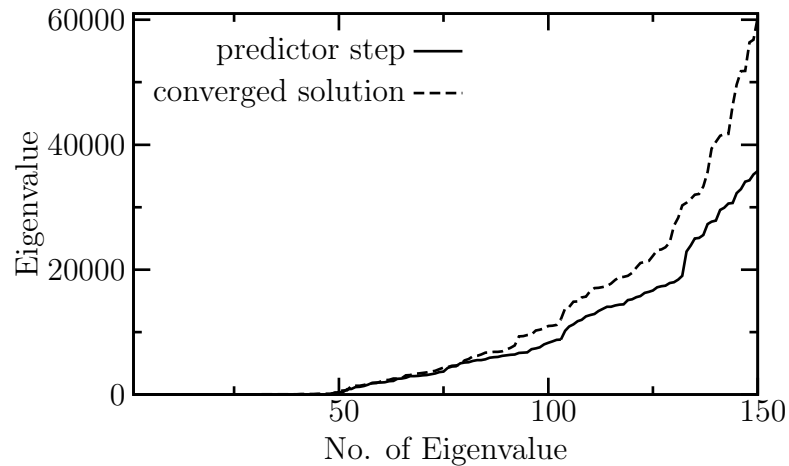


**Figure 4.5:** Stretching of a neo-HOOKEan hyperelastic block. Distribution of the eigenvalues of  $\nabla^2 I_h$ : a) for a predictor step defined by the standard minimization principle (4.9); b) for the converged solution

The convexity of the minimization problem and the singularity of the HESSIAN can be monitored by means of the eigenvalues of  $\nabla^2 I_h$ , Fig. 4.5. The dashed and solid lines in the figure correspond to the converged  $r$ -adaptive scheme and a predictor step, respectively. Owing to the large number of null or nearly-null eigenvalues the problem is highly singular. Furthermore, the smallest eigenvalue obtained for the predictor step is  $\lambda_{\min} = -5.19745$  which illustrates the lack of convexity of the problem. In consequence, a direct NEWTON's iteration applied to the unregularized problem does not converge in general. However, it should be noted that two-dimensional problems and boundary motion constraints, such as considered by [ASKES, KUHLE & STEINMANN 2004], add to the stability of the problem.

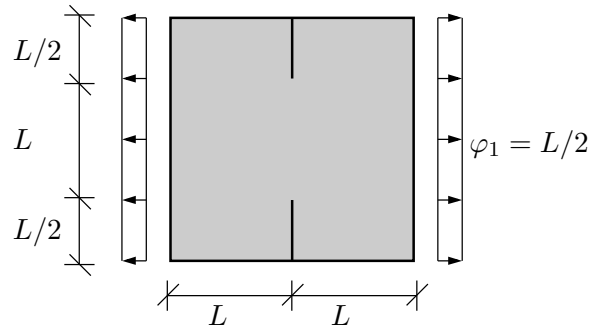


**Figure 4.6:** Numerical study of a uniaxial tensile test of a notched specimen: dimensions and loading conditions; thickness of the solid  $L$

Under those conditions it is often possible to solve for the  $r$ -adapted solution directly without regularization.

## 4.6.2 Uniaxial tensile test of a notched specimen

Next, the  $r$ -adaption is applied to the numerical analysis of a uniaxial tensile test of a notched specimen. The dimensions of the structure and the boundary conditions are depicted in Fig. 4.6. The material model is the one used in the previous subsection. Since the structure is symmetric with respect to three orthogonal surfaces, only an eight of the system is discretized.

### 4.6.2.1 $r$ -adaption based on viscous-type relaxation of configurational forces

The initial finite element mesh is shown in Fig. 4.7a). It contains 1280 tetrahedral elements. First, the deformation of the body is computed by the standard minimization principle (4.10). The results are shown in Fig. 4.7b). The energy associated with this solution is about  $I_h^{(1)} = 5.557644 \cdot 10^4$  MNm.

The results obtained from the  $r$ -adaption are given in Fig. 4.8. As in the previous example, the nodes move towards the region of highest energy density, i. e., towards the crack tip. For this example, the proposed adaption leads to an improvement of the solution of about 3.9% ( $I_h^{(2)} = 5.350944 \cdot 10^4$  MNm).

### 4.6.2.2 On enforcing small aspect ratios of the finite elements

For some applications it is important to avoid elements with large aspect ratios. For instance, if iterative solvers are used, the number of necessary iterations depends on the condition of the HESSIAN. It is well known that this number converges to infinity for degenerated elements, cf. [SHEWCHUK 2002]. Thus, highly distorted elements can slow

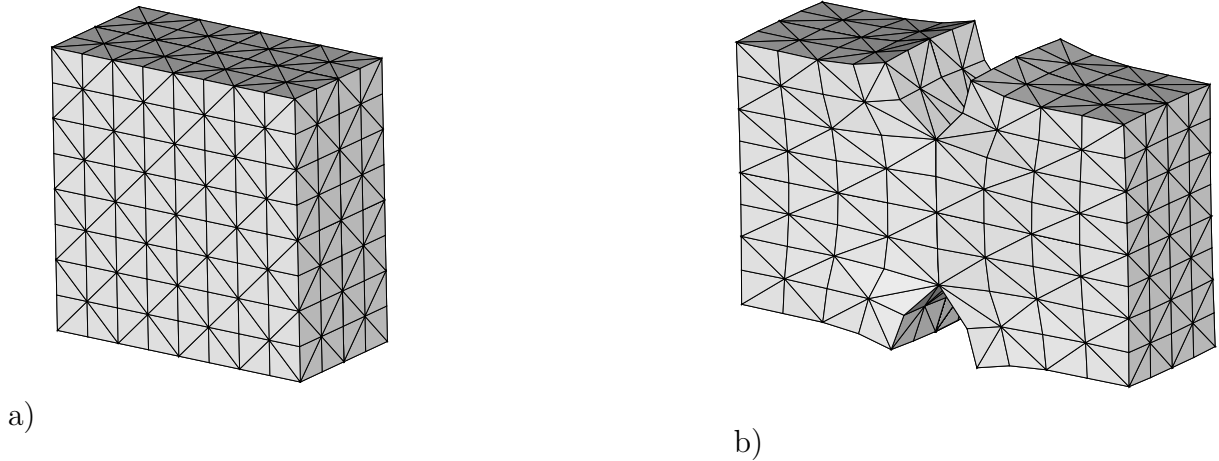


**Figure 4.7:** Numerical study of a uniaxial tensile test of a notched specimen: results computed from the standard problem (4.9): a) undeformed mesh; b) deformed mesh

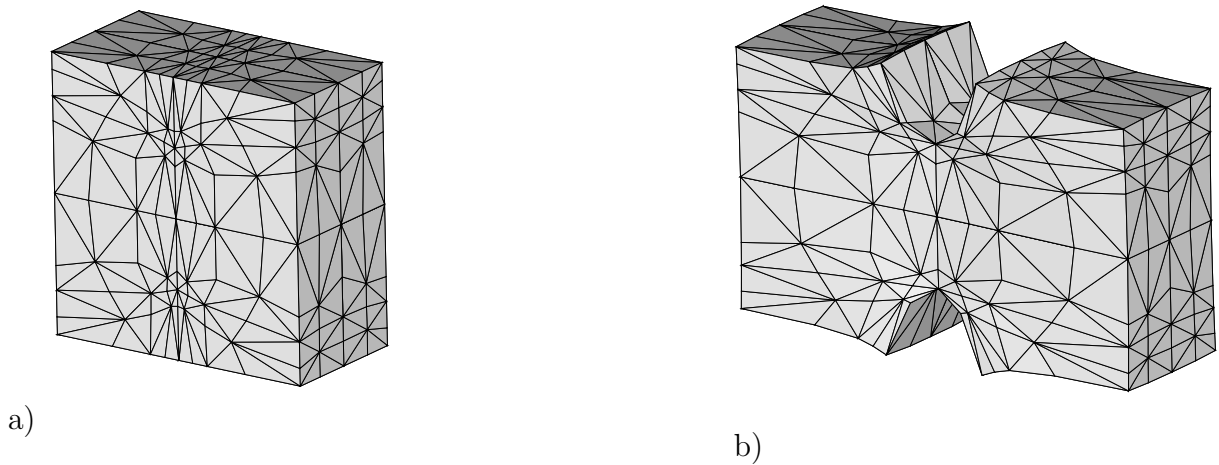


**Figure 4.8:** Numerical study of a uniaxial tensile test of a notched specimen: results obtained from the proposed r-adaption: a) undeformed mesh; b) deformed mesh

down the computation. As a consequence, the effect of enforcing small aspect ratios of the finite elements on the solution is analyzed in this paragraph. For that purpose, an additional r-adaption is performed. However, the viscous-type relaxation is not used anymore. Instead, the alternative relaxation

$$\tilde{I}(\mathbf{x}_h, \mathbf{X}_h) = I_h(\mathbf{x}_h, \mathbf{X}_h) + \tilde{\alpha} I_{\text{geo}}(\mathbf{X}_h) \quad (4.42)$$

is adopted here. According to Eq. (4.42), the objective function to be minimized consists of the classical physical energy  $I_h$  and a purely geometrical part. More specifically,  $I_{\text{geo}}$

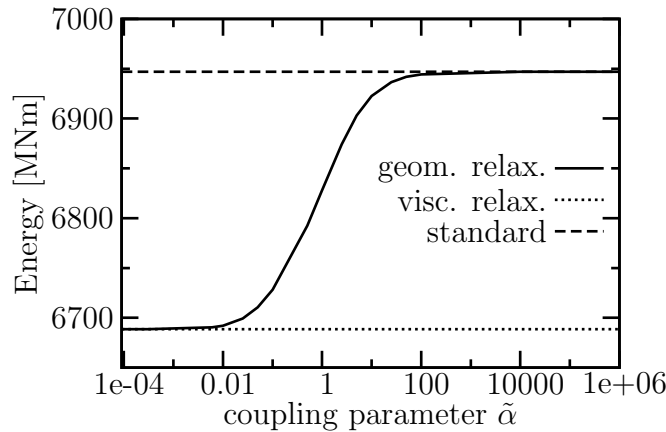


**Figure 4.9:** Numerical study of a uniaxial tensile test of a notched specimen: energy  $I_h$  computed by using different strategies: optimization of  $\tilde{I}$  according to Eq. (4.42) (geom. relax.); the viscous-type relaxation (4.33) (visc. relax.); optimization of  $I_h$  with respect to  $\mathbf{x}_h$  only (standard). The energy corresponds to an octant of the system.

depends only on the geometry of the undeformed configuration. Clearly, since

$$\frac{\partial \tilde{I}}{\partial \mathbf{x}_h} = \frac{\partial I_h}{\partial \mathbf{x}_h}, \quad (4.43)$$

every minimum of Eq. (4.42) fulfills the discrete equilibrium conditions in the sense of NEWTON. However, the configurational forces are not necessarily in equilibrium. Based on a suitable choice for  $I_{\text{geo}}$ , elements showing a relatively large aspect ratio can be penalized. In this paragraph,  $I_{\text{geo}}$  is specified by

$$I_{\text{geo}} = \sum_{e=1}^{n_{\text{ele}}} f^{-1}(\Omega^e), \quad (4.44)$$

with  $f$  denoting a *tetrahedral shape measure*, cf. Remark 4.6.2.1 and Appendix A. This function assures that  $I_{\text{geo}}$ , and consequently  $\tilde{I}$ , converge to infinity, if an element degenerates (its volume converges to zero). Evidently, the minimum of  $I_{\text{geo}}$  is attained for meshes consisting of elements with relatively small aspect ratios.

Based on minimizing Eq. (4.42) an additional  $r$ -adaption is performed. As a shape measure, a function  $f$  depending on the element condition number is used, cf. [KNUPP 2000A; KNUPP 2000B; FREITAG & KNUPP 2002]. More details can be found in Appendix A. Again, the minimization problem is computed by applying NEWTON's method, together with the line search strategy according to Remark 4.5.2.1.

The physical energies  $I_h$  predicted by the optimization problem  $\inf \tilde{I}(\mathbf{x}_h, \mathbf{X}_h)$  are summarized in Fig. 4.9. Obviously, the results depend on the regularization parameter  $\tilde{\alpha}$ . For the sake of comparison, the energies as obtained from the viscous-type relaxation

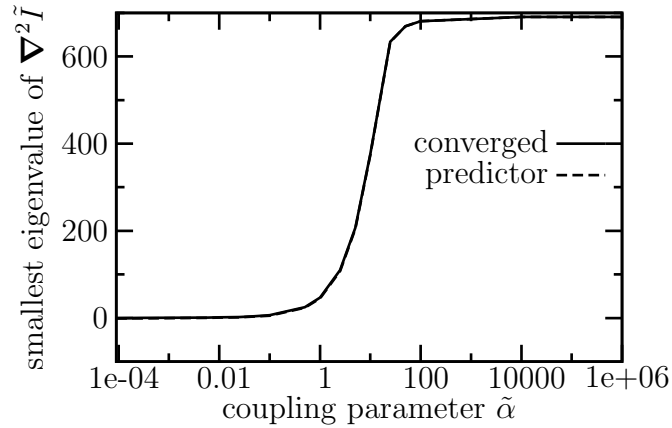


**Figure 4.10:** Numerical study of a uniaxial tensile test of a notched specimen: smallest eigenvalues of  $\nabla^2 \tilde{I}$ : a) for a predictor step; b) for the converged solution

discussed in Subsection 4.5.3. and the standard formulation ( $\mathbf{X}_h$  is kept fixed) are shown as well. It can be seen that enforcing elements with small aspect ratios (large values of  $\tilde{\alpha}$ ) conflicts with minimizing the physical energy of the mechanical system. In the case of the analyzed example, the initial discretization represents the minimum of the problem  $\inf I_{\text{geo}}$ . As a consequence, the solution associated with large values of  $\tilde{\alpha}$  is identical to the classical approach ( $\mathbf{X}_h = \text{const}$ ). On the other hand, if  $\tilde{\alpha}$  is sufficiently small, the solution of  $\inf \tilde{I}$  converges to the one predicted by the purely mechanical minimization problem  $\inf I_h$ . It is evident from this example that the optimum of the purely geometrical criterion  $\inf I_{\text{geo}}$  and that of  $I_h$  do not coincide in general. Thus, from a mechanical point of view, enforcing small aspect ratios of the elements does not make sense.

It is noteworthy that Eq. (4.44) indeed eliminates the ill-posedness of the original problem  $\inf I_h$ . More precisely, if  $\tilde{\alpha}$  is chosen sufficiently large, the term  $\tilde{\alpha} I_{\text{geom}}$  makes the HESSIAN of  $\tilde{I}$  positive definite. This effect is illustrated in Fig. 4.10.

The analysis of the presented numerical example leads to the idea to consider the minimization problem (4.42) for sufficiently small values of  $\tilde{\alpha}$  alternatively to the viscous-type relaxation. This approach would be physically and mathematically sound, since the mechanical problem (the minimum of  $I_h$ ) does not change, and the well-posedness is enforced by elements having small aspect ratios. Unfortunately, this method does not work in general. For instance, if it is applied to the example in Subsection 4.6.1, the problem requires a relatively large value of  $\tilde{\alpha}$  to eliminate the ill-posedness. Hence, the effect of the term  $I_{\text{geom}}$  becomes more dominant and as a result, the difference between the physical energies  $I_h$  predicted by the problems  $\inf \tilde{I}$  and  $\inf I_h$  is significant.

**Remark 4.6.2.1** *Several different definitions of tetrahedral shape measures can be found in the literature. A widely accepted one is given in [DOMPIERRE, LABBE & CAMERERO 1984]. Here, the defining criteria are re-written by using a different notation. A function  $f$  depending on the vertex coordinates  $\mathbf{X}^e = \{\mathbf{X}_1^e, \mathbf{X}_2^e, \mathbf{X}_3^e, \mathbf{X}_4^e\}$  of a tetrahedron  $e$  is*

referred to as a tetrahedral shape measure, if the following properties are fulfilled:

- $f \in \mathcal{C}(\mathbf{X}^e, [0, 1])$
- $f = 0 \iff e$  is degenerated
- $f = 1 \iff e$  is ideal (all edges have the same length)
- $f(\mathbf{X}^e) = f(\tilde{\mathbf{X}}^e)$  with  $\tilde{\mathbf{X}}_i^e = c \mathbf{Q} \mathbf{X}_i^e + \mathbf{a}$ ,  $\forall c > 0$ ,  $\forall \mathbf{a} \in \mathbb{R}^3$  and  $\forall \mathbf{Q} \in SO(3)$

The last point enumerated enforces that the shape measure is invariant with respect to translations, rotations and the size of the considered element. It should be noted that the invariance of  $f$  with respect to the size of the elements was not postulated in [DOMPIERRE, LABBE & CAMERERO 1984]. Further details on tetrahedral shape measures are given in Appendix A.

## 4.7 Node migration in and out of the boundary

Throughout the preceding developments the constraints have been enforced that surface nodes remain in the surface and move within their corresponding surface component, namely within their faces or edges; and that vertices in the boundary representation of the domain remain fixed. As a consequence, the number of nodes in every edge and face of the boundary remains constant. These boundary conditions introduce topological constraints that limit the range of attainable meshes. A more general and flexible approach that allows nodes to migrate in and out of the boundary is presented next.

Node migration from the interior to the boundary can happen spontaneously during the solution scheme presented in the foregoing and requires no additional algorithmic development. When an interior node collides with the boundary, zero volume elements, or *slivers*, are generated. These slivers are then eliminated during the mesh-improvement phase of the solution.

### 4.7.1 Fundamentals

In order to have a practical  $O(N)$  method for allowing nodes to migrate out of the boundary two approximations are introduced: the problem is localized by considering one boundary node and its ring of adjacent elements in turn; and the energy release is estimated locally by fixing the remaining nodes of the model. Thus, the algorithm is applied by traversing the boundary nodes in turn. For each node that is not a vertex the ring of elements adjacent to the node is identified (the *local neighborhood*). Next, the node is pushed inside its local neighborhood and the local mesh is reconstructed. In so

doing, care must be exercised in ensuring that all vertices, edges and faces in the boundary representation of the domain be preserved. Based on this new mesh topology, a local optimization is effected. It consists of: equilibrating the node, now in the interior; and optimizing its position and the local triangulation. In the course of this local optimization the displacements and positions of all remaining nodes in the model are held fixed. The move is accepted, if the energy release  $-\Delta I_{\text{loc}}$  thus estimated is positive and exceeds a prespecified tolerance. Otherwise, the node is left unchanged.

The complete  $r$ -adaption procedure accounting for boundary node migration is:

1. Initialize  $\mathbf{x}_h = \mathbf{x}_0$ ,  $\mathbf{X}_h = \mathbf{X}_0$ , set  $n = 0$ .
2. Compute the solution  $(\mathbf{x}_{n+1}, \mathbf{X}_{n+1})$  of the regularized problem (4.33) using a NEWTON iteration.
3. Migrate boundary nodes into the interior.
4. If  $\|\mathbf{x}_{n+1} - \mathbf{x}_n\| < \text{TOL}$ ,  $\|\mathbf{X}_{n+1} - \mathbf{X}_n\| < \text{TOL}$  and no boundary nodes migrate into the interior exit.
5. Reset  $n$  to  $n + 1$ , go to 2.

As in the preceding cases, the iterative procedure produces a monotonically decreasing sequence of energies. Consequently, under displacement control, the energies are bounded below and, hence, the energy is guaranteed to converge.

It is noted that the energy release  $-\Delta I_{\text{loc}}$  computed from the local procedure is a lower bound on the maximum energy release  $-\Delta I_h$  attainable by the migration of the node to the interior. This makes the scheme conservative, i. e., it tends to suppress node migration into the interior. Evidently, better local energy release estimates can be obtained – at some increase in computational complexity – by considering larger local neighborhoods of the boundary nodes including additional rings of elements. The algorithm guarantees that node migration from the boundary indeed lowers the energy of the body. In addition, the migration of each boundary node requires the solution of a local problem involving six degrees of freedom only, and the algorithm is  $O(N)$  as desired.

Considerable speed-up may also be achieved in some cases by a simple screening criterion based on the magnitude and direction of the configuration forces. Thus, if  $a$  is a surface node located at a point of smoothness of a face in the boundary representation of the domain,  $\mathbf{N}_a$  is the outward normal at  $a$  and  $\mathbf{R}_a$  is a component of  $\mathbf{R}$  at  $a$ , then

$$f_a = \mathbf{R}_a \cdot \mathbf{N}_a \quad (4.45)$$

is the configuration force tending to push the node into the interior. Equivalently,  $\mathbf{R}_a \cdot \mathbf{N}_a$  is the energy-release rate corresponding to an infinitesimal migration of the node into the

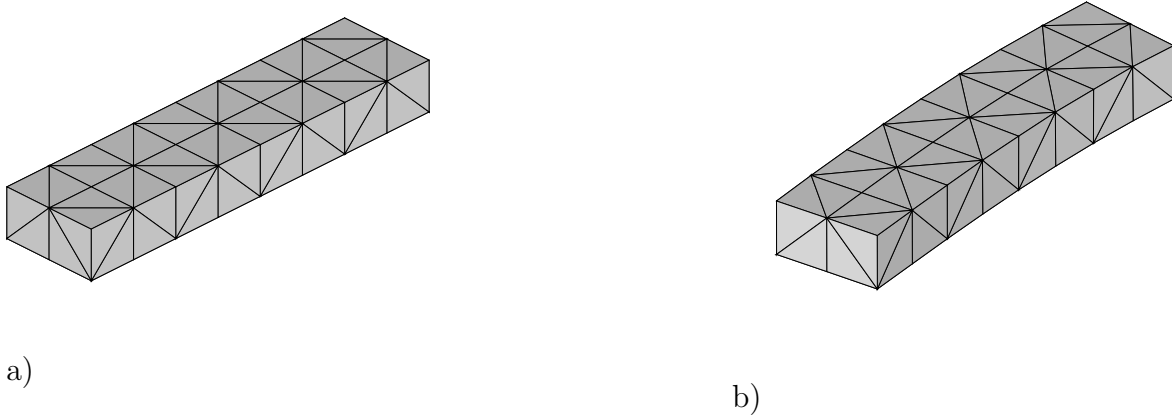


**Figure 4.11:** Bending of a neo-HOOKEan hyperelastic cantilever beam; fixed-mesh solution: a) undeformed configuration; b) deformed configuration

interior. If  $a$  is a non-smooth point of the boundary, the corresponding configurational force is

$$f_a = \max_{\mathbf{N}_a \in K_a} \mathbf{R}_a \cdot \mathbf{N}_a \quad (4.46)$$

where  $K_a$  is the outward normal cone at  $a$ . Applying Eq. (4.46), target surface nodes for possible migration into the interior are marked, if  $f_a$  exceeds a certain tolerance, and are skipped otherwise.

### 4.7.2 Example: Bending of a cantilever beam

The applicability as well as the efficiency of the proposed node migration algorithm is demonstrated by means of a numerical analysis of a bending problem. The cantilever beam is of dimensions  $L \times L/4 \times L/8$ . The tip of the beam is given a deflection of magnitude  $L/8$  at two nodes. The material is of neo-HOOKEan hyperelastic type with strain-energy density (4.41). The LAMÉ constants are set to  $\lambda = 12115.38 \text{ N/mm}^2$  and  $\mu = 8071.92 \text{ N/mm}^2$ , which corresponds to a YOUNG's modulus  $E = 21000 \text{ N/mm}^2$  and a POISSON's ratio  $\nu = 0.3$ . The energy tolerance for the termination of the iterative solution scheme equals  $1.0 \cdot 10^{-5}$ .

The initial discretization contains 54 nodes and 80 tetrahedral elements, Fig. 4.11a). By way of comparison, the deformation computed without adaption is shown in Fig. 4.11b). The corresponding energy is  $I_h^{(1)} = 57.0510 \text{ MNm}$ .

Next, the problem is recalculated by means of the proposed  $r$ -adaption procedure. First, node migration is not allowed. The resulting extended system has 202 degrees of freedom. The computed optimal node location is shown in the undeformed and deformed configurations in Figs. 4.12a) and Figs. 4.12b), respectively. It is evident from these figures

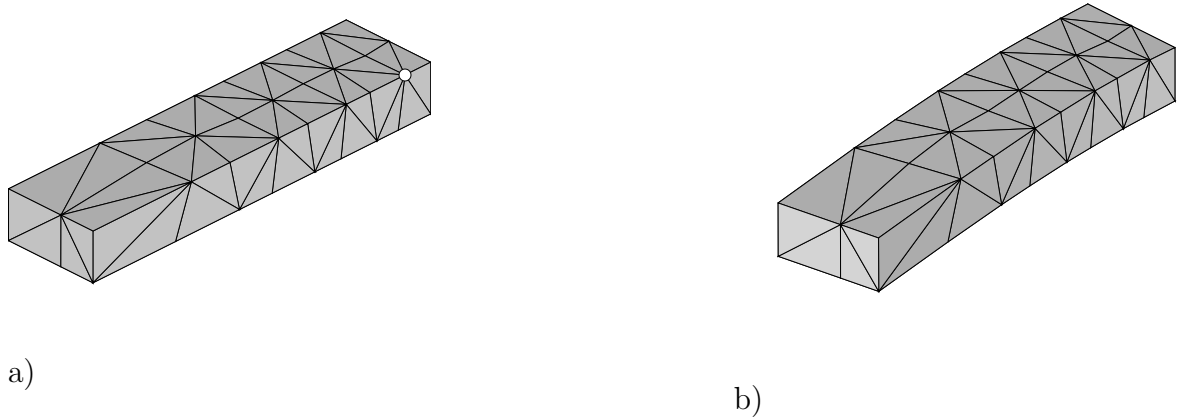


**Figure 4.12:** Bending of a neo-HOOKEan hyperelastic cantilever beam;  $r$ -adapted solution (without node migration to and from the surface): a) undeformed configuration; b) deformed configuration

that the nodes move towards the clamped end, i. e., towards the region of highest energy density. For this calculation, the corresponding energy is  $I_h^{(2)} = 52.9402$  MNm. Hence, the energy could be lowered by 7.8% compared to the fixed-mesh solution.

Finally, the problem is recomputed including  $r$ -adaption and node migration in and out of the surface. The surface node with the highest inward configurational force is marked by a white circle in Fig. 4.12a). This node ends up leaving the surface and entering the interior of the domain. The computed optimal node location and triangulation are shown in the undeformed and deformed configurations in Figs. 4.13a) and Figs. 4.13b), respectively. The final mesh contains 86 elements. The reconstruction of the mesh in the vicinity of the clamped end is particularly noteworthy. The final energy computed by means of the complete  $r$ -adaption procedure is  $I_h^{(3)} = 52.2553$  MNm, corresponding to a 9.2% reduction with respect to the fixed-mesh solution.

## 4.8 Extension of the VALE formulation to standard dissipative media

The VALE formulation as discussed in this section requires that the considered mechanical problem is characterized by a variational structure. More specifically, the primary variable has to be governed by a minimization principle. Since, according to Section 2.5, standard dissipative media comply with this requirement, the presented VALE method can be applied to such models in principle.

However, a careful analysis of the advocated VALE formulation reveals two problems. First, standard dissipative media such as plasticity theories are based on rate equations.

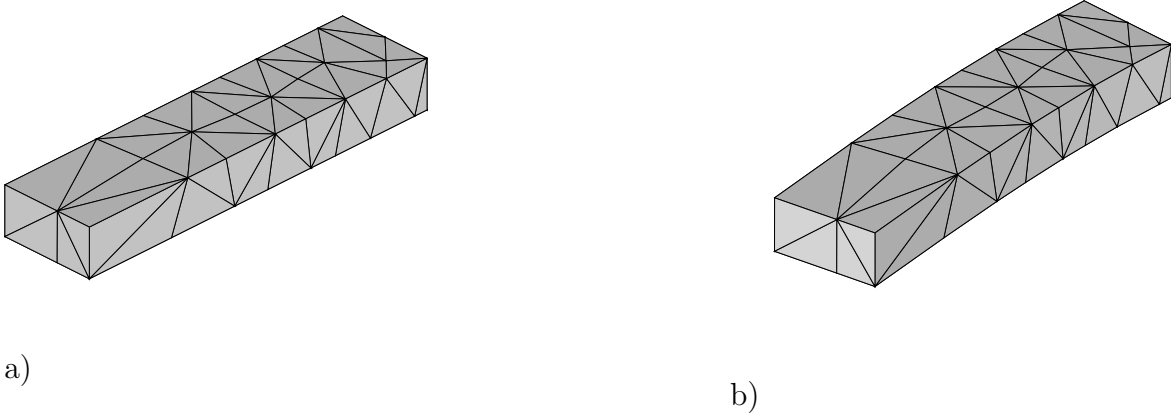


**Figure 4.13:** Bending of a neo-HOOKEAN hyperelastic cantilever beam;  $r$ -adapted solution and node migration to and from the surface: a) undeformed configuration; b) deformed configuration. The surface node marked with a white circle in Fig. 4.12a) migrates into the interior of the domain.

For instance, the evolution equations of the plastic velocity gradient and the internal variables according to Eqs. (2.46) or (2.49) are rate dependent. Such equations include the material time derivative, i. e.,

$$\dot{f} = \left. \frac{\partial f}{\partial t} \right|_{\mathbf{X}=\text{const}}. \quad (4.47)$$

Adopting this to a VALE framework leads to

$$\begin{aligned} \dot{f} &= \left. \frac{\partial f}{\partial t} \right|_{\xi=\text{const}} + \frac{\partial f}{\partial \xi} \cdot \frac{\partial \xi}{\partial \mathbf{X}} \cdot \frac{\partial \mathbf{X}}{\partial t} \\ &= \left. \frac{\partial f}{\partial t} \right|_{\xi=\text{const}} + \frac{\partial f}{\partial \xi} \cdot \mathbf{F}^{-1} \cdot \dot{\mathbf{X}} \end{aligned} \quad (4.48)$$

(see Fig. 4.1). Thus, the derivative consists of two parts. While the first of those is standard, the second term is related to advection. Clearly in classical LAGRANGIAN formulations  $\dot{\mathbf{X}} = \mathbf{0}$  and hence, this term drops out. However, within the proposed VALE framework, advection has to be taken into account what can cause numerical problems, cf.[ARMERO & LOVE 2003].

The other problem associated with an extension of the VALE formulation to standard dissipative media is related to the transfer of the history variables. Since a variation of  $\mathbf{X}_h$  leads to a change in the triangulation, the positions of the integration points change as well. Consequently, the history variables which are typically defined pointwise (at the integration points) have to be transferred. Again, this problem does not occur in a classical LAGRANGIAN formulation. It is noted that the problems just discussed are strongly related to one another.

Fortunately, both problems can be solved. According to [ORTIZ & QUIGLEY 1991] (see also [RADOVITZKY & ORTIZ 1999]), the required transfer operator of the history variables follows consistently from the variational principle. However, this operator is not unique, i. e., it depends on the interpolation of the internal variables and thus, several suitable procedures exist. In the present work, those variables are assumed to be piecewise constant over the VORONOI cell containing the GAUSS point  $g$  of the element  $e$ . As mentioned in [RADOVITZKY & ORTIZ 1999], for such an approximation, the transfer of the history variables simplifies considerably. More specifically, the state variable at a new quadrature point is simply the state variable of the nearest old quadrature point. This procedure shows two important properties. First, the numerical implementation is straightforward and if it is coded properly, it is very efficient. Second, internal constraints such that  $\det \mathbf{F}^p = 1$  are preserved.

If the approximation of the history variable  $f$  is constant over the VORONOI cell containing the GAUSS point  $g$  of the element  $e$ , the (approximated) material time derivative yields

$$\dot{f} = \left. \frac{\partial f}{\partial t} \right|_{\boldsymbol{\xi}=\text{const}}, \quad \text{since} \quad \frac{\partial f}{\partial \boldsymbol{\xi}} = \mathbf{0}. \quad (4.49)$$

As a result, the advective term drops out and the standard case is obtained. Consequently, the only crucial modification necessary for the extension of the VALE formulation to standard dissipative media is the implementation of a data structure allowing to compute efficiently the nearest old quadrature point of a given point.

## 4.9 Further improvements of the VALE formulation

In this chapter the optimization problem

$$\inf_{\mathbf{x}_h, \mathbf{X}_h} I_h(\mathbf{x}_h, \mathbf{X}_h, \mathcal{T}_h) \Big|_{\mathcal{T}_h=\text{const}} \quad (4.50)$$

has been considered. That is, the connectivity of the mesh has been kept fixed. However, according to [THOUTIREDDY 2003; THOUTIREDDY & ORTIZ 2004], this may introduce strong topological – or *locking* – constraints. As a result, it may restrict the range of meshes that can be attained and, consequently, the quality of the solution. For this reason a method which improves the connectivity of the mesh is discussed in the next chapter.



# Chapter 5

## A variational-based remeshing strategy

In this chapter, a novel variational-based remeshing strategy is presented. The advocated procedure can be applied to any finite element formulation provided the primary variable follows from an extremum principle such as the principle of minimum potential energy or the postulate of maximum dissipation characterizing standard dissipative media. Based on so-called LAWSON flips, the topology of an initial triangulation is modified locally such that the solution associated with the new discretization is closer to the analytical extremum. As a consequence, the proposed strategy guarantees an improvement of the solution.

### 5.1 Introduction

In the previous chapter, a variational r-adaption governed by the principle

$$\inf_{\mathbf{x}_h, \mathbf{X}_h} I_h(\mathbf{x}_h, \mathbf{X}_h, \mathcal{T}_h) \Big|_{\mathcal{T}_h = \text{const}} \quad (5.1)$$

has been developed. Evidently, the triangulation of a node set is not unique, and the discrete energy depends on the precise manner in which the node set is triangulated. [THOUTIREDDY 2003; THOUTIREDDY & ORTIZ 2004] proposed a VALE formulation in which they constrained the mesh so as to remain DELAUNAY at all times, and the DELAUNAY condition was enforced by means of local LAWSON flips [JOE 1989; JOE 1991]. In two dimensions and in the context of potential theory, the DELAUNAY triangulation does indeed minimize the energy of the body among all possible triangulations [RIPPA 1990]. However, in three dimensions and for general energies the DELAUNAY triangulation is not necessarily energy-minimizing. In the context of finite elasticity or standard dissipative media, where a (pseudo) principle of minimum potential is paramount, it is more natural

to demand that the mesh connectivity itself, in addition to the mesh geometry, be energy minimizing. Hence, the canonical extension of problem (5.1)

$$\inf_{\mathbf{x}_h, \mathbf{X}_h, \mathcal{T}_h} I_h(\mathbf{x}_h, \mathbf{X}_h, \mathcal{T}_h) \quad (5.2)$$

is considered. However, in contrast to the VALE formulation corresponding to Eq. (5.1), finding the energy-minimizing triangulation  $\mathcal{T}_h$  represents a discrete problem, i. e.  $I_h(\mathbf{x}_h, \mathbf{X}_h, \mathcal{T}_h)|_{\mathcal{T}_h=\text{const}} \in \mathcal{C}^n$  but  $I_h(\mathbf{x}_h, \mathbf{X}_h, \mathcal{T}_h)|_{(\mathbf{x}_h, \mathbf{X}_h)=\text{const}} : \mathbb{A} \rightarrow \mathbb{R}$  with  $\text{card}(\mathbb{A}) < \infty$  ( $n$  being sufficiently large). As a consequence, problem (5.2) requires different solution schemes compared to the VALE formulation driven by Eq. (5.1). For this reason, problem (5.2) is decomposed additively. First, the nodal coordinates are optimized by applying the methods discussed in the previous chapter, cf. Eq. (5.1). Subsequently, the optimization problem

$$\inf_{\mathcal{T}_h} I_h(\mathbf{x}_h, \mathbf{X}_h, \mathcal{T}_h) \Big|_{(\mathbf{x}_h, \mathbf{X}_h)=\text{const}} \quad (5.3)$$

is solved. More specifically, a staggered solution scheme is adopted. A novel, efficient procedure for finding the energy-minimizing triangulation according to problem (5.3) is presented in this chapter. It follows to a large extent [MOSLER & ORTIZ 2005].

## 5.2 Fundamentals

Let  $\mathcal{T}_h$  denote a particular triangulation of the node set defined, e. g., by means of a connectivity table. The connectivity table is subject to topological constraints ensuring that the triangulation of the node set defines a simplicial complex and the interpolation is conforming. Problem (5.3) is *discrete* as regards the connectivity optimization and, therefore, its exact solution is generally unattainable for large problems. For instance, for a two-dimensional mesh of  $N$  nodes [AICHHOLZER, HURTADO & NOY 2004] have obtained the lower bound  $0.092 \cdot 2.33^N$  on the number of possible triangulations, which is a staggering number for large meshes. Instead of attempting an exhaustive search of the absolute energy-minimizing triangulation, discretizations are determined in this chapter that are local minima of the energy, i. e., meshes that minimize the energy with respect to a certain class of variations.

According to [LAWSON 1972], any triangulation of a two-dimensional node set can be attained by means of a finite sequence of local transformations, or *edge swaps*. These transformations are sometimes called LAWSON flips [LAWSON 1986] and consist of swapping the diagonals of the quadrilateral defined by pairs of adjacent triangles, see Fig. 5.1. This strategy can be extended to  $n$ -dimensional triangulations [LAWSON 1986]. However, in three dimensions it is not known whether an arbitrary triangulation can be attained by the application of a finite sequence of local transformations to a given mesh. In three dimensions the local transformations represent all possible triangulations of five non-coplanar vertices of adjacent tetrahedra, cf. [LAWSON 1986]. These transformations can

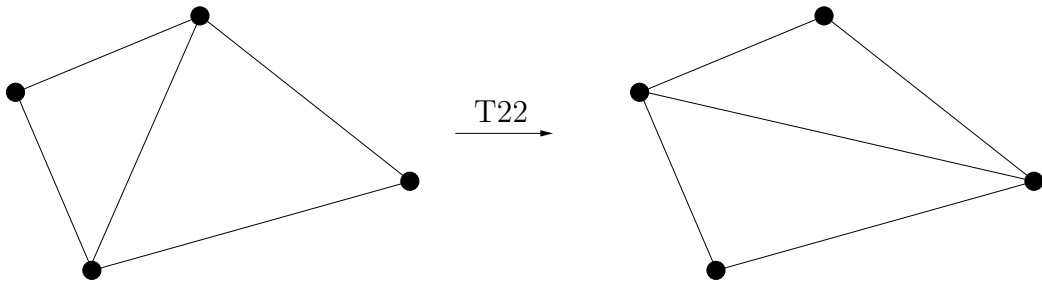


**Figure 5.1:** LAWSON flip in two dimensions

be classified as T23, T32, T22 and T44 according as to whether  $T_{ij}$  transforms  $i$  elements into  $j$  elements [JOE 1989; JOE 1991].

Suppose that  $(\mathbf{x}_h, \mathbf{X}_h)$  are fixed and let  $\mu(\mathcal{T}_h)$  denote the potential energy  $I_h(\mathbf{x}_h, \mathbf{X}_h, \mathcal{T}_h)$  regarded as a function of the connectivity  $\mathcal{T}_h$ . The objective is to determine the triangulation  $\mathcal{T}_h$  that minimizes  $\mu(\mathcal{T}_h)$  with respect to all local transformations  $T_{ij}$ . To this end, following [JOE 1995] the faces that are removed by the application of a local transformation are listed. Next, the face list is traversed sequentially and the local optimality of the faces with respect to the function  $\mu$  is evaluated. Thus, the face is said to be locally optimal if  $\mu$  is increased by the application of all transformations  $T_{ij}$  that remove the face. If a face is  $\mu$ -locally optimal then no transformation is applied. Otherwise, the best possible local transformation is selected. The algorithm terminates when all faces are locally optimal.

Evidently, by virtue of the energy criterion the application of a local transformation necessarily decreases the energy. However, a locally energy-minimizing mesh is not necessarily globally energy-minimizing, since only local optimality is ensured. Thus, the algorithm just described does not guarantee that a mesh not attainable by local transformations does not decrease the energy further. It should be noted that in applying the preceding algorithm a list of excluded faces that are not to be removed can be specified arbitrarily. In particular, the algorithm can be applied in such a way as to leave the boundary of the body unchanged. Hence, convexity of the domain is not required. It should also be carefully noted that the algorithm can be employed for minimization problems in general and that it is completely independent of the  $r$ -adaptive procedure described in the foregoing.

**Remark 5.2.0.1** *In two dimensions, a LAWSON flip does not change the number of elements of the discretization. Since any triangulation of a two-dimensional node set can be attained by means of a sequence of those local transformations, all triangulations contained in the set of admissible meshes have the same number of elements. Thus, a LAWSON flip can be interpreted as a transposition and the mapping between two discretizations as a permutation consisting of compositions of LAWSON flips. Clearly, the class of compositions spanned by the proposed remeshing strategy does not contain all admissible transformations. As a result, even in the two-dimensional case, the algorithm just described does not*

guarantee that the global minimum corresponding to problem (5.3) is attained. Following [JOE 1995], the solution of the algorithm can be further improved by enlarging the space of admissible triangulations. More specifically, criterion

$$I_h(\mathcal{T}_{\text{old}}) \geq I_h(\mathcal{T}_{\text{new}}) \quad (5.4)$$

is not only checked after each single LAWSON flip, but also after application of a composition containing more than one local transformation. For further details, the reader is referred to [JOE 1995].

**Remark 5.2.0.2** In what follows,  $x_i = (\mathbf{x}_h, \mathbf{X}_h)$  denotes the converged solution of triangulation  $\mathcal{T}_i$ . Then, the advocated algorithm generates a series of the type

$$I_h(\mathcal{T}_1, x_1) \geq I_h(\mathcal{T}_2, x_1) \geq \dots \geq I_h(\mathcal{T}_n, x_1), \quad (5.5)$$

i. e., the nodal coordinates are fixed, but the interpolation changes. Clearly,

$$I_h(\mathcal{T}_i, x_1) \geq I_h(\mathcal{T}_i, x_i) \quad \forall i \in \{1, \dots, n\} \quad (5.6)$$

and hence,

$$I_h(\mathcal{T}_1, x_1) \geq I_h(\mathcal{T}_n, x_n). \quad (5.7)$$

As a consequence, the proposed algorithm indeed improves the quality of the solution. However, it should be noted that the inequality

$$I_h(\mathcal{T}_i, x_i) \geq I_h(\mathcal{T}_j, x_j) \quad i < j \quad (5.8)$$

does not hold, in general. Consequently, there is no guarantee that the triangulation  $\mathcal{T}_n$  is better than any of the  $\mathcal{T}_i$ 's for  $i \in \{2, \dots, n-1\}$ . Clearly, Ineq. (5.8) can be enforced by equilibrating every new triangulation  $\mathcal{T}_i$ . However, such a strategy is very inefficient, since it requires the computation of several large optimization problems.

### 5.3 Coupling of the energy-based remeshing strategy with variational VALE formulations

Energy-driven mesh-optimization transformations can be built into the  $r$ -adaption procedure according to Chapter 4 simply as follows:

1. Initialize  $\mathbf{x}_h = \mathbf{x}_0$ ,  $\mathbf{X}_h = \mathbf{X}_0$ ,  $\mathcal{T}_h = \mathcal{T}_0$ , set  $n = 0$ .
2. Compute the solution  $(\mathbf{x}_{n+1}, \mathbf{X}_{n+1}, \mathcal{T}_n)$  of the regularized problem (4.33) by a NEWTON iteration.
3. Perform energy-minimizing mesh transformations to obtain  $(\mathbf{x}_{n+1}, \mathbf{X}_{n+1}, \mathcal{T}_{n+1})$ .

4. If  $\|\mathbf{x}_{n+1} - \mathbf{x}_n\| < \text{TOL}$ ,  $\|\mathbf{X}_{n+1} - \mathbf{X}_n\| < \text{TOL}$  and  $\mathcal{T}_n = \mathcal{T}_{n-1}$  exit.
5. Reset  $n$  to  $n + 1$ , go to 2.

Again, the iterative procedure produces a monotonically decreasing sequence of energies and since, under displacement control, the energy is bounded below, the energy is guaranteed to converge. Mesh transformations become important and need to be performed in the course of  $r$ -adaptation. Indeed, the motion of the nodes may lead to mesh entanglement if the transformations are not performed. Conversely, a constant mesh connectivity constitutes a topological constraint that severely limits the meshes that can be attained by  $r$ -adaptivity.

## 5.4 Numerical examples

The applicability as well as the performance of the local remeshing algorithm are demonstrated by means of two examples. While in Subsection 5.4.1, the triangulation of a cantilever slab is optimized using energy-driven LAWSON flips, the efficiency of the coupling of the energy-based remeshing strategy with the VALE formulation as discussed in Chapter 4 is illustrated in Subsection 5.4.2 where a notched beam subjected to bending is analyzed numerically.

### 5.4.1 Cantilever slab

First, the variational remeshing strategy is applied to the analysis of the cantilever slab shown in Figs. 5.2 and 5.3. The dimensions of the slab are  $L \times L \times L/4$ . At the left end the structure is clamped and at the right end a vertical displacement of magnitude  $L/5$  is prescribed at the top of the slab. For the material response, a hyperelastic model defined by the potential (4.41) is adopted. The LAMÉ constants are set to  $\lambda = 12115.38 \text{ N/mm}^2$  and  $\mu = 8071.92 \text{ N/mm}^2$ . They correspond to a YOUNG's modulus  $E = 21000 \text{ N/mm}^2$  and a POISSON's ratio  $\nu = 0.3$ .

At first, the deformation is computed according to the standard problem  $\inf I_h(\mathbf{x}_h)$ , i. e., both the connectivity as well as the nodal coordinates with respect to the undeformed configuration are kept fixed. Subsequently, the proposed remeshing strategy is applied and the deformed configuration is computed again using the minimization problem  $\inf I_h(\mathbf{x}_h)$ .

Two different initial meshes are considered. The results are shown in Figs. 5.2 and 5.3.

According to these figures, the proposed algorithm leads to a remeshing of both initial triangulations. With an initial energy of 18.0995 MNm (16.1732 MNm) and an improved energy of 17.8216 MNm (15.9968 MNm), the reduction of energy is about 1.6% (1.1%) in the case of the coarse (fine) mesh.

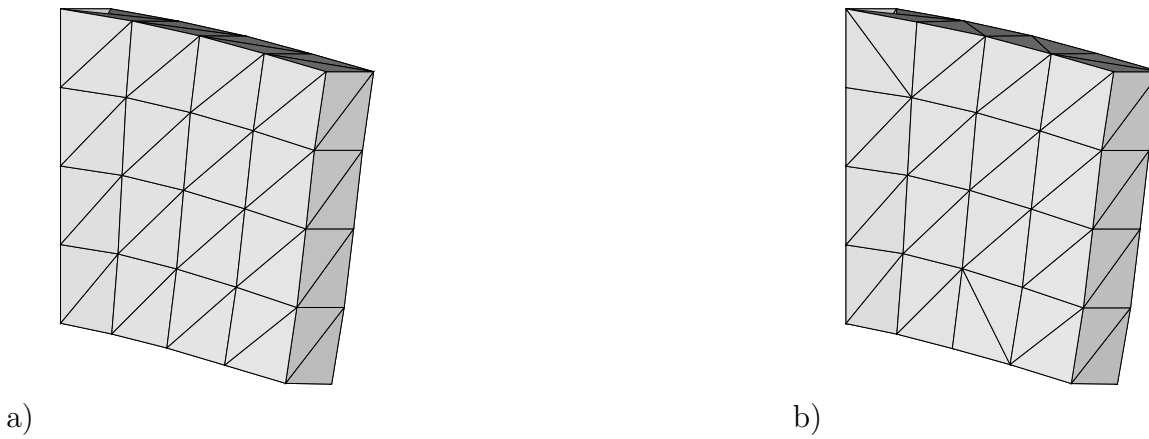


**Figure 5.2:** Numerical study of the energy-based remeshing strategy: deformed configuration before and after applying the energy-based remeshing strategy. The initial and the final mesh contain 50 nodes and 96 tetrahedral elements.



**Figure 5.3:** Numerical study of the energy-based remeshing strategy: deformed configuration before and after applying the energy-based remeshing strategy. The initial mesh contains 243 nodes and 768 tetrahedral elements. The final mesh consists of 767 elements.

It is noteworthy that both meshes illustrated in Fig. 5.2 are equivalent from a purely geometrical point of view. More precisely, all elements shown in Fig. 5.2 have the same quality in the sense of tetrahedral shape measures, cf. Remark 4.6.2.1 and Appendix A. This follows from the fact that such a measure must be invariant to translations and rotations. Hence, the energy-based remeshing strategy indeed differs from purely geometrically based mesh improvement algorithms.

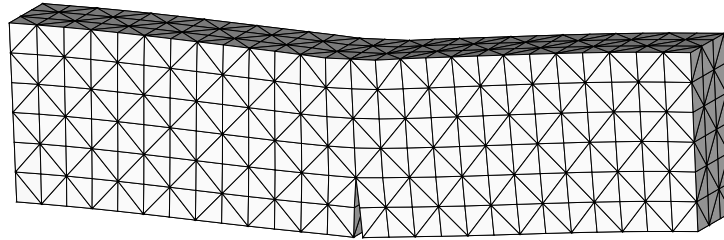


**Figure 5.4:** Bending of a neo-HOOKEAN hyperelastic notched beam. Fixed-mesh solution. One-half of the beam is discretized into 392 nodes and 1170 tetrahedral elements.

### 5.4.2 Bending of a notched beam

The next example is concerned with bending of a notched beam of dimensions  $101.6 \times 25.4 \times 12.7$  [mm], Fig. 5.4. The length of the notch is 8.47 mm. The beam is clamped at both ends. A vertical displacement is applied to a 3.9 mm region of the top surface centered on the symmetry plane. The material is neo-HOOKEAN hyperelastic with strain-energy density (4.41). The LAMÉ constants are set to  $\lambda = 12115.38$  N/mm<sup>2</sup> and  $\mu = 8071.92$  N/mm<sup>2</sup>, which corresponds to a YOUNG's modulus  $E = 21000$  N/mm<sup>2</sup> and a POISSON's ratio  $\nu = 0.3$ . This example illustrates the performance of the coupling of the variational remeshing strategy with the VALE formulation presented in Chapter 4. The energy tolerance for the termination of the VALE scheme according to Subsection 4.5.3 is set to  $1.0 \cdot 10^{-5}$ . The symmetries of the problem are exploited to reduce the domain of analysis to one half of the beam. The problem shows the behavior of the  $r$ -adaption combined with the energy-based remeshing strategy in the presence of strong singularities such as crack tips and corners.

The deformation of the initial finite element mesh is shown in Fig. 5.4. It contains 392 nodes and 1170 tetrahedral elements (half of the structure). The corresponding energy is  $I_h^{(1)} = 75506.8$  MNm.

Next, the solution is improved by applying the  $r$ -adaption procedure presented in Chapter 4, together with the energy-based remeshing strategy. The results are shown in Fig. 5.5.

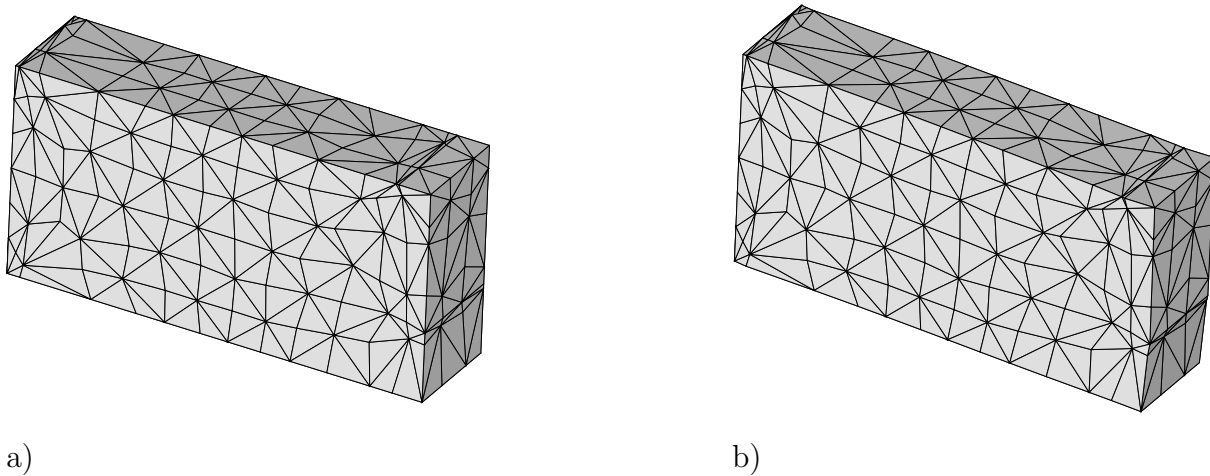


**Figure 5.5:** Bending of a neo-HOOKEan hyperelastic notched beam.  $r$ -adapted solution with energy-based mesh-improvement (without node migration to and from the surface): a) undeformed configuration; b) deformed configuration. The solution is symmetric about the plane of the notch and only one half of the beam is shown in the figures.

The energy of the adapted solution is  $I_h^{(2)} = 69672.2$  MNm, corresponding to a 8.4% reduction with respect to the fixed-mesh solution. As is evident from the figure, the nodes move towards to regions of highest strain-energy density, namely, the tips of the notches, the region under the center loads, and the corners at the clamped ends. The reconstruction of the mesh in those regions resulting from the energy-based mesh improvements is particularly noteworthy. For instance, a careful examination reveals that the optimal mesh is highly anisotropic in the region of the crack tip. The anisotropy of the mesh stands to reason, since the solution near the tip varies slowly along the crack front and rapidly normal to it. That the energy-based criterion should discern this feature of the solution and adapt the mesh to it is quite remarkable.

## 5.5 Further improvements of the VALE formulation and the energy-based remeshing strategy

The coupling of the presented energy-based remeshing strategy with the variational VALE formulations as discussed in Chapter 4 improves significantly the solution predicted by the finite element method. However, in many cases it is necessary to enlarge the space of admissible deformations further. For this reason, a novel variational h-adaption is developed in the next chapter.

# Chapter 6

## A variational h-adaptive finite element formulation

A variational h-adaptive strategy in which the evolution of the mesh is driven directly by the governing minimum principle is proposed in this chapter. This minimum principle is the principle of minimum potential energy in the case of elastostatics (cf. Subsection 2.3.2); and the minimum principle for the incremental static problem of elastoviscoplasticity according to Section 2.5. In particular, the mesh is refined locally when the resulting energy or incremental pseudo-energy released exceeds a certain threshold value. In order to avoid global recomputes, the local energy released by mesh refinement is estimated by means of a lower bound obtained by relaxing a local patch of elements. This bound can be computed locally, which reduces the complexity of the refinement algorithm to  $O(N)$ . The advocated h-adaption can be directly coupled with other refinement strategies driven by energy minimization. As a prototype, a coupled, fully variational h-adaptive strategy is discussed. Because of the strict variational nature of the h-refinement algorithm, the resulting meshes are anisotropic and outperform other refinement strategies based on aspect ratio or other purely geometrical measures of mesh quality. Since many problems in mechanics such as crack propagation are characterized by moving singularities, the proposed h-adaption is completed by an energy-driven coarsening strategy. The versatility and rate of convergence of the resulting approach are illustrated by means of selected numerical examples. The present chapter follows to a large extent [MOSLER & ORTIZ 2006].

### 6.1 Introduction

h-adaptive finite element formulations for linear elliptic problems may be based on standard error estimates. In this context, adaptivity strives to minimize an error bound among all meshes of a fixed size; or by the recursive application of local refinement steps

(cf, e. g., [VERFÜRTH 1996; AINSWORTH & ODEN 2000] for reviews). Error estimation pre-supposes existence and uniqueness of the solution; relies strongly on the linearity of the problem; and in the corresponding HILBERT-space structure of the solution space. In addition, the standard error bounds require a certain regularity of the solution for their validity, and averaging over patches of elements is typically required in order to estimate the local errors (cf, e. g., [CIARLET 1988]). Error estimates break down entirely when the solution lacks regularity; and when loss or near-loss of ellipticity occurs, e. g., as a consequence of localization instabilities.

If error estimation is not without difficulty in a linear framework, it is entirely inimical to strongly nonlinear problems involving finite kinematics. Indeed, these problems often lack uniqueness, owing to instabilities such as buckling, and even existence due to nonconvexity arising from material instabilities, phase transitions and other root causes. Furthermore, the topologies that are natural to these problems are often not normed, and the spaces where solutions are to be found may not have a linear structure at all. As a consequence, the framework of error estimation fails to apply to nonlinear mechanical problems in general and hence, error indicators have to be used.

Even for linear elliptic problems, standard h-adaptive refinement strategies can be improved in many cases. According to [VERFÜRTH 1996], the development of a priori error estimates can be decomposed into two parts. While the first of those is affected by the properties of the considered mechanical problem, the second part results from interpolation theory and consequently, it is problem independent. As regards the latter, shape regularity is usually postulated, i. e., inequality

$$\sup\{h_e/\rho_e \mid e \in \mathcal{T}_h\} < \infty \quad (6.1)$$

is assumed to be fulfilled with  $h_e$  and  $\rho_e$  denoting the diameter of finite element  $e$  and the diameter of the largest ball contained in  $e$ , respectively. However, it is well known that anisotropic meshes which violate Ineq. (6.1) are more efficient in many cases, cf. [SIMPSON 1994; APEL 1999]. Unfortunately, the theory of error estimates for anisotropic meshes is far less understood, see [APEL 1999].

The aforementioned problems motivate the development of adaptive finite element formulations which can be applied to the numerical analysis of complex systems showing a fully nonlinear behavior. Furthermore, provided the mechanical problem under consideration is driven by energy minimization, anisotropic meshes should evolve, if they are energetically favorable.

## 6.2 A local refinement strategy

Variational h-adaption relies on the underlying variational principle to drive the process of mesh refinement and unrefinement. In particular, no error estimates are invoked at any

stage of the adaption procedure. In this work, attention is confined to simplicial meshes and edge bisection (cf. [BÄNSCH 1991B; BÄNSCH 1991A; RIVARA 1991; RIVARA & LEVIN 1992; RIVARA 1997]) as the device for achieving mesh refinement. Two different strategies will be explained in this section.

In what follows, the set of all tetrahedra  $T$  defining the discretization is denoted as  $\mathcal{T}_h$  and  $\mathcal{E}(T)$  represents the set of all edges  $E$  contained in element  $T$ . Consequently,

$$\mathcal{E}(\mathcal{T}_h) = \bigcup_{T \in \mathcal{T}_h} \mathcal{E}(T) \quad (6.2)$$

is the collection of all edges in the triangulation  $\mathcal{T}_h$ . Furthermore,

$$\omega_E = \bigcup_{E \in \mathcal{E}(T)} T \quad (6.3)$$

is the set of all neighboring elements of the edge  $E$  and the nodes  $\mathbf{X}_a$  of an element  $T$  are contained in  $\mathcal{N}(T)$ , cf. [VERFÜRTH 1996]. Hence,  $\mathcal{N}(\mathcal{T}_h)$  is the set of all nodes.

### 6.2.1 A local refinement strategy based on marked edges

Suppose a physically sound error indicator or a mathematical-based error estimate has marked edges to be refined. Then, the following algorithm is applied:

For all marked edges  $E$ , DO:

- i) Determine  $\omega_E$ .
- ii)  $\forall T \in \omega_E$  : Cut the element  $T$  by bisecting the marked edge  $E$ .

For a certain edge, this method is illustrated in Fig. 6.1. Clearly, the resulting new triangulation is always conforming, i. e., *hanging nodes* cannot be generated. The new nodes are added by computing their positions based on the underlying geometry approximation of the respective parent element. As a consequence, the boundary representation of the structure considered does not change. It should be noted that the prescribed algorithm is not stable. Hence, highly anisotropic meshes may evolve whose elements show large aspect ratios. More precisely, examples can be easily generated demonstrating that the obtained aspect ratios are not even bounded. However, it will be shown that this ratio does not correlate well with performance in problems exhibiting strong directionality.

### 6.2.2 A local refinement strategy based on marked elements

Suppose now that elements have been marked for refinement by an error indicator. In this case, an edge-bisection approach according to [BÄNSCH 1991B; RIVARA 1991] is applied. In contrast to the method described in Subsection 6.2.2, the algorithm is stable.

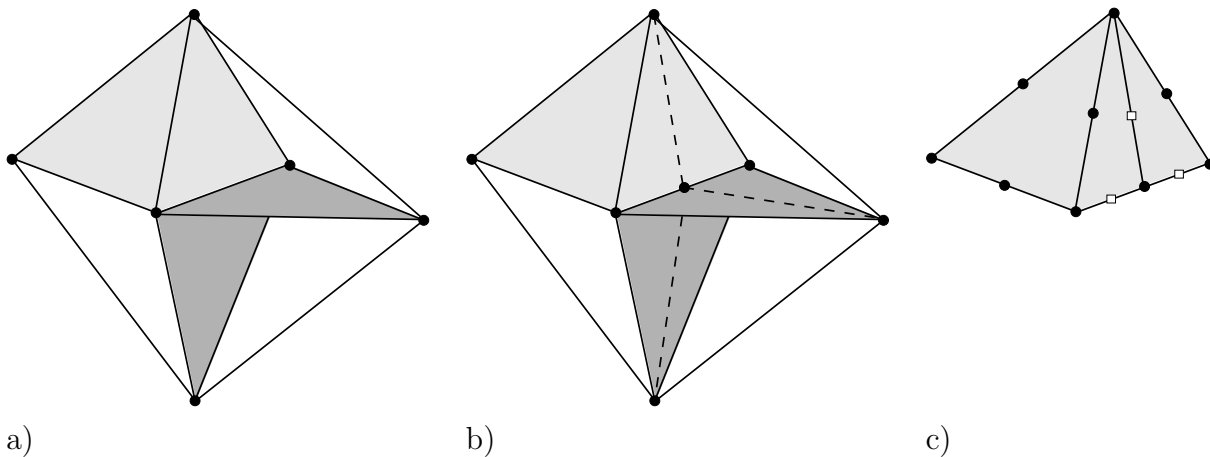


**Figure 6.1:** Edge-bisection of simplicial mesh: a) edge star before bisection; b) bisection and reconstruction of the star of the bisected edge; c) edge bisection in a 10-node tetrahedral element by using edge bisection. The filled circles designed nodes existing prior to bisection; open squares indicate new nodes inserted as a result of bisection

RIVARA's *Longest-Edge Bisection* method is defined as follows: Let  $\mathbb{E}$  denote the list of elements to be refined. Then:

- i) Cut each element  $T \in \mathbb{E}$  by bisecting its longest edge.
- ii) Set  $\mathbb{E}$  to the set of elements having nonconforming (hanging) nodes.
- iii) Is  $\mathbb{E} \neq \emptyset$

YES: GOTO i)

NO: EXIT

Although the simplicity of the algorithm is noteworthy, the efficient handling of hanging nodes is, from an implementational point of view, relatively cumbersome. For this reason, RIVARA's *Backward Longest-Edge Refinement Algorithm* is adopted, cf. [RIVARA 1997]. The interesting feature of this method is that the resulting refined meshes are identical to those of the original method [RIVARA 1991], but hanging nodes are not created at any stage of the algorithm. RIVARA's approach is based on the computation of the so-called *Longest-Edge Propagation Path* (LEPP). Further details are omitted.

**Remark 6.2.2.1** *As mentioned before, the algorithm presented in this subsection is stable. Hence, degenerated elements cannot occur and, in many cases, the aspect ratios of the elements created by this method are relatively small. It is well known that small aspect ratios result in a small condition number of the respective system of equations in general, cf. [SHEWCHUK 2002]. Clearly, this improves the performance of the numerical solution*

scheme, if iterative solvers are used. However, it should be noted that the finite element code developed is based on a sparse direct solver and consequently, decrease of performance due to highly anisotropic meshes is not an issue.

**Remark 6.2.2.2** According to [RIVARA 1997], the Longest-Edge Propagation Path (LEPP) "...is the set of all the neighbor tetrahedra (by the longest edge) having respective longest-edge greater than or equal to the longest edge of the preceding tetrahedra in the path." It is claimed that this path is finite. This property is essential, since otherwise endless loops may be generated. However, this property can only be guaranteed, if all edges in the triangulation have different lengths. For example, consider two edges of a facet between two neighboring tetrahedra elements. Furthermore, assume the edges have the same lengths and they are the longest edges of both elements. If for each of the tetrahedra elements a different edge is marked as the longest one, the LEPP is infinite. As a result, it produces indeed an endless loop. It should be noted that such a problem is not of academic nature and occurs in applications. In the developed finite element code, this problem is eliminated by choosing the longest-edge having the largest number. However, for more complex problems this simple strategy does not work. Fortunately, in all computations such a case has not been found.

### 6.3 Variational refinement criteria

Within a variational framework, the standard displacement finite element method may be regarded as constrained minimization, with solutions restricted to a finite-dimensional subspace  $V_h \subset V$ . The constrained functional is

$$I_h(\varphi) = \begin{cases} I(\varphi), & \text{if } \varphi \in V \\ +\infty, & \text{otherwise} \end{cases} \quad (6.4)$$

and the reduced problem reads

$$\inf_{\substack{\varphi \in V, \\ \varphi|_{\partial\Omega_1} = \bar{\varphi}}} I_h(\varphi). \quad (6.5)$$

The subspaces  $V_h$  are generated by introducing a triangulation  $\mathcal{T}_h$  of  $\Omega$  and a standard finite element interpolation of the form

$$\varphi_h(\mathbf{X}) = \sum_{a=1}^{N_h} \mathbf{x}_a N_a(\mathbf{X}) \quad (6.6)$$

where  $N_h$  is the number of nodes,  $N_a$  denotes the nodal shape function of node  $a$  and  $\mathbf{x}_a$  is the nodal position vector in the deformed configuration. Classically, one regards  $V_h$  as a sequence of parameterized subspaces, e. g., by the mesh size  $h$ , and seeks a sequence  $\varphi_h$  of approximate solutions such that  $I_h(\varphi_h) \rightarrow I(\varphi)$ .

Suppose instead that  $V_h$  represents a *net* of linear spaces parameterized by a *directed* index set  $A$ . Recall that a directed set is a set  $A$  together with a binary relation  $\leq$  having the following properties: i)  $a \leq a$  for all  $a \in A$  (reflexivity); if  $a \leq b$  and  $b \leq c$ , then  $a \leq c$  (transitivity); for any pair  $a, b \in A$ , there exists  $c \in A$  such that  $a \leq c$  and  $b \leq c$  (directedness). In the present work, nets of subspaces generated by *edge bisection* are considered. Thus,  $V_{h_1} \leq V_{h_2}$  if the triangulation  $\mathcal{T}_{h_2}$  corresponding to  $V_{h_2}$  can be reached from the triangulation  $\mathcal{T}_{h_1}$  corresponding to  $V_{h_1}$  by a sequence of edge bisections. In addition, it is supposed that there is an element  $0 \in A$  that precedes all other elements. The corresponding triangulation  $\mathcal{T}_0$  is the initial mesh, and  $V_0$  is the corresponding initial solution space.

As noted earlier, the variational principle supplies an unambiguous comparison criterion for judging the relative quality of two test functions:  $\varphi_{h_2}$  is *better* than  $\varphi_{h_1}$  if and only if  $I(\varphi_{h_2}) < I(\varphi_{h_1})$ . Hence, the problem of variational mesh adaption can be formulated as the minimum problem

$$\begin{aligned} \inf_{\substack{\varphi \in V, \\ \varphi|_{\partial\Omega_1} = \bar{\varphi}, \\ h \in A}} I_h(\varphi) + \mu_c N_h, \end{aligned} \quad (6.7)$$

where  $N_h$  denotes the number of nodes in the triangulation  $\mathcal{T}_h$ , and  $\mu_c > 0$  is an *energy tolerance*. Evidently,  $\mu_c$  represents the *energy cost* of introducing an additional node in the mesh and, therefore, may be regarded as a *chemical potential*. The role played by the second term in (6.7) is to assign a cost  $\mu_c$  to the introduction of an additional node. This cost in turn sets an upper limit to the size of the mesh. Thus, if  $\mu_c = 0$  minimization of  $I_h$  results in run-away meshes, since the energy is always lowered by the introduction of additional nodes. By way of contrast, suppose that  $\mu_c > 0$  and that the initial triangulation  $\mathcal{T}_0$  is coarse, so that the  $V_0$ -minimizer is not a solution of (6.7). Then, as convergence is approached the addition of nodes results in diminishing energy returns and the second term in (6.7) is expected to dominate, with the result that the process of mesh refinement is eventually held in check.

The problem (6.7) of finding absolute minimizers in the collection of spaces  $\{V_h, h \in A\}$  is of combinatorial complexity and, therefore, intractable in general. Instead, an algorithm will be developed which finds *local minimizers*, i. e., minimizers that are stable with respect to a single edge bisection. In order to formalize this notion, let  $\mathcal{E}(\mathcal{T}_h)$  denote the collection of edges of  $\mathcal{T}_h$ . In addition, for all  $e \in \mathcal{E}(\mathcal{T}_h)$  let  $\sigma_e : A \rightarrow A$  denote a mapping such that  $\mathcal{T}_{\sigma_e(h)}$  is the triangulation resulting from the bisection of  $e$ . Then,  $\mathcal{T}_h$  is defined as *bisection-stable* if

$$\mu(\mathcal{T}_h) = \max_{e \in \mathcal{E}(\mathcal{T}_h)} (\inf I_h - \inf I_{\sigma_e(h)}) \leq \mu_c. \quad (6.8)$$

Thus,  $\mathcal{T}_h$  is bisection-stable, if the addition of one node lowers  $I_h$  at best by an amount  $\mu(\mathcal{T}_h)$  less than  $\mu_c$ , and thus the addition is to be rejected. The basic h-refinement strategy that emerges from these considerations may be summarized as follows:

- i) Initialize  $h = 0$ .
- ii) Find  $e \in \mathcal{E}(\mathcal{T}_h)$  for which  $\mu(\mathcal{T}_h)$  is attained.
- ii) Is  $\mu(\mathcal{T}_h) > \mu_c$

YES: Reset  $h \leftarrow \sigma_e(h)$ , GOTO ii)

NO: EXIT

**Remark 6.3.0.3** *Instead of bisecting single edges sequentially, alternative strategies may be devised by ordering the supercritical edges according to the indicator  $\inf I_h - \inf I_{\sigma_e(h)}$  and targeting for bisection a subset of those edges. For instance, with*

$$\rho(\mathcal{T}_h) = \min_{e \in E(\mathcal{T}_h)} (\inf I_h - \inf I_{\sigma_e(h)}) \quad (6.9)$$

the refinement procedure

$$\text{refine } e \in \mathcal{E}(\mathcal{T}_h) \quad \text{if} \quad \inf I_h - \inf I_{\sigma_e(h)} > \alpha (\mu(\mathcal{T}_h) - \rho(\mathcal{T}_h)) + \rho(\mathcal{T}_h) \quad (6.10)$$

will be applied in Section 6.9. Clearly, the domain of the parameter  $\alpha$  is  $[0, 1]$ . In standard adaptive codes, it is usually set to 0.5, cf. [VERFÜRTH 1996]. For  $\alpha = 0$  all edges are refined, while setting  $\alpha = 1.0$  is identical to the method described in the present section.

**Remark 6.3.0.4** *If the aspect ratio of the elements needs to be maintained, edges can be bisected by means of RIVARA's algorithm as discussed in Subsection 6.2.2, which guarantees a lower bound on the element aspect ratio. More specifically, for the edge  $e \in \mathcal{E}(\mathcal{T}_h)$  characterized by  $\mu(\mathcal{T}_h) > \mu_c$ , all neighboring elements, i. e.,  $T \in \omega_E$ , are refined by applying the method presented in Subsection 6.2.2. However, it should be noted that in a strict variational framework aspect ratio is a poor measure of mesh quality. Indeed, as will become evident from the subsequent examples energy minimization often leads to strongly anisotropic meshes.*

**Remark 6.3.0.5** *Higher-order elements, such as 10-node quadratic tetrahedra are commonly implemented by recourse to GAUSSIAN quadrature. This introduces bounded errors that do not affect convergence in general. However, it should be noted that some of the strict ordering of energies implied by the variational structure of the problems may be lost due to numerical quadrature errors.*

## 6.4 Bisection criteria derived from local energy bounds

Evidently, a drawback of the strategy just outlined is that the energy  $\mu(\mathcal{T}_h)$  released by bisection is costly to compute exactly. An alternative strategy consists of working with a lower bound of  $\mu(\mathcal{T}_h)$ . A convenient such lower bound can be obtained by constraining the relaxation of the displacement field upon bisection of an edge  $e$  to a certain sub-mesh  $\mathcal{S}_h(e)$  of  $\mathcal{T}_h$ , or element *patch*, containing  $e$ . For instance,  $\mathcal{S}_h(e)$  can be set to the ring of elements incident to  $e$ , i. e., the *star*  $\text{St}(e) = \omega_e$ . Evidently,

$$\mu_{\text{loc}}(\mathcal{T}_h) = \max_{e \in E(\mathcal{T}_h)} \left\{ I_h(\varphi_h) - \inf_{\substack{\varphi \in V, \\ \varphi|_{\partial\Omega_1} = \bar{\varphi}, \\ \text{supp}(\varphi - \varphi_h) \subset \mathcal{S}_h(e)}} I_{\sigma_e(h)}(\varphi) \right\} < \mu(\mathcal{T}_h) \quad (6.11)$$

supplies the requisite lower bound. In this expression,  $\varphi_h$  is minimizer of  $I_h$  and  $\text{supp}$  denotes the support of a function. Thus,  $\mu_{\text{loc}}(\mathcal{T}_h)$  is computed by constraining the relaxed displacements  $\varphi$  on the bisected mesh  $\mathcal{T}_{\sigma_e(h)}$  to differ from the minimizer  $\varphi_h$  on the un-bisected mesh  $\mathcal{T}_h$  only within the neighborhood  $\mathcal{S}_h(e)$  of the bisected edge  $e$ . Conveniently, this computation is local and its cost is constant, independent of the size of the mesh. The resulting  $h$ -adaption strategy is:

- i) Initialize  $h = 0$ .
- ii) Find  $e \in \mathcal{E}(\mathcal{T}_h)$  for which  $\mu_{\text{loc}}(\mathcal{T}_h)$  is attained.
- ii) Is  $\mu_{\text{loc}}(\mathcal{T}_h) > \mu_c$

YES: Reset  $h \leftarrow \sigma_e(h)$ , GOTO ii)

NO: EXIT

**Remark 6.4.0.6** *Because of the lower bound property  $\mu_{\text{loc}}(\mathcal{T}_h) < \mu_{\text{loc}}$ , the adaption strategy based on the local estimate  $\mu_{\text{loc}}(\mathcal{T}_h)$  may be expected to accept meshes that would otherwise be bisection-unstable according to the global energy criterion.*

**Remark 6.4.0.7** *When dealing with constant-strain elements, the case of boundary edges connected to one single element, henceforth referred to as sharp edges, may require special handling. For sharp edges, the local patch  $\mathcal{S}_h(e)$  consists of one single constant-strain element in the special case in which the local patch is taken to coincide with the star of the edge,  $\mathcal{S}_h(e) = \text{St}(e)$ . Under these conditions, bisection of a sharp edge leaves the energy invariant, with the result that sharp edges are never targeted for bisection. In order to avoid this artifact the local patches of sharp edges needs to be extended beyond their stars.*

**Remark 6.4.0.8** *The problem of sharp edges alluded to in Remark 6.4.0.7 does not arise when higher-order elements, such as 10-node quadratic tetrahedra, are in use.*

## 6.5 Comparison of the proposed refinement criteria to classical error estimates

Locally constrained problems such as advocated in the previous sections have also been proposed as a basis for deriving *a posteriori* error bounds in linear problems [VERFÜRTH 1996; AINSWORTH & ODEN 2000]. The analogies between those concepts and the variational h-adaption as suggested in the present work are highlighted in this section.

For linear systems the potential energy has the representation

$$I(\mathbf{u}) = \frac{1}{2}a(\mathbf{u}, \mathbf{u}) - l(\mathbf{u}) \quad (6.12)$$

where  $a(\mathbf{u}, \mathbf{u})$  is a quadratic form and  $l(\mathbf{u})$  a bounded linear functional. As mentioned before, edge bisection generates a directed index set. Consequently, the space of interpolations associated with the refined mesh  $\mathcal{T}_h^{\text{new}}$  can be written as a direct sum, i. e.,

$$\mathbf{u}_{\text{new}} \in V_{\text{old}} \oplus \mathcal{V} \quad \text{and} \quad \mathbf{u}_{\text{new}} = \mathbf{u} + \mathbf{v}, \quad \mathbf{u} \in V_{\text{old}}, \quad \mathbf{v} \in \mathcal{V}, \quad (6.13)$$

with  $V_{\text{old}}$  denoting the interpolation space corresponding to the non-refined triangulation  $\mathcal{T}_h^{\text{old}}$ . Using Eqs. (6.13), together with Eq. (6.12), the lower bound of the energy released by bisection of edge  $e$  reads

$$I_h(\mathbf{u}) - \inf_{\substack{\mathbf{v} \in \mathcal{V}, \\ (\mathbf{u}+\mathbf{v})|_{\partial\Omega_1}=\bar{\mathbf{u}}}} I_{\sigma_e(h)}(\mathbf{u} + \mathbf{v}) = \sup_{\substack{\mathbf{v} \in \mathcal{V}, \\ (\mathbf{u}+\mathbf{v})|_{\partial\Omega_1}=\bar{\mathbf{u}}}} \left[ -a(\mathbf{u}, \mathbf{v}) - \frac{1}{2}a(\mathbf{v}, \mathbf{v}) + l(\mathbf{v}) \right]. \quad (6.14)$$

Clearly, the stationarity condition associated with the optimization problem (6.14) is

$$a(\mathbf{u} + \mathbf{v}, \mathbf{w}) = l(\mathbf{w}) \quad \forall \mathbf{w} \in \mathcal{V}. \quad (6.15)$$

Substituting the admissible choice  $\mathbf{w} = \mathbf{v}$  into Eq. (6.15) and the resulting equation into Eq. (6.14), finally gives

$$I_h(\mathbf{u}) - \inf_{\substack{\mathbf{v} \in \mathcal{V}, \\ (\mathbf{u}+\mathbf{v})|_{\partial\Omega_1}=\bar{\mathbf{u}}}} I_{\sigma_e(h)}(\mathbf{u} + \mathbf{v}) = \frac{1}{2}a(\mathbf{v}, \mathbf{v}), \quad (6.16)$$

with  $\mathbf{v}$  computed from the weak form (6.15).

The by now classical error estimate  $\eta$  proposed in [BABUŠKA & RHEINBOLDT 1978; BERNADI, MÉTIVET & VERFÜRTH 1993] can be recast into the variational form

$$\eta = \|\nabla \mathbf{v}\|_{0,2} \quad \text{with} \quad \mathbf{v} = \arg \inf_{\tilde{\mathbf{v}} \in \mathcal{V}} I_E(\tilde{\mathbf{v}}), \quad I_E(\mathbf{v}) = \frac{1}{2}a(\mathbf{u} + \mathbf{v}, \mathbf{u} + \mathbf{v}) - l(\mathbf{v}). \quad (6.17)$$

For further details, cf. [VERFÜRTH 1996]. Evidently, the stationarity condition of  $I_E$  is given by Eq. (6.15). Since for linearized elasticity theory the energy norm is equivalent to the  $L_2$  norm  $\|\nabla \mathbf{v}\|_{0,2}$ , the equivalent indicator

$$\eta = \frac{1}{2}a(\mathbf{v}, \mathbf{v})^{1/2} \quad (6.18)$$

can be considered without loss of generality. By comparing Eq. (6.18) to Eq. (6.16) the analogy between the variational h-adaption presented in this work and classical error estimates becomes apparent. In this respect, the variational method can be understood as the canonical extension of the classical method.

It should be carefully noted that the functional framework just outlined does not carry over to general nonlinear problems. For instance, in problems such as finite elasticity it is natural to resort to weak topologies, with the result that the solution space is not a normed space. Furthermore, if geometrical constraints such as local invertibility of the deformations are appended the solution space is not even a linear space. Finally, the minimizers are *a fortiori* non-unique by virtue of geometrical instabilities such as buckling or material instabilities such as twinning. Under these conditions the notion of *error*, defined as the norm distance between approximate solutions and a unique minimizer, fails to apply.

**Remark 6.5.0.9** *Error estimates for linear elliptical problems according to Eq. (6.17) require the introduction of an enriched space  $\mathcal{V} \ni \mathbf{v}$ . In the present work,  $\mathcal{V} = V_{\text{new}}/V_{\text{old}}$  is defined as the space spanned by the global interpolation functions associated with the nodes newly inserted by edge-bisection. In classical error estimates for linear elliptical problems,  $\mathcal{V}$  is usually spanned by bubble functions, cf. [VERFÜRTH 1996].*

## 6.6 h-adaption combined with VALE formulations

In principle, variational r-adaption according to Chapter 4 and h-adaptive finite element formulations as discussed in the present chapter can be combined sequentially to obtain a variational hr-adaption strategy. A limited application of variational r-adaption in the context of variational h-adaption is for purposes of optimizing the location of the nodes inserted by bisection. Conveniently, when local energy estimates are used the r-optimization can also be performed locally in combination with the solution of problem (6.11).

## 6.7 Energy-based mesh coarsening

Analogously, to Section 6.4, a local bound of the energy released by edge-bisection is used in order to drive mesh coarsening. More specifically,  $\mu_{\text{loc}}(\mathcal{T}_h)$  according to Eq (6.14) and

$$\rho_{\text{loc}}(\mathcal{T}_h) = \min_{e \in E(\mathcal{T}_h)} \Delta I_h(e), \quad (6.19)$$

with

$$\Delta I_h(e) = I_h(\varphi_h) - \inf_{\substack{\varphi \in V, \\ \varphi|_{\partial\Omega_1} = \bar{\varphi}, \\ \text{supp}(\varphi - \varphi_h) \subset \mathcal{S}_h(e)}} I_{\sigma_{e(h)}}(\varphi) \quad (6.20)$$

are computed first. Then, the following combined refinement/de-refinement algorithm can be developed:

- i) For all  $e \in \mathcal{E}(\mathcal{T}_h)$  DO:
  - a) IF  $\Delta I_h(e) > \alpha_{\text{ref}} (\mu_{\text{loc}}(\mathcal{T}_h) - \rho_{\text{loc}}(\mathcal{T}_h)) + \rho_{\text{loc}}(\mathcal{T}_h)$ , mark  $e$  for refinement.
  - b) IF  $\Delta I_h(e) < \alpha_{\text{coarse}} (\mu_{\text{loc}}(\mathcal{T}_h) - \rho_{\text{loc}}(\mathcal{T}_h)) + \rho_{\text{loc}}(\mathcal{T}_h)$ , mark  $e$  for coarsening.
- ii) Apply coarsening.
- iii) Compress arrays and update the data structure.
- iiii) Apply refinement.

Here,  $\alpha_{\text{ref}} \in [0, 1]$  and  $\alpha_{\text{coarse}} \in [0, \alpha_{\text{ref}})$  are numerical parameters controlling mesh refinement and coarsening, respectively. According to this procedure, a previously refined edge is coarsened if de-refinement of this edge results in only a relatively small energy increase. Step iii) is necessary, since coarsening leads to "holes" in the arrays storing the edges, the nodes and the elements.

Except for step ii), the given pseudo-code is well-defined. The local coarsening strategy presented in this subsection is different compared to the procedures developed in [RIVARA 1991; BÄNSCH 1991B; BÄNSCH 1991A]. It can be understood as the inverse of the refinement method discussed in Subsection 6.2.1 and 6.2.2. This implies two consequences. First, only previously refined edges are allowed to be coarsened and second, the order of de-refinement is important. This is highlighted in Fig. 6.2. To guarantee the correct order of coarsening additional information is required. For that purpose, the simple data structure as given in Appendix C has been coded. For a compact notation, the following definitions are introduced:

**Definition 1** *Mesh refinement by bisecting an edge  $p$  generates the children  $c_1 \subset p$  and  $c_2 \subset p$  and some additional edges  $a_1 \dots, a_i \not\subset p$ . The set  $\{c_1, c_2, a_1, \dots, a_i\}$  is referred to as the set of edges generated by bisection of  $p$  and edge  $p$  as the parent of  $c_1$  and  $c_2$ .*

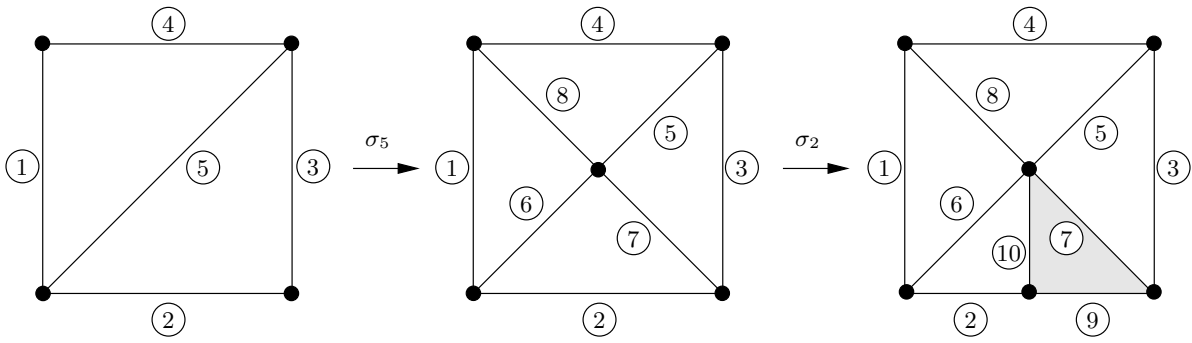


**Figure 6.2:** Mesh refinement in two dimensions by applying edge-bisection ( $\sigma_5$  and  $\sigma_2$  according to Section 6.3). Coarsening of edge 7 of the final mesh requires elimination of edge 10 first, i. e., de-refinement of edge 2 and 9.

**Definition 2** For an element  $T$  generated by bisection of  $p$ , the so-called child edge is the child  $c_1$  or  $c_2$  which belongs to  $\mathcal{E}(T)$  (see Eq. (6.2)).

Based on those definitions, together with the data structure contained in Appendix C, the following unrefinement algorithm is proposed:

For each edge  $e$  marked for coarsening DO:

i) Has  $e$  been generated by bisection of an edge  $p$ ?

YES: Get the children  $c_1$  and  $c_2$  of  $p$ .

NO: Next edge, GOTO i)

ii) Have  $c_1$  and  $c_2$  not been bisected once again? AND

Is for every  $T \in \omega_{c_1} \cup \omega_{c_2}$  (see Eq. (6.3))  $c_1$  or  $c_2$  the child edge of  $T$ ? AND

Is every edge belonging to the *set of edges generated by bisection of  $p$*  not marked for refinement?

YES: Coarsen all elements in  $\omega_{c_1} \cup \omega_{c_2}$  by unrefining  $c_1$  and  $c_2$ .

NO: Next edge, GOTO i)

For example, suppose edge  $e = 10$  in Fig. 6.2 is to be coarsened. Edge  $e = 10$  has been generated by bisection of the old edge  $p = 2$  which has the children edge  $c_1 = 2$  (new) and  $c_2 = 9$ . Consequently, the neighboring elements  $\omega_{c_1} \cup \omega_{c_2}$  of edges 2 and 9 are given by elements (2, 6, 10) and (7, 9, 10), respectively. As a result, de-refinement of edge 10 removes those elements and creates the new element (2(old), 6, 7).

**Remark 6.7.0.10** Clearly, since RIVARA's algorithm is also based on edge-bisection, the proposed coarsening strategy can be applied to this method as well. However, in RIVARA's implementation, elements are marked for de- or refinement. In the case of refinement,

the modifications have already been mentioned in Remark 6.3.0.4. For coarsening, all neighboring edges  $\mathcal{E}(T)$  of an element  $T$  are marked for de-refinement, if they were not marked for refinement before.

## 6.8 Transfer of history variables

If h-refinement is applied to mechanical problems requiring the use of history variables such as plasticity theory, these variables have to be mapped between different meshes. As already mentioned in Section 4.8, the transfer operator of the history variables follows consistently from the variational principle, cf. [ORTIZ & QUIGLEY 1991; RADOVITZKY & ORTIZ 1999]. In the present work, those variables are assumed to be piecewise constant over the VORONOI cell containing the GAUSS point  $g$  of the element  $e$ . In this case, the variational transfer operator maps the state variable of the nearest old quadrature point to the new quadrature point. This procedure shows several advantages, cf. Section 4.8.

Suppose that the quadrature points  $i = 1, \dots, n$  corresponding to the refined mesh  $\mathcal{T}_h^{(\text{fine})}$  have the same nearest old quadrature point associated with the parent mesh  $\mathcal{T}_h^{(\text{coarse})}$ . Then, for mesh refinement, the just described transfer operator reads

$$\alpha_i^{(\text{fine})} = \alpha^{(\text{coarse})}, \quad \forall 1 \leq i \leq n, \quad (6.21)$$

or alternatively in matrix notation

$$\boldsymbol{\alpha}^{(\text{fine})} = \underbrace{[1, \dots, 1]}_{= \mathbf{A} \in \mathbb{R}^n} \alpha^{(\text{coarse})}. \quad (6.22)$$

Clearly, tensor-valued variables are mapped by applying Eq. (6.22) to each component.

If h-refinement is coupled to a coarsening strategy such as that discussed in the previous section, the inverse relation of Eq. (6.22) is required additionally. More specifically, a vector  $\mathbf{B} \in \mathbb{R}^n$  has to be derived such that

$$\alpha^{(\text{coarse})} = \mathbf{B} \cdot \boldsymbol{\alpha}^{(\text{fine})}. \quad (6.23)$$

Evidently, since Eq. (6.23) is a pseudoinverse of Eq. (6.22), the composition of  $\mathbf{B}$  and  $\mathbf{A}$  has to represent the identity on  $\mathbb{R}$ , i. e.,

$$\mathbf{B} \cdot \mathbf{A} = 1. \quad (6.24)$$

Since the components of  $\mathbf{B}$  are weighting coefficients, it is natural to postulate  $B_i > 0$ . However, these restrictions are not sufficient to compute the vector  $\mathbf{B}$  uniquely. In this work, this problem is solved by choosing a physically motivated pseudoinverse. More precisely, this inverse is based on dissipation considerations.

In what follows,  $\Omega$  denotes the domain of the VORONOI cell containing the quadrature point of the coarse mesh. Then,

$$\mathcal{D}_{\text{tot}} = \int_{\Omega} \int_{t=0}^T \mathcal{D} \, dt \, dV \quad (6.25)$$

represents the total energy dissipated in  $\Omega$ . Since the adaptive h-refinement strategy presented in this chapter is purely energy-driven, it is canonical to enforce the postulate

$$\mathcal{D}_{\text{tot}}(\mathcal{T}_h^{(\text{coarse})}) =: \mathcal{D}_{\text{tot}}^{(\text{coarse})} = \mathcal{D}_{\text{tot}}^{(\text{fine})} =: \mathcal{D}_{\text{tot}}(\mathcal{T}_h^{(\text{fine})}). \quad (6.26)$$

This condition ensures that the dissipated energy is not affected by the mesh transfer operator. Based on Eq. (6.26) the vector  $\mathbf{B}$  can be computed.

In many cases, postulate (6.26) can be simplified significantly. For instance, if standard dissipative solids based on a positively homogeneous yield function of degree one are considered, the dissipation reads  $\mathcal{D} = \lambda \sum_{\text{ini}}^{\text{eq}}$ , cf. Remark 2.4.1.6. If additionally the internal variable  $\alpha$  governing isotropic hardening/softening obeys the evolution equation  $\dot{\alpha} = \lambda$  with  $\alpha(t=0) = 0$  (which is fulfilled for many material models), Eq. (6.25) simplifies to

$$\mathcal{D}_{\text{tot}}^{(\text{coarse})} = \sum_{\text{ini}}^{\text{eq}} \alpha^{(\text{coarse})}|_{t=T} V, \quad (6.27)$$

since the state variables are constant over  $\Omega$  (in the case of the coarse mesh). Here,  $V$  is the volume of the domain  $\Omega$ . Analogously, the dissipated energy obtained from the refined discretization is given by

$$\mathcal{D}_{\text{tot}}^{(\text{fine})} = \sum_{\text{ini}}^{\text{eq}} \sum_{i=1}^n \alpha^{(i)}|_{t=T} V^{(i)}. \quad (6.28)$$

Thus, enforcing condition (6.26) leads to the mesh transfer operator

$$\alpha^{(\text{coarse})}|_{t=T} = \sum_{i=1}^n \frac{V^{(i)}}{V} \alpha_i^{(\text{fine})}|_{t=T}. \quad (6.29)$$

It can be verified easily that  $B_i = V^{(i)}/V > 0$  and  $\mathbf{A} \cdot \mathbf{B} = 1$ . As a consequence,  $\mathbf{B}$  indeed represents a pseudoinverse of  $\mathbf{A}$ .

## 6.9 Numerical examples

The performance of the novel h-adaption presented in this chapter is demonstrated by means of several examples: a notched specimen in uniaxial tension; the indentation of a hyperelastic block; and the indentation of an elastic-plastic block. One clear performance measure of primary importance is the rate of convergence. Specifically, the influence of

variational h-adaptation and combined hr-adaptation on the convergence rate is analyzed. An additional central question concerns the characterization of the mesh geometries that are energetically optimal. A common rule-of-thumb is to assume that the quality of an element is commensurate with its aspect ratio, defined as the ratio between the outer and inner radii of the element. However, the aspect ratio enters error estimates as a direct consequence of the use of matrix-norm bounds that are isotropic in nature and, consequently, not tight in general. In particular, those estimates are insensitive to the directionality of the gradients in the error function. Aspect ratio bounds can be maintained throughout the mesh refinement process, e. g., by recourse to RIVARA's Longest-Edge Propagation Path (LEPP) bisection algorithm [RIVARA 1991; BÄNSCH 1991B; RIVARA & LEVIN 1992; RIVARA 1997]. Therefore, it is ascertained whether appending constraints on the aspect ratio of the elements speeds up or slows down convergence.

### 6.9.1 Uniaxial tensile test of a notched specimen

The first example is the numerical analysis of a uniaxial tensile test of a notched specimen. This mechanical problem has already been computed by using the VALE formulation according to Chapter 4. The complete description of the system is given in Fig. 4.6. Analogous to Subsection 4.6.2, a hyperelastic material model defined by the energy functional (2.29) is considered. The LAMÉ constants are assumed to be  $\lambda = 12115.38 \text{ N/m}^2$  and  $\mu = 8071.92 \text{ N/m}^2$ .

The response of the specimen is baselined by means of a coarse discretization consisting of 10-node quadratic tetrahedral elements. The corresponding finite element mesh, deformation and the stored energy distribution are shown in Fig. 6.3. As expected, the energy density attains its maximum in the vicinity of the crack tip; and is nearly uniform in the thickness direction of the slab.

Based on the initial mesh, four different adaptive computations are performed: an unconstrained variational h-adaptation calculation according to the algorithm on page 143 with  $\alpha_{\text{ref}}$  set to 0.5, 0.7 and 1.0 and a constrained variational h-adaptation calculation, in which a lower bound on the aspect ratio of the elements is maintained by means of RIVARA's Longest-Edge Propagation Path (LEPP) bisection algorithm [RIVARA 1991; BÄNSCH 1991B; RIVARA & LEVIN 1992; RIVARA 1997]. For the computation based on RIVARA's method,  $\alpha_{\text{ref}}$  is set to 1.0. Coarsening is not considered throughout this subsection.

Fig. 6.4 shows the results of the four adaptive calculations. The final meshes obtained by constrained and unconstrained variational h-adaptation stand in sharp contrast to one another, Fig. 6.4. Thus, unconstrained variational h-adaptation clearly allocates resources in such a way as to exploit the directionality of the gradients in the variation of the solution, Fig. 6.4a) - c). In particular, it results in highly *anisotropic* mesh refinement: a high degree of mesh refinement in the directions normal to the crack tip; and simultaneously a

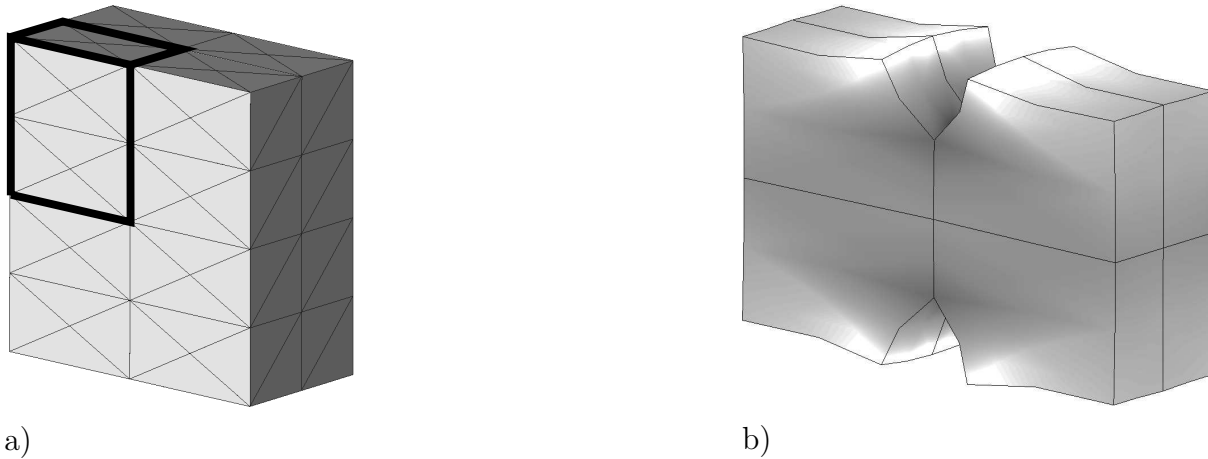


**Figure 6.3:** Geometry of the hyperelastic three-dimensional notched specimen undergoing large deformations in uniaxial tension. a) initial discretization; the octant of the specimen considered in the calculations is highlighted; b) deformed body and stored-energy distribution, showing concentration at the crack tips and nearly uniform variation across the specimen

nearly uniform mesh size in the direction of the crack tip from, i. e., across the thickness of the specimen. It bears emphasis that this anisotropic refinement occurs spontaneously as an energetic optimum, and is not the result of empirical criteria built into the adaption strategy. By way of contrast, the constrained variational  $h$ -adaption calculation results in *isotropic* mesh refinement, with equi-axed elements distributed through the thickness of the specimen, Fig. 6.4d).

The influence of  $\alpha_{\text{ref}}$  on the discretizations can be seen by comparing the meshes in Fig. 6.4a) - c). The greater  $\alpha_{\text{ref}}$ , the more localized is the refined region. However, it will be shown that all adaptive schemes based on the purely energy-driven algorithm lead to almost identical results.

The convergence rates in energy of the constrained and unconstrained variational  $h$ -adaption calculations are compared in Fig. 6.5 with the convergence rate resulting from uniform refinement. It is noteworthy that in the linear range, the energy error plotted in the ordinate reduces to:  $a(u_h, u_h) - a(u, u) = a(u_h - u, u_h - u) = \|u_h - u\|_E^2$ , and hence may be thought of as generalizing the conventional energy-norm error to the nonlinear range. Clearly, the performance of unconstrained variational  $h$ -adaption is superior to that of constrained variational  $h$ -adaption. In particular, anisotropic mesh refinement results in higher convergence rates than isotropic mesh refinement. Thus, far from being detrimental, highly-elongated elements oriented according to the gradients in the solution are beneficial to performance. Conversely, constraints designed to eliminate elongated elements, while resulting in meshes that are more "pleasing to the eye", have a detrimental effect on the rate of convergence.

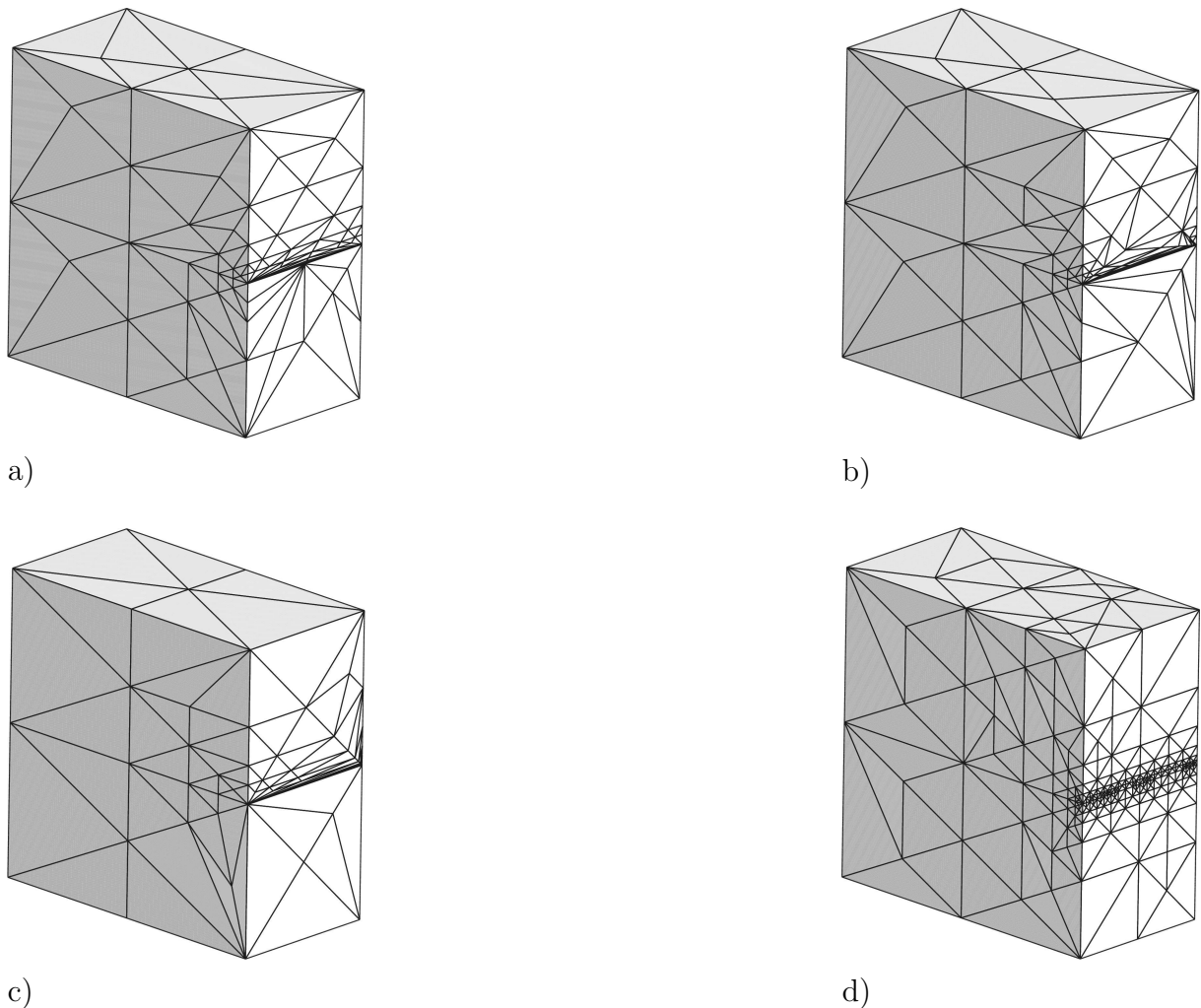


**Figure 6.4:** Hyperelastic three-dimensional notched specimen undergoing large deformations in uniaxial tension. Final mesh geometries resulting from: a) unconstrained variational h-adaptation  $\alpha_{\text{ref}} = 0.5$ ; b)  $\alpha_{\text{ref}} = 0.75$ ; c)  $\alpha_{\text{ref}} = 1.0$ ; d) constrained variational h-adaptation using RIVARA's LEPP algorithm

According to Fig. 6.5, the influence of  $\alpha_{\text{ref}}$  on the performance seems to be negligible. Unfortunately, a closed form solution for the best  $\alpha_{\text{ref}}$  does not exist (not even in linearized elasticity) and furthermore, it would depend on the physical problem under investigation. For the particular example analyzed in this subsection,  $\alpha_{\text{ref}} = 0.5$  is preferred, since it leads to almost the same results as  $\alpha_{\text{ref}} = 0.75$  and  $\alpha_{\text{ref}} = 1.0$  by requiring only 15 refinement steps instead of 29 and 105, respectively. The choice  $\alpha_{\text{ref}} = 0.5$  is well accepted in adaptive finite element formulations, cf. [VERFÜRTH 1996].

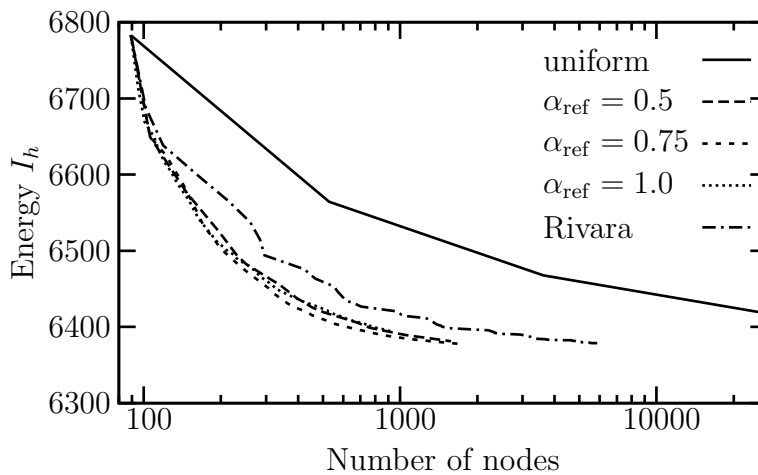


**Figure 6.5:** Hyperelastic three-dimensional notched specimen undergoing large deformations in uniaxial tension. Convergence rates resulting from unconstrained and constrained variational  $h$ -adaptation. The convergence rate corresponding to uniform refinement is also shown for comparison.

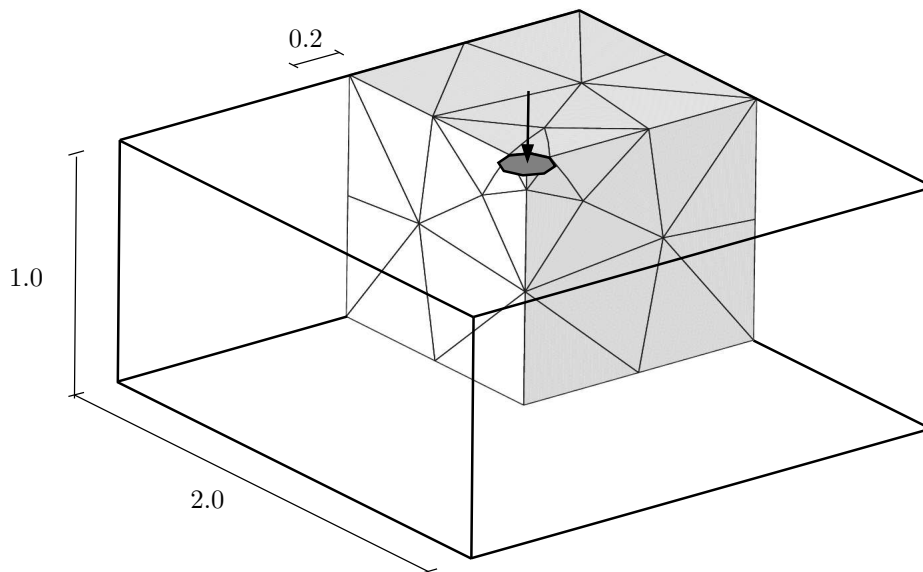


**Figure 6.6:** Indentation of a hyperelastic block by a circular rigid punch. Initial discretization: dimensions (in m), loading conditions and initial discretization

### 6.9.2 Indentation of a block: fixed force

Next, indentation of a block is analyzed numerically by using the presented  $h$ -adaptation. The dimensions, loading conditions together with the initial discretization are depicted in Fig. 6.6. Loading is controlled by prescribing the vertical displacements within the grey colored circle (see Fig. 6.6). Symmetry of the geometry and the boundary conditions have been taken into account. As a consequence, only one quarter of the system has been

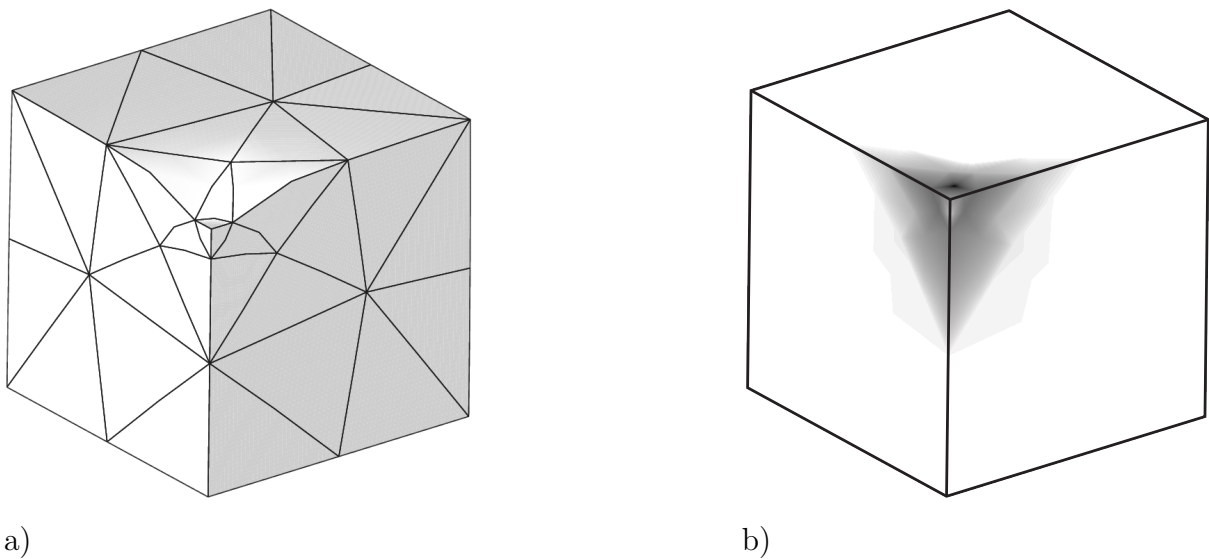


**Figure 6.7:** Indentation of a hyperelastic block by a circular rigid punch, initial mesh: a) deformed configuration; b) stored-energy distribution

discretized.

### 6.9.2.1 Hyperelastic material model

At first, the material response is assumed to be governed by the hyperelastic potential (2.29). The LAMÉ constants are identical to those in Subsection 6.9.1.

The response predicted by the initial finite element mesh, consisting of 10-node quadratic tetrahedral elements, is shown in Fig. 6.7. It corresponds to an amplitude of the displacement of  $u = 0.1$  m. As expected, the strain-energy attains its maximum under the punch and exhibits power-law decay away from it, Fig. 6.7b). However, the region immediately under the punch is highly confined and is in a state of high triaxiality and comparatively lower energy. Owing to the concentration and fine structure of the strain-energy, the problem lends itself ideally to mesh adaption.

Fig. 6.8 displays the final meshes obtained by means of three adaption strategies: unconstrained variational h-adaption; unconstrained variational hr-adaption; and constrained variational h-adaption using RIVARA's LEPP algorithm to maintain a lower bound on the aspect ratio of the elements. As remarked earlier, the variational hr-adaption procedure employed in the calculations consists of alternating edge bisection and the variational r-adaption scheme described in [MOSLER & ORTIZ 2005]. In all cases, only the energetically most favorable edge is bisected at each step ( $\alpha_{\text{ref}} = 1.0$ ). As in the case of the notched specimen described in the foregoing, the strain-energy distribution under punch exhibits not only concentration but also marked directionality. Thus, whereas the strain-energy displays rapid variation in the radial direction, it varies slowly in the orthogonal

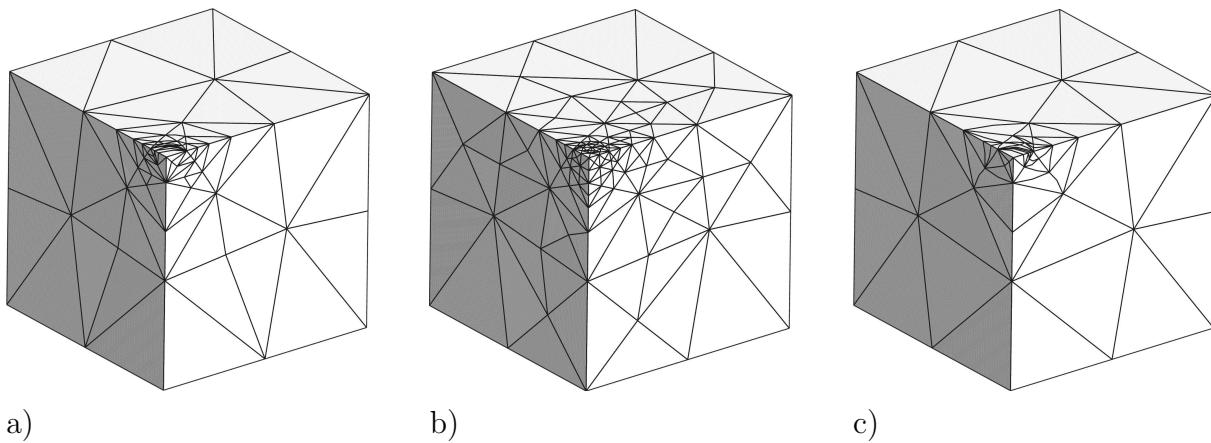


**Figure 6.8:** Indentation of a hyperelastic block by a circular rigid punch. Final meshes after: a) unconstrained variational  $h$ -adaption; b) constrained variational  $h$ -adaption using RIVARA's LEPP algorithm; c) unconstrained variational  $hr$ -adaption

directions, and, in particular, it is constant in the circumferential direction. As expected, the LEPP-constrained scheme results in an isotropic mesh that is insensitive to the directionality of the solution. In consequence, at any given depth of indentation it inserts a larger number of nodes than the remaining algorithms. In contrast, unconstrained  $h$ - and  $hr$ -adaption result in highly anisotropic and directional meshes that trace the fine structure of the energy-density field.

Fig. 6.9 compares the energy convergence behavior of the three methods. As may be seen from this comparison,  $hr$ -adaptivity results in appreciable but modest gains in the rate of convergence relative to  $h$ -adaptivity. In addition, both  $h$ - and  $hr$ -adaptivity handily out-perform constrained  $h$ -adaptivity. For instance, a 676-node unconstrained  $h$ -adaption solution has lower energy than a 1490-node constrained computation. If, in addition,  $r$ -adaption is allowed for, the size of the mesh can be further reduced to 491 nodes at no increase in energy. These performance differentials, similar to those observed in the notched specimen example, provide compelling demonstration of the fact that element aspect ratio does not correlate well with performance in problems exhibiting strong directionality in the energy-density field.

### 6.9.2.2 Elastoplastic material model

Next, the applicability of the variational approach to inelastic materials is demonstrated. The problem is identical in every way to that treated in the preceding paragraph with the sole exception that the material is now assumed to obey multiplicative  $J_2$ -flow theory of plasticity. As discussed in Section 2.5, a time discretization using variational constitutive updates [ORTIZ & STAINIER 1999; RADOVITZKY & ORTIZ 1999] confers the

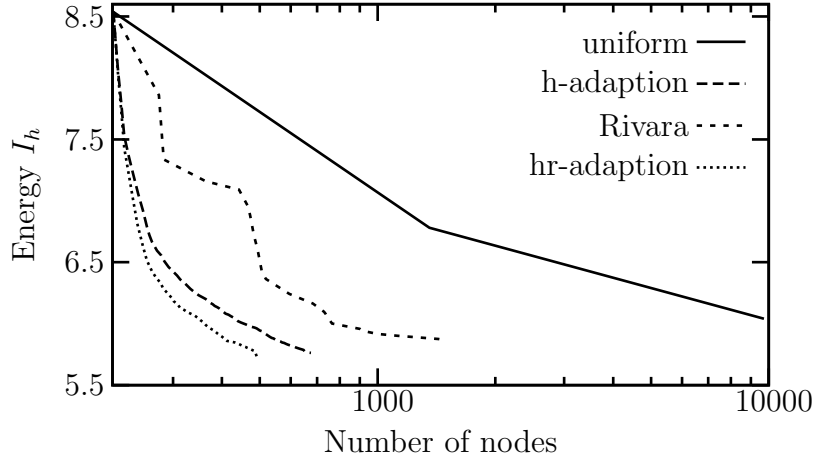


**Figure 6.9:** Indentation of a hyperelastic block by a circular rigid punch. Convergence in energy resulting from: unconstrained variational h-adaption; constrained variational h-adaption using RIVARA’s LEPP algorithm; unconstrained variational hr-adaption; and uniform mesh refinement

incremental problem a variational structure identical to that of a hyperelastic problem. In particular, the deformation mapping at time  $t_{n+1}$  minimizes an incremental potential energy defined in terms of an effective strain-energy density that encodes both the elastic and the inelastic behavior of the material. In this setting, variational h-adaptivity consists of optimizing the mesh at every time step with respect to the incremental potential energy. In particular, for any given time step the variational h-adaptivity solution procedure is identical to that pertaining to an elastic problem.

The maximum depth of indentation considered in the calculations is 0.02 m. All meshes consist of 10-node quadratic tetrahedral elements. For definiteness, the implementation is based on the variational constitutive update as discussed in Chapter 2.5. More specifically, the VON MISES model described in Subsection 2.5.3 is adopted. The elastic dilatant material response is specified by Eq. (2.96), i. e., a HENCKY model is applied. The part of the energy due to plastic work is chosen according to

$$\Psi^p(\varepsilon^p) = \frac{n\sigma_0\varepsilon_0^p}{n+1} \left[ 1 + \left( \frac{\varepsilon^p}{\varepsilon_0^p} \right) \right]^{(n+1)/n}. \quad (6.30)$$

In addition, the yield function (2.88) is modified such that

$$\phi(\boldsymbol{\Sigma}, Q) = \|\text{dev}[\boldsymbol{\Sigma}]\|_2 - Q(\varepsilon^p), \quad (6.31)$$

with  $Q := \partial\Psi^p/\partial\varepsilon^p$ . The material parameters used in the calculations are summarized in Table 6.1.

The state variables are assumed to be piecewise constant over the VORONOI cells defined by the quadrature points. More specifically, the transfer of the history variables follows the algorithm discussed in Section 6.8.

| E (kN/m <sup>2</sup> ) | $\nu$ | $\sigma_0$ (kN/m <sup>2</sup> ) | $\varepsilon_0^P$   | $n$ |
|------------------------|-------|---------------------------------|---------------------|-----|
| 200                    | 0.2   | 1.0                             | $0.5 \cdot 10^{-3}$ | 10  |

**Table 6.1:** Indentation of an elastoplastic block: material parameters

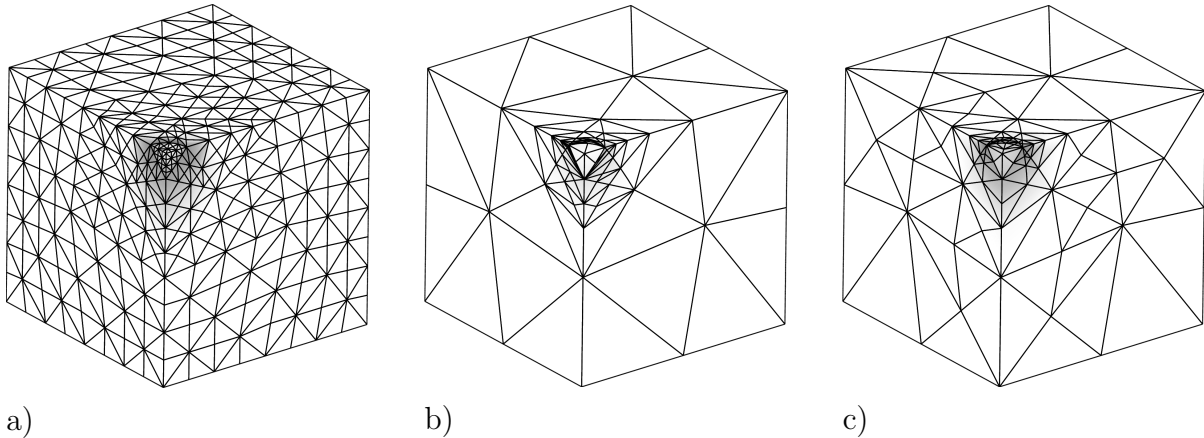


**Figure 6.10:** Indentation of an elastic-plastic block. Distribution of effective plastic strain  $\varepsilon^P$ : a) two uniform refinement steps; b) unconstrained h-adaptation; c) constrained h-adaptation using RIVARA's LEPP algorithm

As in the previous examples, two different adaptive computations are performed: unconstrained variational h-adaptation; and constrained variational h-adaptation using RIVARA's LEPP algorithm to maintain a lower bound on the aspect ratio of the elements. In addition, two uniform refinement steps are evaluated by way of baseline. The distribution of the effective plastic strain  $\varepsilon^P$  is given in Fig. 6.10. Fig. 6.10a) shows a mesh generated by applying two uniform refinement steps to the initial discretization of Fig. 6.6. The meshes in Figs. 6.10b) and c) are the result of the unconstrained and constrained variational h-adaptation schemes, respectively. As in the preceding examples, the contrast between the unconstrained and constrained adaptation schemes is clearly evident in Figs. 6.10b) and c). Thus, the unconstrained variational h-adaptation strategy results in a highly anisotropic and localized mesh that is in sharp contrast to the isotropic and diffuse mesh produced by the constrained strategy. In particular, the unconstrained mesh traces a *slip cone* that separates the triaxial plug under the indenter from the matrix. The elements tiling the slip cone are flat and elongated, with the result that the entire slip-cone mechanism is represented with a modicum of degrees of freedom. The corresponding plastic strain field is highly localized to the slip cone, and elastic unloading occurs elsewhere. By way of contrast, the constrained plastic strain field is diffuse and does not show signs of localization. This excessive *numerical diffusion* effectively eliminates all traces of the slip cone and results in an artificially smooth plastic strain distribution.

The various load-displacement diagrams are collected in Fig. 6.11 for ease of comparison.

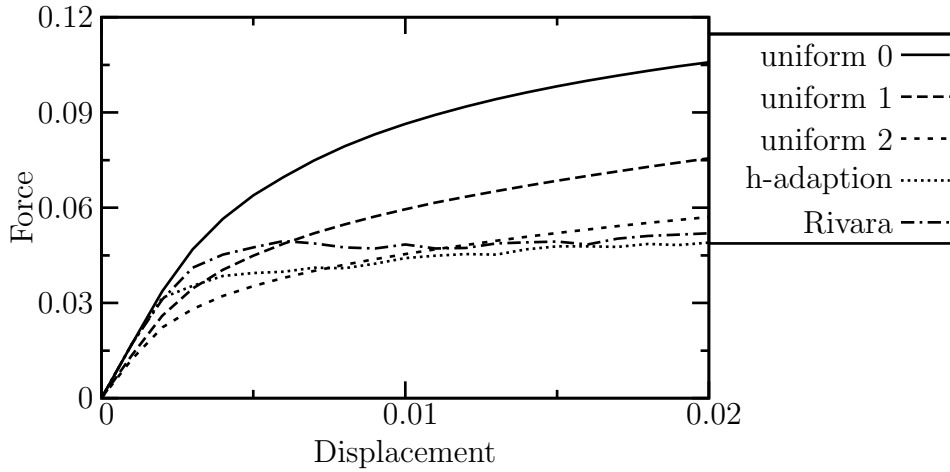


**Figure 6.11:** Indentation of an elastic-plastic block. Load-displacement diagrams obtained from: initial mesh (uniform 0); two uniform refinement steps (uniform 1 and 2); and variational h-adaption

As expected, the coarse discretizations overestimate the indentation load and stiffness. Uniform refinement progressively relaxes the predicted response, but an overly stiff response remains even at the finest level of refinement. In contrast, the adaptive solutions predict a clear failure load, with the most compliant response corresponding to the unconstrained solution. However, a certain lag is observed initially in the adaptive solutions which results from the gradual way in which refinement is introduced. Control over this lag can be exerted through the choice of energy tolerance  $\mu_c$ .

**Remark 6.9.2.1** *It should be noted that the curve corresponding to the h-adaptive computations illustrated in Fig. 6.11 are based on different discretizations and hence, cannot be interpreted as standard load-displacement diagrams. However, the two different energy-based mesh adaptations can be roughly compared to one another. By choosing  $\alpha_{\text{ref}} = 0.75$  in the case of the unconstrained algorithm and  $\alpha_{\text{ref}} = 1.0$  for the coupling with RIVARA's LEPP, the predicted number of nodes within each load step is similar for both methods.*

### 6.9.3 Indentation of a block: moving force

The performance of the energy-based h-refinement combined with the variational coarsening strategy according to Section 6.7 is demonstrated by means of a numerical analysis of an indentation of a block. The dimensions of the cube are:  $1.0 \times 1.0 \times 1.0$  [m]. For the material response, the hyperelastic model according to Subsection 6.9.2.1 is adopted. Except on the top of the cube, the normal component of displacement field is set to zero on the boundaries. As displayed in Fig. 6.12a) a vertical displacement of magnitude 0.1 m is prescribed on the left corner of the front of the structure first. Then, the combined refinement / coarsening formulation according to Section 6.7 is applied resulting in the

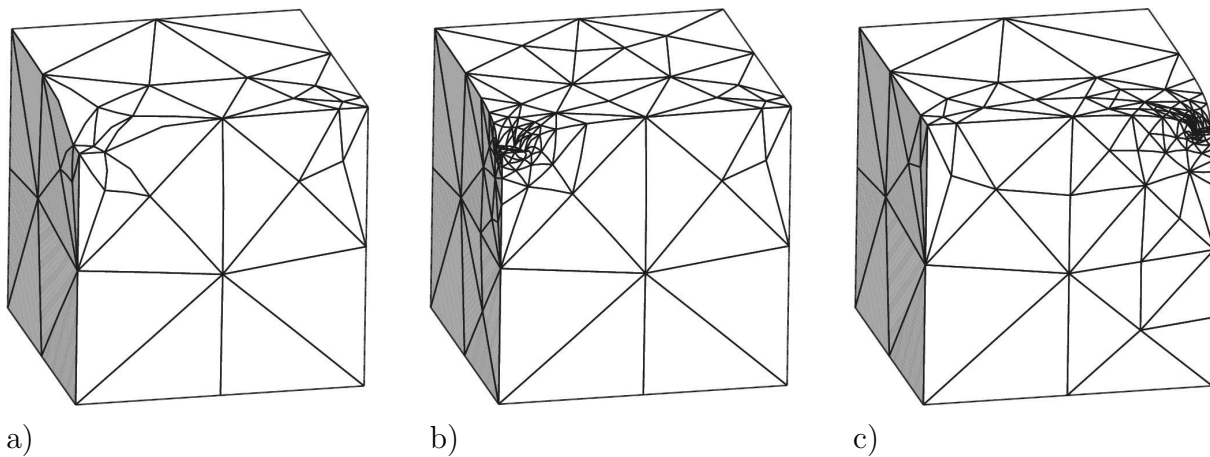


**Figure 6.12:** Indentation of an elastic block. Final meshes after constrained variational  $h$ -adaption coupled to variational coarsening

new triangulation presented in Fig. 6.12b). Subsequently, the load is moved to the right corner of the structure and the mesh adaption is performed once again, see Fig. 6.12c). Refinement and coarsening is controlled by setting  $\alpha_{\text{ref}} = 0.02$  and  $\alpha_{\text{coarse}} = 0.01$ . However, different values of  $\alpha_{\text{ref}}$  and  $\alpha_{\text{coarse}}$  lead to almost identical results. The aspect ratio of the elements is maintained by means of RIVARA's Longest-Edge Propagation Path (LEPP) bisection algorithm.

It is evident from the figures that the combined algorithm leads to a mesh-refinement of regions showing large energy densities and to coarsening where the energy is relatively low. As a consequence, and fully analogous to the VALE formulated presented in Chapter 4, the adaptive finite element formulation can be applied to problems characterized by moving singularities. Clearly, in particular for the numerical analysis of crack propagation, this is of utmost importance. In Chapter 7.2, some first ideas concerning the coupling of cohesive elements with variational-based mesh adaptations will be sketched.

# Chapter 7

## Conclusion and outlook

### 7.1 Conclusion

**Variational constitutive updates** In the first part of the present work, a state of the art review on constitutive updates has been given. Special emphasis has been on a class of updates characterized by a variational structure. More precisely, within this framework, the deformation mapping as well as the history variables follow jointly from minimizing an incremental potential. This minimization principle represents the essential ingredient for all variational adaptive schemes discussed in this work. Since slightly different variational constitutive updates can be found in the literature, attention has been turned to a coherent representation.

**Strong discontinuity approaches** A novel class of finite element formulations allowing for the numerical analysis of localized material failure at finite strains has been proposed in Chapter 3. The model is characterized by a discontinuous approximation of the displacement field, and it is based on the Enhanced Assumed Strain (EAS) concept. More specifically, it falls into the range of the *Strong Discontinuity Approach* (SDA). Since the approximation of the deformation is essential for the model, a detailed analysis of the kinematics has been given. In contrast to other approaches dealing with displacement discontinuities such as the eXtended Finite Element Method (X-FEM) or classical interface laws, the SDA shows a coupling of the strains across the surface defined by the displacement jumps. A comparison between different SDAs has demonstrated that, except for the notation, the kinematics of all models are equivalent in the case of standard constant strain triangle elements. For the development of the interface laws connecting the displacement discontinuity with the traction vector, a new method has been proposed. It is based on the fact that the condition of traction equilibrium can be re-written such that it is formally identical to the necessary condition of yielding known from classical plasticity theories (continuous deformation mapping). This concept highlights the similarities

between standard constitutive models and those based on cohesive traction-separation laws. This similarity suggests an implementation of the SDA being analogous to nowadays classical computational plasticity. Consequently, a predictor-corrector algorithm has been adopted. More precisely, a return-mapping-type method has been developed, i. e., in contrast to SDAs published previously which are based on the static condensation, the novel implementation is formally identical to that of standard computational plasticity theory. As a result, existing subroutines can be used with only minor modifications necessary. Referring to the class of interface laws or the type of finite elements, no special assumption has been made. Consequently, the suggested numerical framework can be applied to a broad range of different traction-separation laws. Furthermore, it allows for higher order displacement approximations.

Since the computation of the topology of the singular surface characterized by displacement discontinuities is not unique, different methods for choosing the physically most relevant topology have finally been compared to each other. It has been shown that for a quite general class of constitutive models, the postulate of maximum dissipation, the postulate of maximum inelastic deformations and an approach based on maximizing the compatibility between the smooth and the discontinuous part of the deformation mapping are equivalent.

**Variational Arbitrary Lagrangian-Eulerian (VALE) formulations** Since the results predicted by cohesive finite element formulations such as the SDA depend significantly on the quality of the numerical approximation of the continuous deformation, a family of adaptive strategies has been discussed in Chapter 4. Based on the variational constitutive updates presented in Chapter 2, a Variational Arbitrary Lagrangian-Eulerian (VALE) formulation has been advocated. In contrast to classical finite element models, the proposed method seeks to minimize the energy function governing the underlying physical problem with respect to both the finite element mesh over the deformed as well as the undeformed configuration of the body. Unfortunately, the solution of the resulting optimization problems is not without difficulty. More specifically, it has been shown that the problem is nonconvex and highly singular (i. e., the respective HESSIAN). For that reason, an algorithm based on a viscous-type relaxation combined with effective line search strategies has been elaborated. This method eliminates the aforementioned difficulties without changing the solution of the unrelaxed problem. Within the numerical optimization, constraints have been enforced that surface nodes remain in the surface and move within their corresponding surface component, namely within their faces or edges; and that vertices in the boundary representation of the domain remain fixed. This restriction can be relaxed by allowing nodes to migrate in and out of the boundary. For that purpose, a fully variational algorithm having  $O(N)$  complexity has been developed. The energy release corresponding to node migration is estimated by means of a local optimization problem depending on only six degrees of freedom. The resulting finite element

method can be applied to any physical model characterized by an extremum principle. Details necessary for standard dissipative solids such as the transfer of the history variables have been discussed. Finally, it has been shown that the discretizations generated by the energy-driven adaptive scheme outperform triangulations in which elements with large aspect ratios are avoided a priori.

**Variational-based remeshing strategies** Within the VALE formulation according to Chapter 4 the mesh connectivity has been kept constant. However, this may lead to strong topological constraints that severely limit the meshes that can be attained by  $r$ -adaptivity. Therefore, a novel variational-based remeshing strategy has been advocated in Chapter 5. Based on local mesh transformations, the connectivity of an initial triangulation is modified such that the solution associated with the new discretization is closer to the analytical extremum. Hence, improvement of the solution is guaranteed. Numerical analyses have demonstrated the performance of the energy-driven remeshing method and the combined VALE-remeshing algorithm. The examples have shown that the proposed approach leads to meshes that outperform those resulting from purely geometrical element measures.

**Variational h-adaptive finite element formulation** The variational adaptive finite element formulations presented in Chapters 4 – 5 improve significantly the numerical solution. However, sometimes a further improvement is desirable. For that reason, a variational h-adaptation has been developed in Chapter 6. Analogous to the VALE formulation and the energy-driven remeshing strategy, the proposed h-adaptive method can be applied to any mechanical problem characterized by a minimization principle, provided the deformation field is sufficiently smooth, i. e., continuous. Mesh refinement realized by using edge-bisection algorithms is applied when the released energy or incremental pseudo-energy exceeds a certain threshold value. In order to avoid global recomputes, the energy release by mesh refinement is estimated by a lower bound obtained by relaxing a local patch of elements. This bound can be computed locally, which reduces the complexity of the refinement algorithm to  $O(N)$ . By comparing the proposed error indicator to classical error estimates it has been shown that both concepts are almost identical for linearized elasticity theory. In this respect, the novel variational method can be understood as a canonical extension of classical concepts. The resulting algorithm allows for energy-driven mesh refinement as well as coarsening. For standard dissipative solids, a consistent transfer operator necessary for mapping the history variables between different meshes has been developed. It is noteworthy that the variational strategies presented in Chapters 4 – 6 can be easily combined. As a prototype, a variational hr-adaptive method has been implemented. The performance of the energy-driven h-refinement has been illustrated by several numerical examples. It is remarkable that anisotropic mesh refinement arises spontaneously, without recourse to empirical rules, as a result of variational h-

adaption. The resulting elements, while optimal in an energy sense, are highly elongated or flattened, and supply varying degrees of spatial resolution in different directions. The ability to resolve sharp gradients in one direction without excessive mesh refinement in the remaining directions is of critical importance for dealing efficiently with features such as slip surfaces and shear bands. Indeed, in these cases isotropic mesh refinement inevitably leads to rapid growth of the problem size.

Although highly anisotropic meshes are, in many cases, very efficient from an energetical point of view, sometimes it may be desirable to enforce elements having relatively small aspect ratios. For instance, if iterative solvers are used, highly distorted meshes may slow down the computation. Consequently, the variational h-adaption has been combined with RIVARA's longest-edge bisection algorithm guaranteeing an upper bound of the aspect ratio. However, it should be emphasized once again that in contrast to the purely energy-driven formulation, the combined method is not optimal from an energetical point of view.

## 7.2 Outlook and future work

In the present work, different numerical models for the simulation of material failure at finite strains have been discussed. Conceptually, these approaches can be grouped into cohesive finite element formulations and variational mesh adaptations. The performance of these methods has been demonstrated by several numerical examples. However, for more complex mechanical problems such as cracking in large engineering structures, a combination of both classes of algorithms seems to be necessary. The coupling of variational mesh adaption with cohesive finite element formulations represents one of the ongoing research subjects. First ideas can be found in [NEGRI 2005B; MOSLER, ORTIZ & PANDOLFI 2006]. They will be briefly discussed in the remaining part of this section.

Following [FRANCFORT & MARIGO 1998; BOURDIN, FRANCFORT & MARIGO 2000; DAL MASO & ZANINI 2005; YANG, MOTA & ORTIZ 2005], crack propagation in brittle materials or the formation of slip bands can be recast into a minimization principle of the type

$$\inf_{\varphi, [\mathbf{u}]} I_h(\varphi, [\mathbf{u}]) \quad (7.1)$$

defined by the (pseudo) potential

$$I_h(\varphi, [\mathbf{u}]) = \int_{\Omega} \Psi(\varphi) \, dV + \int_{\partial_s \Omega} \tilde{\Psi}([\mathbf{u}]) \, dA \quad (7.2)$$

depending on the continuous deformation mapping  $\varphi$  and the displacement discontinuity  $[\mathbf{u}]$ . Here,  $\Psi$  represents the (pseudo) bulk energy and  $\tilde{\Psi}$  is associated with the energy

corresponding to the cohesive surfaces. It is noteworthy that the limit of integration of the second term can be re-written as

$$\partial_s \Omega = \{ \mathbf{X} \in \Omega \mid \| \llbracket \mathbf{u} \rrbracket (\mathbf{X}) \| \neq 0 \}. \quad (7.3)$$

Clearly, if the space of special functions with bounded variations (SBV) is chosen as the domain of  $\varphi$ ,  $\llbracket \mathbf{u} \rrbracket = \llbracket \varphi \rrbracket$ , and the minimization problem (7.1) reads simply  $\inf_{\varphi} I_h$ . Unfortunately, the solution of the optimization problem (7.1) is not without difficulty.

Very recently, [NEGRI 2005B] and [ORTIZ & PANDOLFI 2005; MOSLER, ORTIZ & PANDOLFI 2006] published first ideas for solving the minimization problem (7.1). Roughly speaking, these authors combined the VALE method according to Chapter 4 with classical interface cohesive finite elements, cf. [ORTIZ & PANDOLFI 2005]. As mentioned before, one essential problem associated with interface elements is that the topology of  $\partial_s \Omega$  is approximated by facets between neighboring bulk elements. As a consequence, the space of admissible  $\partial_s \Omega$  is relatively small which results, in many cases, in locking effects. More specifically, the numerically computed dissipation is often overestimated, cf. [GAN-GULY, VAVASIS & PAPOULIA 2005]. However, within the numerical methods advocated in [NEGRI 2005B; MOSLER, ORTIZ & PANDOLFI 2006] the finite element mesh over the reference configuration of the body follows from the underlying physical minimization problem (7.1) as well. This leads to an improvement of the topology of the cohesive surfaces and hence, reduces locking effects. More precisely, [NEGRI 2005B] proved (under certain assumptions) that the finite element discretization of Eq. (7.1)  $\Gamma$ -converges to the original problem (in the space of special functions with bounded variations). The first numerical results obtained from the combined VALE cohesive finite element formulation are very promising. However, further investigations are necessary.

Alternatively, the variational h-adaption as discussed in Chapter 6 can be coupled with cohesive finite elements. The performance of such an algorithm is illustrated here. For the sake of simplicity, cracking is modeled by using traction-free internal surfaces. Furthermore, those surfaces are defined explicitly by changing the essential boundary conditions. However, it should be noted that although the more general case, i. e., traction-separation laws with a continuous softening response, requires a transfer of the history variables, it does not lead to further problems in principle. Based on the prototype model, the problem shown in Fig. 4.6.2 is re-analyzed numerically. First, the variational h-adaption presented in Chapter 6 is applied. Subsequently, crack propagation is taken into account by modifying the DIRICHLET boundaries and the energy-driven mesh-refinement/coarsening strategy is used once again. It can be seen that before cracking (Fig. 7.1a)), the discretization in the vicinity of the crack tip is very fine, while the triangulation of the remaining part of the structure is relatively coarse. Due to crack growth, the region showing high energy densities moves. According to Fig. 7.1b), this leads to a re-meshing. More precisely, the variational h-refinement algorithm automatically adapts the mesh such that only domains characterized by high energy densities are refined. As a consequence, the

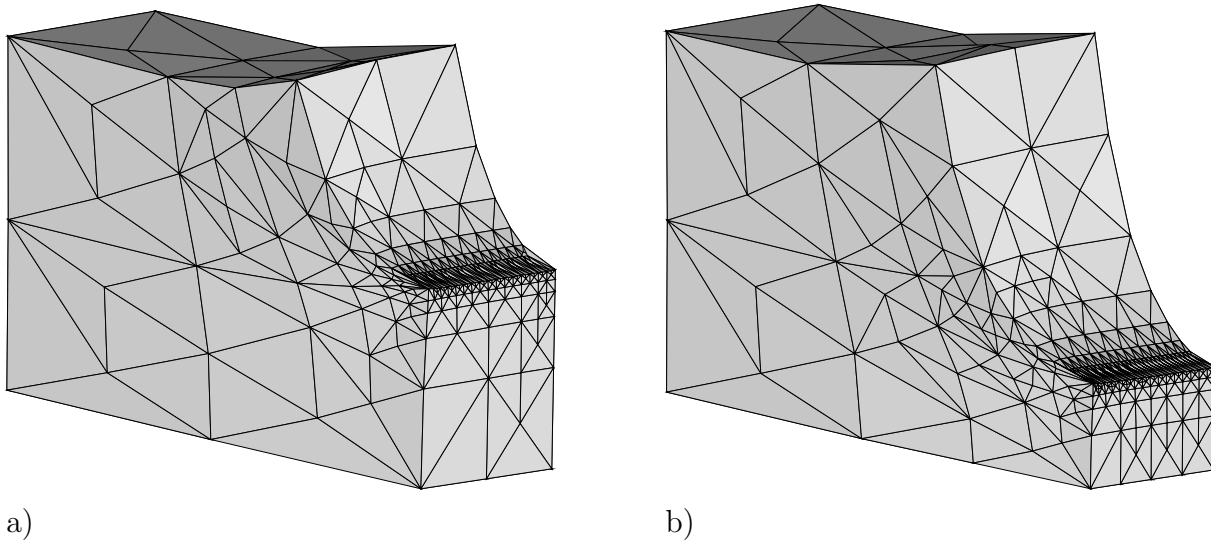


**Figure 7.1:** Numerical analysis of the notched specimen shown in Fig. 4.6 by using the variational h-adaptive finite element formulation according to Chapter 6 combined with RIVARA's LEPP algorithm. The solution is symmetric about three orthogonal axes and only one eighth of the system is given, cf. Fig. 6.3a). Crack propagation is approximated by changing the essential boundaries: a) deformed configuration before cracking; b) after crack propagation.

combination of cohesive finite element approaches with variational h-adaption seems to be very promising. Clearly, further work in this direction is required.

As the final prototype model, classical interface models are combined with the energy-driven remeshing strategy advocated in Chapter 5. For cracking in brittle materials, the finite element framework proposed in [ORTIZ & PANDOLFI 1999] is adopted. However, the Strong Discontinuity Approach (SDA) presented in Chapter 3 could be applied as well. It is an educated guess that the variational remeshing method leads to a new triangulation whose facets are aligned with the crack surface corresponding to the analytical solution. First results obtained from the coupled approach are given in Fig. 7.2. The figures correspond to different stages of cracking in a plain concrete slab subjected to mode-I loading. It is evident from this example that the variational method leads to remeshing and hence, to a different set of admissible crack paths compared to the initial mesh. For the analyzed structure, this does not have a strong effect on the structural behavior of the system, since the facets of the initial mesh are already aligned with the expected path of the primary crack. However, the topology of the secondary cracks which are hard to see in Fig. 7.2 are optimized. More precisely, the local mesh transformations lower the pseudo energy, and hence, the energy-driven remeshing strategy improves the quality of the solution.





# Bibliography

- AICHHOLZER, O., F. HURTADO AND M. NOY (2004). A lower bound on the number of triangulations of planar point sets. *Computational Geometry: Theory and Applications* 29(2), 135–145.
- AINSWORTH, M. AND J.T. ODEN (1997). A posteriori error estimation in finite element analysis. *Computer Methods in Applied Mechanics and Engineering* 142, 1–88.
- AINSWORTH, M. AND J.T. ODEN (2000). *A Posterior Error Estimation in Finite Element Analysis*. Wiley.
- ALBERTY, J., C. CARSTENSEN AND D. ZARRABI (1999). Adaptive numerical analysis in primal elastoplasticity with hardening. *Computer Methods in Applied Mechanics and Engineering* 171, 175–204.
- ALFAIATE, J., A. SIMONE AND L. J. SLUYS (2003). Non-homogeneous displacement jumps in strong embedded discontinuities. *International Journal for Solids and Structures* 40(21), 5799–5817.
- AMBROSIO, L., N. FUSCO AND D. PALLARA (2000). *Special Functions of Bounded Variation and Free Discontinuity Problems*. Oxford University Press, Oxford.
- ANTMAN, S.S. (1995). *Nonlinear Problems of Elasticity*. Springer.
- APEL, T. (1999). *Anisotropic Finite Elements: Local Estimates and Applications*. Habilitation, TU Chemnitz, Germany.
- ARMERO, F. (1999). Large-scale modeling of localized dissipative mechanisms in a local continuum: applications to the numerical simulation of strain localization in rate-dependent inelastic solids. *Mechanics of Cohesive-Frictional Materials* 4, 101–131.
- ARMERO, F. AND K. GARIKIPATI (1995). Recent advances in the analysis and numerical simulation of strain localization in inelastic solids. In D.R.J. Owen, E Oñate, and E. Hinton (Eds.), *Proc., 4th Int. Conf. Computational Plasticity*, Volume 1, 547–561.
- ARMERO, F. AND K. GARIKIPATI (1996). An analysis of strong discontinuities in multiplicative finite strain plasticity and their relation with the numerical simulation of strain localization in solids. *International Journal for Solids and Structures* 33, 2863–2885.

- ARMERO, F. AND E. LOVE (2003). An arbitrary Lagrangian-Eulerian finite element method for finite strain plasticity. *International Journal for Numerical Methods in Engineering* 57, 471–508.
- ASARO, R.J. (1983). Micromechanics of crystals and polycrystals. *Advances in Applied Mechanics* 23.
- ASKES, H., E. KUHL AND P. STEINMANN (2004). An ALE formulation based on spatial and material settings of continuum mechanics. Part 2: Classification and applications. *Computer Methods in Applied Mechanics and Engineering* 193(39-41), 4223–4245.
- BABUŠKA, I. AND J.M. MELENK (1996). The partition of unity finite element method: Basic theory and applications. *Computer Methods in Applied Mechanics and Engineering* 139, 289–314.
- BABUŠKA, I. AND J.M. MELENK (1997). The partition of unity method. *International Journal for Numerical Methods in Engineering* 40, 727–758.
- BABUŠKA, I. AND W.C. RHEINBOLDT (1978). Error estimates for adaptive finite element computations. *SIAM J. Numer. Anal.* 15, 736–754.
- BAŞAR, Y AND D. WEICHERT (2000). *Nonlinear continuum mechanics of solids*. Springer.
- BALL, J.M. (1978). Convexity conditions and existence theorems in nonlinear elasticity. *Arch. Rat. Mech. Anal.* 63, 337–403.
- BÄNSCH, E. (1991a). An adaptive finite-element strategy for the three-dimensional time-dependent navier-stokes equations. *Journal of Computational and Applied Mathematics* 36, 3–28.
- BÄNSCH, E. (1991b). Local mesh refinement in 2 and 3 dimensions. *Impact of Computing in Science and Engineering* 3, 181–191.
- BARENBLATT, G.I. (1962). The mathematical theory of equilibrium cracks in brittle fracture. *Adv. Appl. Mech.* 7, 55–129.
- BATHE, K.J. (1995). *Finite element procedures*. Springer.
- BAŽANT, Z.P. AND G. PIJAUDIER-CABOT (1988). Nonlocal damage, localization, instability and convergence. *Journal of Applied Mechanics* 55, 287–293.
- BELYTSCHKO, T. AND T. BLACK (1999). Elastic crack growth in finite elements with minimal remeshing. *International Journal for Numerical Methods in Engineering* 45, 601–620.
- BELYTSCHKO, T., J. FISH AND B.E. ENGELMANN (1988). A finite element with embedded localization zones. *Computer Methods in Applied Mechanics and Engineering* 70, 59–89.
- BELYTSCHKO, T. AND J.M. KENNEDY (1978). Computer models for subassembly simulations. *Nuclear Engineering and Design* 49, 17–38.

- BELYTSCHKO, T., W.K. LIU AND B. MORAN (2000). *Nonlinear Finite Elements for Continua and Structures*. Wiley: New York.
- BERNADI, C., B. MÉTIVET AND R. VERFÜRTH (1993). Analyse numérique d'indicateurs d'erreur. Technischer Bericht 93025, Université Pierre et Marie Curie, Paris VI.
- BERTRAM, A. (1999). An alternative approach to finite plasticity based on material isomorphisms. *International Journal of Plasticity* 15, 353–374.
- BERTRAM, A. (2005). *Elasticity and Plasticity of Large Deformations*. Springer-Verlag, Berlin.
- BETTEN, J. (1993). *Kontinuumsmechanik*. Springer.
- BIOT, M.A. (1956). Thermoelasticity and irreversible thermodynamics. *Journal of Statistical Physics* 27, 250–253.
- BIOT, M.A. (1958). Linear thermodynamics and the mechanics of solids. In *Proceedings of the Third U.S. National Congress of Applied Mechanics*, 1–18.
- BORJA, R.I. (2000). A finite element model for strain localization analysis of strongly discontinuous fields based on standard galerkin approximation. *Computer Methods in Applied Mechanics and Engineering* 190, 1529–1549.
- BORJA, R.I. (2002). Finite element simulation of strain localization with large deformation: capturing strong discontinuity using a Petrov-Galerkin multiscale formulation. *Computer Methods in Applied Mechanics and Engineering* 191, 2949–2978.
- BORJA, R.I. AND A.R. REGUEIRO (2001). Strain localization in frictional materials exhibiting displacement jumps. *Computer Methods in Applied Mechanics and Engineering* 190, 2555–2580.
- BOURDIN, B., G.A. FRANCFORT AND J.-J. MARIGO (2000). Numerical experiments in revisited brittle fracture. *Journal of the Mechanics and Physics of Solids* 48(4), 797–826.
- BRAESS, D. (1997). *Finite Elemente*. Springer.
- BRAIDES (2002). *Gamma-convergence for Beginners*. Oxford University Press.
- BRAUN, M. (1997). Configurational forces induced by finite element discretization,. *Proc. Estonian Acad. Sci. Phys. Math.* 46, 24–31.
- BRUHNS, O.T., H. XIA AND A. MEYERS (2001). A self-consistent Eulerian rate type model for finite deformation elastoplasticity with isotropic damage. *International Journal for Solids and Structures* 38, 657–683.
- BRUHNS, O.T., H. XIAO AND A. MEYERS (2001). Constitutive inequalities for an isotropic elastic strain energy function based on hencky's logarithmic strain tensor. *Proc. Roy. Soc. London, A* 457, 2207–2226.

- CALLARI, C. AND F. ARMERO (2004). Analysis and numerical simulations of strong discontinuities in finite strain poroplasticity. *Computer Methods in Applied Mechanics and Engineering* 193, 2941–2986.
- CAMACHO, G.T. AND M. ORTIZ (1996). Computational modelling of impact damage in brittle materials. *International Journal for Solids and Structures* 30(20-22), 2899–2938.
- CARSTENSEN, C., K. HACKL AND A. MIELKE (2002). Non-convex potentials and microstructures in finite-strain plasticity. *Proc. R. Soc. Lond. A* 458, 299–317.
- CHADWICK, P. (2000). *Continuum mechanics – Concise theory and problems*. Dover, Mineola, New York.
- CHAVES, E.W.V. (2003). *A three dimensional setting for strong discontinuities modelling in failure mechanics*. Ph. D. thesis, UPC Barcelona.
- CHORIN, A.J., T.J.R. HUGHES, M.F. MCCrackEN AND J.E. MARSDEN (1978). Product formulas and numerical algorithms. *Comm. Pure Appl. Math.* 31, 205–256.
- CIARLET, P. (1988). *Mathematical elasticity. Volume I: Three-dimensional elasticity*. North-Holland Publishing Company, Amsterdam.
- CIRAK, F., M. ORTIZ AND A. PANDOLFI (2005). A cohesive approach to thin-shell fracture and fragmentation. *Computer Methods in Applied Mechanics and Engineering* 194, 2604–2618.
- COLEMAN, B.D. (1964). Thermodynamics of materials with memory. *Arch. Rational Mech. Anal.* 17, 1–45.
- COLEMAN, B.D. AND M.E. GURTIN (1967). Thermodynamics with internal state variables. *J. Chem. Phys* 47, 597–613.
- COMI, C., A. CORIGLIANO AND G. MAIER (1991). Extremum properties of finite-step solutions in elastoplasticity with nonlinear hardening. *International Journal for Solids and Structures* 29, 965–981.
- COMI, C. AND U. PEREGO (1995). A unified approach for variationally consistent finite elements in elastoplasticity. *Computer Methods in Applied Mechanics and Engineering* 121, 323–344.
- CUITI NO, A. AND M. ORTIZ (1992). A material-independent method for extending stress update algorithms from small-strain plasticity to finite plasticity with multiplicative kinematics. *International Journal for Numerical Methods in Engineering* 30, 1099–1114.
- DAL MASO, G. (1983). *An introduction to  $\Gamma$ -convergence*. Birkhäuser, Boston.
- DAL MASO, G. AND C. ZANINI (2005). Quasistatic crack growth for a cohesive zone model with prescribed crack pat. submitted, <http://cvgmt.sns.it/people/dalmaso/>.

- DE BORST, R. (1986). *Non-linear analysis of frictional materials*. Ph. D. thesis, Technical University Delft.
- DE BORST, R. (2001). Some recent issues in computational mechanics. *International Journal for Numerical Methods in Engineering* 52, 63–95.
- DE BORST, R. AND H.B. MÜHLHAUS (1992). Gradient-dependent plasticity: Formulation and algorithmic aspects. *International Journal for Numerical Methods in Engineering* 35, 521–539.
- DENZER, R., F.J. BARTH AND P. STEINMANN (2003). Studies in elastic fracture mechanics based the material force method. *International Journal for Numerical Methods in Engineering* 58, 1817–1835.
- DOLBOW, J., N. MOËS AND T. BELYTSCHKO (2002). An extended finite element method for modeling crack growth with frictional contact. *Computer Methods in Applied Mechanics and Engineering* 190, 6825–6846.
- DOMPIERRE, J., P. LABBE AND F. CAMERERO (1984). Proposal of benchmarks for 3D unstructured tetrahedral mesh optimization. In *Seventh International Meshing RoundTable '98*, 459–478.
- DONEA, J. (1983). Arbitrary Lagrangian-Eulerian finite element methods. In T. Belytschko, T.J.R. Hughes, and K.-J. Bathe (Eds.), *Computational Methods in Transient Analyses*, Volume 1 of *Mechanics and Mathematical Methods*, 473–516. North-Holland.
- DUGDALE, D.S. (1960). Yielding of steel sheets containing slits. *Journal of the Mechanics and Physics of Solids* 8, 100–108.
- DUMSTORFF, P. AND G. MESCHKE (2005). Modelling of cohesive and non-cohesive cracks via X-FEM based on global energy criteria. In E. Oñate and D.R.J. Owen (Eds.), *VIII International Conference on Computational Plasticity*.
- DUMSTORFF, P., J. MOSLER AND G. MESCHKE (2003). Advanced discretization methods for cracked structures: The strong discontinuity approach vs. the extended finite element method. In E. Oñate and D.R.J. Owen (Eds.), *VII International Conference on Computational Plasticity*.
- DVORKIN, E.N., A. M. CUITIÑO AND G. GIOIA (1990). Finite elements with displacement interpolated embedded localization lines insensitive to mesh size and distortions. *International Journal for Numerical Methods in Engineering* 30, 541–564.
- ERDOGAN, F. AND G. SIH (1963). On the crack extension in plates under plane loading and transverse shear. *Journal of Basic Engineering* 85, 519–527.
- ERN, A. AND J.-L. GUERMOND (2004). *Theory and practice of finite elements*. Springer New York.
- ESHELBY, J.D. (1951). The force on an elastic singularity. *Phil. Trans. R. Soc. Lond. A* 244, 87–112.

- ESHELBY, J.D. (1975). The elastic energy-momentum tensor. *J. Elasticity* 5, 321–335.
- ETEROVIC, A.L. AND K.-J. BATHE (1990). A hyperelastic-based large strain elastoplastic constitutive formulation with combined isotropic-kinematic hardening using the logarithmic stress and strain measures. *International Journal for Numerical Methods in Engineering* 30, 1099–1114.
- FANCELLO, E., J.-P. PONTHOT AND L. STAINIER (2005). A variational formulation of constitutive models and updates in non-linear finite viscoelasticity. *International Journal for Numerical Methods in Engineering*. in press.
- FEIST, C. AND G. HOFSTETTER (2005). An embedded strong discontinuity model for cracking in plain concrete. *Computer Methods in Applied Mechanics and Engineering*. in press.
- FELIPPA, C. (1976). Numerical experiments in finite element grid optimization by direct energy search. *Appl. Math. Modelling* 1, 93–96.
- FETECAU, R.C., J.E. MARSDEN AND M. WEST (2003). Variational multisymplectic formulations of nonsmooth continuum mechanics. In E. Kaplan, J.E. Marsden, and K.R. Sreenivasan (Eds.), *Perspectives and Problems in Nonlinear Science*, 229–261. Springer-Verlag.
- FRANCFORT, G.A. AND J.-J. MARIGO (1998). Revisiting brittle fracture as an energy minimization problem. *Journal of the Mechanics and Physics of Solids* 46(8), 1319–1342.
- FREITAG, L.A. AND P.M. KNUPP (2002). Tetrahedral mesh improvement via optimization of the element condition number. *International Journal for Numerical Methods in Engineering* 53, 1377–1391.
- FREY, P.J. AND F. ALAUZET (2005). Anisotropic mesh adaptation for CFD computations. *Computer Methods in Applied Mechanics and Engineering* 194(48-49), 5068–5082.
- GANGULY, P., S. VAVASIS AND K. PAPOULIA (2005). An algorithm for two-dimensional mesh generation based on pinwheel tiling. *SIAM Journal on Scientific Computing*. submitted.
- GARIKIPATI, K. (1996). *On strong discontinuities in inelastic solids and their numerical simulation*. Ph. D. thesis, Stanford University.
- GARIKIPATI, K. AND T.J.R. HUGHES (1998). A study of strain localization in a multiple scale framework - the one-dimensional problem. *Computer Methods in Applied Mechanics and Engineering* 159(3-4), 193–222.
- GASSER, TH.C. AND G.A. HOLZAPFEL (2003). Geometrically non-linear and consistently linearized embedded strong discontinuity models for 3D problems with an application to the dissection analysis of soft biological tissues. *Computer Methods in Applied Mechanics and Engineering* 192, 5059–5098.

- GASSER, TH.C. AND G.A. HOLZAPFEL (2005). Modelling 3D crack propagation in unreinforced concrete using PUFEM. *Computer Methods in Applied Mechanics and Engineering* 194, 2859–2896.
- GASSER, TH.C. AND G.A. HOLZAPFEL (2006). 3d crack propagation in unreinforced concrete. A two-step algorithm for tracking 3d crack paths. *Computer Methods in Applied Mechanics and Engineering*. in press.
- GEERS, M.G.D., T. PEIJS AND R. BREKELMANS, W.A.M. DE BORST (1996). Experimental monitoring of strain localization and failure behaviour of composite materials. *Composite Science Technology* 56, 1283–1290.
- GEIGER, C. AND C. KANZOW (1999). *Numerische Verfahren zur Lösung unrestringierter Optimierungsaufgaben*. Springer.
- GERMAN, P., Q.S. NGUYEN AND P. SUQUET (1983). Continuum thermodynamics. *J. Appl. Mech.* 50, 1010–1020.
- GREEN, A.E. AND P.M. NAGHDI (1965). A general theory of an elastic-plastic continuum. *Arch. Rat. Mech. Anal.* 18, 251–281.
- GURTIN, M.E. (2000). *Configurational forces as basic concepts of continuum physics*, Volume 137 of *Applied Mathematical Sciences*. Springer.
- HACKL, K. (1997). Generalized standard media and variational principles in classical and finite strain elastoplasticity. *Journal of the Mechanics and Physics of Solids* 45(5), 667–688.
- HADAMARD, J. (1903). *Leçons sur la Propagation des Ondes*. Librairie Scientifique A. Hermann et Fils, Paris.
- HAIRER, E. AND G. WANNER (2000). *Solving ordinary differential equations II, Stiff and differential-algebraic problems*. Springer series in Computational Mathematics. Springer, Berlin, Heidelberg, New York.
- HALPHEN, B. AND Q.S. NGUYEN (1975). Sur les matériaux standards généralisés. *J. Mécanique* 14, 39–63.
- HAUPT, P. (2000). *Continuum mechanics and theory of materials*. Springer Verlag, Berlin - Heidelberg - New York.
- HILL, R. (1958). A general theory of uniqueness and stability in elastic-plastic solids. *Journal of the Mechanics and Physics of Solids* 6, 236–249.
- HILL, R. (1968). On constitutive inequalities for simple materials. *Journal of the Mechanics and Physics of Solids* 16, 229–242;315–322.
- HILL, R. (1978). Aspects of invariance in solid mechanics. *Advances in Appl. Mech.* 18, 1–75.

- HILLERBORG, A., M. MODEER AND P.E. PETERSSON (1976). Analysis of crack formation and crack growth in concrete by means of fracture mechanics and finite elements. *Cement and Concrete Research* 6, 773–782.
- HOFFMANN, C. M. (1989). *Geometric and Solid Modeling*. San Mateo, California: Morgan Kaufmann Publishers.
- HUGHES, T.J.R., W.K. LIU AND T.K. ZIMMERMANN (1981). Lagrangian-Eulerian finite element formulations for incompressible viscous flows. *Computer Methods in Applied Mechanics and Engineering* 29, 329–349.
- HUTTER, K. (1977). The foundations of thermodynamics, its basic postulates and implications. *Acta Mechanica* 27, 1–54.
- ITSKOV, M. (2001). *Theorie von Tensoren zweiter und vierter Stufe und ihre Anwendungen in der finiten anisotropen Elastizität und Plastizität*. Habilitation, Universität Bayreuth.
- ITSKOV, M. (2003). Computation of the exponential and other isotropic tensor functions and their derivatives. *Computer Methods in Applied Mechanics and Engineering* 192(35-36), 3985–3999.
- ITSKOV, M. (2004). On the application of the additive decomposition of generalized strain measures in large strain plasticity. *Mechanics Research Communications* 31, 507–517.
- JANSSON, N.E. (2002). *Modelling of delamination growth in composite structures*. Ph. D. thesis, Department of Applied Mechanics, Chalmers University of Technology.
- JIRÁSEK, M. (2000). Comparative study on finite elements with embedded cracks. *Computer Methods in Applied Mechanics and Engineering* 188, 307–330.
- JIRÁSEK, M AND T. BELYTSCHKO (2002). Computational resolution of strong discontinuities. In *Fifth World Congress on Computational Mechanics*.
- JIRÁSEK, M. AND T. ZIMMERMANN (2001). Embedded crack model: Part I: Basic formulation, Part II: Combination with smeared cracks. *International Journal for Numerical Methods in Engineering* 50, 1269–1305.
- JOE, B. (1989). Three-dimensional triangulations from local transformations. *SIAM J. SCI. COMPUT.* 10(4), 718–741.
- JOE, B. (1991). Construction of three-dimensional Delaunay triangulations using local transformations. *Computer Aided Geometric Design* 8, 123–142.
- JOE, B. (1995). Construction of three-dimensional improved-quality triangulations using local transformations. *SIAM J. SCI. COMPUT.* 16(6), 1292–1307.
- KLISINSKI, M., T. OLOFSSON AND R. TANO (1995). Mixed mode cracking of concrete modelled by inner softening band. In D.R.J. Owen, E Oñate, and E. Hinton (Eds.), *Proc., 4th Int. Conf. Computational Plasticity*, Volume 2, 1595–1606.

- KLISINSKI, M., K. RUNESSON AND S. STURE (1991). Finite element with inner softening band. *Journal of Engineering Mechanics (ASCE)* 117(3), 575–587.
- KNUPP, P.M. (2000a). Achieving finite element mesh quality via optimization of the Jacobian matrix norm and associated quantities. Part I – a framework for surface mesh optimization. *International Journal for Numerical Methods in Engineering* 48, 401–420.
- KNUPP, P.M. (2000b). Achieving finite element mesh quality via optimization of the Jacobian matrix norm and associated quantities. Part II – a framework for volume mesh optimization and the condition number of the Jacobian matrix. *International Journal for Numerical Methods in Engineering* 48, 1165–1185.
- KRAJGINOVIC, D. (1996). *Damage mechanics*. North Holland.
- KRAWIETZ, A. (1986). *Materialtheorie*. Springer-Verlag Berlin, Heidelberg, New York, Tokyo.
- KUHL, E., H. ASKES AND P. STEINMANN (2004). An ALE formulation based on spatial and material settings of continuum mechanics. Part 1: Generic hyperelastic formulation. *Computer Methods in Applied Mechanics and Engineering* 193(39-41), 4207–4222.
- LARSSON, R. AND K. RUNESSON (1996). Element-embedded localization band based on regularized displacement discontinuity. *Journal of Engineering Mechanics (ASCE)* 122, 402–411.
- LARSSON, L., K. RUNESSON AND M. ÅKESSON (1995). Embedded localization band based on regularized strong discontinuity. In D.R.J. Owen, E Oñate, and E. Hinton (Eds.), *Proc., 4th Int. Conf. Computational Plasticity*, Volume 1, 599–610.
- LARSSON, R. AND N. JANSSON (2002). Geometrically non-linear damage interface based on regularized strong discontinuities. *International Journal for Numerical Methods in Engineering* 54, 473–497.
- LARSSON, R., P. STEINMANN AND K. RUNESSON (1998). Finite element embedded localization band for finite strain plasticity based on a regularized strong discontinuity. *Mechanics of Cohesive-Frictional Materials* 4, 171–194.
- LAWSON, C.L. (1972). Transforming triangulations. *Discrete Math.* 3, 365–372.
- LAWSON, C.L. (1986). Properties of n-dimensional triangulations. *Computer Aided Geometric Design* 3, 231–246.
- LEE, E.H. (1969). Elastic-plastic deformation at finite strains. *Journal of Applied Mechanics* 36, 1–6.
- LEHMANN, T. (1960). Einige Betrachtungen zu den Grundlagen der Umformtechnik. *Ing. Arch.* 29, 1–21.

- LEMAITRE, J. (1985). A continuous damage mechanics model for ductile fracture. *J. Eng. Mat. Techn.* 107, 83–89.
- LI, X., M.S. SHEPHARD AND M.W. BEALL (2005). 3d anisotropic mesh adaptation by mesh modification. *Computer Methods in Applied Mechanics and Engineering* 194(48-49), 4915–4950.
- LIU, D.C. AND J. NOCEDAL (1989). On the limited memory method for large scale optimization. *Mathematical Programming B* 45(3), 503–528.
- LUBLINER, J. (1972). On the thermodynamic foundations of non-linear solid mechanics. *International Journal of Non-Linear Mechanics* 7, 237–254.
- LUBLINER, J. (1997). *Plasticity theory*. Maxwell Macmillan International Edition.
- MAIER, G. AND T. HUECKEL (1979). Nonassociated and coupled flow rules of elastoplasticity for rock-like materials. *Int. J. Rock Mech. Min. Science* 16, 77–92.
- MANDEL, J. (1966). Conditions de stabilité et postulat de Drucker. In *Proceedings of the IUTAM Symposium on Rheology*, 58–68. Springer: Berlin.
- MANDEL, J. (1972). *Plasticité Classique et Viscoplasticité*. Cours and Lectures au CISM No. 97. International Center for Mechanical Sciences, Springer-Verlag, New York.
- MANTYLA, M. (1988). *An Introduction to Solid Modeling*. Rockville, Maryland: Computer Science Press.
- MARSDEN, J.E. AND T.J.R. HUGHES (1994). *Mathematical foundation of elasticity*. Dover, New York.
- MATTHIES, H., G. STRANG AND E. CHRISTIANSEN (1979). The saddle point of a differential program. In Glowinski, Robin, and Zienkiewicz (Eds.), *Energy methods in finite element analysis*, 309–318. J. Wiley and sons: London.
- MAUGIN, A.M. (1992). *The thermodynamics of Plasticity and Fracture*. Cambridge University Press.
- MAUGIN, G.A. (1993). *Material Inhomogeneities in Elasticity*. Applied Mathematics and Mathematical Computation. Chapman & Hall.
- MAUGIN, G.A. (2001). *Configurational mechanics of materials*. Springer Wien.
- MCNEICE, G.M. AND P.V. MARCAL (1973). Optimization of finite-element grids based on minimum potential-energy. *Journal of Engineering for Industry-Transactions of the ASME* 95(1), 186–190.
- MIEHE, C. (1993). *Kanonische Modelle multiplikativer Elasto-Plastizität. Thermodynamische Formulierung und numerische Implementierung*. Habilitation, Forschungs- und Seminarbericht aus dem Bereich der Mechanik der Universität Hannover, Nr. F 93/1.

- MIEHE, C. (2002). Strain-driven homogenization of inelastic microstructures and composites based on an incremental variational formulation. *International Journal for Numerical Methods in Engineering* 55, 1285–1322.
- MIEHE, C., N. APEL AND M. LAMBRECHT (2002). Anisotropic additive plasticity in the logarithmic strain space: modular kinematic formulation and implementation based on incremental minimization principles for standard materials. *Computer Methods in Applied Mechanics and Engineering* 191, 5383–5425.
- MIEHE, C. AND M. LAMBRECHT (2003). Analysis of micro-structure development in shearbands by energy relaxation of incremental stress potentials: Large-strain theory for standard dissipative materials. *International Journal for Numerical Methods in Engineering* 58, 1–41.
- MIEHE, C. AND J. SCHRÖDER (1994). Post-critical discontinuous analysis of small-strain softening elastoplastic solids. *Archive of Applied Mechanics* 64, 267–285.
- MOËS, N., J. DOLBOW AND T. BELYTSCHKO (1999). A finite element method for crack growth without remeshing. *International Journal for Numerical Methods in Engineering* 46, 131–150.
- MOËS, N., A. GRAVOUIL AND T. BELYTSCHKO (2002a). Non-planar 3d crack growth by the extended finite element an level sets–Part I: Level set update. *International Journal for Numerical Methods in Engineering* 53, 2569–2586.
- MOËS, N., A. GRAVOUIL AND T. BELYTSCHKO (2002b). Non-planar 3d crack growth by the extended finite element an level sets–Part I: Mechanical model. *International Journal for Numerical Methods in Engineering* 53, 2549–2568.
- MOLINARI, J.F. AND M. ORTIZ (2002). Three-dimensional adaptive meshing by subdivision and edge-collapse in finite-deformation dynamic plasticity problems with application to adiabatic shear banding. *International Journal for Numerical Methods in Engineering* 53, 1101–1126.
- MOSLER, J. (2002). *Finite Elemente mit sprungstetigen Abbildungen des Verschiebungsfeldes für numerische Analysen lokalisierter Versagenszustände in Tragwerken*. Ph. D. thesis, Ruhr University Bochum.
- MOSLER, J. (2004). On the modeling of highly localized deformations induced by material failure: The strong discontinuity approach. *Archives of Computational Methods in Engineering* 11(4), 389–446.
- MOSLER, J. (2005a). Modeling strong discontinuities at finite strains - a novel numerical implementation. *Computer Methods in Applied Mechanics and Engineering*. in press.
- MOSLER, J. (2005b). A novel algorithmic framework for the numerical implementation of locally embedded strong discontinuities. *Computer Methods in Applied Mechanics and Engineering* 193(45-47), 4731–4757.

- MOSLER, J. (2005c). Numerical analyses of discontinuous material bifurcation: Strong and weak discontinuities. *Computer Methods in Applied Mechanics and Engineering* 194(9-11), 979–1000.
- MOSLER, J. (2005d). On advanced solution strategies to overcome locking effects in strong discontinuity approaches. *International Journal for Numerical Methods in Engineering* 63(9), 1313–1341.
- MOSLER, J. (2005e). On the efficient implementation of an elastoplastic damage model for large-scale analyses of material failure: A multiscale approach. *Computers & Structures* 83(4-5), 369–382.
- MOSLER, J. AND O.T. BRUHNS (2004). A 3D anisotropic elastoplastic-damage model using discontinuous displacement fields. *International Journal for Numerical Methods in Engineering* 60, 923–948.
- MOSLER, J. AND G. MESCHKE (2004). Embedded cracks vs. smeared crack models: A comparison of elementwise discontinuous crack path approaches with emphasis on mesh bias. *Computer Methods in Applied Mechanics and Engineering* 193(30-32), 3351–3375.
- MOSLER, J. AND G. MESCHKE (2000). 3D FE analysis of cracks by means of the strong discontinuity approach. In E. Oñate, G. Bugeda, and B. Suárez (Eds.), *European Congress on Computational Methods in Applied Sciences and Engineering*.
- MOSLER, J. AND G. MESCHKE (2001). FE-modeling of displacement discontinuities in inelastic continua. *Zeitschrift für Angewandte Mathematik und Mechanik* 81(Suppl. 4), 875–876.
- MOSLER, J. AND G. MESCHKE (2003). 3D modeling of strong discontinuities in elastoplastic solids: Fixed and rotating localization formulations. *International Journal for Numerical Methods in Engineering* 57, 1533–1576.
- MOSLER, J. AND M. ORTIZ (2005). On the numerical implementation of variational arbitrary Lagrangian-Eulerian (VALE) formulations. *International Journal for Numerical Methods in Engineering*. in press.
- MOSLER, J. AND M. ORTIZ (2006). h-adaption in finite deformation elasticity and plasticity. *International Journal for Numerical Methods in Engineering*. submitted.
- MOSLER, J., M. ORTIZ AND A. PANDOLFI (2006). Variational cohesive fracture models and three-dimensional crack tracking. In *7th World Congress on Computational Mechanics*. accepted.
- MUELLER, R. AND G.A. MAUGIN (2002). On material forces and finite element discretizations. *Computational Mechanics* 29, 52–60.
- MÜHLHAUS, H.B. AND E.C. AIFANTIS (1991). A variational principle for gradient plasticity. *International Journal for Solids and Structures* 28, 845–857.

- NAGHDI, P.M. (1990). A critical review of the state of finite plasticity. *Zeitschrift für Angewandte Mathematik und Physik* 315-394, 41.
- NEEDLEMAN, A. (1990). An analysis of decohesion along an imperfect interface. *International Journal of Fracture* 42, 21–40.
- NEGRI, M. (2005a). Convergence analysis for a smeared crack approach in brittle fracture. submitted, <http://cvgmt.sns.it/papers/>.
- NEGRI, M. (2005b). A discontinuous finite element approximation of free discontinuity problems. *Advances in Mathematical Sciences and Applications* 15, 283–306.
- NEMAT-NASSER, S. (2004). *Plasticity : A Treatise on Finite Deformation of Heterogeneous Inelastic Materials*. Cambridge University Press.
- NOLL, W. (1972). A new mathematical theory of simple materials. *Arch. Rational Mech. Anal.* 48, 1–50.
- NUISMER, R. (1975). An energy release rate criterion for mixed mode fracture. *International Journal of Fracture* 11, 245–250.
- OGDEN, R.W. (1997). *Non-linear elastic deformations*. Dover, Mineola, New York.
- OHLSSON, U. AND T. OLOFSSON (1997). Mixed-mode fracture and anchor bolts in concrete: Analysis with inner softening bands. *Journal of Engineering Mechanics (ASCE)* 123, 1027–1033.
- OLIVER, J. (1995a). Continuum modelling of strong discontinuities in solid mechanics. In D.R.J. Owen, E Oñate, and E. Hinton (Eds.), *Proc., 4th Int. Conf. Computational Plasticity*, Volume 1, 455–479.
- OLIVER, J. (1995b, 12). Continuum modelling of strong discontinuities in solid mechanics using damage models. *Computational Mechanics* 17(1-2), 49–61.
- OLIVER, J. (1996). Modelling strong discontinuities in solid mechanics via strain softening constitutive equations part 1: Fundamentals. part 2: Numerical simulations. *International Journal for Numerical Methods in Engineering* 39, 3575–3623.
- OLIVER, J. (2000). On the discrete constitutive models induced by strong discontinuity kinematics and continuum constitutive equations. *International Journal for Solids and Structures* 37, 7207 – 7229.
- OLIVER, J., M. CERVERA AND O. MANZOLI (1999, 3). Strong discontinuities and continuum plasticity models: The strong discontinuity approach. *International Journal of Plasticity* 15, 319–351.
- OLIVER, J., A.E. HUESPE, S. BLANCO AND D.L. LINERO (2006). Stability and robustness issues in numerical modeling of material failure with the strong discontinuity approach. *Computer Methods in Applied Mechanics and Engineering*. in press.

- OLIVER, J., A.E. HUESPE, M.D.G. PULIDO AND E. SAMANIEGO (2003). On the strong discontinuity approach in finite deformation settings. *International Journal for Numerical Methods in Engineering* 56, 1051–1082.
- OLIVER, J., A.E. HUESPE, M.D.G. PULIDO AND E. SAMANIEGO (2005). A comparative study on finite elements with embedded discontinuities: E-fem vs. x-fem. *Computer Methods in Applied Mechanics and Engineering*. in press.
- OLIVER, J., A.E. HUESPE, E. SAMANIEGO AND E.W.V. CHAVES (2002). On Strategies for Tracking Strong Discontinuities in Computational Failure Mechanics. In *Fifth World Congress on Computational Mechanics*.
- OLIVER, J. AND J.C. SIMO (1994). Modelling strong discontinuities in solid mechanics by means of strain softening constitutive equations. In H. Mang, N. Bićanić, and R. de Borst (Eds.), *Computational Modelling of concrete structures*, 363–372. Pineridge press.
- OLIVER, X. (1998). The strong discontinuity approach: An overview. *Computational Mechanics*, 1–19.
- OLOFSSON, T., M. KLISINSKI AND P. NEDAR (1994). Inner softening bands: A new approach to localization in finite elements. In H. Mang, N. Bićanić, and R. de Borst (Eds.), *Computational Modelling of Concrete Struct.*, 373–382. Pineridge press.
- ORTIZ, M. (1987). An analytical study of the localized failure modes of concrete. *Mechanics of Materials* 6, 159–174.
- ORTIZ, M. (2002). Computational Solid Mechanics – Lecture Notes. *California Institute of Technology*.
- ORTIZ, M. (2003). Continuum Mechanics – Lecture Notes. *California Institute of Technology*.
- ORTIZ, M., Y. LEROY AND A. NEEDLEMAN (1987). A finite element method for localized failure analysis. *Computer Methods in Applied Mechanics and Engineering* 61, 189–214.
- ORTIZ, M. AND A. PANDOLFI (1999). Finite-deformation irreversible cohesive elements for three-dimensional crack-propagation analysis. *International Journal for Numerical Methods in Engineering* 44 (9), 1267–1282.
- ORTIZ, M. AND A. PANDOLFI (2004). A variational Cam-clay theory of plasticity. *Computer Methods in Applied Mechanics and Engineering* 193, 2645–2666.
- ORTIZ, M. AND A. PANDOLFI (2005). Variational cohesive fracture models and three-dimensional crack tracking. unpublished.
- ORTIZ, M. AND J.J. QUIGLEY (1991). Adaptive mesh refinement in strain localization problems. *Computer Methods in Applied Mechanics and Engineering* 90, 781–804.

- ORTIZ, M., R.A. RADOVITZKY AND E.A. REPETTO (2001). The computation of the exponential and logarithmic mappings and their first and second linearizations. *International Journal for Numerical Methods in Engineering* 52(12), 1431–1441.
- ORTIZ, M. AND E.A. REPETTO (1999). Nonconvex energy minimisation and dislocation in ductile single crystals. *J. Mech. Phys. Solids* 47, 397–462.
- ORTIZ, M. AND L. STAINIER (1999). The variational formulation of viscoplastic constitutive updates. *Computer Methods in Applied Mechanics and Engineering* 171, 419–444.
- PANDOLFI, A., P. KRYSL AND M. ORTIZ (1999). Finite element simulation of ring expansion and fragmentation: The capturing of length and time scales through cohesive models of fracture. *International Journal of Fracture* 95(1-4), 279–297.
- PAPADOPOULOS, P. AND J. LI (1998). A general framework for the numerical solution of problems in finite elasto-plasticity. *Computer Methods in Applied Mechanics and Engineering* 159, 1–18.
- PAPOULIA, K., S. VAVASIS AND P. GANGULY (2005). Spatial convergence of crack nucleation using a cohesive element model on a pinwheel-based mesh. *International Journal for Numerical Methods in Engineering*. in press.
- PIJAUDIER-CABOT, G. AND Z.P. BAŽANT (1987). Nonlocal damage theory. *Journal of Engineering Mechanics (ASCE)* 113, 1512–1533.
- PINSKY, P.M., M. ORTIZ AND K.S. PISTER (1983). Numerical integration of rate constitutive equations in finite deformation analysis. *Computer Methods in Applied Mechanics and Engineering* 40, 137–158.
- RADIN, C. AND L. SADUN (1996). The isoperimetric problem for pinwheel tilings. *Commun. Math. Phys.* 177, 255–263.
- RADOVITZKY, R. (1998). *On mesh adaption in strongly nonlinear problems*. Ph. D. thesis, California Institute of Technology, Pasadena, USA.
- RADOVITZKY, R. AND M. ORTIZ (1999). Error estimation and adaptive meshing in strongly nonlinear dynamic problems. *Computer Methods in Applied Mechanics and Engineering* 172, 203–240.
- RADOVITZKY, R. AND M. ORTIZ (2000). Tetrahedral mesh generation based on node insertion in crystal lattice arrangements and advancing-front-delaunay triangulation. *Computer Methods in Applied Mechanics and Engineering* 187(3-4), 543–569.
- RANIECKI, B. AND O.T. BRUHNS (1981). Bounds to bifurcation stresses in solids with non-associated plastic flow law at finite strains. *Journal of the Mechanics and Physics of Solids* 29(2), 153–172.
- REQUICHA, A. A. G. (1980). Representations for Rigid Solids: Theory, Methods and Systems. *Computing Surveys* 12, 437–465.

- RICE, J.R. (1976). The localization of plastic deformation. In *Theoretical and Applied Mechanics*, 207–220. North-Holland.
- RICE, J.R. AND J.W. RUDNICKI (1980). A note on some features of the theory of localization of deformation. *International Journal for Solids and Structures* 16, 597–605.
- RIPPA, S. (1990). Minimal roughness property of the delaunay triangulation. *Computer Aided Geometric Design* 7, 489–497.
- RIVARA, M.-C. (1991). Local modification of meshes for adaptive and / or multigrid finite-element methods. *Journal of Computational and Applied Mathematics* 36, 79–89.
- RIVARA, M.-C. (1997). New longest-edge algorithms for the refinement and/or improvement of unstructured triangulations. *International Journal for Numerical Methods in Engineering* 40, 3313–3324.
- RIVARA, M.-C. AND CH. LEVIN (1992). A 3-D refinement algorithm suitable for adaptive and multi-grid techniques. *Communications in Applied Numerical Methods* 8, 281–290.
- ROCKAFELLAR, R.T. (1970). *Convex analysis*. Princeton University Press.
- RODRIGUEZ-FERRAN, A., PÉREZ-FOGUET AND A. HUERTA (2002). Arbitrary Lagrangian-Eulerian (ALE) formulations for hyperelastoplasticity. *International Journal for Numerical Methods in Engineering* 53, 1831–1851.
- RUDNICKI, J.W. AND J.R. RICE (1975). Conditions for localization of deformation in pressure-sensitive dilatant materials. *Journal of the Mechanics and Physics of Solids* 23, 371–394.
- SCHMIDT-BALDASSARI, M. AND K. HACKL (2006). Advanced time integration algorithms for rate independent finite strain elastoplasticity. *Computer Methods in Applied Mechanics and Engineering*. submitted.
- SCHNABEL, R.B. AND E. ESKOW (1990). A new modified cholesky factorization. *SIAM J. of Scientific Statistical Computing* 11, 1136–1158.
- SHEWCHUK, J. (2002). What is a good linear finite element? Interpolation, Conditioning, Anisotropy, and Quality Measures. <http://www.cs.cmu.edu/~jrs/jrspapers.html>.
- SIH, G. (1974). Strain-energy-density factor applied to mixed-mode crack problems. *International Journal of Fracture* 10, 305–321.
- SIMO, J.C. (1992). Algorithms for static and dynamic multiplicative plasticity that preserve the classical return mapping schemes of the infinitesimal theory. *Computational Mechanics* 99, 61–112.
- SIMO, J.C. (1998). Numerical analysis of classical plasticity. In P.G. Ciarlet and J.J. Lions (Eds.), *Handbook for numerical analysis*, Volume IV. Elsevier, Amsterdam.

- SIMO, J.C. AND F. ARMERO (1992). Geometrically non-linear enhanced strain mixed methods and the method of incompatible modes. *International Journal for Numerical Methods in Engineering* 33, 1413–1449.
- SIMO, J.C., F. ARMERO AND R.L. TAYLOR (1993). Improved versions of assumed enhanced strain tri-linear elements for 3d deformation problems. *Computer Methods in Applied Mechanics and Engineering* 110, 359–386.
- SIMO, J.C. AND T.J.R. HUGHES (1998). *Computational inelasticity*. Springer, New York.
- SIMO, J.C. AND J.W. JU (1989). On continuum damage-elastoplasticity at finite strains. *Computational Mechanics* 5, 375–400.
- SIMO, J.C. AND J. OLIVER (1994). A new approach to the analysis and simulation of strain softening in solids. In Z.P. Bažant, Z. Bittnar, M. Jirásek, and J. Mazars (Eds.), *Fracture and Damage in Quasibrittle Structures*, 25–39. E. & F.N. Spon, London.
- SIMO, J.C., J. OLIVER AND F. ARMERO (1993). An analysis of strong discontinuities induced by strain softening in rate-independent inelastic solids. *Computational Mechanics* 12, 277–296.
- SIMO, J.C. AND M. ORTIZ (1985). A unified approach to finite deformation elastoplasticity based on the use of hyperelastic constitutive equations. *Computer Methods in Applied Mechanics and Engineering* 49, 221–245.
- SIMO, J.C. AND K.S. PISTER (1984). Remarks on rate constitutive equations for finite deformation problems. *Computer Methods in Applied Mechanics and Engineering* 46, 210–215.
- SIMO, J.C. AND S. RIFAI (1990). A class mixed assumed strain methods and the method of incompatible modes. *International Journal for Numerical Methods in Engineering* 29, 1595–1638.
- SIMO, J.C. AND R.L. TAYLOR (1991). Quasi-incompressible finite element elasticity in principal stretches. Continuum basis and numerical algorithms. *Computer Methods in Applied Mechanics and Engineering* 85, 273–310.
- SIMONE, A., H. ASKES AND L.J. SLUYS (2004). Incorrect initiation and propagation of failure in non-local and gradient-enhanced media. *International Journal for Solids and Structures* 41, 351–363.
- SIMONE, A., G.N. WELLS AND L. SLUYS (2003). From continuous to discontinuous failure in a gradient-enhanced continuum damage model. *Computer Methods in Applied Mechanics and Engineering* 192, 4581–4607.
- SIMPSON, R.B. (1994). Anisotropic mesh transformation and optimal error control. *Applied Numerical Mathematics* 14, 183–198.
- SNYMAN, M. F., W. W. BIRD AND J. B. MARTIN (1991). A simple formulation of a dilatant joint element governed by Coulomb friction. *Engineering Computations* 8, 215–229.

- SPENCER, A.J.M. (1971). *Theory of invariants*, Chapter Continuum physics, 239–353. Academic Press, New York.
- SPENCER, A.J.M. AND R.S. RIVLIN (1962). Isotropic integrity basis for vectors and second-order tensors. *Arch. Rational Mech. Anal.* 9, 45–63.
- STAKGOLD, I. (1967). *Boundary value problems of mathematical physics*, Volume I. Macmillan Series in Advanced Mathematics and theoretical physics.
- STAKGOLD, I. (1998). *Green's functions and boundary value problems*. Wiley.
- STEIN, E. AND F.-J. BARTHOLD (1995). Elastizitätstheorie. *Skriptum, Universität Hannover*.
- STEINMANN, P. (2002). On spatial and material settings of hyperelastodynamics. *Acta Mechanica* 156, 193–218.
- STEINMANN, P. AND P. BETSCH (2000). A localization capturing FE-interface based on regularized strong discontinuities at large inelastic strains. *International Journal for Solids and Structures* 37, 4061–4082.
- STEINMANN, P., R. LARSSON AND K. RUNESSON (1997). On the localization properties of multiplicative hyperelasto-plastic continua with strong discontinuities. *International Journal for Solids and Structures* 34, 969–990.
- STOLARSKA, M., D.L. CHOPP, N. MÖES AND T. BELYTSCHKO (2001). Modelling crack growth by level sets in the extended finite element method. *International Journal for Numerical Methods in Engineering* 58(8), 943–960.
- SUKUMAR, N., N. MOËS, B. MORAN AND T. BELYTSCHKO (2000). Extended finite element method for three-dimensional crack modelling. *International Journal for Numerical Methods in Engineering* 48, 1549–1570.
- SVENDSON, B. (1998). A thermodynamic formulation of finite-deformation elastoplasticity with hardening based on the concept of material isomorphism. *International Journal of Plasticity* 14, 473–488.
- SZABÓ, B.A. AND I. BABŮSKA (1991). *Finite Element Analysis*. John Wiley & Sons, Inc.
- TAYLOR, G.I. AND H. QUINNEY (1937). The latent remaining in a metal after cold working. *Proc. R. Soc. Lond. A* 163, 157–181.
- TEMAN, R. AND G. STRANG (1980). Functions of bounded deformations. *Archive for Rational Mechanics and Analysis* 75, 7–21.
- THOMAS, Y. (1961). *Plastic Flow and Fracture of Solids*. Academic Press: New York.
- THOUTIREDDY, P. (2003). *Variational Arbitrary Lagrangian-Eulerian method*. Ph. D. thesis, California Institute of Technology, Pasadena, USA.

- THOUTIREDDY, P. AND M. ORTIZ (2004). A variational r-adaption and shape-optimization method for finite-deformation elasticity. *International Journal for Numerical Methods in Engineering* 61, 1–21.
- TRUESDELL, C. AND W. NOLL (1965). The nonlinear field theories. In S. Flügge (Ed.), *Handbuch der Physik*, Volume 3. Springer-Verlag, Berlin.
- TRUESDELL, C. AND R. TOUPIN (1960). The classical field theories. In S. Flügge (Ed.), *Handbuch der Physik*, Volume 3. Springer-Verlag, Berlin.
- VERFÜRTH, R. (1996). *A review of a priori error estimation and adaptive mesh-refinement techniques*. Wiley-Teubner.
- VERFÜRTH, R. (1999). A review of a posteriori error estimation techniques for elasticity problems. *Computer Methods in Applied Mechanics and Engineering* 176, 419–440.
- WANG, C.-C. AND C. TRUESDELL (1973). *Introduction to rational elasticity*. Noordhoff International Publishing Leyden.
- WEBER, G. AND L. ANAND (1990). Finite deformation constitutive equations and a time integration procedure for isotropic, hyperelastic-viscoplastic solids. *Computer Methods in Applied Mechanics and Engineering* 79, 173–202.
- WELLS, G.N. AND L.J. SLUYS (2001a). Analysis of slip planes in three-dimensional solids. *Computer Methods in Applied Mechanics and Engineering* 190, 3591–3606.
- WELLS, G.N. AND L.J. SLUYS (2001b). A new method for modelling cohesive cracks using finite elements. *International Journal for Numerical Methods in Engineering* 50, 2667–2682.
- WELLS, G.N. AND L.J. SLUYS (2001c). Three-dimensional embedded discontinuity model for brittle fracture. *International Journal for Solids and Structures* 38, 897–913.
- XIAO, H., O.T. BRUHNS AND A.T.M. MEYERS (2006). Elastoplasticity beyond small deformations: Basic variables, essential structures, and constitutive and computational implications. *Acta Mechanica*. in press.
- YANG, Q. (2004). *Thermomechanical variational principles for dissipative materials with application to strain localization in bulk metallic glasses*. Ph. D. thesis, California Institute of Technology, Pasadena, USA.
- YANG, Q., A. MOTA AND M. ORTIZ (2005). A class of variational strain-localization finite elements. *International Journal for Numerical Methods in Engineering* 62(8), 1013–1037.
- YANG, Q., L. STAINIER AND M. ORTIZ (2005). A variational formulation of the coupled thermo-mechanical boundary-value problem for general dissipative solids. *Journal of the Mechanics and Physics of Solids* 33, 2863–2885.



# Appendix A

## A tetrahedral shape measure

In this appendix, a tetrahedral shape measure fulfilling the conditions enumerated in Remark 4.6.2.1 is briefly presented. It was advocated in [KNUPP 2000A; KNUPP 2000B; FREITAG & KNUPP 2002]. The shape measure is based on the condition number of the mapping connecting an element  $e$  to its ideal counterpart (all edges have the same length). Clearly, this mapping measures the deviation of the physical to the ideal simplex. According to Fig. A.1, this mapping is given by  $\mathbf{F} \in \mathcal{L}(\mathbb{R}^3, \mathbb{R}^3)$  with  $\mathbf{F} : \boldsymbol{\xi} \mapsto \mathbf{J} \mathbf{W}^{-1} \boldsymbol{\xi}$ .

In the present work, the reference element

$$\Omega_M = \text{span}\{\mathbf{0}, \mathbf{e}_1, \mathbf{e}_2, \mathbf{e}_3\} \quad (\text{A.1})$$

is chosen. It can be seen directly, that the simplex

$$\Omega_{\text{ideal}} = \text{span}\{\mathbf{0}, \mathbf{e}_1, (1/2, \sqrt{3}/2, 0), (1/2, \sqrt{3}/6, \sqrt{2}/\sqrt{3})\} \quad (\text{A.2})$$

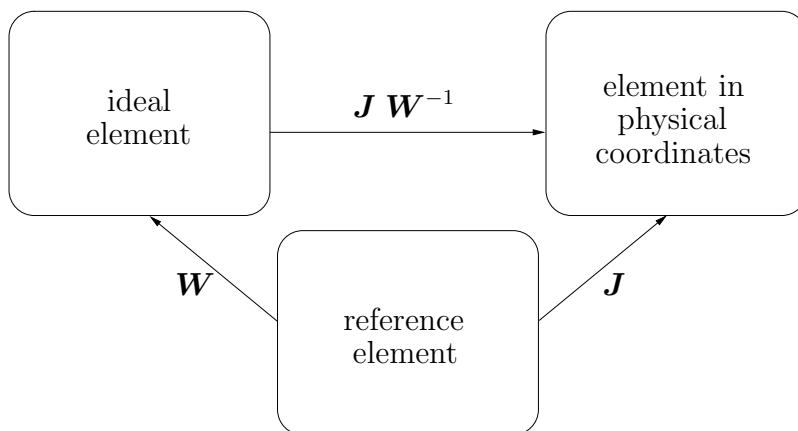


**Figure A.1:** Different configurations of a simplex element

is ideal, i. e., all edges of this element have the same length. Consequently, the mapping connecting  $\Omega_M$  to  $\Omega_{\text{ideal}}$  is characterized by the matrix

$$\mathbf{W} := \begin{pmatrix} 1 & 1/2 & 1/2 \\ 0 & \sqrt{3}/2 & \sqrt{3}/6 \\ 0 & 0 & \sqrt{2}/\sqrt{3} \end{pmatrix} \quad (\text{A.3})$$

and  $\mathbf{J}$  is the classical JACOBIAN matrix. It can be shown in a straightforward manner that

$$g(\mathbf{J}) = \min_{\mathbf{A}} \kappa(\mathbf{A} \mathbf{W}^{-1}) / \kappa(\mathbf{J} \mathbf{W}^{-1}) \quad (\text{A.4})$$

is a shape measure for simplex elements with  $\kappa$  being a condition number, i. e.,  $g$  fulfills the criteria according to Remark 4.6.2.1 and the shape of two simplex elements can be compared to one another by simply evaluating the function  $g$ , i. e.,

$$g(\mathbf{J}^{(1)}) > g(\mathbf{J}^{(2)}) \iff \text{the shape of element 1 is better.} \quad (\text{A.5})$$

Evidently, this maximum principle is equivalent to

$$\kappa(\mathbf{J}^{(1)} \mathbf{W}^{-1}) < \kappa(\mathbf{J}^{(2)} \mathbf{W}^{-1}) \iff \text{the shape of element 1 is better.} \quad (\text{A.6})$$

It is noteworthy that this criterion is equivalent to minimizing the interpolation error. More precisely, the local interpolation error for affine meshes is given by

$$|v - \mathcal{I}_k v|_{m,p} \leq c (\|\mathbf{J}\| \|\mathbf{J}^{-1}\|)^m \|\mathbf{J}\|^{l+1-m} |v|_{l+1,p} \quad \forall v \in W^{l+1,p}(\Omega). \quad (\text{A.7})$$

Here,  $\mathcal{I}_k v$ ,  $|\bullet|_{m,p}$ ,  $c$ ,  $\|\bullet\|$  and  $W^{a,b}(\Omega)$  denote the LAGRANGIAN interpolation of  $v$  by polynomials of order  $k$ , a semi-norm defining the classical SOBOLEV norms, a constant greater than zero, the induced EUCLIDIAN norm and the SOBOLEV spaces over the physical simplex  $\Omega$ , respectively, cf. [ERN & GUERMOND 2004]. For sufficiently smooth functions  $v$ , the estimate (A.7) is optimal.

If, without loss of generality, the ideal element is chosen as the reference element and the condition number based on the EUCLIDIAN norm is used, criterion (A.6) reads

$$\|\mathbf{J}^{(1)}\| \|\mathbf{J}^{(1)^{-1}}\| < \|\mathbf{J}^{(2)}\| \|\mathbf{J}^{(2)^{-1}}\| \iff \text{the shape of element 1 is better.} \quad (\text{A.8})$$

However, since  $\|\mathbf{J}^{(e)}\| \leq \tilde{c} \text{diam}(\Omega^e)$ , criterion (A.8) is equivalent to minimizing the local interpolation error (A.7) (if element 1 and 2 have almost the same diameter). As a consequence, the shape measure as defined by Eq. (A.4) is mathematically sound. It should be noted that several other shape measures exist which do not show this property, cf. [SHEWCHUK 2002].

Based on criterion (A.6) a given initial triangulation can be improved (with respect to the interpolation error) by applying the optimization strategy

$$\inf_{\mathbf{X}_h} I_{\text{geom}} \quad \text{with} \quad I_{\text{geom}} = \sum_{i=1}^{n_{\text{ele}}} (f(\mathbf{J}_i))^p \quad \text{and} \quad f(\mathbf{J}) = \kappa(\mathbf{J} \mathbf{W}^{-1}). \quad (\text{A.9})$$

In what follows, the exponent  $p$  is set to  $p = 2$ . Although the induced EUCLIDIAN norm appears canonically in the error estimate (A.7), it is not well suited for numerical computations. Hence, the condition number based on the FROBENIUS norm  $|\mathbf{A}| := \sqrt{\mathbf{A} : \mathbf{A}}$  is used, i. e.,  $\kappa^2(\mathbf{A}) = (\mathbf{A} : \mathbf{A}) (\mathbf{A}^{-1} : \mathbf{A}^{-1})$ .

If principle (A.9) (with  $p = 2$ ) in conjunction with a NEWTON iteration is applied to improve an initial discretization, the first and second derivatives of  $I_{\text{geom}}$  are required. Hence, the derivatives of  $\kappa^2(\mathbf{J} \mathbf{W}^{-1})$  with respect to the nodal coordinates  $\mathbf{X}^{(i)}$  ( $1 \leq i \leq 4$ ) have to be computed. They are summarized below.

With  $\mathbf{A} := \mathbf{J} \mathbf{W}^{-1}$  and  $f(\mathbf{J}) := (\mathbf{A} : \mathbf{A}) (\mathbf{A}^{-1} : \mathbf{A}^{-1})$ ,

$$\frac{\partial f}{\partial \mathbf{X}} = \frac{\partial f}{\partial \mathbf{A}} : \frac{\partial \mathbf{A}}{\partial \mathbf{J}} : \frac{\partial \mathbf{J}}{\partial \mathbf{X}} \quad (\text{A.10})$$

and hence,

$$\frac{\partial f}{\partial X_z} = \frac{\partial f}{\partial A_{oj}} W_{jp}^{-T} \frac{\partial J_{op}}{\partial X_z}. \quad (\text{A.11})$$

Using

$$\mathbf{J} = \begin{bmatrix} X_1^{(2)} - X_1^{(1)} & X_1^{(3)} - X_1^{(1)} & X_1^{(4)} - X_1^{(1)} \\ X_2^{(2)} - X_2^{(1)} & X_2^{(3)} - X_2^{(1)} & X_2^{(4)} - X_2^{(1)} \\ X_3^{(2)} - X_3^{(1)} & X_3^{(3)} - X_3^{(1)} & X_3^{(4)} - X_3^{(1)} \end{bmatrix}, \quad (\text{A.12})$$

Eq. (A.11) reads

$$\frac{\partial f}{\partial \mathbf{X}^{(i)}} = \frac{\partial f}{\partial \mathbf{A}} \cdot \mathbf{W}^{-T} \cdot \mathbf{n}^{(i)}, \quad (\text{A.13})$$

with

$$\begin{aligned} \mathbf{n}^{(1)} &= (-1; -1; -1) \\ \mathbf{n}^{(2)} &= ( 1; 0; 0) \\ \mathbf{n}^{(3)} &= ( 0; 1; 0) \\ \mathbf{n}^{(4)} &= ( 0; 0; 1) . \end{aligned} \quad (\text{A.14})$$

The second derivatives are given by

$$\left[ \frac{\partial^2 f}{\partial \mathbf{X}^{(x)} \partial \mathbf{X}^{(y)}} \right]_{ij} = \left[ \frac{\partial^2 f}{\partial \mathbf{A}^2} \right]_{iojp} [\mathbf{W}^{-T} \cdot \mathbf{n}^{(x)}]_o [\mathbf{W}^{-T} \cdot \mathbf{n}^{(y)}]_p. \quad (\text{A.15})$$

Finally, applying

$$\frac{\partial[|\mathbf{A}|^2]}{\partial \mathbf{A}} = 2 \mathbf{A} \quad (\text{A.16})$$

and

$$\frac{\partial[|\mathbf{A}^{-1}|^2]}{\partial \mathbf{A}} = 2 \mathbf{A}^{-1} : \frac{\partial \mathbf{A}^{-1}}{\partial \mathbf{A}} = -2 \mathbf{A}^{-T} \cdot \mathbf{A}^{-1} \cdot \mathbf{A}^{-T}, \quad (\text{A.17})$$

the first derivative of  $f(\mathbf{A})$  with respect to  $\mathbf{A}$

$$\frac{\partial[\kappa(\mathbf{A})^2]}{\partial \mathbf{A}} = 2 |\mathbf{A}^{-1}|^2 \mathbf{A} - 2 |\mathbf{A}|^2 \mathbf{A}^{-T} \cdot \mathbf{A}^{-1} \cdot \mathbf{A}^{-T} \quad (\text{A.18})$$

and the second derivative of  $f(\mathbf{A})$

$$\begin{aligned}
\frac{\partial^2[\kappa(\mathbf{A})^2]}{\partial \mathbf{A}^2} = & 2 |\mathbf{A}^{-1}|^2 \mathbf{1} \otimes \mathbf{1} - 4 \mathbf{A} \otimes [\mathbf{A}^{-T} \cdot \mathbf{A}^{-1} \cdot \mathbf{A}^{-T}] \\
& - 4 [\mathbf{A}^{-T} \cdot \mathbf{A}^{-1} \cdot \mathbf{A}^{-T}] \otimes \mathbf{A} \\
& + 2 |\mathbf{A}|^2 \mathbf{A}^{-T} \otimes [\mathbf{A}^{-1} \cdot \mathbf{A}^{-T} \cdot \mathbf{A}^{-1}] \\
& + 2 |\mathbf{A}|^2 [\mathbf{A}^{-T} \cdot \mathbf{A}^{-1}] \otimes [\mathbf{A}^{-1} \cdot \mathbf{A}^{-T}] \\
& + 2 |\mathbf{A}|^2 [\mathbf{A}^{-T} \cdot \mathbf{A}^{-1} \cdot \mathbf{A}^{-T}] \otimes \mathbf{A}^{-1}
\end{aligned} \tag{A.19}$$

are calculated. Here,  $[\mathbf{A} \overline{\otimes} \mathbf{B}]_{ijkl} := A_{ik} B_{jl}$  and  $[\mathbf{A} \underline{\otimes} \mathbf{B}]_{ijkl} := A_{il} B_{jk}$ .

## Appendix B

# Derivatives of a neo-HOOKEan energy functional

Closed form expressions for the stress tensors and their derivatives defined by the free energy functional

$$\Psi = \frac{1}{2}\lambda \log^2 J + \frac{1}{2}\mu (\text{tr}\mathbf{C} - 3 - 2 \log J), \quad J = \det \mathbf{F}, \text{tr}\mathbf{C} = \mathbf{C} : \mathbf{1} \quad (\text{B.1})$$

are summarized in this appendix. They have been given earlier in [THOUTIREDDY 2003; THOUTIREDDY & ORTIZ 2004; KUHLE, ASKES & STEINMANN 2004].

Using Eq. (B.1), the first PIOLA-KIRCHOFF stress tensor reads

$$\mathbf{P} = \frac{\partial \Psi}{\partial \mathbf{F}} = (\lambda \log J - \mu) \mathbf{F}^{-T} + \mu \mathbf{F} \quad (\text{B.2})$$

and the MANDEL stresses result in

$$\mathbf{M} = \Psi \mathbf{1} - \mathbf{F}^T \cdot \mathbf{P} = (\Psi - \lambda \log J + \mu) \mathbf{1} - \mu \mathbf{C}. \quad (\text{B.3})$$

Computing the second derivatives of  $\Psi$ , closed form expressions of the tangent tensors

$$\frac{\partial \mathbf{P}}{\partial \mathbf{F}} = \lambda \mathbf{F}^{-T} \otimes \mathbf{F}^{-T} + \mu \mathbf{1} \bar{\otimes} \mathbf{1} + (\mu - \lambda \log J) \mathbf{F}^{-T} \underline{\otimes} \mathbf{F}^{-1} \quad (\text{B.4})$$

$$\begin{aligned} \mathbb{C} = \mathbf{F}^{-T} \cdot \frac{d^2(\Psi J)}{d[\mathbf{F}^{-1}]^2} \cdot \mathbf{F}^{-T} = & J (\Psi - 2 \lambda \log J + 2 \mu + \lambda) \mathbf{1} \otimes \mathbf{1} \\ & - J (\Psi - \lambda \log J + \mu) \mathbf{1} \underline{\otimes} \mathbf{1} \\ & + J \mu (\mathbf{C} \underline{\otimes} \mathbf{1} + \mathbf{1} \underline{\otimes} \mathbf{C} - \mathbf{C} \otimes \mathbf{1} - \mathbf{1} \otimes \mathbf{C} + \mathbf{C} \bar{\otimes} \mathbf{1}) \end{aligned} \quad (\text{B.5})$$

and

$$\frac{\partial \mathbf{M}}{\partial \mathbf{F}} = [\lambda (\log J - 1) - \mu] \mathbf{1} \otimes \mathbf{F}^{-T} + \mu [\mathbf{1} \otimes \mathbf{F} - \mathbf{1} \underline{\otimes} \mathbf{F}^T - \mathbf{F}^T \bar{\otimes} \mathbf{1}] \quad (\text{B.6})$$

are computed. Here,  $[\mathbf{A} \bar{\otimes} \mathbf{B}]_{ijkl} := A_{ik} B_{jl}$  and  $[\mathbf{A} \underline{\otimes} \mathbf{B}]_{ijkl} := A_{il} B_{jk}$ .

# Appendix C

## Data structure for coarsening of a finite element mesh

In this appendix, a simple data structure providing all information necessary for the local mesh refinement/coarsening strategy according to Section 6.7 is given. Its main ingredients are two vectors of the type `Element` and `Edge`. Parts of the respective classes are shown in Fig. C.1.

```
class Edge
{
private:
    int Nr;
    std::vector<int > Element_List;           // neighboring elements
    std::vector< pair< int, int> > Parents;   // parent edges (the vertices)
    int Node_List[3];                       // nodes defining the edge
    int Cut;                                 // = 1 for refinement
    .                                        // =-1 for coarsening
    .
    .
}

class Element
{
private:
    int Nr;
    int Node_List[10];                      // nodes defining the element
    int Edge_List[6];                       // edges
    std::vector< pair< int, int> > Child_Edge; // list of child edges (vertices)
    .
    .
    .
}
```

**Figure C.1:** Parts of the c++ classes storing the information of the edges and the element objects